Elaboration et caractérisation de composites intelligents NiTi/ époxyde : effets de la transformation martensitique sur le comportement mécanique et sur la décohésion interfaciale

Yousef Payandeh

2010-ENAM-0032

École doctorale n° 432 : Science des Matériaux de l'Ingénieur

Doctorat ParisTech

T H È S E

pour obtenir le grade de docteur délivré par

l'École Nationale Supérieure d'Arts et Métiers

Spécialité " Mécanique et Matériaux "

présentée et soutenue publiquement par

Yousef PAYANDEH

le 14 décembre 2010

Elaboration et caractérisation de composites intelligents NiTi/ époxyde Effets de la transformation martensitique sur le comportement mécanique et sur la décohésion interfaciale

Directeur de thèse : **Fodil MERAGHNI**

Co- directeur de thèse : **Etienne PATOOR**

Jury :

Mme Shabnam ARBAB CHIRANI	Maitre de conférences HDR, LBMS, ENIB- Brest	Rapporteur
M. Joris DECRIECK	Professeur, Université de Gent, Belgique,	Rapporteur
M. Frédéric JACQUEMIN	Professeur, Université de Nantes	Examinateur
M. André EBERHARDT	Professeur	Examinateur
M. Fodil MERAGHNI	Professeur, LPMM, ENSAM, Metz	Examinateur
M. Etienne PATOOR	Professeur, LPMM, ENSAM, Metz	Examinateur

T H È S E

Arts et Métiers ParisTech - Centre de Metz
Laboratoire de Physique et Mécanique des Matériaux

Abstract

In this work a near equiatomic NiTi shape memory wire epoxy matrix composite is studied. The NiTi wire in as drawn condition was subjected to three heat treatments in order to prepare the wires with different transformation characteristics. Three metallic moulds were designed for different types of samples, namely pull-out, tensile and heterogeneous test specimens. The composite specimens were elaborated by casting followed by curing and post curing process. The tests were conducted at three temperatures (20, 80 and 90 °C) and at a constant cross-head speed.

The single NiTi wire specimens with a long embedded length were subjected to the pull-out test in order to study the effect of martensitic transformation/reorientation on the debonding initiation and also on the debonding propagation. For comparison, several steel wire samples were prepared through the same procedure. From in-situ observations, the debonding begins from wire entry point and proceeds to the embedded end. It was observed that when no phase transformation occurs in the wire, the debonding propagates rapidly whilst it is slow when there is wire phase transformation or martensitic reorientation. It was found that the debonding rate depends on the displacement rate as well as the length change during phase transformation. It has been experimentally found that, the interfacial shear strength increases when the martensitic transformation takes place.

The mechanical behavior of the resin matrix and the effect of test temperature, wire volume fraction have been determined using standard tensile test. The tests have been conduced at three temperatures. It is found that the martensitic transformation occurring in the wire affect the mechanical behavior of the composite specimens. In this way, using the wire with larger transformation stress enhances the composite tensile strength. This is achieved either by increasing the test temperature or by using the wires heat treated at lower temperatures. It is proposed that on the constraint of matrix, the transformation occurs simultaneously at several points that result in intermittent debonded and bonded zones.

In this work the samples with complex geometry were designed and fabricated in order to estimate the elastic properties of the composite material in two directions (perpendicular and parallel to the wire axis). The specimens with random speckle were then subjected to the simple loading. The heterogeneous displacement/strain fields generated due to the complex geometry of the composite samples were measured. An inverse method was established in this work and the material parameters were identified. The results were then compared to the results obtained by Mori-Tanaka method. Moreover, the numerical strain fields obtained using the identification parameters was compared to the experimental ones. A good correlation was found in both cases.

To:

My parents

my wife

and

my son.

Acknowledgements

I am deeply grateful to my supervisors Fodil Meraghni, Etienne Patoor and André Eberhardt for their scientific ideas and help during my five years in "Arts et Metiers ParisTech". I also wish to thank them for their kind and encouragements.

I would like to express my gratitude to Professor Joris Degrieck, Shabnam Arbab Shirani and Frederic Jaquemin for accepting to be on my thesis committee.

I would like to thank all my colleagues who helped me during this work, Bagher, Abderrahim, Nadine, Laurent, Oussama, Hedi, Rachid, Célia, Stephan, Alain, Gael, Olivier, Daniel, Marc and Badis.

Although a 5000-Km distance separates me from my parents, family and friends in Iran, please be assured that you are very close in my heart! I am grateful to all my friends for helping me from this long distance, in particular Hossein, Abbas, Mehrdad, and Hassan.

I am thankful to Ali Siadat and Fathallah Qods for advises and helps during my life in Metz. I wish to thank Bagher, Behrooz, Esmaeil, Somayeh, Hojat, Sahar, Shahab, Mohammad, Amir, Hossein and Vahid for their kind.

Special thank to my wife for her patience and encouragements.

Table of contents

Part I: Thesis

Table of figures viii

List of tables xiii

Introduction 1

Chapter 1. shape memory alloys and smart composites 4

1.1. Description of Shape Memory Alloys 4

1.1.1. General Properties 4

1.1.1.1. Introduction 4

1.1.1.2. Martensitic phase transformation 5

1.1.1.3. Shape memory effect (SME) 7

1.1.1.4. Superelasticity (SE) 8

1.1.2. Martensitic transformation in NiTi based alloys 12

1.2. State of the art of SMA composites 14

1.2.1. SMA-Polymer composite 15

1.2.1.1. NiTi-Epoxy matrix composite 17

1.2.1.2. Interfacial properties 19

1.2.2. SMA/metal matrix composites 19

1.2.3.1. Al matrix 20

1.2.3.2. Sn / In matrix 20

1.3. Identification techniques and Digital Image Correlation 21

1.3.1. Techniques d'identification 21

1.3.1.1. Introduction 21

1.3.1.2. Méthode de recalage par éléments finis 22

1.3.1.3. Méthode de l'erreur en relation de comportement 23

1.3.1.4. Méthode de l'écart à l'équilibre 24

1.3.1.5. Méthode des champs virtuels 25

1.3.2. Techniques de mesure de champs cinématiques 26

1.3.2.1. Généralités 26

1.3.2.2. Techniques de corrélation d'images numériques 28

1.3.2.2.1. Logiciel de corrélation d'images numériques Correli LMT et Q4 33

Algorithme de calcul et traitement numérique 33

Les particularités du logiciel Correli Q4 34

Performances sur les déplacements et les déformations 36

1.3.2.2.2. Logiciel de corrélation d'images numériques Vic2D 39

Reference 41

Chapter 2. Material elaboration and characterization methodologies 57
2.1. Objectives 57
2.2. Materials description 57
2.2.1. SMA wire 59
2.2.2. Epoxy matrix 66
2.3. Sample preparation 72
2.4. Pull-out test 74
2.5. Uniaxial tensile test 76
2.6. Heterogeneous test 77
References 80

Chapter 3. Characterization of the matrix/wire interface- influence of the martensitic transformation 83
3.1. Introduction 83
3.2. Analytical method 84
3.3. Effect of martensitic transformation on debonding initiation 88
3.4. Effect of martensitic transformation on debonding propagation 93
3.5. Conclusion 97
References 99

Chapter 4. Tensile properties: characterization and micromechanical modeling- influence of the martensitic transformation 102
4. 1. Introduction 102
4. 2. Experimental results 104
4. 3. Micromechanical analysis 111
4.3.1. Model development 111
4.3.2. Numerical results 117
4.4. Discussion 119
4.4.1. Comparison of micromechanical and experimental results 119
4.4.2. Effect of martensitic transformation on the mechanical behavior 127
4.4.3. Effect of martensitic transformation on the debonding mechanism 129
4.5. Conclusion 134
References 136

Chapter 5. Parameters identification of NiTi/epoxy composite 139
5.1. Introduction 139
5.2. Inverse Method 140
Identification algorithm 140
Cost function 140
Optimization algorithms 141
a- Gauss-Newton method 141
b- Levenberg-Marquardt 143
Determination of the sensitivity matrix 144
Stop criteria 145
5.3. Application to the NiTi wire composite 145
5.3.1. Convergence and stability analysis 148
5.3.1.1. Convergence test 148
Influence of the experimental database 148
Influence of the number of element and mesh size 149
Influence of the initial estimation 151
Influence of the regularization parameter (μ) 153
5.3.1.2. Stability analysis 154
5.4. Application for experimental strain fields 155
Correli-Q4 software 155
Vic2D software 156
5.4. Identification results 157
5.4.1. Identification results using Correli-Q4 157
4.4.2. Identification results using Vic2D 159
5.5. Conclusion 164
References 165

Conclusion 169

Appendix A: Mechanical behavior of the composite samples 172
A.1. Experimental results 172
A.2. Micromechanical results 175

Part II: Résumé étendu

Résumé étendu 180

Résumé 180
1. Introduction 182
2. Processus de fabrication et méthodologie de caractérisation 183
3. Caractérisation de l'interface matrice/ fils - Influence de la transformation martensitique 189
4. Propriétés en traction : caractérisation et modélisation micromécanique, influence de la transformation martensitique 197
5. Identification des paramètres 204
6. Conclusion 210

Table of figures

Chapter 1

Fig. 1.1. Free energy changes during martensitic phase transformation

Fig. 1.2. Schematic representation of the SME. The SMA material is deformed (AB) and unloaded (BC) at a temperature below M_f (M_{Mf}). The resulting deformation is restored during heating to a temperature above A_f (CD). The original dimensions are re-gained (DA) [Parlinska et al. 2001].

Fig. 1.3. Isothermal and isobaric pseudoelastic loading paths. The two most commonly encountered pseudoelasticity loading paths - and isothermal and isobaric one. For clarity, the initial loading from austenite to achieve the required constant stress for the isobaric path is not shown [Patoor et al. 2006].

Fig. 1.4. Schematic of isothermal, pseudoelastic stress-strain curve. The critical stresses σ^{Ms}, σ^{Mf}, σ^{As} and σ^{Af} required for initiation and completion of the forward and reverse transformation are obtained from the phase diagram on Figure 3. The maximum uniaxial transformation strain H^t is also shown [After Patoor et al. 2006].

Fig. 1.5. Schematic of isobaric, cooling/heating cycle. The critical temperatures $M^{\sigma s}$, $M^{\sigma f}$, $A^{\sigma s}$ and $A^{\sigma f}$ required for initiation and completion of the forward and reverse transformation are obtained from the phase diagram on Figure 3. [After Patoor et al. 2006].

Fig. 1.6. Typical Stress-Strain-Temperature curves for the Shape Memory alloys [Bernal 2004].

Fig. 1.7. Schematic representation for the appearance of shape memory effect and superelasticity, which is termed as ‘‘Transformation Pseudoelasticity’’ here, in temperature–stress space [Otsuka and Shimizu 1986].

Fig. 1.8. Three transformation paths in Ti–Ni-based alloys [Otsuka and Ren 2005]

Fig. 1.9. Stress–strain curves as a function of temperature of a Ti–50.5Ni single crystal, which was aged at 673 K for 1 h after solution-treatment. The S–S curves are related with R-phase transformation or deformation of R-phase. T‘R= Rs [Miyazaki et al. 1988].

Fig. 1.10: Schématisation des termes métrologiques de résolution, incertitude et limite de détection [Triconnet 2007].

Figure 1.11: Schéma d’un montage de corrélation d’images numériques bidimensionnel, [Sutton et al. 1999].

Figure 1.12 : Exemple pour un déplacement de corps rigide du mouchetis (a) image et imagette de référence et (b) image et imagette déformée à l’instant t.

Fig. 1.13 : Principe de la technique de corrélation d’images numériques avec Correli Q4 [El Bartali 2007]

Chapter 2

Fig. 2.1. DSC for M-550 and M450 with 5 K/min in Ar and M-400 wires with 10 K/min in He atmosphere

Fig. 2.2. Stress -Strain diagram for a) M-400, b) M-450 and c) M-550 wires at room temperature

Fig. 2.3. Stress -Strain diagram for a) M-400, b) M-450 and c) M-550 wires at 80 °C

Fig. 2.4.Stress --Strain diagram for a) M-400, b) M-450 and c) M-550 wires at 90 °C

Fig. 2.5. Variation of M_s under stress for all three wires

Fig.2.6. DSC results for TR3, TR4 and TR5, 10 K/min in air atmosphere

Fig. 2.7. Mechanical behavior of epoxy matrix at room temperature.

Fig. 2.8. Mechanical behavior of the epoxy matrix at different temperatures (TR4).

Fig. 2.9. Mechanical behavior of the epoxy matrix for two post curing temperatures (TR3 and TR4).

Fig.2.10. The mould for pull-out specimensFig. 2.11. The mould using to prepare the simple tensile samples and the specimens with complex geometry

Fig. 2.12. Macroscopic cracks existing in the samples fabricated with a brittle matrix

Fig.2.13. Residual thermal stress for a M-550 NiTi wire epoxy matrix composite using photoelastisity

Fig.2.14. Experimental set-up

Fig.2.15 (a) Experimental set-up (b) side section (c) up view

Fig. 2.16. The simple tensile test specimen

Fig. 2.17. Heterogeneous strain fields generated in Meuwissen-type sample, applied displacement: 0.6 mm

Fig. 2.18. The Heterogeneous test specimen

Fig. 2.19. The experimental set-up with a Meuwissen sample. View of the random speckle pattern.

Chapter 3

Fig. 3.1- Maximum shear stress vs. applied stress, τ_i and σ_p^* are interfacial shear strength and debonding stress, respectively

Fig. 3.2. Maximum shear stress vs. applied stress for different embedded wire lengths

Fig3.3- Beta vs. embedded wire length for different applied stresses

Fig. 3.4- Beta vs. embedded wire length for different specimen diameters

Fig. 3.5- Beta vs. embedded wire length for different wire's Young moduli

Fig3.6- Beta vs. embedded wire length for different wire radius

Fig. 3.7- Debonding process along the wire embedded length during the test. (a) M-550, (b) M-450, (c) M-400 and (d) Steel wire. In all cases, the first image (left hand side) was taken before test and in the first case the last one was taken just after completed debonding. The arrows show the position of debonding.

Fig. 3.8- Force - Displacement diagram for the specimens with (a) M-550 and (b) M450 wire

Fig. 3.9- Force - Displacement diagram for the specimens with M-400 wire (a) without and (b) with transformation

Fig. 3.10 - Force - Displacement diagram for the specimens with steel wire Fig. 3.11- Maximum shear stress vs. applied stress for different wire's Young moduli

Fig. 3.12- Debonding rate for a specimen with a) M-550, b) M-400 and c) M-400 wires d) a, b and c for comparisonFig. 3.13- Normalized force and debonding rate for the specimen of Fig. 3.9-b and 3.12-c, the force is divided by transformational load and the DR is divided by the average rate.

Chapter 4

Fig. 4.1- Stress -Strain diagram for the composite samples with M450 wire, at 80 °C and with v_f=0.06.

Fig. 4.2- Stress -Strain diagram for the composite samples with M550 wire, at 80 °C and with v_f=0.06.

Fig. 4.3- Stress -Strain diagram for the composite samples with M550 wire, at 80 °C and with v_f=0.12.

Fig. 4.4. Stress -Strain diagram for the composite samples with M550 wire at 80 °C for different wire volume fractions.

Fig. 4.5. Stress -Strain diagram for the composite samples with M550 wire with V_f=0.06, at different temperatures.

Fig. 4.6. Stress -Strain diagram for the composite samples with M550 wire with v_f=0.12, at different temperatures.

Fig. 4.7. Stress -Strain diagram for the composite samples with v_f=0.06 at 80 °C for two different wires.

Fig. 4.8. Stress -Strain diagram for the composite samples with v_f =0.12 at 90 °C for three different wires.

Fig. 4-9. Axial and shear stress distribution along an embedded wireFig. 4-10. Axial and shear stress distribution along an embedded wire

Fig. 4-10. Axial and shear stress distribution along an embedded wire

Fig. 4-11. Stress-strain behavior of the matrix, wire and composite at 20 °C

Fig. 4.12. Stress -Strain diagram for the composite samples with different wires at 20°C for V_f=0.12.

Fig. 4.13- Stress -Strain diagram of composite samples with M550 wire v_f=0.12 at three temperatures.

Fig. 4.14- Stress -Strain diagram for the composite samples with M550 wire at 90°C for three V_f.

Fig. 4.15. Mechanical behavior of the M550 wire composite for V_f=0.06 at 80 °C

Fig. 4.16. Mechanical behavior of the M550 wire composite for V_f=0.12 at 80 °C

Fig. 4.17. Mechanical behavior of the M550 wire composite for V_f=0.12 at 80 °C

Fig. 4.18. Mechanical behavior of the M550 wire composite for V_f=0.06 at 90 °C

Fig. 4.19. Mechanical behavior of the M450 wire composite for V_f=0.06 at 80 °C

Fig. 4.20. Mechanical behavior of the M450 wire composite for V_f=0.12 at 90 °C

Fig. 4.21. Mechanical behavior of the M400 wire composite for V_f=0.12 at 90 °C

Fig. 4.22. Young modulus vs. temperature for three volume fractions

Fig. 4.23. Young modulus vs. volume fraction for three temperatures

Fig. 4.24. Tensile strength vs. temperature for three volume fractions

Fig. 4.25. Tensile strength vs. volume fraction for three temperatures

Fig. 4.22. Tensile strength for samples with three wires (V_f=0.12) at 90 °C

Fig. 4.27. Normalized debonded length (L_d) vs. applied strain for different wires at 20 °C.

Fig. 4.28. Normalized debonded length (L_d) in 0. 5% applied strain for different wires at 20 °C.

Fig. 4.29. Normalized debonded length (L_d) in 0. 5% applied strain for NiTi wires vs. temperature.

Fig. 4.30. Applied strain at which the debonding begins vs. temperature for NiTi wire samples

Fig. 4.31- Interfacial shear stress vs. length for steel wire in three strain levels.

Fig. 4.32- Interfacial shear stress vs. length for M550 wire in three strain levels.

Fig. 4.33- Stress -Strain diagram for the composite samples with M450 and M550 wires, at 80 °C.

Fig. 4-33. The debonded regions taking place in NiTi wire composites

Fig. 4.34- longitudinal stress distribution for M550 wire composite samples in four strain levels (at 20°C, V_f=0.06).

Fig. 4.35. Stress distribution in the embedded M550 wire with martensitic reorientation at T=20 °C

Fig. 4.36. Stress distribution in embedded steel wires (without MT) at 20 °C

Fig. 4.37. Stress distribution in embedded M450 wires with MT at 20 °C

Chapter 5

Fig. 5.1. Identification method

Fig. 5.2. Calculation of sensitivity matrix for *n* parameters

Fig. 5.3. Effect of mesh size on the reaction force

Fig. 5.4. The zones of interest (ZOI) with a) 656, b) 400, c) 336 elements

Fig. 5.5. Variation of a) the cost function and b) the parameters versus iteration number.

Fig. 5.6. Variation of a) the cost function and b) the parameters versus iteration number.

Fig. 5.7. Variation of a) the cost function and b) the parameters versus iteration number.

Fig. 5.8. Variation of a) the cost function and b) the parameters versus iteration number for 5% error.

Fig. 5.9. Variation of a) the cost function and b) the parameters versus iteration number for 10% error.

Fig. 5.10- The element size and the sub-image location in a) FE and b) experimental studied areas

Fig.5.11- Strain ε_{22} calculated numerically in each element using the identified parameters compared to the experimental values

Fig.5.12- Strain ε_{11} calculated numerically in each element using the identified parameters compared to the experimental values

Fig.5.13- Strain ε_{12} calculated numerically in each element using the identified parameters compared to the experimental values

Fig. 5.14. Strain fields determined experimentally using VIC2D are compared to the numerical ones

Fig. 5.15. Displacement fields determined experimentally using VIC2D are compared to the numerical ones

Fig. 5.16. Identification results compared to the results obtained from tensile test

Fig. 5.17. Identification results compared to the results calculated by Marfia and Sacco [25]

Fig. 5.18. Identification results compared to the results obtained using Mori-Tanaka's model

List of tables

Chapter 2

Table 2.1. Some characteristics of NiTi wires subjected to different heat treatments

Table 2.2. Transformation temperatures (°C) of NiTi alloys after selected heat treatments

Table 2.3- The stress at which the transformation begins in the wires

Table 2.4. The preparation and curing conditions and obtained glass transition temperatures (T_g ° C)

Chapter 3

Table 3.1. Variation of the parameters in the model of Fu [2] for different wire lengths and Young's moduli using a = 0.5 mm, b = 7.5 mm, σ_p = 100 MPa

Table 3.2. The calculated model dimensionless constants for different wire lengths and Young's moduli using a = 0.5 mm, b = 7.5 mm

Table 3.3. Results summary

Table 3.4- Debonding rate, v_d, displacement rate V_i (mm/min) and ε^{tr} and their relationship

Chapter 4

Table 4.1. Young modulus and stress at 2% strain for M550 wire composites at different temperatures

Table 4. 2. Stress at 2% strain for composites with different wires at 90 °C

Table 4. 3. Change of trend in stress-strain curve at different temperature for M550 wire samples

Table 4. 4. Change of trend in stress-strain curve for composites with different wires at 90

Chapter 5

Table 5.1. Identification results obtained using artificial database for three sets of reference parameters

Table 5.2. Effect of applied displacement on method's convergence, using 336-element set

Table 5.3. Effect of the mesh size on the identifiably of parameters, applied displacement=0.6 mm

Table 5.4. Effect of the number of elements on method's convergence, applied displacement=1.2 mm

Table 5.5. Identification results for three different sets of initial guess

Table 5.6- Variation of the cost function and the parameters with iteration number.

Table 5.7. Identification results using perturbed experimental database (stability study)

Table 5.8- Identification results, the experimental database created using Correli-Q4 software

Table 5.9- Identification results, the experimental database created using VIC2D software

Table 5.10. Material parameters and results obtained by Jarali et al. [26] and Marfia and Sacco [25]

Table 5.11. Material parameters obtained using Mori-Tanaka's model (E_f=30000 MPa, ν_f=0.3)

Introduction

Shape Memory Alloys (SMAs) are a group of alloys that exhibit a phenomenon known as the shape memory effect, (SME). This effect gives these alloys the ability to "recover" their original shape after being heated above a certain transition temperature. These materials present a large recovery strain, of up to 8%, associated with the transition.

Shape recovery, constraint recovery and superelastisity are the most important properties associated with SMAs. A large number of innovative applications is now developed from these properties in many different areas like aerospace, oil industry and biomedical. In recent years, SMAs properties found new applications with the development of smart composites for shape control, vibration control and damage resistance.

There is a need to produce "smart" materials which are able to sense, actuate and respond to the surrounding environment. Much research is being directed towards these new "smart" materials. The term "adaptive" is used also for these materials which become increasingly popular. This thesis focuses on SMAs reinforced matrix and investigates several aspects of these new materials.

With the possibility of using SMA-composites in real structures such as in aviation, high speed transport industry and the automotive industry, there are increasing demands on knowing how these composites will react under everyday conditions. A special attention is required because some SMA fiber characteristics change during phase transformation that can affect the interfacial properties. Therefore, prior to implementing these composites into functional structures, it needs to work on the fiber phase transformation in embedded situation and interfacial characteristics of these kinds of composite.

In this work, near equiatomic NiTi wires were embedded into the matrix material which consists of epoxy resin and an amine hardener. The experimental procedure including the elaboration process and testing the composite samples is detailed in chapter 2. Thermo-mechanical characterization of the SMA wires and epoxy matrix is also studied and discussed in this chapter.

The strain recovery of NiTi wire embedded in the matrix induces a high interfacial stress which can generate an interfacial debonding. Moreover, during the mechanical test the interface can be debonded because the properties of the matrix and wire are different. Thus it is necessary to study the wire/matrix interface in order to evaluate its mechanical response

and developing a well designed interface. Chapter 3 focuses mainly on the mechanical characterization of NiTi/epoxy interface.

Chapter 4 deals with the investigation of thermo-mechanical behavior of composite samples. In this chapter the effects of wire volume fraction, type of wire and test temperature have been investigated. To this end, specimens with three different wires and different wire volume fractions (0, 6, and 12%) are studied when subjected to the tensile load at room temperature (20), 80 and 90 °C. The influence of the martensitic transformation in wires on the overall behavior of the composite specimens is discussed. A micromechanical model is developed to better understanding the role of NiTi wires in the composite.

When a material is isotropic, it is possible to identify the parameters just by performing a standard tensile test. But for an anisotropic material, such as studied composites material, several standard tests are required to identify the material parameters. For this purpose, a heterogeneous test was carried out by applying simple load on the samples with complex geometry. This kind of tests allows the simultaneous identification of different parameters. The main problem is to measure the heterogeneous displacement/strain fields generated during these types of tests. Another problem is the fact that for heterogeneous tests there is no explicit relationship between displacement and the applied load which means that the stress tensor would be unknown. Therefore, an inverse method is required to identify the material parameters. In chapter 5 of this work the identification procedure is explained. This strategy is developed to identify the four independent elastic constants E_{11}, E_{22}, G_{12} and ν_{12} of the composite samples.

Chapter 1.

Shape memory alloys and smart composites

1.1. Description of Shape Memory Alloys

1.1.1. General Properties

1.1.1.1. Introduction

1.1.1.2. Martensitic phase transformation

1.1.1.3. Shape memory effect (SME)

1.1.1.4. Superelasticity (SE)

1.1.1.5. Two way shape memory effect (TWSME)

1.1.2. Martensitic transformation in NiTi based alloys

1.2. State of the art of SMA composites

1.2.1. SMA-Polymer

1.2.1.1. Epoxy matrix composite

1.2.1.2. Interface

1.2.2. SMA/metal matrix composites

1.2.3.1. Al matrix

1.2.3.2. Sn / In matrix

1.3. Identification techniques and Digital Image Correlation

1.3.1. Techniques d'identification

1.3.1.1. Introduction

1.3.1.2. Méthode de recalage par éléments finis

1.3.1.3. Méthode de l'erreur en relation de comportement

1.3.1.4. Méthode de l'écart à l'équilibre

1.3.1.5. Méthode des champs virtuels

1.3.2. Techniques de mesure de champs cinématiques

1.3.2.1. Généralités

1.3.2.2. Techniques de corrélation d'images numériques

1.3.2.2.1. Logiciel de corrélation d'images numériques Correli LMT et Q4

Algorithme de calcul et traitement numérique

Les particularités du logiciel Correli Q4

Performances sur les déplacements et les déformations

1.3.2.2.2. Logiciel de corrélation d'images numériques Vic2D

References

1.1. Description of Shape Memory Alloys

1.1.1. General Properties

1.1.1.1. Introduction

Shape Memory Alloys (SMAs) are metallic alloys exhibiting martensitic phase transformations when they are subjected to thermo-mechanical loads. They can return to the original shape which yields to recover some percents of permanent strains after heating to a certain temperature (A_f). At this temperature the crystal undergoes the reverse transformation from martensite to parent austenitic phase with a high symmetry. The martensitic phase transformation is the key characteristic of SMAs. The martensitic transformation is a shear-dominant diffusionless solid-state phase transformation occurring by nucleation and growth of the martensitic phase from the parent austenitic phase [Olson and Cohen 1982]. The Shape Memory Effect (SME) and superelasticity (Pseudoelasticity) are the main characteristics of SMAs which make them to be different from other materials.

During Martensitic Transformation (MT), the SMAs transform from a high-symmetry (austenitic) phase to a low-symmetry phase (martensitic). In absence of applied stresses, the MT takes place in a self-accommodating manner in which the variants of the martensitic phase usually arrange themselves through twinning. In this case neither macroscopic shape change nor inelastic strain is observable. By applying a load, however, the martensitic reorientation occurs in which the martensitic variants reorient into a single variant (detwinning). This phenomenon leads to large inelastic strains which can be as large as 8%. After heating above certain temperature, the reverse transformation takes place and the inelastic strains are recovered. This effect is known as the SME. Superelasticity occurs when the crystal in austenitic phase is subjected to thermo-mechanical loading. In this case, the MT is induced by applied load (Stress Induced Martensite: SIM) and detwinned martensite is directly produced from austenite. The large inelastic strains produced in this process are recovered upon unloading due to the reverse phase transformation [Wayman 1983]. The extensive list of alloys exhibiting SME and superelasticity includes the Ni-Ti alloys, and many copper-, iron-, silver- and gold-based alloys [Nishiyama 1978].

Martensitic transformations are usually divided into two groups: thermoelastic and nonthermoelastic [Popov 2005]. The nonthermoelastic transformations occur mainly in ferrous alloys. They are associated with non-mobile martensite-parent phase interfaces pinned by permanent defects and proceed by successive nucleation and growth. Due to re-nucleation of austenite during the reverse transformation, these transformations are crystallographically nonreversible in the sense that the martensite can not revert to the parent phase in the original orientation [Patoor et al. 2006]. The thermoelastic martensitic transformations, on the other

hand, are associated with mobile interfaces between the parent and martensitic phases. These interfaces are capable of "backward" movement during the reverse transformation by shrinkage of the martensitic plates rather than nucleation of the parent phase, which leads to a crystallographically reversible transformation [Otsuka and Wayman 1999]. The unique properties of SMAs (i.e. SME, SE) are the result of thermoelastic martensitic transformation [Patoor et al. 2006].

The MT takes place when the chemical free energy of the martensitic phase is less than that of the austenitic phase. According to Tamura [Tamura 1992] the free energy change ($\Delta G^{A\rightarrow M}$) during martensitic transformation can be described as:

$$\Delta G^{A\rightarrow M} = \Delta G_C + \Delta G_{NC} \qquad (1.1)$$

where ΔG_C is the chemical free energy change resulting from the structural change (austenite to martensite) and ΔG_{NC} is the non chemical energy. The ΔG_{NC} which opposing the transformation involves two terms: an elastic strain energy change (stored in the system when the transformation proceeds on cooling) and a surface energy change resulting from the production of internal interfaces during the transformation. $\Delta G^{A\rightarrow M}$ is the driving force for the transformation. By applying an external load or cooling to a certain temperature (M_f), the transformation goes right and the reverse transformation takes place by heating or removing the external load. Fig. 1.1 explains schematically the transformation in the term of free energy.

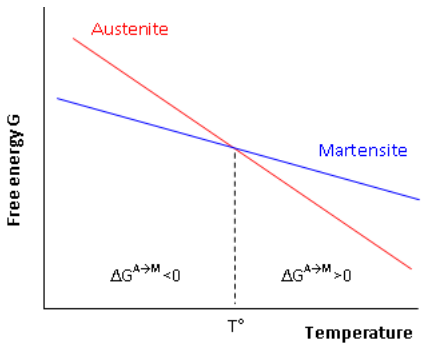

Fig. 1.1. Free energy changes during martensitic phase transformation

1.1.1.2. Martensitic phase transformation

The martensitic transformation is diffusionless, inelastic deformation of the crystal lattice; it is a result of cooperative and collective motion of atoms (i.e. atomic layer by atomic layer) in which each atom moves over a distance smaller than the lattice parameters [Otsuka and

Wayman 1999]. The crystal structure of transformed material will be different and occupies a different volume in comparison to the austenite [Tsoi 2002]. The phase transformation is highly sensitive to temperature and applied stresses [Delaey 1990].

During the martensitic transformation, new structure must change shape via slip or twinning accommodation. Twinning accommodation is fully reversible. For the shape memory effect, to be reversible, twinning must be and is the dominant process. Twin boundaries have a very low energy and are also very mobile. If a stress is applied to the structure the twin boundaries are able to move very easily to accommodate the stress [Tsoi 2002].

When the martensitic transformation takes place, numerous physical properties are modified. During the transformation, the latent heat is released or absorbed depending on the transformation direction. The forward, austenite-to-martensite transformation (denoted A → M) is an exothermic phase transformation and the reverse one is accompanied by the absorption of heat corresponding to a change in the transformation enthalpy [Patoor et al. 2006, Tsoi 2002]. Thus, the release or absorption of latent heat allows measuring the transformation temperatures using a differential calorimetry. The two phases also have different electrical resistance due to their different crystallographic structures. The change in electrical resistance is used to determine the transformation temperatures [Popov 2005].

In this section, at first the zero applied stress is considered because, as mentioned, the phase transformation is sensitive to applied external stress. The forward A→M transformation occurs when the free energy of martensite becomes lower than the free energy of austenite (i.e. $\Delta G^{A\rightarrow M}<0$). The free energy depends on the temperature and at a critical temperature T^0 the free energies of the two phases are equal (Fig. 1.1) which leads the system to be in thermodynamic equilibrium. As the temperature is lowered below T^0, the transformation does not begin exactly at T^0. Like a solidification process, there is a nucleation barrier to the formation of martensite. Thus significant supercooling is necessary to provide enough free energy which acts as the driving force for the nucleation of the M phase. At a temperature M_s (martensite start temperature at zero stress), the required free energy difference is available for the transformation [Delaey 1990]. The transformation continues as the temperature decreases to a temperature M_f (martensitic finish temperature at zero stress) is reached. The same argument applies to the reverse transformation (denoted M→ A) where considerable superheating is required. In this case the transformation begins at the temperature A_s, higher than T^0. When a temperature A_f is reached the material is entirely in the austenitic phase. The terms A_s and A_f are used to signify the austenite start and finishing temperatures at zero stress. The equilibrium temperature T^0 is approximately $(M_s + A_s)/2$ [Tong and Wayman 1974].

For shape memory alloys, the transformation temperatures M_s, M_f, A_s, A_f, are important factors in characterizing shape memory behavior. The transformation temperatures depend mainly on the alloy's composition and processing such as heat treatment conditions.

Microstructural defects, degree of order and grain size of the parent phase can also alter the transformation temperatures [Macqueron et al. 1991]. Note that the existence of exact temperatures Ms, M_f, A_s and A_f is an assumption. In reality, small amounts of either phase can exist beyond the finish temperatures and be formed before the start temperatures [Patoor et al. 2006].

Upon cooling of the SMA, the martensite is generated in twinned structures [Otsuka and Wayman, 1999], which accommodate the transformation strain of the individual martensitic variants. Two twinned variants are formed on each side of a mirror plane, so that no observable macroscopic strain is generated. The defects and inhomogeneities introduced during the manufacturing or treating the material can hinder the formation of twins [Otsuka and Wayman 1999].

Due to the displacive character of the martensitic transformation, applied stress plays a very important role. The application of stress on a volume of austenite has the effect of orienting the different martensitic variants in the direction of the stress during the A→M phase transformation. This leads to the development of large inelastic strains composed of a shearing component that induces shape change and an expansion component that effects volume change. The shearing component is the dominating one and is oriented in the direction of the stress [Popov 2005]. As a result positive work (the inelastic strains and stress have the same direction) is done by the material, thus its total energy is reduced. Therefore, the A→M phase transformation starts at higher temperature compared to the zero stress case. Moreover, if an appropriate stress field is applied, twinned martensite (denoted by M^t) is forced to reorient or detwin which forms detwinned martensitic (denoted by M^d) [Popov 2005].

1.1.1.3. Shape memory effect

As mentioned earlier, the shape memory effect (or SME) is a property of SMAs undergoing thermoelastic martensitic transformation. It is exhibited when the SMA is deformed while in the martensitic phase and then unloaded while still at a temperature below M_f. When subsequently heated above A_f it regains its original shape by transforming back into the austenitic phase. During the cooling of the parent phase to a temperature lower than M_f it transforms to twinned martensite. Fig. 1.2 shows the shape memory effect schematically. Loading the material at this temperature causes stress induced detwinning and development of inelastic strains. Upon unloading the material remains in detwinned state and the inelastic strains are not recovered. Finally, when it is heated above A_f, the SMA returns to its parent phase and the inelastic strains are recovered.

The stress-free cooling of austenite produces self-accommodating growth of the martensitic variants such that there is no macroscopic transformation strain [Saburi et al. 1980]. The self-accommodated morphology is a characteristic of the crystallography of the alloy used. For

example, in copper-based alloys, twenty-four variants of martensite constitute six self-accommodated groups scattered around the ⟨011⟩ poles of austenite with typical diamond morphology. The growth of such groups produces no macroscopic transformation strain, but the multiple interfaces present in these structures (boundaries between the martensite variants and twinning interfaces) are very mobile. This great mobility is at the heart of the shape memory effect. Movement of these interfaces accompanied by detwinning is obtained at stress levels far lower than the plastic yield limit of martensite. This mode of deformation, called reorientation of variants, dominates at temperatures lower than M_f.

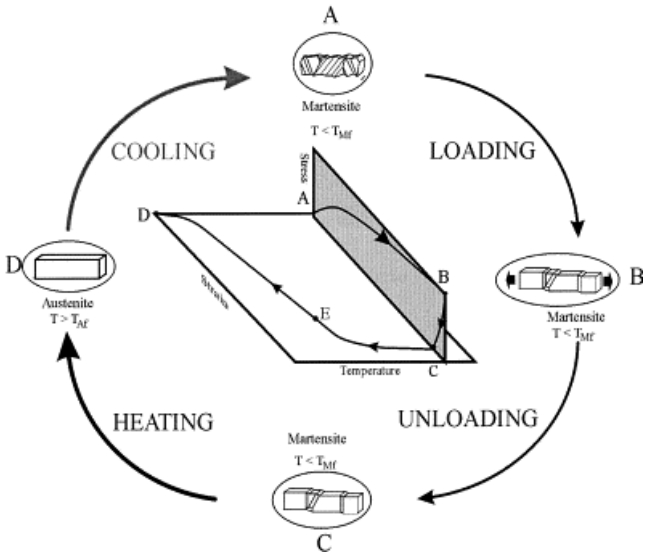

Fig. 1.2. Schematic representation of the SME. The SMA material is deformed (AB) and unloaded (BC) at a temperature below M_f (M_{Mf}). The resulting deformation is restored during heating to a temperature above A_f (CD). The original dimensions are re-gained (DA) [Parlinska et al. 2001].

During the second stage, the mechanical loading in the martensitic phase leads to reorientation of the variants and results in development of large inelastic strains. This inelastic strain is not recovered upon unloading. During the last step, heating the sample above A_f induces the reverse transformation and recovers the inelastic strain. When the material approaches A_f, the martensitic phase becomes unstable in the absence of stress. This results in a complete transformation to the parent phase. Since martensite variants have been reoriented by stress, the reversion to austenite produces a large transformation strain having the same amplitude but opposite direction to the inelastic strain. As a result, the SMA returns to the original shape that it had in the austenitic state.

1.1.1.4. Superelasticity

The superelastic behavior of SMAs is associated with stress induced strain recovery upon unloading at temperatures above A_f. Under most general conditions, superelastic thermo-

mechanical loading paths start at zero stress in the austenitic region, then move to the detwinned martensite region and then unload again to the starting point. An example is the isothermal loading paths shown schematically on Figure 1.3. Note that isothermal condition can be achieved only by quasi-static (small strain increments) loadings, so that the latent heat generated/absorbed during the phase transformation has time to dissipate.

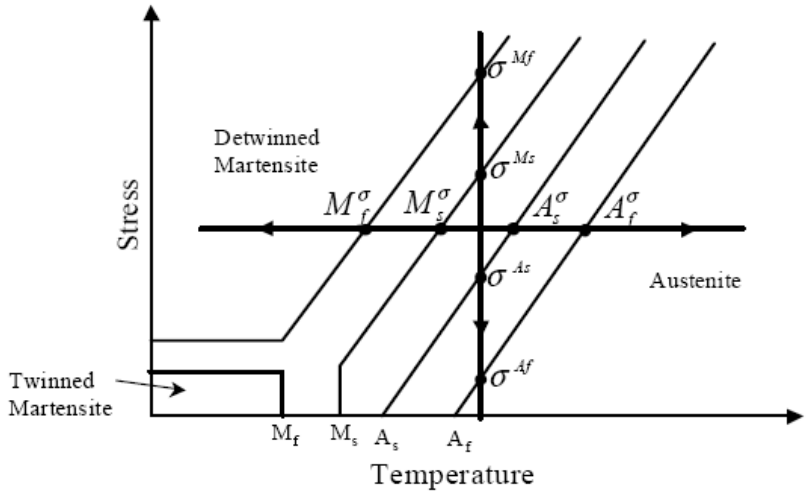

Fig. 1.3. Isothermal and isobaric pseudoelastic loading paths. The two most commonly encountered pseudoelasticity loading paths - and isothermal and isobaric one. For clarity, the initial loading from austenite to achieve the required constant stress for the isobaric path is not shown [Patoor et al. 2006].

To better illustrate the uniaxial stress strain response, consider the (quasi-static), isothermal loading path shown on Figure 1.3, and the corresponding schematic of the stress-strain response in Figure 1.4. The path begins at zero-stress, zero strain state in the austenitic region and proceeds by monotonously increasing the stress level. The initial material response is elastic, until the critical stress σ^{Ms} is reached. At this point on the stress-temperature diagram, the material hits the forward $A \rightarrow M^d$ transformation strip and begins to develop large inelastic strains. The transformation proceeds until the critical stress σ^{Mf} is reached. The maximal uniaxial transformation strain is denoted by H^t (Figure 1.4). Further increase in stress leads to elastic material response. The transformation region is characterized by significant decrease in stiffness as can be seen from stress-strain response in Figure 1.4. Upon unloading, the material response is again linear until the stress decreases to the critical level σ^{As}, when the reverse transformation strip $M^d \rightarrow A$ is reached. The completion of the reverse transformation occurs at a critical stress level σ^{Af}. Further unloading is characterized again by elastic response.

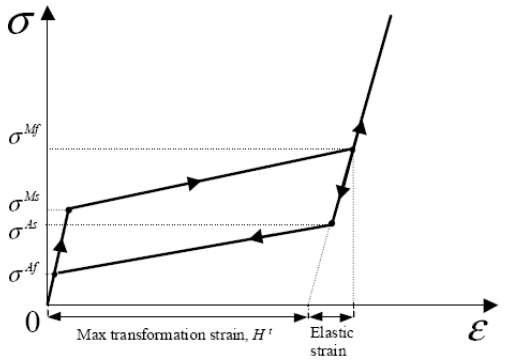

Fig. 1.4. Schematic of isothermal, pseudoelastic stress-strain curve. The critical stresses σ^{Ms}, σ^{Mf}, σ^{As} and σ^{Af} required for initiation and completion of the forward and reverse transformation are obtained from the phase diagram on Figure 1.3. [After Patoor et al. 2006].

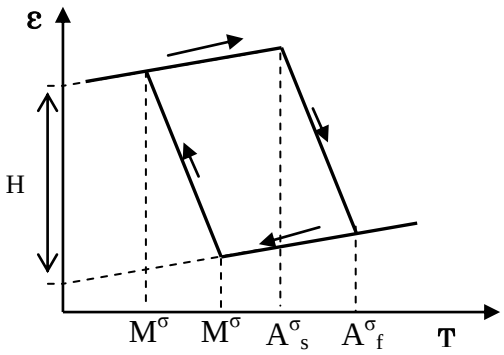

Fig. 1.5. Schematic of isobaric, cooling/heating cycle. The critical temperatures $M^{\sigma s}$, $M^{\sigma f}$, $A^{\sigma s}$ and $A^{\sigma f}$ required for initiation and completion of the forward and reverse transformation are obtained from the phase diagram on Fig. 1.3. [After Patoor et al. 2006].

The response of an SMA under isobaric cooling/heating exhibits similar hysteretic behavior. Under cooling at constant applied stress σ (Figures 1.3 and 1.5) the material initially shows small thermoelastic change in strain until the critical temperature M^{σ}_s is reached. The forward phase transformation $A \rightarrow M^d$ is characterized again by development of large transformation strain H^t and is complete when the martensitic finish temperature M^{σ}_f is reached. Further cooling leads to only thermoelastic change in strain. The reverse transformation occurs when the material is heated to temperature A^{σ}_s and is complete by A^{σ}_f.

In some cases aging of martensite phase can enable reversal of martensitic twins. This phenomenon of reversible detwinning and twinning of the martensitic variants creates an S-S curve similar to the pseudoelastic curve. This phenomenon is called rubber-like effect [Otsuka and Wayman 1999]. This effect, first observed in an Au-Cd alloy [Olander 1932], constitutes the first studied manifestation of shape memory effect. This type of behavior is a characteristic of the martensitic phase ($T < M_f$). It is observed in specific SMA materials, and unlike the superelastic phenomenon, this involves reorientation within the same phase. Since twin boundaries are very mobile, the critical stress required to move them is very small (a few MPa). Temperature plays only a secondary role in this behavior since there is no phase change. When the motion of twin boundaries is not reversible, the loading/unloading path results in an inelastic strain. However, when the twin boundary motion is reversible during unloading (e.g., in Au-Cd alloys), the macroscopic strain thus obtained is composed of the usual elastic strain and a reversible component associated with the movement of these interfaces. Some authors [Otsuka et al. 1976; Otsuka and Wayman 1999] use the term pseudoelasticity to denote both austenite to detwinned martensite phase transformations and the rubber-like effect of reversible detwinning of twinned martensite. In order to distinguish

between the two, the term superelasticity is used for the first process. In this work the term superelasticity will be used.

Figure 1.6 shows the relationship between stress, strain and temperature with respect to the SME and SE effects of SMAs [Bernal 2004].

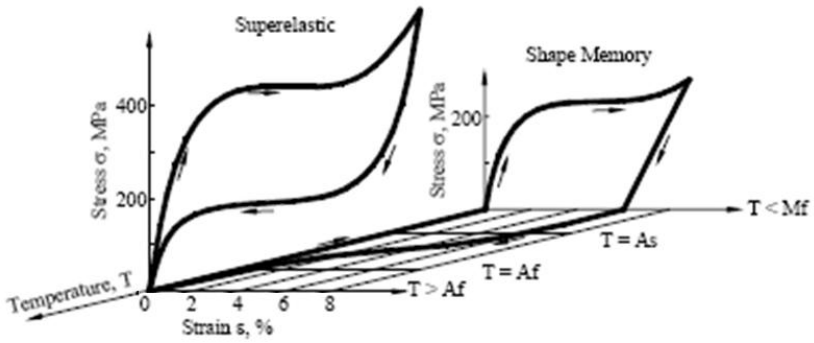

Fig. 1.6. Typical Stress-Strain-Temperature curves for the Shape Memory alloys [Bernal 2004].

The Clausius–Clapeyron relationship [Burkart and Read 1953, Wollants et al. 1979] helps to analyze the stress-induced martensitic transformation and can be summarized in the following form:

$$d\sigma/dT = -\Delta S^{tr}/\varepsilon = -\Delta H^{tr}/T\varepsilon \qquad (1.2)$$

where σ is a uniaxial applied stress, ε a transformation strain, ΔS^{tr} and ΔH^{tr} are the entropy and enthalpy of transformation per unit volume, respectively. When a crystal in austenitic state transforms to martensite, ΔS^{tr} and ΔH^{tr} are negative. Thus the slope of dσ/dT must be positive for SIM. In Fig. 1.7, the critical stress for stress-induced transformation is shown.

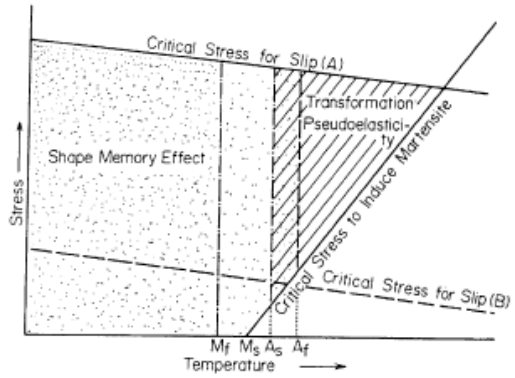

Fig. 1.7. Schematic representation for the appearance of shape memory effect and superelasticity, which is termed as ‘‘Transformation Pseudoelasticity’’ here, in temperature–stress space [Otsuka and Shimizu 1986].

However, it is almost impossible to observe superelasticity in NiTi alloys in solution-treated condition, because the critical stress for slip is so low. This critical stress for slip corresponds

to the case (B) in Fig. 1.7. Thus, when a specimen is subjected to an applied stress at a temperature above A_f slip occurs before the onset of the stress-induced transformation, and thus the superelasticity does not appear. This is one of the characteristics of NiTi alloys compared to other ß-phase shape memory alloys. In NiTi alloys, the critical stress for slip must be increased using adequate thermo-mechanical treatments (cold working, precipitation strengthening, grain refinement) [Otsuka and Ren 2005]. In these alloys for a given chemical composition, the shape memory properties can be strongly modified by thermal treatments. This large versatility is one of the advantages presents by these alloys. This ability to adjust the thermo-mechanical response of a given alloy, will be an advantage in the present study (see chapter 2, SMA wire properties in section 2.2.1)

1.1.2. Martensitic transformation in NiTi based alloys

There are three distinct types of martensitic transformations in NiTi-based alloys. The first type is obtained when binary NiTi alloys are quenched from high temperature (parent phase). The martensite in this case is called B19' (monoclinic).

The second type is a two-step transformation. The first transformation upon cooling is called ''R-phase transformation''. The second one is the transformation from R-phase to B19'. The R-phase has a trigonal structure [Otsuka and Ren 2005]. It was shown that the R-phase transformation is a martensitic transformation [Hwang et al. 1983, Miyazaki and Otsuka 1984, Khachin et al. 1979, Khachin et al. 1978, Ling and Kaplov 1980, Ling and Kaplov 1981]. The R-phase transformation competes with the subsequent martensitic transformation from R-phase to B19' [Otsuka and Ren 2005].

The third type of transformation is obtained when Ni is substituted by Cu in a binary NiTi alloy. In this case the transformation occurs in two steps upon cooling. The martensite upon the first transformation is called B19 (**orthorhombic**), and the second transformation represents the one from B19 to B19'. The martensitic transformations in $Ti_{50}Ni_{50-x}Cu_x$ alloys depend on composition [Otsuka and Ren 2005]. Thus the three types of transformations may be classified as shown in Fig. 1.8.

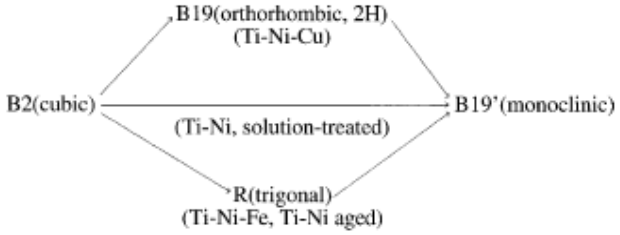

Fig. 1.8. Three transformation paths in Ti–Ni-based alloys [Otsuka and Ren 2005]

There are three cases in which the R-phase transformation occurs [Miyazaki and Otsuka 1986]:

- A few % of Ni in Ti–50Ni alloy is substituted by Fe or Al;
- Ni-rich NiTi alloys are aged at proper temperatures (say 400 °C) to cause the precipitationof Ti_3Ni_4 phase;
- Heat-treatment of NiTi alloys after cold-working to create rearranged dislocation structures.

In these cases, both R-phase and B19' phase are affected by the third element (Fe or Al), stress field of precipitates (recently it turned out that the effect of precipitates is more complex), and stress field of high density rearranged dislocations, respectively [Otsuka and Ren 2005].

The mechanical behavior associated with the R-phase was first observed by Khachin and co-workers [Khachin et al. 1979, Khachin et al. 1978] by tensile tests on binary NiTi alloys. They observed two-stage yielding in the S–S curve, and ascribed the first stage due to the rearrangement of R-phase variants, and the second stage to the stress-induced martensitic transformation from the R-phase to B19' martensite. They also observed the strain recovers by heating to a temperature above R_s.

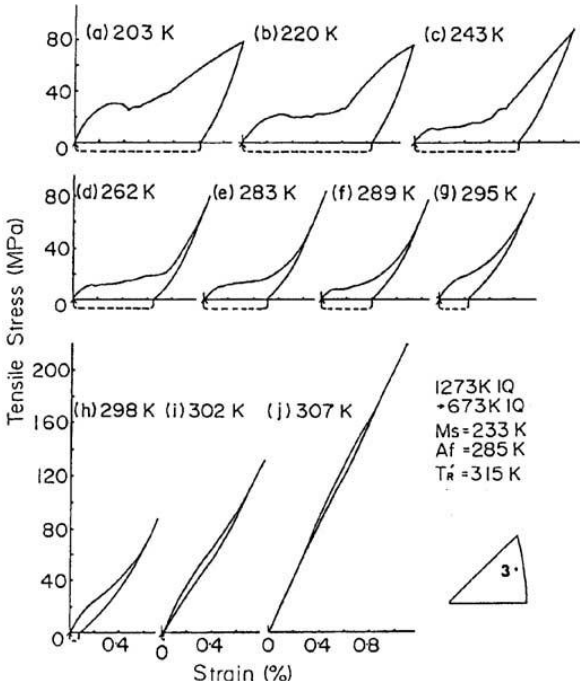

Fig. 1.9. Stress–strain curves as a function of temperature of a Ti–50.5Ni single crystal, which was aged at 673 K for 1 h after solution-treatment. The S–S curves are related with R-phase transformation or deformation of R-phase. $T'_R = R_s$ [Miyazaki et al. 1988].

Miyazaki et al. [Miyazaki et al. 1988] measured S–S curve associated with R-phase transformation as a function of temperature for various orientations. One example of such S–S curves is shown in Fig. 1.9. They found that the recovered strain is a function of deformation temperature and increases with decreasing temperature. They reported also that in ordinary shape memory alloys, the lattice parameters of martensite do not change significantly with temperature whilst the parameters of R-phase changes sharply with temperature.

Miyazaki and co-workers [Miyazaki et al. 1988, Miyazaki and Otsuka 1986] studied the shape memory and superelasticity effects for NiTi polycrystals. From these studies, the flow stress for detwinning/ twinning of R-phase in the alloy with high density of dislocation is much higher than that for the alloy with precipitates. This means that high density of dislocations compared to precipitates is more resistant for twin boundary movement of R-phase.

The R-phase transformation in SMAs does produce a SME and superelasticity [Otsuka 1990]. The austenite to R-phase transformation is fully reversible and the size of the hysteresis is dependent on the interfacial energies of the phase boundaries [Otsuka and Ren 2005].

The details of the R-phase transformation can be found in many papers, including Ling and Kaplow (1981), Stachowiak and McCormick (1988), Leclerq et al. (1994) and Sittner et al. (2006). Tobushi et al. (1996) showed that the thermo-mechanical properties, including the shape memory effect and superelasticity, due to the R-phase transformation, are stable under cyclic deformation. Ling and Kaplow (1981) showed that a recoverable strain of 1.37% can be obtained with the R-phase transformation, before the martensitic transformation occurs.

Due to the properties of the R-phase transformation, these alloys can be used for such devices as thermal actuators, where a small temperature hysteresis and reliability are required.

1.2. State of the art of SMA composites

A large numbers of SMA composite materials have been studied by the researchers. The metallic matrices such as Al and Sn were used as well as the polymeric ones. Various kinds of smart hybrid composites can be designed by incorporating shape-memory material components with composite materials. Wei and co-workers [Wei et al. 1998] have reviewed the design, fabrication, characterization and performance of various hybrid smart composites based on the shape-memory materials.

Researchers have investigated many applications for SMA embedded composite structures including their use in changing the camber of aircraft wings [Beauchamp et al 1992], as well as in vibration control [Friend and Mattey 1998, Bidaux et al. 1997, Gotthardt and Bidaux 1988, Bidaux et al. 1996, Hebda et al. 1995 and Simpson and Boller 2002] and reduction of impact damage [Tsoi et al. 2003, Paine and Rogers 1994a, Paine and Rogers 1994b and Paine and Rogers 1994c]. They also used them to enhance the performance of structures [Tsoi et al.

2004]. The shape-memory hybrid composites can be utilized to tailor or tune the overall performance of a smart structural system due to some unique properties such as self-strengthening, active modal modification, damage resistance and control [Wei et al. 1998]. This type of composite can be used for noise reduction in rotor blade systems [Lau 2002a] and sound transmission/radiation of composite panels [Liang et al. 1991]. Lau [Lau 2002a] has demonstrated that the natural frequency and damping properties of composite structures could be actively controlled by using embedded pre-strained SMA wires. It is reported that the use of embedded SMA actuators for composite beams deflection and buckling controls provided very promising results in which the composite beams could sustain further external loads without failures by high deflection or buckling. The embedded SMA actuators could induce an additional bending moment, in order to provide an additional strength to the composite beams. It therefore altered the overall beams' stiffness [Lau 2002]. It has already been demonstrated the ability of SMA fiber to enhance the mechanical properties of composites by adding a compressive stress to the matrix when the shape-memory effect is activated [Liu et al. 2008].

Several authors have been studied the material properties of composite structures embedding SMA components. The integrity of SMA wires with respect to the shape memory effect has been investigated by Paine and Rogers [Paine and Rogers 1991]. Jonnalagadda and Sottos [Jonnalagadda and Sottos 1997] investigated the internal stresses induced by actuation of a thin SMA ribbon embedded in a polymer matrix. Rogers et al. [Rogers et al. 1991] conducted experimental and analytical analyses of embedded SMA hybrid composites using photoelastic techniques to determine the stress–strain distribution. The stress distribution in the SMA composites during activation of the wires is also investigated by other researchers [Psarras et al. 2001 and Parthenios et al 2001].

Tsoi and co-workers studied the thermo-mechanical behavior of SMA-composites [Tsoi et al. 2004]. Some researchs have been conducted to determine the transformational behavior of SMA composites [Zheng et al. 2003a, Tsoi et al. 2002, Stalmans et al. 2000, Schrooten et al 2000]. Li et al. [Li et al. 2001] studied the reverse martensitic transformation characteristics of pre-strained TiNi shape memory alloy (SMA) wires embedded in metal, polymer and cement composite matrixes.

1.2.1. SMA-Polymer composites

Since the initial attempts of embedding Nitinol wires into polymers [Liang et al. 1989, Roger 1990a], much efforts have been made to study the properties of SMA-polymer composites. General aspects of hybrid systems consisting of polymers and NiTi SMAs were discussed by Neuking et al. [Neuking et al. 2005]. Investigations concerning the design of shape memory hybrid polymer matrix composites have shown the influence of volume fraction [Schrooten et

al. 2001], surface treatment [Jonnalagadda et al. 1997], pre-strain of the shape memory components [Schrooten et al. 2001, Zheng et al. 2002], and matrix curing process [Vokoun et al. 2003] on the properties of SMA hybrid composites. Some other works have been performed in the last decade. Kim [Kim 2006] developed a polymer-composite actuator with thin SMA strips. Tahiri et al. [Tahiri et al. 2004] and Winzek et al. [Winzek et al. 2003] increased the functionality of a SMA actuator by combining the SMA with a polymer and exploiting the difference between the phase transition temperature of the SMA and the glass transition temperature of the polymer. Murasawa et al. [Murasawa et al. 2004] investigated mechanical behaviour and failure of SMA/polymer-composites. It was highlighted that surface quality strongly affects the adhesion between the polymer and the metal [Neuking et al. 2008]. Good adhesion between polymer and NiTi shape memory alloys is necessary for all potential applications of this type of hybrid system [Poon et al. 2005] and [Ehrenstein 2004]. Smith et al. [Smith et al. 2004] reported recently, that they could increase the adhesive force between NiTi and a polymer matrix by using silane coupling agents. The effect of mechanical, chemical and physical parameters on the adhesion between a NiTi /polymer matrix has been studied by Neuking [Neuking et al. 2008]. They found that surface treatments can strongly improve adhesion between a NiTi shape memory ribbon and polyamide (PA6) [Neuking et al. 2008]. The damping capacity and toughness of NiTi fibers polymer matrix was evaluated by Raghavan et al. [Raghavan et al. 2010]. Appreciable improvement was observed in damping, tensile, and impact properties of the polymer matrix due to reinforcement with superelastic SMA fibers. However a slight loss in toughness was observed when the SMA fibers were pre-strained to enhance the damping capacity.

Schrooten et al. [Schrooten et al. 2001] predicted the behavior of the SMA-composites starting from the experimental results on SMA-wires and the knowledge of composite materials. The results were compared to the experimental ones obtained from thermo-mechanical experiments which were performed on the SMA-composites [Schrooten et al. 2001]. Jonnalagadda [Jonnalagadda et al. 1998] studied a thin SMA ribbon in a polymer matrix to quantify the internal stresses induced by the actuation [Jonnalagadda et al. 1998]. The research carried out by Yamashita and Shimamoto [Yamashita and Shimamoto 2004] deals with the mechanical strengthening and crack closure effect of shape-memory alloy (TiNi) fiber reinforced polycarbonate (PC) composite [Yamashita and Shimamoto 2004].

It is reported that increasing the pre-strain level enhances the ability of the composites to close crack tips [Shimamoto et al. 2004] and results higher yield strength [Yamada et al. 1993]. However, according to research performed by Zheng and co-workers, a high pre-strain does not improve significantly the thermo-mechanical behavior of shape memory hybrid composites [Zheng et al. 2005a], but reduces significantly the quality of the interface and the actuating ability of the composites [Zheng et al. 2002] and [Zheng et al.2003a].

1.2.1.1. NiTi/ epoxy matrix composite

There are numerous systems consisting of an epoxy matrix in which SMA elements in the form of wires, ribbons or strips have been incorporated [Bollas et al. 2007] [Lau et al. 2002b] [Lau et al. 2002c] [Lau et al. 2002d] [Shimamoto and Taya 1997]. The integrity of the SMA–epoxy resin interface, the integrated SMA displacements, the development of stress contours along the SMA and the host deformation are some of the parameters that have been studied [Jonnalagadda et al. 1997], [Jonnalagadda et al. 1998], [Yamashita and Shimamoto 2004] and [Murusawa et al. 2004].

In some works, SMA elements have been incorporated into composite materials that consist of an epoxy matrix reinforced by conventional fibers such as glass, graphite or aramid. Representative systems studied are beams of epoxy/graphite fibers/SMA wires and epoxy/glass fibers/SMA wires [Hebda et al. 1995] and [Xu et al. 2004]. The reason for using a fibrous composite as a host material is the excellent mechanical properties per unit weight that these materials offer, which make them ideal for structural "adaptive" or "smart" systems [Bollas et al. 2007].

Turner [Turner 2001] studied an epoxy resin/glass fiber/SMA ribbon system in which they recorded the generated stress as a function of the activation temperature for various pre-strain levels. A great deal of data concerning the deformation of an epoxy resin/glass fiber/NiTiCu system as a function of the activation duration, deformation rate and the SMA pre-strain level, for different volume fractions of SMA wires, have been generated by Zheng and co-workers [Zheng et al. 2003a] [Zheng et al. 2005a] and [Zheng et al. 2005b]. Bollas et al. [Bollas et al. 2007] made an effort to assess the capability of pre-strained SMA wires as stress generators in epoxy resin/aramid fiber composites, at the macro and micro-scale. Tsoi et al. [Tsoi et al. 2002] investigated the transformational behaviour of NiTi binary and NiTiCu ternary wires embedded into a Kevlar 29 fibre reinforced epoxy composite. According to the work of Tsoi and co-workers the constraining matrix effectively suppresses the progress of the transformation of the oriented martensite, which is related to the generation of recovery stresses [Tsoi et al. 2002].

The impact resistance of the graphite/epoxy composites can be improved by hybridizing them with NiTi fibers [Paine and Rogers 94b, 94c]. The thermo-mechanical response of SMA-composites has been investigated by Tsoi et al. [Tsoi et al. 2004]. The SMA-composites consisted of two layers of Kevlar epoxy system and one layer of pre-strained NiTiCu wires [Tsoi et al. 2004]. Hybrid SMA composites based on Kevlar-epoxy host composite matrix and thin embedded NiTiCu wires were investigated by Parlinska et al. [Parlinska et al. 2001]. Upon activation, the composites showed a recovery stress and corresponding shift of the resonance frequency to higher values [Parlinska et al. 2001]. Shape memory alloy (SMA) wires have been integrated in an epoxy/aramid fibres composite laminates in order to measure

the internal stress distribution [Psarras et al. 2001]. A similar work has been performed by Parthenios to measure the internal stress distribution of NiTiCu/Kevlar-epoxy composite at relatively high activation temperatures of 80 and 100°C. The results show that the higher stresses appear in the middle of the mid-wire distance [Parthenios et al 2001]. TiNi12 wt%Cu shape memory alloy wire reinforced Kevlar/epoxy composites were produced and the thermo-mechanical behaviors of the composites were studied by Zheng et al [Zheng et al. 2005a]. Results showed that the pre-strain level does not affect significantly the stress-strain and stress–temperature behaviors of the TiNiCu composites. Only the strain-temperature behavior of the composites is sensitive to the pre-strain level. Composites with a small pre-strain level show a larger hysteresis and a larger strain rate upon heating than those with a large pre-strain level [Zheng et al. 2005a].

Thin NiTiCu wires were incorporated into a glass-epoxy unidirectional laminate during lay-up. Then the whole structure was subjected to different curing procedures [Grando and Salvia 1996]. The thermal response of glass fibre/epoxy composites embedded with TiNiCu wires was studied by Zheng et al. [Zheng et al. 2002]. Pre-strained TiNiCu wires can generate large recovery stresses in a constrained condition and, therefore, modify the physical and mechanical properties of the composites if they are heated above the reverse transformation temperature of the wires [Zheng et al. 2002].

Roger [Roger 1990] found that the dynamic behavior, vibration amplitude, and structurally radiated noise of composite structures could be modulated by using embedded SMA elements. Ostachowicz et al. [Ostachowicz et al. 1999] provided a detail study on the effects of natural frequency of composite plates with embedded SMA actuators using a computation method. They reported that the natural frequency of the plates could be controlled by the embedded SMA actuators under a condition of heat applied. Since the SMA materials possess super-elastic property at a temperature greater than A_f, the superelasticity of SMA fibers is able to suppress or damp structural vibration by applying internal forces (distributed and/or localized) to structures in such a way as to dissipate the energy within the structures. Therefore, the superelastic SMA fibers could reduce vibration amplitudes and increase the damping ratio of the structure [Lau 2002].

1.2.1.2. Interfacial properties

Most SMA composite applications require transfer of strain from the wire to the matrix. In these applications, maximum interfacial adhesion between the SMA wire and the polymer matrix is desirable. A strong interfacial bond also increases the structural integrity of the final composite. Thus it is essential to have some measure of the interfacial bond strength between the SMA wire and host matrix for the evaluation of mechanical response and the development

of well designed interfaces. Adhesive strength is commonly regarded as the mechanical resistance to separation of the adhesive from the substrate [Jonnalagadda et al. 1997].

One of the most important factors which lead to the failure of composite materials is the interfacial debonding between fibers and matrix. When shear stress between the constituents increases upon the interfacial shear strength, interfacial debond will start immediately. It is generally agreed that the higher the critical debonding stress, the stronger the composite material will be [Poon et al. 2005]

Shimamoto et al. [Shimamoto et al. 1997] found that SME in SMA-reinforced composites can reduce the stress concentration and increase the fracture toughness. Obviously, since the recovery actions of the prestrained SMA wires normally act in opposite direction of the externally applied load (tensile stress), extra loading is probably required to satisfy the fracture criterion. According to [Poon et al. 2004], interfacial failure tends to occur at both the loading and embedded ends. Partial debond occurred at loading end is due to externally applied load on SMA wire. However, the similar interfacial failure happened at free end is actually a result of over-actuation [Poon et al. 2004].

The microscopic interfacial properties have been investigated by several researchers [Elspass and Kunzmann 1991, Paine and Rogers 1993, Kline et al 1995, Balta et al. 1999, Balta et al. 2000, Balta et al. 2001, Sadrnezhaad et al. 2009].

Lau et al. [Lau et al. 2002b] presented experimental observations on the interface of pre-strained NiTi/epoxy composites by using scanning electron microscopy (SEM). The reverse martensitic transformation characteristics of pre-strained TiNi shape memory alloy (SMA) fibers embedded in metal, epoxy and cement composite matrixes were studied by Li et al. [Li et al. 2001] using differential scanning calorimeter (DSC) measurements.

1.2.3. SMA/metal matrix composites

1.2.3.1. Al matrix

The NiTi fiber-reinforced Al matrix composites have been processed, and improved mechanical properties in terms of the yield stress, fatigue life, and damping capacity have been experimentally observed by several researchers [Furuya et al. 1993, Furuya and Taya 1996, Armstrong et al. 1998, Armstrong and Lorentzen 1997, Hamada et al. 1998, Lee 2003]. The experiments were rigorously conducted by Hamada et al. [Hamada et al. 1998] to examine the effect of fiber volume fraction, prestrain, and matrix yield stress. In particular, the amount of prestrain in the composite was considered as a design parameter, which controls the phase transformation of SMA fibers between martensite and austenite start temperatures to strengthen the composite [Lee and Taya 2004].

Yamada et al. [Yamada et al. 1993] made an effort to strengthening of an Al metal matrix composite (MMC) by the shape memory effect of dispersed TiNi particles. The interface in a NiTi short-fiber-reinforced 6061 aluminum matrix has been investigated by Liu et al. [Liu et al. 2008] using transmission electron microscopy and energy dispersive spectroscopy. It is found that by selecting the chemical composition of the Al alloy matrix, it is possible to control the chemical composition at the interface and further control the mechanical properties of the composites. Armstrong and co-workers [Armstrong et al. 1998, Armstrong and Lorentzen 1997] reported the macroscopic thermal mechanical and *in-situ* neutron diffraction measurements from Ni–Ti fiber actuated 6082-T6 aluminum matrix composite. Ni-Ti shape memory alloy fiber reinforced 6061-T6 aluminum alloy matrix composite was investigated by Armstrong and Kino [Armstrong and Kino 1995]. The reverse martensitic transformation of TiNi fibers embedded in Al matrix smart composite has been studied by Zheng et al. [Zheng et al. 2000]. The martensite fraction-temperature diagrams of TiNi wires embedded in a pure aluminum matrix were studied by Zheng and Cui [Zheng and Cui 2004] using differential scanning calorimetry (DSC) measurement. Furuya et al. [Furuya et al. 1993] investigated the damping and Mechanical tensile properties of TiNi fiber reinforced/Al metal matrix composite (SM-MMC). According to their results, the mechanical properties such as stiffness and yield strength were improved by the strengthening mechanism. Damping capacity of the composite was also increased.

1.2.3.2. Sn / In matrix

A new kind of high-damping metal matrix composites has been produced by embedding Cu–Al–Ni SMA particles with indium (IN) and In–Sn alloys matrices [Barrado et al. 2009], [López et al.2008] and [López et al.2009].

Silvain [Silvain et al. 1999] has shown the simultaneous improvement of the stiffness and the ductility of the SnPbAg alloy by embedding NiTi particles. Fouassier and co-workers [Fouassier et al. 2002] incorporated copper coated NiTi particles into a lead free solder paste in order to improve mechanical performances of solder joints. Single-fiber composite solders with NiTi reinforcement were investigated to evaluate the potential of a NiTi/solder system to minimize creep deformation [Wang et al. 2006a]. Wang et al. experimented with a lead-free solder reinforced with a NiTi shape memory alloy (SMA) in order to improve solder joint life [Wang et al. 2006b].

1.3. Identification Techniques and digital image correlation

In this work, an identification method is developed to identify the material parameters of a NiTi SMA composite. In this section the identification techniques are reviewed. A brief description of digital image correlation is given as well. The principles of the software (Correli-Q4 and Vic2D) used in this study are also described.

This section is written in French due to the requirements of ParisTech. Doctorate ParisTech thesis can not be written entirely in English and has to include about 20% of the manuscript written in French.

1.3.1. Techniques d'identification

1.3.1.1. Introduction

Cette partie a pour objectif de présenter certaines méthodes d'identification basées sur la minimisation d'une fonction objective définie par la somme des écarts quadratiques entre grandeurs calculées et mesurées. Dans la littérature, plusieurs méthodes ont été proposées pour l'identification de paramètres de lois de comportement à partir de champs cinématiques hétérogènes, des méthodes itératives et des méthodes non itératives.

Le calcul par éléments finis a longtemps été la méthode la plus utilisée pour résoudre à la fois le problème direct et inverse par l'utilisation du recalage à l'équilibre. Le problème direct consiste à déterminer les champs de déformation/contrainte en connaissant le modèle et les paramètres qui le pilotent. Tandis que le problème inverse est celui de la détermination des paramètres qui interviennent dans la réponse de la structure à partir de la connaissance de grandeurs mesurées (déplacements, déformation, …) et de la sollicitation appliquée

L'identification par analyse inverse revient à déterminer l'ensemble des paramètres d'une loi de comportement pour lesquels on obtient la meilleure superposition entre les mesures expérimentales et les valeurs calculées par le modèle direct. Cette superposition est quantifiée à l'aide de la minimisation d'une fonction objectif construite par une des méthodes décrites aux paragraphes suivant. Plusieurs méthodes de résolution du problème inverse peuvent être utilisées pour résoudre le problème de minimisation, on peut les classifier en 3 catégories [Tillier 1998] :

- Méthodes de régression linéaire si l'expression des grandeurs calculées est linéaire par rapport aux paramètres à identifier, ou permet la linéarisation.
- Méthodes d'évaluations successives de la fonction objectif pour différentes jeux de paramètres choisis avec des critères de recherche linéaire (algorithme de type simplex), génétique ou statistique (méthode de Monte-Carlo).

- Méthodes de type gradient (1er ou 2ème ordre) permettent la détermination des paramètres par une méthode d'approximations itérative. Cette méthode impose d'évaluer simultanément la fonction objectif et son gradient (méthode de la plus grande pente, méthode du gradient conjugué, méthode de Newton, méthode de Gauss-Newton, …).

Le choix d'une de ces méthodes se fait par l'expérience et surtout en fonction du type de modèle direct de calcul, le degré de complexité lié à la résolution et des caractéristiques de la fonction objectif : convexité, existence de plusieurs minima ou présence de paliers. Pour les modèles non linéaires, il est généralement préférable d'utiliser des méthodes itératives de type gradient [Tillier 1998].

Cependant, de nouvelles méthodes d'identification ont été proposées ces dernières années comme l'erreur en relation de comportement [Constantinescu 1995, Bonnet et al. 2003], le recalage par éléments finis et la méthode des champs virtuels. Nous présenterons brièvement le principe de chaque méthode. Le lecteur est renvoyé aux travaux de Marc BONNET, notamment l'article de synthèse présentant les différentes techniques d'identification [Bonnet et al. 2003].

1.3.1.2. Méthode de recalage par éléments finis

La méthode du recalage consiste à minimiser une fonction objectif noté $J(P)$ construite au sens des moindres carrées et traduisant la somme des écarts quadratiques entre les grandeurs calculées par la méthode des éléments finis et les grandeurs mesurées :

$$J(P) = \frac{1}{2}\sum_{i=1}^{N_{pts}} \left(M(P)_i - \overline{M}_i \right)^2 \qquad (1.3)$$

où : N_{pts} : Nombre de points de mesure ; P : Paramètres à identifier ; $M(P)_i$: grandeur calculée en fonction des paramètres à identifier P au point i ; $\overline{M}_i$: Grandeur mesurée.

Généralement la minimisation de $J(P)$ conduit à un problème mal posé dont il est nécessaire de régulariser. Différentes techniques de régularisation pouvant être utilisée parmi lesquelles la technique de Levenberg-Marquardt [Levenberg 1944, Marquardt 1963].

De nombreux auteurs ont utilisé cette technique d'identification sur la base d'une fonction objective donnée par l'équation 1.3.

1.3.1.3. Méthode de l'erreur en relation de comportement

La méthode de l'erreur en relation de comportement (ERC) a été introduite par Ladeveze [Ladeveze 1975 and 1977] pour le contrôle des calculs par la méthode des éléments finis. L'approche inverse fondée sur la minimisation d'une norme énergétique formulée par l'erreur en relation de comportement a été proposée par plusieurs auteurs pour l'identification des propriétés élastiques à partir d'un seul essai [Nouri 2009, Mohammad Sadeghi 2010]. En régime élastique, l'erreur en relation de comportement est formulée par une fonction $E\ u,\sigma,C$ définie comme la somme de deux fonctions convexes traduisant l'énergie potentielle et complémentaire. En l'absence de forces de volume, et en tenant compte des conditions aux limites, la fonction $E\ u,\sigma,C$ peut être réécrite pour des champs de contraintes σ statiquement admissibles et des champs de déplacements u cinématiquement admissibles de façon à faire apparaître l'écart en relation de comportement comme suit :

$$E\ u,\sigma,C\ = \frac{1}{2}\int_{\Omega} \sigma - C:\varepsilon\ u\ \ :C^{-1}:\ \sigma - C:\varepsilon\ u\ \ d\Omega \tag{1.5}$$

Une conséquence des principes variationnels utilisés dans le cadre de l'élasticité montre que l'on a pour un tenseur d'élasticité C donné :

$$\min_{u_{CA},\sigma_{SA}} E\ u,\sigma,C\ = 0 \tag{1.6}$$

Les paramètres définissant le tenseur C peuvent alors être identifiés via la minimisation de l'énergie donnée par l'équation 1.6.

Une méthode similaire a été appliquée à l'identification de paramètres élastiques par Constantinescu [Constantinescu 1995]. Elle consiste à faire intervenir des problèmes d'équilibres élastiques de deux types classiques, à déplacements imposés et à forces imposées. D'autres méthodes basées sur l'erreur en relation de comportement consistent à rajouter une fonction d'écart à la mesure sur les frontières avec des facteurs de pondération.

L'identification de la loi de comportement sur la base de la méthode de l'erreur en relation de comportement a été appliquée dans le cadre de la thèse de Merzouki [Merzouki 2008] (encadrée par F. Meraghni) afin de comparer l'identifiabilité de 4 configurations d'essais hétérogènes. Cette estimation a été également appliquée à l'échelle d'un multi cristal d'AMF pour identifier le comportement local de grains d'austénite à partir de mesure de champs de déformations locales à l'échelle des grains.

1.3.1.4. Méthode de l'écart à l'équilibre

La méthode de l'écart à l'équilibre a été utilisée par Claire et al. [Claire et al. 2002] pour l'identification des paramètres de lois d'endommagement anisotrope ou isotrope, en traction

bi-axiale. L'endommagement est considéré discontinu sur la structure. La formulation du problème d'identification est alors associée à une représentation de type éléments finis où l'endommagement est considéré constant par élément (sous domaines de la structure étudiée). L'identification de la distribution des paramètres se fait par la minimisation d'un écart à l'équilibre sur tous les sous domaines à l'intérieur desquelles ces paramètres sont constants. Après développement, un système surdimensionnée est construit où les paramètres par élément sont les inconnues. Un système linéaire final est résolu par une méthode du gradient conjugué. Cette méthode a été appliquée pour l'identification des conductivités thermiques et des propriétés élastiques locales par analyse de champs [Claire et al. 2003].

1.3.1.5. Méthode des champs virtuels

La méthode des champs virtuels permet d'identifier directement et simultanément des paramètres pilotant des lois de comportement. Cette méthode a été introduite par Grédiac [Grédiac 1996, Grédiac et al. 2002] pour le comportement élastique. Elle a été appliquée au comportement élastique endommageable de composite dans le cadre du travail de thèse de Chalal [Chalal 2005] (co-encadrée par F. Meraghni).

Elle est basée sur l'utilisation du principe des travaux virtuels.

En l'absence de forces volumiques extérieures, l'équilibre statique global du solide s'écrit :

$$-\int_{\Omega}\sigma\varepsilon(u^*)d\Omega=\int_{d\Omega_f}Tu^*dS \tag{1.7}$$

avec σ est le champ de contraintes, u^* champ de déplacement virtuel cinématiquement admissible, $\varepsilon(u^*)$ le champ de déformation associé à celui de déplacement virtuel, T le chargement surfacique sur la surface extérieure $d\Omega_f$.

Le principe de la méthode repose sur l'écriture du tenseur des contraintes σ en fonction du tenseur de déformations ε à partir de la loi de comportement. Les déformations sont calculées à partir d'un champ de déplacement obtenu par une technique de mesure de champs cinématiques telle que la corrélation d'image. Ensuite, il s'agit de choisir le bon champ de déplacement virtuel u^*, c'est-à-dire des champs sensibles aux paramètres de la relation de comportement que l'on souhaite identifier.

Grédiac et al. [Grédiac and Pierron 2006] ont introduit une précaution supplémentaire pour le choix de champ virtuel. Avril et al. [Avril et al. 2004] ont étudié d'une façon approfondie la sensibilité de la méthode. Les travaux de Chalal et al. [Chalal et al 2004, Chalal 2005, Chalal et al. 2006] présentent l'extension de la méthode des champs virtuels à un comportement élastique endommageable. Seul l'endommagement en cisaillement est considéré. La méthode des champs virtuels non linéaires a été appliquée par Grédiac et al. [Grédiac 1996, Grédiac et

al. 2002, Grédiac and Pierron 2006] au comportement élastoplastique avec écrouissage isotrope.

Dans ce travail de thèse, la méthode de type gradient proposé par Levenberg et Marquardt [Levenberg 1944, Marquardt 1963] basé sur l'algorithme de Gauss Newton est appliquée pour la résolution du problème inverse. L'utilisation de cette méthode est limitée par les instabilités caractérisant les problèmes mal conditionnés. Pour cela, plusieurs méthodes de stabilisation sont proposées dans la littérature. Toutes ces méthodes ont pour but de borner la zone admissible de recherche de jeux optimaux de paramètres.

1.3.2. Techniques de mesure de champs cinématiques

1.3.2.1. Généralités

L'étude des lois de comportement pour tous les types de matériaux nécessite un certain nombre de techniques de détermination de l'état de déformation et/ou de contrainte du matériau sous sollicitations mécaniques. L'importance de l'étude du comportement des matériaux sous charges complexes et des hétérogénéités des déformations, conduit à utiliser des techniques de mesure de champs cinématiques en 2D et 3D.

Les techniques de mesure de champs sont des méthodes expérimentales alternatives aux techniques dites classiques de mesures locales de déplacements, de déformations et de températures (e.g. jauges de déformation, capteurs de déplacement, thermocouple, etc.). Elles ont connu un développement important ces dernières années et ont fait l'objet de publications de synthèse ou de comparaison [Pan et al. 2009] [Bornert et al. 2009]. Les techniques de mesure de champs cinématiques et thermiques sont des outils précis et non destructifs. L'absence totale de contact entre la pièce et l'instrument de mesure supprime certaines erreurs. Les évolutions incessantes de la technologie du matériel informatique et des caméras numériques modifient continuellement les conditions d'utilisation et les performances de ces techniques. Températures [Gau 1999], déplacements [Forquin et al. 2004], déformations [Sutton et al. 1986], formes ([Surrel 1998] et [Garcia et al. 2002]) sont les variables les plus couramment mesurées par des techniques de mesure de champs.

Le choix d'une technique de mesure dépend de plusieurs éléments : la géométrie et les dimensions de l'éprouvette, la taille de la zone d'intérêt et l'échelle d'observation, les conditions d'essai mécanique, l'utilisation et la précision souhaitée sur les quantités obtenues. Quelques définitions utilisées dans cette étude sont rappelées ci-dessous ([Triconnet 2007] et [Surrel 2004]).

La *mesure* - Une valeur (variable aléatoire dont la valeur exacte n'est généralement pas connue) qui exprime la grandeur physique particulière obtenue par une méthode de mesure.

Chaque valeur de mesure doit de préférence comprendre trois éléments : une valeur, une unité et l'incertitude sur cette valeur, Fig. 1.10 [ISO04].

On distingue trois types de mesures (résultats) obtenues par des techniques de mesure de champs ; les mesures optiques directes (e.g. images de niveaux de gris), les mesures intermédiaires déduites par traitement numérique des mesures directes (e.g. champs de déplacement ou de phase), et enfin les mesures « décodées » qui sont les informations de mesure en relation avec un gradient des données intermédiaires (e.g. champs de déformations).

Le seuil de détection - Le seuil de détection d'une méthode de mesure est défini par la valeur minimale théorique que doit avoir la grandeur mesurée pour que le résultat soit significativement différent de celui obtenu pour le mesurage du blanc (Fig. 1.14). Ce seuil est calculé dans des conditions parfaites de mesure (pas de bruit, pas d'erreurs numériques, etc.).

La sensibilité d'une méthode - La sensibilité d'une méthode est définie par le quotient de la variation de la quantité qui doit être mesurée sur la variation de la mesure. Cette valeur est en quelque sorte le gain du système de mesure.

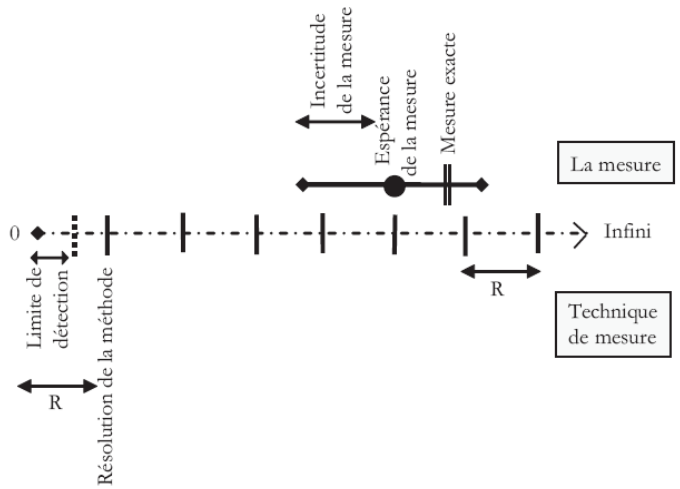

Fig. 1.10: Schématisation des termes métrologiques de résolution, incertitude et limite de détection [Triconnet 2007].

Incertitude de la mesure - L'incertitude de la mesure est un paramètre quantitatif qui caractérise la dispersion des valeurs attribuées à la mesure, (Fig. 1.10) [Neuilly and Courtier 1997]. La dispersion des valeurs mesurées a de nombreuses sources comme : une variation incontrôlée des grandeurs, (intensité, contraste, déplacement de corps rigide, etc.) influant sur la variable mesurée. L'instrument de mesure mais aussi la personne effectuant la mesure peuvent introduire une certaine dispersion sur la mesure.

La résolution de la mesure - La résolution de la mesure représente la plus petite fluctuation de la grandeur mesurée (Fig. 1.10) détectable par la mesure. Cette valeur, contrairement au seuil

de détection, est une valeur pratique qui prend en compte l'ensemble de la chaîne de mesure et les bruits éventuels qui perturbent la mesure. La résolution correspond au plus petit écart entre deux valeurs de la mesure qui peut être attribué avec certitude aux phénomènes physiques qui font réagir la mesure.

La résolution spatiale : Ce terme est spécifique aux méthodes de mesure de champs. La résolution spatiale correspond à la distance minimale entre deux points de mesure indépendants [Surrel 2004]. Suivant la technique de mesure, cette définition de la résolution spatiale est plus ou moins adéquate, d'autres définitions peuvent être adoptées [Triconnet 2007].

Les déformations peuvent être obtenues indirectement par dérivation numérique des champs de déplacements mesurés (speckle interférométrique, Moiré géométrique ou interférométrique, interférométrie holographique, corrélation d'images numériques, méthode de grille, etc.) ou directement lors de la procédure de mesure (shearography). Les techniques de mesure de champs cinématiques (déplacements ou déformations) se répartissent dans deux catégories :

1. Les techniques basées sur les lois de l'optique (diffractions et interférences de faisceaux laser) : la photoélasticimétrie, le speckle interférométrique, etc.
2. Les techniques basées sur les principes de l'analyse et de la corrélation d'images.

Ces techniques sont nombreuses et ont chacune leur champ d'application, qui peut être représenté par exemple en termes d'échelle d'observation et de résolution en déformation. Dans le cadre de cette étude, il est essentiel de pouvoir analyser les hétérogénéités de déformations sur des zones relativement grandes : de quelques dizaines à quelques milliers de millimètres carrés. La résolution en déformation n'est pas critique pour cette étude : les conditions expérimentales sont donc celles qui autorisent l'application des mesures de déformations par Corrélation d'Images Numériques (DIC : Digital Image Correlation en anglais). Les images peuvent être enregistrées avec des caméras numériques équipées d'objectifs relativement classiques (28 à 75 mm).

Toutes ces techniques cependant ne donnent que des informations sur les déformations sur la surface libre et observable mais en aucun cas ne donnent de renseignements quantitatifs sur ce qui se passe sous la surface, et donc au cœur de la matière.

1.3.2.2. Techniques de corrélation d'images numériques

Le but des techniques de corrélation d'images est d'abord de fournir une description quantitative de la surface d'un objet à travers la prise d'une image (répartition spatiale des niveaux de gris). Si deux caméras prennent deux images simultanées de l'objet avec deux angles de vue pas trop différents (angle autour de 30 degrés entre les caméras), il est possible

de reconstituer la forme tridimensionnelle de la surface observée. La corrélation bidimensionnelle d'images (respectivement la stéréocorrélation) est basée sur la comparaison de deux images (respectivement deux paires d'images) représentatives respectivement des états initial et déformé de la structure étudiée. Le mouvement de l'ensemble des repères attachés à la surface de l'objet (texture de la surface en terme de niveaux de gris) est analysé et sert à déterminer, à l'aide d'algorithmes numériques, d'une part les éventuels déplacements de l'objet par rapport à un repère fixe par rapport à la caméra (aux caméras), et d'autre part, les déplacements relatifs entre les repères entre les deux états (déformations de la surface). Dans ce cas, la comparaison des images aboutit au calcul du champ de déformation « autour de chacun des repères ». L'évolution temporelle et spatiale des déplacements des points répartis sur la surface est calculée à partir de séquences d'images successives. Des applications de ces techniques existent dans différents domaines de la science : science des matériaux, science de la vie, géologie, robotique, etc.

Le dispositif expérimental de corrélation d'images numériques en 2D se compose d'une caméra, combinée à un microscope électronique ou optique ou simplement équipé d'un zoom ou d'un objectif au grossissement adapté. Les signaux lumineux, émis par la surface observée, sont transformés en image (un niveau de gris par pixel du capteur CCD) par la caméra numérique et sont traités par un ordinateur qui calcule les déplacements et les déformations. Les caméras donnent des informations sur la surface de plus en plus riches (caméras à plusieurs MégaPixels) et les images sont acquises à des cadences de plus en plus élevées. Il faut cependant toujours faire un compromis entre vitesse d'acquisition et taille de l'image, le taux de transfert d'informations entre le capteur CCD et la mémoire de la caméra ou de l'ordinateur étant limité par la technologie. Ce sont les dispositifs d'observation et de prise d'images qui déterminent le grossissement et donc l'échelle, mais il faut aussi que le marquage de la surface de l'objet soit adapté au niveau d'observation souhaité.

- Méthodes de grille ([Liu and Fischer 1997], [Wang et al. 2000], [Doumalin 2000], [Soppa et al. 2004], [Surrel 2004] et [Garcia et al. 2006]). La méthode de suivi de marqueurs ou de grille est la technique la plus ancienne, car elle permettait un dépouillement « à la main ». Ensuite, avec les techniques d'analyse d'images puis de corrélation d'images, le dépouillement a été automatisé et est devenu en conséquence plus rapide et aussi plus précis.

  Les méthodes de grille ne sont généralement pas aussi fiables et précises que les nouvelles techniques de corrélation d'images sur des mouchetis aléatoires. Néanmoins, elles sont utilisées dans certains cas car l'approche est simple, et peu coûteuse en temps de calcul.

- Méthodes de corrélation d'images sur mouchetis aléatoire. Ces méthodes sont apparues au début des années 80 et ont rapidement trouvé leur place dans les études scientifiques et les applications industrielles. Le principe de ces techniques consiste également à comparer deux images en utilisant les variations de texture sur la surface de l'objet observé. Cette texture est généralement générée artificiellement : un motif aléatoire, mouchetis de peinture par exemple fournit le codage nécessaire de la surface pour permettre ensuite la corrélation. Le motif aléatoire rend possible la reconnaissance des points homologues les uns par rapport aux autres. Il est à noter que généralement le dépôt d'un mouchetis prend à peine quelques minutes, ce qui est un gros avantage par rapport aux méthodes utilisant des grilles qui sont beaucoup plus délicates à déposer.

  Des études récentes montrent que l'adaptation du système d'observation optique peut permettre des observations très fines avec des niveaux de déplacements de l'ordre d'une dizaine de nanomètres ([Jin and Bruck 2004] et [Berfield et al. 2007]). La Fig. 1.11 représente le schéma d'un système d'acquisition de données pour un montage de corrélation d'images numériques bidimensionnel.

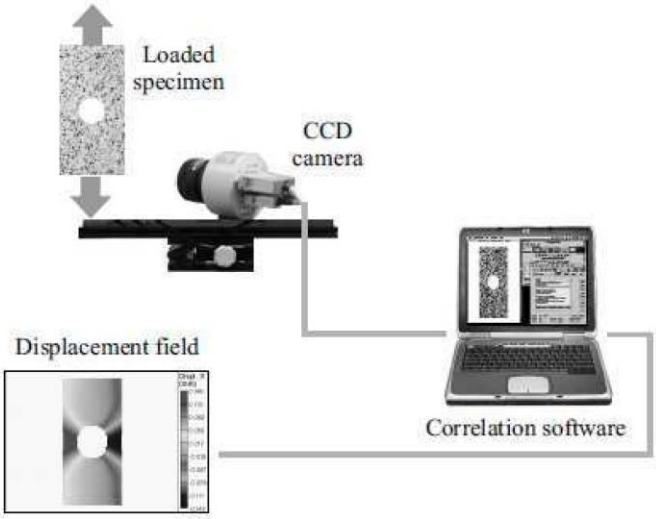

Figure 1.11: Schéma d'un montage de corrélation d'images numériques bidimensionnel, [Sutton et al. 1999].

Dans la plupart des essais mécaniques standards, il est possible de se contenter des champs de déplacements mesurés en 2D, puisque l'éprouvette est plane et doit rester plane au cours de l'essai. Ceci suppose que les variations d'épaisseur engendrent des erreurs de mesures du même ordre de grandeur ou plus petite que la précision attendue sur les valeurs mesurées ([Soppa et al. 2004] et [Sutton et al. 2008]).

Les techniques de corrélation d'images bidimensionnelle ou tridimensionnelle se déroulent en trois étapes successives :

I. Préparation de la surface (réalisation d'une grille ou d'un mouchetis).

Différents types de marquage sont utilisés :

- *Dépôts de peinture*
- *Dépôts par microélectrolithographie.*
- *Gravure chimique*

II. Acquisition des images

Le dispositif expérimental d'acquisition des images est constitué d'une caméra CCD ou d'un appareil photo numérique, d'un ordinateur contenant une carte et un logiciel d'acquisition, et d'un système d'éclairage. Les images sont soit temporairement stockées dans la mémoire de la caméra ou de l'appareil photo, soit directement transférées dans la mémoire de l'ordinateur. Le réglage du système d'éclairage est fondamental, car de la qualité de l'image dépend une grande partie de la résolution sur les déplacements et les déformations.

La caméra CCD ou l'appareil photo sont équipés d'un objectif permettant d'observer une zone réduite de la surface utile de l'éprouvette. L'objectif permet évidemment de s'adapter aussi bien à des études à l'échelle microscopique qu'à l'échelle macroscopique. La surface de l'éprouvette observée par la caméra CCD est généralement rectangulaire. Ses dimensions sont exprimées en pixels puis en millimètres. La caméra effectue des prises de vue successives, une première considérée comme image de référence, puis d'autres considérées comme images déformées à différents instants de l'essai. La caméra doit suivre le déplacement moyen de la zone observée pour que les champs de déplacement soient calculés sur une zone qui reste relativement grande par rapport à la taille de l'image. Si les déplacements sont petits, la caméra peut être fixe par rapport à la machine d'essai.

III. Détermination des champs de déplacement et de déformation par corrélation d'images numériques

La détermination des champs de déplacement et de déformation se fait en général en post-traitement, une fois toutes les images enregistrées. Les logiciels de corrélation d'images se distinguent entre eux par leurs performances qui sont liées entre autres aux choix faits au moment de la programmation de l'algorithme. Les logiciels varient surtout au niveau :

- de la prise en compte ou non des distorsions optiques de l'image générées par le dispositif d'observation ;
- du choix du coefficient d'intercorrélation, ce qui est plus ou moins lié à la prise en compte d'une possible variation de contraste et/ou de luminosité entre l'image de référence et l'image déformée ;
- de la procédure de recherche du minimum de la fonction de corrélation, résolution du processus de minimisation dans l'espace réel ou dans l'espace de Fourier ;

- des hypothèses sur la forme du champ de déplacement sur l'imagette, qui « impose » la forme de l'imagette sur l'image déformée ;
- du degré de la fonction d'interpolation des niveaux de gris, qui autorise le calcul sub-pixel des champs de déplacements ;
- du choix des déformations calculées (logarithmique, Euler-Lagrange, etc.) et de la méthode utilisée pour les calculer (calcul direct, dérivation numérique avec ou sans lissage préalable du champ de déplacement, etc.)

De ces choix dépendent une grande partie de la précision des résultats (interpolation niveaux de gris [Sutton et al. 1988] [Schreier et al. 2000], déformation de l'imagette [Lu and Cary 2000] [Schreier and Sutton 2002], etc.), même si d'autres facteurs liés à la mise en œuvre des essais et des mesures peuvent être tout aussi importants.

Tous ces choix ne sont pas forcément connus des personnes autres que les développeurs de ces logiciels. Certains logiciels ne sont pas commercialisés et sont transmis seulement entre chercheurs de la même communauté. Il existe divers logiciels de corrélation d'images développés dans la communauté scientifique française et internationale. Développés en France et les plus cités dans la bibliographie sont : CorreliLMT [Hild 2002], CorreliQ4 [Besnard 2006] [Hild and Roux 2008], Icasoft [Mguil-Touchal 1997] [Mguil-touchal et al.1997] [Vacher et al.1999], 7D [Vacher 2003], Granu [Brillaud 2002] [Lagattu 2004], Correla, etc. Les logiciels utilisés en France mais développés à l'étranger et commercialisés à l'échelle mondiale sont : Vic 2D (société Correlated Solutions), Aramis 2D (Société Gom), Istra 3 (Société Dantec Dynamics), DaVis (Société La Vision). Chacun de ces logiciels a ses propres performances [Bornert et al. 2009] et ses propres limites d'utilisation.

Le principe de la corrélation d'images est le même dans tous les logiciels. La base des algorithmes de corrélation est la comparaison de deux images d'une même zone de la surface d'un échantillon à deux états différents : un état dit de référence et un deuxième état dit déformé. La procédure de détermination du champ de déplacement comprend trois étapes :

1. Définir la région d'étude (RE) ou zone de corrélation (ROI : « Region of interest » en anglais) de l'image de référence qui n'est pas nécessairement toute l'image acquise (Fig. 1.12).
2. « Découper » la région d'étude en zones d'étude élémentaires (ZEE) ou imagettes, que l'on appelle aussi zones d'intérêt (ZOI : Zone Of Interest). Ces imagettes sont identifiées par les valeurs de niveau de gris de leurs pixels. Elles sont généralement carrées d'une taille « l » de l'ordre de la dizaine de pixels ou davantage. Elles sont régulièrement espacées d'un pas « *p* » de manière à recouvrir toute la zone d'étude. Elles peuvent se recouvrir partiellement ou au contraire être jointives (p = l). « l » et « p » sont des paramètres de corrélation à choisir lors des calculs.

3. Corréler les imagettes, c'est à dire trouver pour chaque imagette « son image » à l'état déformé.

C'est durant cette étape, que le logiciel tente de déterminer le déplacement d'une imagette par la procédure de corrélation d'images, afin de retrouver la position du motif qui ressemble le plus à l'imagette de l'image de référence. Le déplacement d'une imagette entre l'image de référence et l'image déformée correspond à un décalage spatial de l'intensité du signal numérisé par la caméra CCD. Le champ de déplacement sur l'ensemble de l'image est déterminé en évaluant le déplacement de l'ensemble des centres de chaque imagette, (Fig. 1.12). Suivant les logiciels de corrélation d'images, l'imagette recherchée sur l'image déformée gardera ou non la forme de l'imagette de l'image de référence. Différentes hypothèses peuvent être faites sur le déplacement et/ou la déformation de l'imagette.

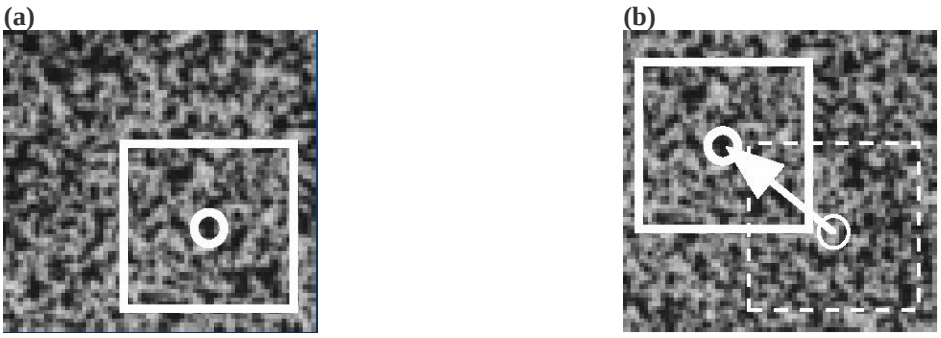

Figure 1.12 : Exemple pour un déplacement de corps rigide du mouchetis (a) image et imagette de référence et (b) image et imagette déformée à l'instant t.

La corrélation peut se faire entre l'image non déformée et les images déformées prises l'une après l'autre ou bien entre deux images successives. C'est la corrélation incrémentale. Elle peut être nécessaire si les déformations sont très grandes, mais elle conduit à des erreurs plus grandes qu'une corrélation globale. Les erreurs de chaque corrélation sur les incréments de déplacements se cumulent. Dans le paragraphe suivant, les principes et les procédures d'utilisation des logiciels CorreliQ4 et Vic2D sont rapidement rappelés.

1.3.2.2.1. Logiciel de corrélation d'images numériques Correli LMT et Q4

Les versions successives du logiciel de corrélation d'images Correli ont été développées au LMT Cachan par F. Hild et ses collaborateurs ([Hild 2002], [Besnard 2006]). C'est la version de Correli dite « Q4 » qui a été majoritairement utilisée pour l'exploitation 2D des essais mécaniques réalisés dans le cadre de ce travail.

Algorithme de calcul et traitement numérique

La détermination du champ de déplacement « réel » $\vec{u}$ par rapport à un champ de déplacement test $\vec{v}(\vec{x})$ à partir de la seule connaissance de f et g (f et g sont les fonctions de

niveau de gris associés respectivement à l'images de la référence et aux images acquises aux différents états de déformation) est obtenue dans Correli en minimisant la fonction $F(\vec{v})$ qui est une norme de la différence entre $g(\vec{x})$ et $f(\vec{x}-\vec{v})$, au sens des moindres carrés :

$$F(\vec{v}) = \left\| g(\vec{x}) - f(\vec{x}-\vec{v}) \right\|^2 \tag{1.8}$$

avec $\|f\|^2 = \int_{-\infty}^{+\infty} |f(x)|^2 dx$ (norme quadratique), c'est à dire :

$$F(\vec{v}) = \int_{-\infty}^{+\infty} g(\vec{x}) - f(\vec{x}-\vec{v})^{\,2} d\vec{x} \tag{1.9}$$

Cette fonction atteint sa valeur minimale, 0, en l'absence de bruit ($b(x)=0$) lorsque $\vec{v}=\vec{u}$. Le problème de minimisation de l'équation 1.9 équivaut à maximiser $g * f$ par rapport à $\vec{v}(\vec{x})$. $g * f$ représente l'intercorrélation des fonctions f et g :

$$Min\ F = Max\left[\ g * f\ \right] = \int_{-\infty}^{+\infty} g(\vec{x}).f(\vec{x}-\vec{v})\, d\vec{x} \tag{1.10}$$

C'est de cette constatation que part la programmation des anciennes versions de Correli. L'intégrale de l'équation 1.10 s'exprime assez facilement en utilisant la transformée de Fourier des fonctions f et g [Hild 2002]. Dans les versions successives de Correli, ce qui a évolué ce sont essentiellement les hypothèses sur la fonction $\vec{v}(\vec{x})$. Le programme est toujours écrit avec Matlab et la corrélation est toujours résolue dans l'espace de Fourier et non dans l'espace réel.

Les particularités du logiciel Correli Q4

Dans Correli Q4, les fonctions f et g sont supposées suffisamment régulières aux petites échelles et l'amplitude du déplacement relativement petite. Alors, minimiser la fonctionnelle $F(\vec{v})$ (équation 1.9) équivaut à minimiser le développement de Taylor au premier ordre de $F(\vec{v})$, c'est-à-dire :

$$F(\vec{v}) = \int\int \left[g(\vec{x}) - f(\vec{x}) + \vec{v}(\vec{x}).\vec{\nabla} f(\vec{x}) \right]^2 d\vec{x} \tag{1.11}$$

Le champ de déplacement test $\vec{v}(\vec{x})$ est alors écrit comme une combinaison linéaire de champs de déplacements simples, dans une base de l'espace E_k, telle que :

$$\vec{v}(\vec{x}) = \sum_i v_i \psi_i(\vec{x}), \tag{1.12}$$

$\psi_i(\vec{x})$ sont des vecteurs de base de E_k, v_i sont les composantes de $\vec{v}$ sur cette base.

$F(\vec{v})$ devient alors une forme quadratique en amplitude, où les v_i sont inconnues. La recherche d'extremum (Eq. 1.10) revient à résoudre :

$$\left(\int\int \left[\vec{\nabla} f \otimes \vec{\nabla} f \quad \vec{x} \right] : \psi_i \otimes \psi_k \quad \vec{x} \right] d\vec{x} \Big) v_k = \int\int \left[f(\vec{x}) - g(\vec{x}) \right] \vec{\nabla} f(\vec{x}) \psi_i(\vec{x}) \Big] d\vec{x} \qquad (1.13)$$

où $\otimes$ représente le produit tensoriel.

Le problème consiste alors à résoudre un système linéaire écrit sous forme matricielle :

$$[M]\{w\} = \{m\} \qquad (1.14)$$

{w} est le vecteur contenant les composantes inconnues v_i . [M] et {m} sont des quantités connues dépendantes des fonctions f, g et de ψ.

Le choix de l'espace E_k , donc l'expression des fonctions de base $\psi_i(\vec{x})$, est arbitraire et peut être changé en fonction du problème à traiter. Dans la version Q4 du logiciel Correli utilisée dans cette thèse, il s'agit des fonctions polynomiales P1 ([Wagne 2002], [Besnard 2006]) définies dans l'espace $[-1, 1]^2$ par (1-x) (1-y), x (1-y), (1-x) y, x y. Ces fonctions permettent d'exprimer les déplacements en un point contenu dans l'espace $[-1, 1]^2$ comme des fonctions bilinéaires des déplacements aux extrémités du domaine (-1, -1) (-1, 1) (1, -1) et (1, 1). Le champ de déplacement ainsi « interpolé » est similaire à celui obtenu par la méthode des éléments finis avec des éléments carrés à quatre nœuds dits éléments Q4P1. Par cette méthode, le champ de déplacement est continu et dérivable sur l'image ce qui assure un calcul possible des déformations par dérivation.

L'image de référence, ou plutôt la zone d'étude, est discrétisée en zones d'études élémentaires (imagettes), qui définissent les éléments carrés de taille « l ». Les nœuds forment alors un maillage (Fig. 1.13). Pour chaque élément, une matrice élémentaire M^e_{ij} et un vecteur m^e_i sont calculés en utilisant les équations précédentes.

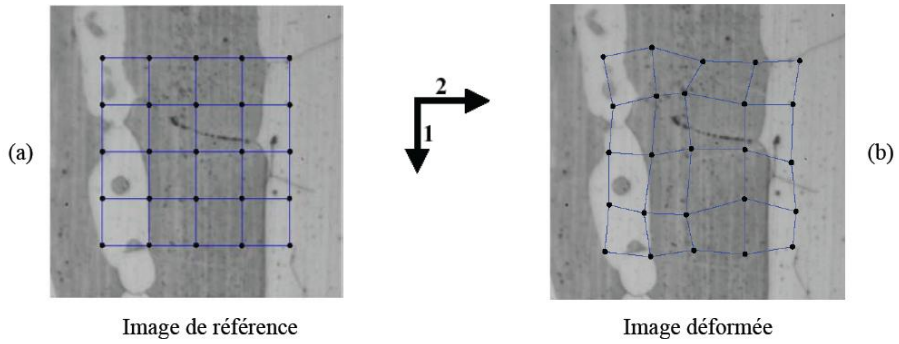

Fig. 1.13 : Principe de la technique de corrélation d'images numériques avec Correli Q4 [El Bartali 2007]

Le système (Eq. 1.14) se construit par assemblage des matrices élémentaires comme dans toute méthode basée sur des éléments finis. Le champ de déplacement est alors calculé par

inversion du système. Comme le champ de déplacement est globalement continu, le seul paramètre de corrélation à choisir lors des calculs est la taille des éléments « l ». Le champ de déformation est déduit par une dérivation discrète du champ de déplacement.

Dans la version Q4 de Correli, les imagettes sont donc obligatoirement jointives, alors que dans les versions précédentes du logiciel, il était possible de choisir l'espacement entre les imagettes pour avoir un certain recouvrement et donc plus de mesures (non indépendantes cependant).

Le logiciel de corrélation version Correli Q4 a été choisi au départ de l'étude car son formalisme type éléments finis doit faciliter l'identification à partir des champs de déformations puisque les variations suivent les mêmes fonctions locales. On pourra également faire correspondre le maillage EF avec les zones discrétisées.

Performances sur les déplacements et les déformations

Les performances sont fonctions de nombreux paramètres de l'image (distribution des niveaux de gris : taille et répartition spatiale des taches ou texture locale de la surface), des moyens optiques (nombre de bits du codage en niveaux de gris, nombre de pixels du capteur CCD, éclairage…) et du logiciel de corrélation (principe de résolution, résolution globale ou incrémentale, taille des imagettes, …).

Pour étudier ces performances, il est nécessaire de déterminer la résolution de la méthode et la précision sur les valeurs mesurées (résolution en déplacement et en déformation, incertitudes sur les résultats).

Résolution spatiale : Puisque dans la version Q4 de Correli il n'y a pas recouvrement entre les imagettes, la résolution spatiale est définie par la taille de l'imagette choisie pour chaque calcul par l'opérateur. Elle sera donnée à chaque présentation de résultats sous forme de champs.

L'incertitude ou erreur sur la mesure des logiciels de corrélation sont souvent évaluées sur des transformations simples, e.g. un déplacement de corps rigide (mouvement de translation, faible rotation) ou une déformation homogène ([Chu et al. 1985], [Wattrisse 1999], [Doumalin 2000], [Schreier and Sutton 2002], [Hild and Roux 2006], [Pan Bing and Fu-long 2006], [Bornert 2006], [Wang et al. 2007]). Le résultat de la corrélation : valeur moyenne du déplacement et/ou de la déformation est comparé au déplacement ou à la déformation imposée (connue). Il est également intéressant et indispensable d'analyser les écarts types obtenus sur ces mesures, ce sont eux qui donnent l'incertitude sur la valeur mesurée.

Il est souvent assez difficile d'estimer le seuil de détection et/ou la résolution de la méthode de mesure employée. Ce ne sont pas des quantités importantes pour cette étude, car les déplacements et les déformations sont toujours sensiblement plus élevés que le seuil de

détection. Cependant, le logiciel Correli Q4, donne une estimation de cette résolution qui est calculée à partir d'une image translatées numériquement. Cette résolution est sans doute inférieure à la résolution « pratique ».

A chaque étape de l'acquisition ou du traitement des données du système de mesure, des erreurs d'origines variées peuvent être introduites. Ces erreurs jouent sur la précision des résultats, les plus importantes sont listées ci-dessous :

1. Erreurs de positionnement de la caméra par rapport à l'éprouvette. Un mauvais réglage de la perpendicularité entre la caméra et la surface observée génère des erreurs de mesure.
2. Erreurs initiées par la procédure d'enregistrement. Une mauvaise qualité du capteur CCD, une perte d'informations lors des transferts, une compression des images dégrade la qualité des mesures.
3. Erreurs dues aux vibrations extérieures. Les vibrations influent sur les déplacements, mais a priori par sur les déformations, elles engendrent des déplacements de corps rigides du système de mesures par rapport à la caméra.
4. Erreurs dues aux variations de l'éclairage. L'idéal est de faire des mesures dans une pièce où le soleil n'entre pas et de choisir un bon éclairage, diffusant une intensité constante au cour du temps. Un déplacement de la zone observée par rapport au système d'éclairage peut engendrer des variations de lumière sur le mouchetis. Certains logiciels sont programmés pour corriger les variations d'éclairage.
5. Erreurs dues au mouvement de corps rigide. Si les déplacements sont grands par rapport à la taille de l'image, il faut déplacer le système d'observation de façon à ce que la zone d'étude reste dans le champ de l'image.
6. Erreurs dues à la procédure d'extraction des résultats. Certaines des hypothèses faites pour la programmation du logiciel jouent un rôle sur la précision des mesures (interpolation, dérivation numérique, recherche d'extremum, etc.).
7. Erreurs dans les traitements des données.

Résolution en déplacement : La résolution en déplacement est la valeur du plus petit déplacement mesurable qu'il est possible de mesurer quels que soient les paramètres de corrélation. Cette résolution n'est pas fondamentale pour cette étude. Une résolution « théorique » est donnée par Correli. Cette résolution ne prend en compte que les points 6 et 7 cités ci-dessus.

Incertitude sur le déplacement : Cette incertitude est estimée dans Correli Q4 à partir d'une image du mouchetis translatée numériquement. Le mouchetis n'étant pas forcément de même qualité à chaque essai, l'incertitude devrait être estimée pour chaque essai. Même si ce sont

les déformations qui seront utilisées par la suite, l'estimation de l'incertitude sur le déplacement est importante, car l'incertitude en déformation dépend directement de l'incertitude en déplacement (voir plus loin). L'incertitude en déplacement diminue lorsque « « l », la taille de l'imagette augmente (les taches qui servent de motifs élémentaires sont plus nombreuses). La relation qui lie l'incertitude sur les déplacements, σ_u, et la taille l'imagette « l » est du type :

$$\sigma_u = A^{\alpha+1} l^{-\alpha} \tag{1.15}$$

A est une constante. Dans un diagramme en échelles logarithmiques, α est la pente de la droite de tendance de la courbe d'incertitude sur les déplacements (exprimés en pixels) par rapport à la taille de l'imagette exprimée en pixels elle aussi.

Résolution en déformation : Pour une transformation appliquée à l'image de type déplacement de corps rigide, la déformation doit être nulle (en théorie). La déformation calculée par le logiciel de corrélation pour un tel déplacement donne la résolution en déformation. Les bruits apparus pendant le calcul des déplacements sont amplifiés par la procédure de dérivation nécessaire aux calculs des déformations. La dispersion sur les valeurs locales du déplacement génère une déformation artificielle. La résolution en déformation ainsi déterminée est une résolution théorique (propre à l'algorithme). Lors d'un essai, une déformation est déterminée entre deux images successives du même état de solliccitation. Entre ces deux images il peut y avoir eu des perturbations extérieures.

Incertitude en déformation : L'incertitude sur les déformations, σ_ε est approximée par la relation [Hild 2002] :

$$\sigma_\varepsilon = B^{\beta+1} l^{-\beta} \tag{1.16}$$

B est une constante et β est la pente de la droite de tendance de la courbe d'incertitude sur les déplacements (sans unité) par rapport à la taille de l'imagette exprimée en pixels.

Les déformations sont déterminées à partir des déplacements par la méthode des différences finies, c'est-à-dire en calculant :

$$\varepsilon = \frac{U(\boldsymbol{X} + \Delta\boldsymbol{X}) - U(\boldsymbol{X})}{\Delta\boldsymbol{X}} \tag{1.17}$$

L'incertitude sur les déformations peut donc être déduite de l'incertitude sur les déplacements, selon la relation [Surrel 2004], [Bergonnier et al. 2005]:

$$\sigma_\varepsilon \approx \frac{\sqrt{2}\sigma_u}{\Delta\boldsymbol{X}} \tag{1.18}$$

$\Delta\boldsymbol{X}$ est la résolution spatiale, elle s'identifie à la taille de l'imagette « l » [Bergonnier et al. 2005].

Des équations 1.18 et 1.15, il est simple de déduire que β de l'équation 1.16 est peu différent de α +1. L'influence de la taille de l'imagette est donc plus importante sur l'incertitude en déformation que sur l'incertitude en déplacement. Les bruits et donc l'incertitude sur les déplacements sont amplifiés lors de la dérivation nécessaire au calcul des déformations.

Mais il ne faut pas oublier qu'une augmentation de la taille de l'imagette correspond aussi à une dégradation de la résolution spatiale. Les champs calculés sont plus grossiers, les gradients sont lissés, car le nombre de points de mesure est moindre. Pour chaque type d'essai, il faut trouver un compromis entre la précision attendue des résultats et une résolution spatiale suffisante pour observer et quantifier les phénomènes importants pour l'étude (hétérogénéités de déformation, ou valeurs moyennes précises…).

Deux types de résultats de corrélation d'images sont utiles dans cette thèse : des résultats calculés par moyenne sur des zones relativement grandes (plusieurs imagettes) par la commande « gauge » de Correli et des résultats présentés sous forme de champs. Pour les champs de déformations, les incertitudes indiquées sont généralement les incertitudes théoriques données par le logiciel. Elles sont désignées par les noms utilisés dans la page précédente. Les incertitudes sur les valeurs moyennes sont estimées par calcul à partir des formules données et par extrapolation à la taille de la « jauge virtuelle ».

1.3.2.2.2. Logiciel de corrélation d'images numériques Vic2D

Acquis en janvier 2010, le logiciel Vic2D a été préféré à Correli pour l'exploitation de certains essais et en particulier dans les cas nécessitant une connaissance des gradients de déformations sur la totalité de la zone filmée. Vic2D permet de choisir assez simplement des zones d'étude de formes complexes, beaucoup plus facilement que Correli. Il est possible de définir des zones d'intérêt en formes de polygones quelconques, ce qui permet de suivre au mieux les hétérogénéités de déformations sur certaines éprouvettes de formes complexes (biaxiales, Meuwissen, etc.).

Ce logiciel, comme Correli d'ailleurs, permet d'extraire des fichiers de résultats exploitables ensuite par d'autres logiciels. Les fichiers (x, y, ε_{xx}, ε_{yy}, ε_{xy}) pour un ensemble de points (x, y) de l'image initiale et pour différents états de chargement extérieur sont indispensables aux développements des travaux de cette thèse et en particulier pour l'identification des paramètres des lois de comportement à partir de mesures de champs cinématiques.

Comme dans Correli, la détermination du champ de déplacement « réel » $\vec{u}$ à partir de la seule connaissance de f et g est obtenue en minimisant la fonction de corrélation $F(\vec{v})$ (Eq. 1.8). $F(\vec{v})$ appelé coefficient de corrélation est habituellement une norme de la différence entre $g(\vec{x})$ et $f(\vec{x}-\vec{v})$, au sens des moindres carrés, avec $\vec{v}(\vec{x})$ un champ de déplacement test

(ce coefficient correspond à l'option « SSD » dans Vic). La norme est définie à l'équation 1.9. Ce coefficient n'est pas toujours adapté, de corrélation est sensible aux variations d'éclairage.

Dans Vic2D, deux autres coefficients de corrélation peuvent être utilisés :

- « ZSSD : Zero mean Sum of Squared Differences » qui prend en compte un décalage constant sur toute l'image des niveaux de gris entre l'image initiale et l'image déformée (translation de l'histogramme en niveau de gris vers le blanc ou le noir).

- « ZNCC : Zero mean Normalized Cross Correlation » qui prend en compte une translation et une « dilatation » de l'histogramme (variation de contraste).

Les algorithmes de minimisation du coefficient de corrélation sont construits à partir de variables continues or les fonctions « f » et « g » sont des fonctions discrètes. Les valeurs connues pour des valeurs de x et y entières, doivent être définies partout entre ces points. Il est donc nécessaire d'effectuer un calcul d'interpolation des niveaux de gris. Plusieurs types d'interpolation sont utilisables dans Vic2D (voir [Doumalin 2000] page 207 à 209 pour les explications):

- interpolation bilinéaire
- interpolation bicubique B-spline
- Interpolation quintic B-spline.

Pour rechercher le champ de déplacement, il est nécessaire de faire des hypothèses sur sa forme. Ces hypothèses ont pour conséquences d'imposer la forme de l'imagette après déformation.

Si le champ de déplacement est recherché sous la forme d'un déplacement de corps rigide :

$$u(x,y) = u_0 \quad \text{et} \quad v(x,y) = v_0 \tag{1.19}$$

l'imagette peut simplement s'être déplacée, mais elle ne peut pas s'être déformée, elle est toujours carrée. C'est une hypothèse contrainte souvent trop forte.

Si le champ de déplacement est recherché sous une forme affine :

$$u(x,y) = u_0 + u_1 x + u_2 y \quad \text{et} \quad v(x,y) = v_0 + v_1 x + v_2 y \tag{1.20}$$

l'imagette peut s'être déplacée, avoir tourné et s'être déformée en cisaillement ou en traction - compression. L'imagette déformée prend la forme d'un quadrilatère quelconque, la déformation est constante sur une imagette. Cette hypothèse convient dans un grand nombre de cas si les imagettes sont assez petites et les gradients de déformations relativement faibles.

Dans les autres cas, l'hypothèse d'une transformation quadratique est nécessaire :

$$u(x,y) = u_0 + u_1 x + u_2 y + u_3 x y + u_4 x^2 + u_5 y^2 \tag{1.21a}$$

$$v(x,y) = v_0 + v_1 x + v_2 y + v_3 x y + v_4 x^2 + v_5 y^2 \tag{1.21b}$$

L'hypothèse prise dans Vic est au moins de prendre en compte la déformation de l'imagette. La notice ne fait cependant pas état explicitement de ce choix.

La recherche du déplacement d'un point de l'image de référence associé à l'état représenté par l'image déformée N utilise comme départ du processus de recherche à la fois le déplacement du même point associé à l'image N-1 et le déplacement de ces voisins. Dans le logiciel Vic2D, le logiciel commence la corrélation en partant d'un point qu'il a défini lui-même entre l'image de référence et l'image 1 ou bien en partant d'un point qui aura été désigné manuellement sur ces 2 images.

References

[Armstrong and Kino 1995]. W.D. Armstrong and H. Kino. Martensitic Transformations in a NiTi Fiber Reinforced 6061 Aluminum Matrix Composite, J Intell Mater Syst Struct 6 (1995), p. 809.

[Armstrong and Lorentzen 1997]. W.D. Armstrong and T. Lorentzen. Fiber phase transformation and matrix plastic flow in a room temperature tensile strained NiTi shape memory alloy fiber reinforced 6082 aluminum matrix composite, Scripta Mater 36 (1997), p. 1037-1043.

[Armstrong et al. 1998]. W.D. Armstrong, T. Lorentzen, P. Brondsted and P.H. Larsen. An experimental and modeling investigation of the external strain, internal stress and fiber phase transformation behavior of a NiTi actuated aluminum metal matrix composite, Acta Mater 46 No. 10 (1998) p. 3455-3466.

[Avril et al. 2004]. S. Avril, F. Pierron and M. Grédiac. Evaluation de l'identifiabilité d'une loi de comportement anisotrope par la méthode des champs virtuels. Proceedings Colloque Photomécanique (2004), p. 57-64.

[Balta et al. 1999]. J.A. Balta, V. Michaud, M. Parlinska, R. Gotthardt and J.A Manson. Adaptive composites with embedded shape memory alloy wires, in: Materials for Smart Systems III, 30 November–12 December, 1999, Boston, MA, Materials Research Society 604 (2000), p. 141–146.

[Balta et al. 2000]. J.A. Balta, V. Michaud, M. Parlinska, R. Gotthardt and J.A Manson. Adaptive composite materials processing, in Proceedings of Structural Development upon Polymer: Physical Aspects, 24–28 October, Guimaraes, Portugal, European Physical Society, (2000), p. 33–34.

[Balta et al. 2001]. J.A. Balta, V. Michaud, M. Parlinska, R. Gotthardt and J.A. Manson. Adaptive composites with embedded shape memory alloy wires, in: C. Lynch (Ed.), Proceedings of SPIE; Smart Materials and Structures; Active Materials; Behaviour and Mechanics, 4–8 March, Newport Beach, CA, vol. 4333 (2001), p. 377–386.

[Barrado et al. 2009]. M. Barrado, G.A. López, M.L. Nó and J. San Juan, Composites with ultra high damping capacity based on powder metallurgy shape memory alloys, Materials Science and Engineering: A 521-522 (15) (2009), p. 363-367.

[Beauchamp et al 1992]. C.H. Beauchamp, R.H. Nadolink, S.C. Dickinson and L.M. Dean. Shape memory alloy adjustable camber (SMAAC) control surfaces, in: Proceedings of the First European Conference on Smart Structures and Materials, Glasgow (1992), p. 189–192.

[Berfield et al. 2007]. T.A. Berfield, J.K. Patel, R.G. Shimmin, P.V. Braun, J. Lambros and N.R. Sottos. Micro and nanoscale deformation measurement of surface and internal planes via digital image correlation. Experimental Mechanics 47 (2007), p. 51-62.

[Bergonnier et al. 2005]. S. Bergonnier, F. Hild, J. Rieunier and S. Roux. Strain heterogeneities and local anisotropy in crimped glass wool. Journal of Materials Science 40 (2005), p. 5949–5954.

[Bernal 2004]. L. I. Barbero Bernal. Cyclic Behavior of Superelastic Ni-T and NiTiCr Shape Memory Alloys, PhD thesis. Georgia Institute of Technology, December 2004.

[Besnard 2006]. G. Besnard, F. Hild and S. Roux Finite-Element. Displacement fields analysis from digital images: Application to Portevin–Le Châtelier bands. Experimental Mechanics, 46 (2006), p. 789–803.

[Bidaux et al. 1996]. J.-E. Bidaux, J.-A.E. Manson and R. Gotthardt. Active modification of the vibration frequencies of a polymer beam using shape memory alloy fibres, Third ICIM/ECSSM'96, Lyon, (1996), p. 517–522.

[Bidaux et al. 1997]. J.E. Bidaux, J.-A.E. Manson and R. Gotthardt. Active stiffening of composite materials by embedded shape-memory-alloy fibres, Mat. Res. Soc. Symp. Proc. 459 (1997), p. 107–117.

[Bollas et al. 2007]. D. Bollas, P. Pappas, J. Parthenios and C. Galiotis. Stress generation by shape memory alloy wires embedded in polymer composites, Acta Materialia 55 (2007), p. 5489-5499.

[Bonnet et al. 2003]. M. Bonnet, B.D. Bui and A. Constantinescu. Principes variationnels et exploitation de mesures de champs en élasticité. Mécanique et Industries 4 (2003), p.687-697.

[Bornert 2006]. M. Bornert. Resolution and spatial resolution of digital image correlation techniques. In: Proceedings of Photomechanics 2006, International Conference on full-field measurement technique and their application in experimental solid mechanics, CD ROM, Grédiac, M. & Huntley, J. eds. Clermont-Ferrand, France (2006)..

[Bornert et al. 2009]. M. Bornert, F. Brémand, P. Doumalin, J.-C. Dupré, M. Fazzini, M. Grédiac, F. Hild, S. Mistou, J. Molimard, J.-J. Orteu., L, Robert Y. Surrel, P. Vacher and B. Wattrisse. Assessment of digital image correlation measurement errors: methodology and results. Experimental Mechanics 49 (2009), p. 353-370.

[Brillaud 2002]. J. Brillaud and F. Lagattu. Limits and possibilities of laser speckle and white light image correlation methods: theory and experiments. Appl Opt; 41 (2002), p. 6603-6613.

[Burkart and Read 1953]. MW. Burkart, and TA. Read. Diffusionless phase change in the Indium–Thallium system; Trans AIME (1953), p.197-1516.

[Chalal 2005]. H. Chalal. Identification numérique et expérimentale de lois de comportement non-linéaires de matériaux composites à partir de mesures de champs cinématique. PhD thesis, Ecole Supérieure d'Arts et Métiers, Centre de Chalons en Champagne, 2005.

[Chalal et al. 2004]. H. Chalal, F. Meraghni, F. Pierron, M. Grédiac Direct identification of the damage behaviour of composite materials using the virtual fields method. Composites Part A 35 (5) (2004), p. 841-848.

[Chalal et al. 2006]. H. Chalal, S. Avril, F. Pierron and F. Meraghni. Expérimental identification of a nonlinear model for composites using the grid technique coupled to the virtual fields method. Composite Part A 37(2006), p. 315-325,

[Chu et al. 1985]. T.C. Chu, W.F. Ranson, M.A Sutton and W.H. Peters. Applications of digital image correlation techniques to experimental mechanics. Experimental Mechanics 25 (1985), p. 232-244.

[Claire et al. 2002]. D. Claire, F. Hild and S. Roux. Identification of damage fields using kinematic measurements. Comptes rendus Mécanique 330 (2002), p.729-734.

[Claire et al. 2003]. D. Claire, S. Roux and F. Hild. Identification de conductivités thermique et de propriétés élastique locales par analyse de champs-Identification of thermal conductivities and élastic properties by field analyses. Mécanique et Industries, 4(6), (2003), p. 655-665.

[Constantinescu 1995]. A. Constantinescu. On the identification of elastic moduli from displacement-force boundary measurements. Inverse Problems in Engineering, 1 (1995), p. 293-315.

[Delaey 1990]. L. Delaey. Diffusionless transformations. In: Cahn, R. W., Haasen, P., Kramen, E. J. (Eds.), Phase Transformations in Materials. Vol. 5 of Material Science and Technologies. VCH Publishers, New York, Ch. 6 (1990), p. 339–404.

[Doumalin 2000]. P. Doumalin. Microextensométrie locale par corrélation d'images numériques-Application aux études micromécaniques par microscopie électronique à balayage. PhD thesis, Ecole Polytechnique (LMS, France), 2000.

[Ehrenstein 2004]. G.W. Ehrenstein. Polymeric Materials, Carl Hanser Publisher, Munich (2004).

[El Bartali 2007]. A. El Bartali. Apport des mesures de champs cinématiques à l'étude des micromécanismes d'endommagement en fatigue plastique d'un acier inoxydable duplex. PhD thesis, Ecole Centrale de Lille (France), 2007.

[Elspass and Kunzmann 1991]. W.J. Elspass and J. Kunzmann. in: I. Chopra (Ed.), Proceedings of SPIE on Smart Structures and Materials: Smart Structures and Integrated Systems, vol. 2717 (1991), p. 320–329.

[Forquin et al. 2004]. P. Forquin, L. Rota, Y. Charles and F. Hild. A method to determine the macroscopic thoughness scatter of brittle materials, International Journal of Fracture, 125 (1) (2004), p. 171-187.

[Fouassier et al. 2002]. O. Fouassier, J.Chazelas, JF. Silvain. Conception of a consumable copper reaction zone for a NiTi/SnAgCu composite material, Composites: Part A 33 (2002), p.1391–1395.

[Friend and Mattey 1998]. C.M. Friend and C.R.D. Mattey. Active vibration control of shape memory hybrid Composites, in: G.R. Tomlinson, W.A. Bullough (Eds.), Proceedings of the

Fourth ESSM and Second MIMR Conference, Harrogate, Institute of Physics, 6–8 July (1998), p. 107–114.

[Furuya and M. Taya 1996]. Y. Furuya and M. Taya. Enhancement of high temperature mechanical strength of TiNi fiber/Al composite induced by shape memory effect, Trans. Jpn Inst. Metals 60 12 (1996), p. 1163–1172.

[Furuya et al. 1993]. Y. Furuya, A. Sasaki and M. Taya. Enhanced mechanical properties of TiNi shape memory fiber/Al matrix composite, Mater Trans JIM 34 (1993), p. 224-227.

[Garcia et al. 2002]. D. Garcia, J.-J. Orteu and L. Penazzi. A combined temporal tracking and stereo-correlation technique for accurate measurement of 3D displacements: Application to sheet metal forming. J. Mater. Process. Techno., 125-126 (2002), p. 736-742.

[Garcia et al. 2006]. C. Garcia, D. Celentano, F. Flores, J.-P. Ponthot and O. Oliva. Numerical modelling and experimental validation of steel deep drawing processes: Part II: Applications. J. Mater. Process. Techno. 172 (2006), p. 461-471.

[Gau 1999]. G. Gaussorgues. La thermographie infrarouge : principes, technologies applications. Technique et Documentation, Lavoisier (1999).

[Gavrus 1999]. A. Gavrus, E. Massoni and J.L. Chenot. The rheological parameter identification formulates as an inverse finite element problem. Inverse Problem in Engineering, 7 (1999), p. 1-41.

[Gotthardt and Bidaux 1988]. R. Gotthardt and J.-E. Bidaux. Functional materials based on polymeric matrix composites with embedded shape memory alloy fibres in: K. Inue (Ed.), International Conference on Displacive Phase Transfer and their Application in Material Engineering, TMS Publication (1988), p. 157–166.

[Grando and Salvia 1996]. J. Grando and M. Salvia. Influence of processing conditions on actuation properties of adaptive hybrid composites, In: P.F. Gobin et al., Editors, Proceedings of the Third International Conference on Intelligent Materials, (ICIM/ECSSM'96), Lyon, France (1996), p. 530.

[Grédiac 1996]. M. Grediac. On the direct determination of invariant parameters governing anisotropic plate bending problems. International Journal of Solids and Structures, 33(27), (1996), p. 3969-3982.

[Grédiac et al. 2002]. M. Grédiac, E. Toussaint and F. Pierron. Special virtual fields for the direct determination of material parameters with the virtual fields method. Part1- Principle and definition. International Journal of Solids and Structures, 39(2002), p. 2691-2705.

[Grédiac and Pierron 2006]. M. Grédiac and F. Pierron. Applying the Virtual Fields Method to the identification of elasto-plastic constituve parameters. International Journal of Plasticity, 22(4) (2006), p.602-627.

[Hamada et al. 1998]. K. Hamada, J.H. Lee, K. Mizuuchi, M. Taya and K. Inoue. Thermomechanical behavior of NiTi shape memory alloy fiber reinforced 6061 aluminum matrix composite; Metall. Mater. Trans. 29A (1998), p. 1127–1135.

[Hamming et al. 2008]. L.M. Hamming, X.W. Fan, P.B. Messersmith and L.C. Brinson. Mimicking mussel adhesion to improve interfacial properties in composites, J Compos Sci Technol 68 (2008), p. 2042–2048.

[Hatanaka et al. 1992]. K. Hatanaka, T. Fujimitsu and H. Inoue. A measurement of three-dimensional strains around a creep-crack tip. Optics and lasers in Engineering, 32(3) (1992), p. 211-17.

[Hebda et al. 1995]. D.A. Hebda, M.E. Whitlock, J.B. Ditman and S.R. White. Manufacturing of Adaptive Graphite/Epoxy Structures with Embedded Nitinol Wires, J. Intell. Mat. Syst. Struct. 6 (1995), p. 220-228.

[Hild 2002]. F. Hild. CORRELILMT: A software for displacement field measurements by digital image correlation. Internal report n°254, ENS Cachan (LMT Cachan, France), 2002.

[Hild and Roux 2006]. F. Hild and S. Roux. Digital Image Correlation: from displacement measurement to identification of elastic properties- a review. Strain, 42(2006), p. 69-80.

[Hild and Roux 2008]. F. Hild and S. Roux. CORRELI-Q4: A software for "Finite-element" displacement field measurements by digital image correlation. Internal report n°269, ENS Cachan (LMT Cachan, France), (2008).

[Hwang et al. 1983]. CM. Hwang, M. Meichle, MB. Salamon, CM. Wayman. Transformation behaviour of a Ti50Ni47Fe3 alloy II. Subsequent premartensitic behaviour and the commensurate phase; Philos Mag A; 47 (1983), p. 31-62.

[ISO04]. ISO (International Organization for Standardization) (2004) International vocabulary of basic and general terms in metrology (VIM) - Draft, ISO/DGuide 99999.

[Jin and Bruck 2004]. J. Jin and H.A. Bruck. Objective AFM and digital image correlation for evaluation of deformations in advanced materials at the microscale and nanoscale. Procceedings of the 12th International Conference on Experimental Mechanics (ECCM12), 29 August-2 september (2004), Politecnico di Bari, Italy

[Jonnalagadda and Sottos 1997] K.D. Jonnalagadda and N.R. Sottos. Transformation of embedded shape memory alloy ribbons, in: V.V. Varadan, J. Chandra (Eds.), Proceedings of SPIE on Smart Structures and Materials: Mathematics and Control in Smart Structures 3039 (1997), p. 242–253.

[Jonnalagadda et al. 1997]. K. Jonnalagadda, G.E. Kline and N.R. Sottos. Local displacements and load transfer in shape memory alloy composites, Exp. Mech. 37 (1997), p. 78-86.

[Jonnalagadda et al. 1998]. KD. Jonnalagadda, NR. Sottos, MA. Qidwai and DC. Lagoudas. Transformation of embedded shape memory alloy ribbons, J Intell Mater Syst Struct; 9(5), (1998), p. 379-390.

[Ju and Shimamoto 1999]. D.Y. Ju and A. Shimamoto. Damping property of epoxy matrix composite beams with embedded shape memory alloy fibres. J Intel Mater Sys Struct 10 (1999), p. 514–520.

[Khachin et al. 1978]. VN. Khachin, YI. Paskal, VE. Gunter, AA. Monasevich and VP. Sivokha. Structural Transformation, Physical Properties and Memory Effects in the NiTi and Ti-based Alloys; Phys Met Metallogr 46 (1978), p. 49-57.

[Khachin et al. 1979]. VN. Khachin, VE. Gjunter, VP. Sivokha and AS. Savvinov. Lattice instability, martensitic transformation, plasticity and anelasticity of NiTi; Proc Int Conf on Martensitic Transformation (ICOMAT- 79), Cambridge, MA, (1979). p. 474.

[Kim 2006]. C. Kim. A Smart Polymer Composite Actuator with Thin Sma Strips, Int. J. Mod. Phys. B 20 (25–27), (2006), p. 3733–3738.

[Kline et al 1995]. G.E. Kline, K. Jonnalagadda and N.R. Sottos. Adaptive Material Systems, ASME, AMD vol. 206/MD 58, (1995), p. 121–128.

[Ladeveze 1975]. Ladeveze. Comparaison de modèles de milieux continus, PhD thesis, Université P et M. Curie, Paris (France), 1975.

[Ladeveze 1977]. Ladeveze. Nouvelles procedures d'estimation d'erreur relative à la méthode des éléments finis et applications, Proc. Journées éléments finis, Rennes (France), 1977.

[Lagattu 2004]. F., Lagattu J. Brillaud and M. Lafarie-Frenot. High strain gradient measurements by using digital image correlation technique. Materials Characterization 53 (1), (2004), p. 17– 28.

[Lau 2002]. K.T. Lau. Control of natural frequencies of a clamped–clamped composite beam with embedded shape memory alloy wires. Comp Struct 58 (2002), p. 39–47.

[Lau et al. 2002b]. K.T. Lau, C.K. Poon, L.H. Yam and L.M. Zhou. Bonding behaviour at a NiTi/epoxy interface: SEM observation and theoretical study. Mater Sci Forum 394–395 (2002), p. 527–530.

[Lau et al. 2002c]. K.T. Lau, W.L. Chan, S.Q. Shi and L.M. Zhou. Debond induced by strain recovery of an embedded NiTi wire at a NiTi/epoxy interface: micro-scale observation. Mater Des 23 (2002), p. 265–270.

[Lau et al. 2002d]. K.T. Lau, W.Y. Tam, X.L. Meng and L.M. Zhou. Morphological study on twisted NiTi wires for smart composites systems, Mater Lett 57 (2002), p. 364–368.

[Leclerq et al. 1994]. S. Leclerq, C. Lexcellent, H. Tobushi and P.H. Lin. Thermodynamical modeling of recovery stress associated with r-phase transformation in TiNi shape memory alloys, Materials Transactions, JIM, 35, (5), (1994), p. 325-331.

[Lee 2003]. J.K Lee. AE characteristic of the damage behavior of TiNi/Al6061 SMA composite, Comp. Struct. 60 (2003), p. 255–263.

[Lee and Taya 2004, M61]. J. K. Lee and M. Taya. Strengthening mechanism of shape memory alloy reinforced metal matrix composite, Scripta Materialia 51 (5) (2004), p. 443-447.

[Levenberg 1944]. K. Levenberg. A method for the solution of certain non-linear problems in least squares», Quarterly of Applied Mathematics 2 (1944), p. 164–168.

[Li et al. 2001]. Yan Li, Lishan Cui, Yanjun Zheng and Dazhi Yang. DSC study of the reverse martensitic transformation in prestrained TiNi shape memory alloy in different composites, Materials Letters 51(2001), p.73–77.

[Liang and Rogers 1997]. C. Liang and C.A. Rogers. Design of shape memory alloy actuators. J Intel Mater Syst Struct 8 (1997), p. 303–313.

[Liang et al. 1989]. C. Liang, J. Jia, C. Rogers. Behavior of shape memory alloy reinforced composite plates, Part II: results. In: Proceedings of the 30th Structures, structural dynamics and materials conference, AIAA-89-1331-CP; (1989), p. 1504-1510.

[Liang et al. 1991]. C. Liang, C. A. Rogers and C. R. Fuller. Acoustic transmission and radiation analysis of adaptive shape-memory alloy reinforced laminated plates, Journal of Sound and Vibration 145 (1) (1991), p. 23-41.

[Ling and Kaplov 1980]. H.C. Ling, R. Kaplov. Phase Transition and Shape Memory in NiTi; Metall Trans A 11(1980), p. 77-83.

[Ling and Kaplov 1981]. H.C. Ling, R. Kaplov. Stress-Induced Shape Changes and Shape Memory in the R and Martensite Transformations in Equiatomic NiTi; Metall Trans A 12 (1981), p. 2101-2111.

[Ling and Kaplow 1981]. H.C. Ling, and R. Kaplow. Stress-induced shape changes and shape memory in the R and martensitic transformations in equiatomic NiTi, Metallurgical Transactions A 12 (1981), p. 2101-2111.

[Liu and Fischer 1997]. Y.L. Liu and G. Fischer. In situ measurement of local strain in a metal matrix composite by the object grating technique. Scripta Materialia, 36 (10) (1997), p. 1187-1194.

[Liu et al. 2008]. Y. Liu, Basem Al-Matar and Golam Newaz. An Investigation on the Interface in a NiTi Short-Fiber-Reinforced 6061 Aluminum Composite by Transmission Electron Microscope, Metallurgical and Materials Transactions A 39 (2008), p. 2749-2759.

[López et al. 2009]. G.A. López, M. Barrado, J.M. San Juan and M.L. Nó. Mechanical spectroscopy measurements on SMA high-damping composites, Materials Science and Engineering A 521–522 (2009), p. 359–362.

[López et al.2008]. G.A. López, M. Barrado, E.H. Bocanegra, J.M. San Juan, M.L. Nó. Influence of the matrix and of the thermal treatment on the martensitic transformation in metal matrix composites, Materials Science and Engineering: A 481-482 (2008), p. 546-550.

[Lu and Cary 2000]. H. Lu and P.D. Cary. Deformation measurements by digital image correlation: implementation of a second-order displacement gradient. Experimental Mechanics, 40 (4) (2000), p. 393-400.

[Macqueron et al. 1991]. J. L. Macqueron, , M. Morin, , G. Guénin, , A. Planes, , J. Elgueta, and T. Castan. Atomic ordering and martensitic transition in a Cu-Zn-Al shape memory alloy. Journal de Physique IV 1 (9), (1991), C4, p. 259–263.

[Marfia and Sacco 2005]. S. Marfia and E. Sacco. Micromechanics and homogenization of SMA-wire-reinforced materials, J. Appl. Mech. 72 (2), (2005), p. 259–268.

[Marquardt 1963]. D. W. Marquardt. An algorithm for least-squares estimation of non-linear parameters. Journals on Applied Mathematics 11(1963), p 431-441.

[Merzouki 2008]. T. Merzouki. Identification expérimentale et modélisation du comportement d'un multicrista en alliage à mémoire de forme », PhD thesis, Arts et Metiers ParisTech, Metz, 2008.

[Mguil-Touchal 1997]. S. Mguil-Touchal. Une technique de corrélation directe d'images numériques : application à la détermination des courbes limites de formage et proposition d'un critère de striction. PhD thesis, INSA de Lyon (France), 1997.

[Mguil-Touchal et al.1997]. S. Mguil-Touchal, F. Morestin and M. Brunet. Various experimental applications of digital image correlation methods. Computer Meth. and Expl Measmt, (1997), p. 46–58.

[Miyazaki and Otsuka 1984]. S. Miyazaki and K. Otsuka. Mechanical behaviour associated with the premartensitic rhombohedral-phase transition in a Ti50Ni47Fe3 alloy"; Philos Mag A 50 (1984), p. 393-408.

[Miyazaki and Otsuka 1986]. S, Miyazaki and K Otsuka. Deformation and transition behavior associated with the R -phase in Ti-Ni alloys"; Metall Trans. A 17 (1986), p.53-63.

[Miyazaki et al. 1988]. S. Miyazaki, S. Kimura, K. Otsuka. Shape-memory effect and pseudoelasticity associated with the R-phase transition in Ti-50.5 at.% Ni single crystals. Philos Mag A 57 (1988), p. 467-478.

[Mohammad Sadeghi 2010]. B. Mohammad Sadeghi. Identification de lois de comportement à partir de mesures de champs cinématiques dans le cas de chargements complexes, Application à la mise en forme des aciers TRIP », PhD thesis, Arts et Metiers ParisTech, Metz, 2010.

[Murasawa et al. 2004]. G. Murasawa, K. Tohgo and H. Ishii. Deformation Behavior of NiTi/Polymer Shape Memory Alloy Composites – Experimental Verifications, J. Compos. Mater. 38 (2004), p. 399–416.

[Neuilly and Courtier 1997]. M. Neuilly and J.-C. Courtier. Vocabulaire de l'analyse - Erreurs et incertitudes de mesure, Techniques de l'ingénieur, traité Analyse et caractérisation, P100 (1997), p. 1-8.

[Neuking et al. 2005]. K. Neuking, A. Abu-Zarifa, S. Youcheu-Kemtchou and G. Eggeler. Polymer/NiTi-composites: Fundamental Aspects, Processing and Properties, Adv. Eng. Mater. 7 (2005), p. 1014–1023.

[Neuking et al. 2008]. K. Neuking, A. Abu-Zafaria and G. Eggler. Surface engineering of shape memory alloy/polymer-composites: improved adhesion between polymers and pseudoelastic shape memory alloys, J Mater Sci Eng A 481–482 (2008), p. 606–611.

[Nishiyama, 1978]. Z. Nishiyama. Martensitic Transformations. Academic Press, San Diego, (1978).

[Nouri 2009]. H. Nouri. Modélisation et identification de lois de comportement avec endommagement en fatigue polycyclique de matériaux composite à matrice thermoplastique, PhD thesis, Arts et Metiers ParisTech, Metz, (2009).

[Olander 1932]. A. Olander. An electrochemical investigation of solid cadmium-gold alloys. Journal of the American Chemical Society 54 (1932), p.3819–3833.

[Olson and Cohen, 1982]. G. B. Olson, M. Cohen. Stress assisted isothermal martensitic transformation: Application to TRIP steels. Metall. Trans. A 13A (1982), p.1907–1914.

[Ostachowicz 1999]. W. Ostachowicz, M. Krawczuk and A. Zak. Natural frequencies of a multilayer composite plate with shape memory alloy wires. Finite Elements in Analysis and Design 32 (1999), p. 71–83.

[Otsuka and Ren 2005]. K. Otsuka, X. Ren. Physical metallurgy of Ti–Ni-based shape memory alloys. Progress in Materials Science 50 (2005), p. 511–678.

[Otsuka and Shimizu 1986]. K. Otsuka, K. Shimizu. Pseudoelasticity and shape memory effects in alloys ; Int Metals Rev (1986), p. 31: 93-114.

[Otsuka and Wayman, 1999]. K. Otsuka, CM. Wayman. Editors, shape memory materials. Cambridge: Cambridge University Press, (1999).

[Otsuka et al. 1976]. K. Otsuka, C. Wayman, , K. Nakai, , H. Sakamoto and K. Shimizu. Superelasticity effects and stress-induced martensitic transformations in Cu-Al-Ni alloy. Acta Metallurgica 24 (1976), p. 207–226.

[Paine and Rogers 1991]. J.S.N. Paine and C.A. Rogers. The Effect of Thermoplastic Composite Processing on the Performance of Embedded Nitinol Actuators, J. Thermoplast. Comp. Mater. 4 (1991), p. 102-122.

[Paine and Rogers 1993]. J.S.N. Paine and C.A. Rogers. Characterization of interfacial shear strength between SMA actuators and host composite material in adaptive composite material systems, Adaptive Structures and Material Systems, ASME, AD-35, (1993), p. 63–70.

[Paine and Rogers 1994a]. J.S.N. Paine and C.A. Rogers. The Response of SMA Hybrid Composite Materials to Low Velocity Impact, J. Intell. Mat. Syst. Struct. 5 (1994), p. 530-535.

[Paine and Rogers 1994b]. J.S.N. Paine and C.A. Rogers. Active Materials and Smart Structures, edited by G. L. Anderson and D. C. Lagoudas, SPIE, Vol.2427 (SPIE, College Station, 1994), p. 358.

[Paine and Rogers 1994c]. J.S.N. Paine, C.A. Rogers, in: E. Garcia, H. Cudney and A. Dagsupta (Eds.). Adaptive Structures and Composite Materials-Analysis and Application, The American Society of Mechanical Engineers, New York, USA, (1994), p. 75–84.

[Paine et al. 1992]. JSN Paine, W.M. Jones and C.A. Rogers. Nitinol actuator to host composite interfacial adhesion in adaptive hybrid composites. In: AIAA; 33rd structural dynamics and materials conference, (1992). p. 556–565.

[Pan Bing and Fu-long 2006]. X.H. Pan Bing and D. Fu-long. Performance of sub-pixel registration algorithms in digital image correlation. Measurement Science and Technology 17 (2006), p. 1615–1621.

[Pan et al. 2009]. B., Pan K. Qian, H. Xie and A. Asundi. Two-dimensional digital image correlation for in-plane displacement and strain measurement: a review; Measurement science and technology journal 20 (2009), p. 1-17.

[Parlinska et al. 2001]. M. Parlinska, J.A. Balta, V. Michaud, J.-E. Bidaux, J.A. Månson and R. Gotthardt. Vibrational response of adaptive composites, J. Phys. IV France 11 (2001), p. 129-134.

[Parlinska et al. 2001]. M. Parlinska, J.A. Balta, V. Michaud, J.-E. Bidaux, J.A. Månson and R. Gotthardt. Vibrational response of adaptive composites, J. Phys. IV France 11 (2001), p. 129-134.

[Parthenios et al 2001]. J. Parthenios, G.C. Psarras and C. Galiotis. Adaptive composites incorporating shape memory alloy wires; Part 2: Development of internal recovery stresses as a function of activation temperature, Composites part A: applied science and manufacturing 32 (2001), p. 1735-1747.

[Patoor et al. 2006]. E. Patoor, D. C. Lagoudas, P. B. Entchev , L. C. Brinson and X. Gao. Shape memory alloys - part I: General properties and modelling of single crystals. Mechanics of Materials 38 (2006), p. 391–429.

[Poon et al. 2004]. Chi-Kin Poon, Li-Min Zhou and Lai-Hang Yam. Size effect on the optimum actuation condition for SMA-composites, Composite Structures 66 (1-4) (2004), p. 503-511.

[Poon et al. 2005]. C.K. Poon, K.T. Lau and L.M. Zhou. Design of pull-out stresses for prestrained SMA wire/polymer hybrid composites, Compos. Part B Eng. 36 (2005), p. 25–31.

[Popov 2005]. P. A. Popov. Constitutive Modelling of Shape Memory Alloys and Upscaling of Deformable Porous Media. PhD thesis. Texas A & M University, 2005.

[Psarras et al. 2001]. G.C. Psarras, J. Parthenios and C. Galiotis. Adaptive composites incorporating shape memory alloy wires; Part 1: Probing the internal stress and temperature distributions with a laser Raman sensor J. Mater. Sci. 36 (2001), p. 1-12.

[Raghavan et al. 2010]. J. Raghavan, T Bartkiewicz, S Boyko, M Kupriyanov, N. Rajapakse and B Yu. Damping, tensile, and impact properties of superelastic shape memory alloy (SMA) fiber-reinforced polymer composites, Composites: Part B 41 (2010), p. 214–222.

[Roger 1990]. C.A. Roger. Active vibration and structural acoustic control of shape memory alloy hybrid composites: experimental results. J Acoust Soc Am No 6 88 (1990), p. 2803–2811.

[Rogers et al. 1991].C.A. Rogers, C. Liang and S. Li. Active damage control of hybrid material systems using induced strain actuators, in: Proceedings of the AIAA/ASME/ASCE/AHS/ASC 32nd Structures, Structural Dynamics and Materials Conference, Technical Papers, Part 2, April (1991), p. 1190–1203.

[Saburi et al. 1980]. T. Saburi, C. M. Wayman, K. Takata and S. Nenno. The shape memory mechanism in martensitic alloys. Acta Metallurgica 28 (1980), p.15–32.

[Sadrnezhaad et al. 2009]. S. K. Sadrnezhaad, N. Hassanzadeh Nemati and R. Bagheri. Improved adhesion of NiTi wire to silicone matrix for smart composite medical applications, Materials and Design 30 (2009), p. 3667–3672.

[Saunders et al 1991]. W.R. Saunders, H.H. Robertshaw, and C.A. Rogers. Structural acoustic control of a shape memory alloy composite beam, Journal of Intelligent Material Systems and Structures 2 (1991), p. 508-527.

[Schreier and Sutton 2002]. H. Schreier and M.A. Sutton. Systematic errors in digital image correlation due to undermatched subset shape functions. Experimental Mechanics, 42 (3), (2002), p. 303-310.

[Schreier et al. 2000]. H. W. Schreier, J.R. Braasch and M. Sutton. Systematic errors in digital image correlation caused by intensity interpolation. Optical Engineering, 39 (11) (2000), p. 2915-2921.

[Schrooten 2000]. J. Schrooten, K.A. Tsoi, R. Stalmans, Y.J. Zheng and P. Sittner. Comparison between generation of recovery stresses in shape memory wires and composites, in: A.R. Wilson, H. Asanuma (Eds.), Proceedings of SPIE, Smart Materials and MEMS, 13–15 December, Melbourne, Australia, vol. 4234, (2000), p. 114–124.

[Schrooten et al. 2001]. J. Schrooten, K.A. Tsoi, R. Stalmans, Y.J. Zheng and P. Šittner. Comparison between generation of recovery stresses in shape memory wires and composites: theory and reality, In: A.R. Wilson and H. Asanuma, Editors, Proceedings of SPIE; Smart Materials vol. 4234 (2001), p. 114–124.

[Shimamoto and Taya 1997]. A. Shimamoto and M. Taya. Reduction in KI by shape memory effect in a TiNi shape-memory fiber-reinforced epoxy matrix composite. Transactions of the Japan Society of Mechanical Engineers, Part A 63 605 (1997), p. 26–31.

[Shimamoto et al. 1997]. A. Shimamoto, Y. Furuya and M. Taya. Active control of crack-tip stress intensity by contraction of shape memory TiNi fibers embedded in epoxy matrix composite. In: Proc. 11th Int. Conf. on Comp. Materials, Gold Coast, Australia, July (1997), p. VI493-9.

[Shimamoto et al. 2004]. A. Shimamoto, H. Ohkawara and F. Nogata. Enhancement of mechanical strength by shape memory effect in TiNi fiber-reinforced composites, Eng. Fract. Mech. 71 (2004), p. 737-746.

[Silvain et al. 1999]. J.F. Silvain, J. Chazelas, M. Lahaye and S. Trombert. The use of shape memory alloy NiTi particles in SnPbAg matrix: interfacial chemical analysis and mechanical characterisation, Materials Science and Engineering A273–275 (1999), p. 818–823.

[Simpson and Boller 2002]. J. Simpson and C. Boller. Performance of SMA-reinforced composites in an aerodynamic profile in: A.-M.R. McGowan (Ed.), Proceedings of SPIE on Smart Structures and Materials, Industrial and Commercial Applications of Smart Structures Technologies 4698 (2002), p. 416–426.

[Sittner et al. 2006]. P. Sittner, M. Landa, P. Lukas and V. Novak. R-phase transformation phenomena in thermomechanically loaded NiTi polycrystals, Mechanics of Materials 38 (2006), p. 475–492.

[Smith et al. 2004]. N.A. Smith, G.G. Antoun, A.B. Ellis and W.C. Crone. Improved adhesion between nickel–titanium shape memory alloy and a polymer matrix via silane coupling agents, Composites A35 (2004), p. 1307–1312.

[Soppa 2004]. E. Soppa, P. Doumalin, P., Binkele T., Wiesendanger M. Bornert and S. Schmauder. Experimental and numerical characterisation of in-plane deformation in two-phase materials. Computational Materials Science, 21(2001), p. 261–275.

[Stachowiak and McCormick 1988]. G.B. Stachowiak and, P.G. McCormick. Shape memory behaviour associated with the R and martensitic transformations in a NiTi alloy"", Acta Metallurgica, 36, 2(1988), p. 291-297.

[Stalmans et al. 2000]. R. Stalmans, K.A. Tsoi and J Schrooten. The transformational behaviour of shape memory wires embedded in a composite matrix, in: P.F. Gobin, C.M. Friend (Eds.), Fifth European Conference on Smart Structures and Materials, Glasgow, Scotland, 22–24 May, 2000, Proceedings of SPIE, vol. 4073, (2000), p. 88-96.

[Surrel 1998]. J. Surrel and Y. Surrel. The fringe projection technique for shape acquisition of live biological objects, Journal of Optics, 29 (1), (1998), p. 6-13.

[Surrel 2004]. Y. Surrel. Les techniques optiques de mesure de champ : essai de classification, Instrumentation Mesure Métrologie RS série I2M, 4, (2004), p. 11-42.

[Sutton et al. 1986]. M. A., Sutton M. Cheng, S. R. McNeill, Y. J. Chao and W. H. Peters. Application of an optimized digital image correlation method to planar deformation analysis, Image and Vision Computing, 4 (3), (1986), p. 143-150.

[Sutton et al. 1988]. M. A. Sutton S. McNeill, J. Jang and M. Babai. Effects of subpixel image restoration on digital correlation error estimates. Optical Engineering, 27 (10), (1988). p. 870-877.

[Sutton et al. 1999]. M. A. Sutton, S. R. McNeill, J. D. Helm and Y. J. Chao. Advances in two-dimensional and three-dimensional computer vision, in Photomechanics, Rastogi P. K. (eds.), Springer-Verlag, Berlin (1999), p. 323-372.

[Sutton et al. 2008]. M.A. Sutton, J.H. Yan, V. Tiwari, H.W. Schreier and J.J. Orteu. The effect of out-of-plane motion on 2D and 3D digital image correlation measurements. Optics and Lasers in Engineering, 46 (2008), p. 746-757.

[Tahiri et al. 2004]. V.L. Tahiri, E. Patoor and A. Eberhardt. An analysis of the thermomechanical behaviour of a shape memory alloy/elastomer composite, J. Phys. IV 115 (2004), p. 195–203.

[Tamura 1992]. I. Tamura. Martensitic transformations and mechanical effects, in Martensite; A Tribute to Morris Cohen, edited by G.B. Olson and W.S. Owen, ASM International (1992), p. 227-242.

[Tillier 1998]. Y. Tillier. Identification par analyse inverse du comportement mecanique des poymeres solides; applications aux sollicitations multiaxiales et rapides, PhD thesis, Ecole Nationale Supérieure des Mines de Paris, Paris, (1998).

[Tobushi et al. 1996]. H. Tobushi, S Yamada., T. Hachisuka, A. Ikai and K. Tanaka. Thermomechanical properties due to martenistic and R-phase transformations of TiNi shape memory alloy subjected to cyclic loadings, Smart Materials and Structures, 5, (6), (1996), p. 788-795.

[Tong and Wayman, 1974]. H. Tong and C. Wayman. Characteristic temperatures and other properties of thermoelastic martensites. Acta Metallurgica 22 (1974), p. 887–896.

[Triconnet 2007]. K. Triconnet. Identification des propriétés mécaniques à partir de mesures de champs dans un matériau multi-phasé. PhD thesis, ENSAM de Paris (France), 2007.

[Tsoi 2002]. K. A. Tsoi. Thermomechanical and Transformational Behaviour and Applications of Shape Memory Alloys and their Composites. PhD thesis; School of Aerospace, Mechanical and Mechatronic Engineering; University of Sydney; September 2002.

[Tsoi et al. 2003]. K.A. Tsoi, R. Stalmans, J. Schrooten and Y.-W. Mai. Impact damage behaviour of shape memory alloy composites, Mat. Sci. Eng. A 342 1–2 (2003), p. 207-215.

[Tsoi et al. 2004]. Kelly A. Tsoi, Jan Schrooten, Yanjun Zheng and Rudy Stalmans. Part II. Thermomechanical characteristics of shape memory alloy composites, Materials Science and Engineering A368 (2004), p. 299–310.

[Tsoi et al. 2002]. K.A. Tsoi, R. Stalmans and J. Schrooten. Transformational behaviour of constrained shape memory alloys, Acta Mater. 50 (2002), p. 3535–3544.

[Turner 2001]. TL. Turner. Thermo-mechanical response of shape memory alloy hybrid composites. PhD thesis. National Aeronautics and Space Administration, Langley Research Center, Hampton, VA, USA, (2001).

[Vacher 2003]. P. Vacher. Apport des techniques de corrélation d'images en mécanique : analyses de déformations et numérisations 3D. Habilitation à diriger des recherches, Université de Savoie (France), (2003).

[Vacher et al. 1999]. P Vacher, S. Dumoulin, F. Morestin and S. Mguil-Touchal. Bidimensional strain measurement using digital images. Proc. Inst. Mech. Eng., Part C 213(1999), p. 811–817.

[Vokoun et al. 2003]. D. Vokoun, P. Sittner and R. Stalmans. Study of the effect of curing treatment in fabrication of SMA/polymer composites on deformational behavior of NiTi–5at.%Cu SMA wires, Scripta Mater. 48 (2003), p. 623-627.

[Wagne 2002]. B. Wagne, S. Roux and F. Hild. Spectral approach to displacement evaluation from image analysis. European Physical Journal Applied Physics 17(2002), p. 247-252.

[Wang et al. 2000]. C.-C.Wang, J. Lee, L.-W. Chen and H.-Y. Lai. A new method for circular grid analysis in the sheet metal forming test. Experimental Mechanics, 40 (2), (2000), p. 190-196.

[Wang et al. 2006a]. Z.X. Wang, I. Dutta and B.S. Majumdar. Thermal cycle response of a lead-free solder reinforced with adaptive shape memory alloy, Materials Science and Engineering A 421 (2006), p. 133–142.

[Wang et al. 2006b]. Z.X. Wang, I. Dutta, B.S. Majumdar. Thermomechanical response of a lead-free solder reinforced with a shape memory alloy, Scripta Materialia 54 (2006), p. 627–632.

[Wang et al. 2007]. Z. Y. Wang, H.Q., Li J.W. Tong and J.T. Ruan. Statistical analysis of the effect of intensity pattern noise on the displacement measurement precision of digital image correlation using self-correlated images. Experimental Mechanics, 47(2007), p. 701-707.

[Wattrisse 1999]. B. Wattrisse. Etude cinématique des phénomènes de localisation dans les aciers par intercorrelation d'images. PhD thesis, Université de Montpellier II (France), (1999).

[Wayman, 1983]. C. M. Wayman. Phase transformations, nondiffusive. In: Cahn, R. W., Haasen, P. (Eds.), Physical Metallurgy. North-Holland Physics Publishing, New York (1983).

[Wei et al. 1998]. Z.G.Wei, R. Sandstrom and S. Miyazaki. Review Shape-memory materials and hybrid composites for smart systems, Part II Shape-memory hybrid composites. Journal of Materials Science 33 (1998), p. 3763-3783.

[Winzek et al. 2003]. B. Winzek, T. Sterzl, H. Rumpf and E. Quandt. Composites of different shape memory alloys and polymers for complex actuator motions, J. Phys. IV 112 (2003), p. 1163–1168.

[Wollants et al. 1979]. P. Wollants, M. De Bonte and JR. Roos. A Thermodynamic Analysis of the Stress-Induced Martensitic Transformation in a Single Cyistal"; Z Metallkd (1979), p. 70- 113.

[Xu et al. 2004]. Y. Xu, K. Otsuka, H. Yoshida, H. Nagai and T. Kishi. novel technique for fabricating SMA/CFRP adaptive composites using ultrathin TiNi wires, Smart Mater Struct 13 (2004), p. 196.

[Yamada et al. 1993]. Y. Yamada, M. Taya and R. Watanabe. Strengthening of metal matrix composite by shape memory effect, Mater. Trans., JIM 34 (1993), p. 254-260.

[Yamashita and Shimamoto 2004]. K. Yamashita and A. Shimamoto. Effect of Temperature Caused for Mechanical Characteristics and Crack Closure Effect of Shape-Memory Alloy Fiber Reinforced Composite, Key Eng Mater (2004); 270–273, p. 2179-2186.

[Zheng and Cui 2004]. Y. Zheng and L. Cui. Martensite fraction-temperature diagram of TiNi wires embedded in an aluminum matrix, Intermetallics 12 (12) (2004), p. 1305-1309.

[Zheng et al. 2000]. Yanjun Zheng, Lishan Cui, Dan Zhu and Dazhi Yang. The constrained phase transformation of prestrained TiNi fibers embedded in metal matrix smart composite, Materials Letters 43 (3) (2000), p. 91-96.

[Zheng et al. 2002]. Y.J. Zheng, J. Schrooten, K. Tsoi and R. Stalman. Thermal response of glass fibre/epoxy composites with embedded TiNiCu alloy wires, Mater Sci Eng 335A (2002), p. 157.

[Zheng et al. 2003]. Y.J. Zheng, J. Schrooten, L.S. Cui and J. Van Humbeeck. Constrained thermoelastic martensitic transformation studied by modulated DSC, Acta Mater 51 (2003), p. 5467-5475.

[Zheng et al. 2003a]. Y.J. Zheng, J. Schrooten, K. Tsoi and P. Sittner. Qualitative and quantitative evaluation of the interface in activated shape memory alloy composites, Exp. Mech. 43 (2003), p. 194-200.

[Zheng et al. 2005b]. Y.J. Zheng, J. Schrooten and L.S. Cui. Thermomechanical properties of TiNiCu12 wire reinforced Kevlar/epoxy composites, Intermetallics 13 (3–4) (2005), p. 305–308.

[Zheng et al. 2005b]. Y.J. Zheng, L.S. Cui and Schrooten. Basic design guidelines for SQMA-Epoxy smart composites, Materials Science and Engineering A 390 (2005), p. 139-143.

Chapter 2.

Material elaboration and characterization methodologies

2.1. Objectives
2.2. Materials description
    2.2.1. SMA wire
    2.2.2. Epoxy matrix
2.3. Sample preparation
2.4. Pull-out test
2.5. Uniaxial tensile test
2.6. Heterogeneous test
References

2.1. Objectives

In this chapter, the experimental procedure for preparing and testing the shape memory NiTi/epoxy matrix composite is explained. A near equiatomic NiTi wire received in as drawn condition was subjected to three heat treatments in order to obtain different transformation temperatures. The matrix material consists of epoxy resin and an amine hardener. At room temperature this mixture is liquid and the curing process shall be done while the resin is still in the mould. Therefore, metallic moulds were designed and machined. The epoxy/amine mass ratio, released mould agent, curing and post curing conditions have been investigated to find the optimal conditions at which one could be able to fabricate the composite samples without cracks and good mechanical properties for the matrix at high test temperatures (about 100 °C). The experimental procedure obtained in this way was used to elaborate the different specimens required in this study.

Single wire composite specimens with a long embedded length were elaborated to study the effect of martensitic transformation/reorientation on the debonding initiation and propagation. These composite samples were subjected to pull-out test.

Mechanical behavior of the epoxy matrix and the effect of test temperature, wire volume fraction have been determined using the uniaxial tensile test. Thus, the specimens with three different wires and also with three wire volume fractions (0, 6, and 12%) were manufactured. The samples were subjected to the tensile load at room temperature (20), 80 and 90 °C.

In order to estimate the elastic properties of the composite material in two directions (perpendicular and parallel to the wire axis), the samples with complex geometry were fabricated, tested and analyzed. For preparing the tensile test specimens and the samples with complex geometry, another two metallic moulds were designed and machined. The specimens with complex geometry and with a random speckle pattern were subjected to the tensile load. Several pictures were taken during the test with a constant step time. The pictures were then analyzed using the software on the basis of digital image correlation (DIC) and the heterogeneous displacement/strain fields were determined. Since, in this type of samples, the stress tensor is unknown, an identification method was developed in order to find the material parameters.

2.2. Material descriptions

The composite material studied in this work is a near equiatomic NiTi shape memory wire epoxy matrix composite. In what follows, the constituents are described and their mechanical and physical characterizations are presented.

2.2.1. SMA wire

Near equiatomic NiTi wire of 1 mm diameter was supplied by the Nimesis Technology Company. NiTi SMA wire was received in as drawn condition. It is known that in this condition the dislocation density is too high which could prevent the wire to present a good shape memory effect.

The thermoelastic transformation [Christian 1965] is characterized by the mobile boundary between parent and martensite, and a small temperature hysteresis, which indicates a small driving force for the forward/reverse transformation, and a negligible possibility of introducing irreversible process such as slip [Otsuka and Ren 2005]. Since mobile boundary upon changing temperature/stress is necessary for superelasticity and the shape memory effect, thermoelastic nature is a required condition for the shape memory effect/superelasticity [Otsuka and Ren 2005]. The mobile boundary can be affected when the dislocation density is too high. Therefore, the wire must be heat treated to reduce the dislocation density required for shape memory effect.

To study the effect of phase transformation different transformation characteristics are required. Thus, heat treatments at various temperatures (350, 400, 450, 500, 550 and 600 °C) have been done. All these treatments were followed by water-quenched. Transformation temperatures were identified, using the DSC technique. Wires were also subjected to tensile load to determine the stress at which the transformation occurs (table 2.1). Three heat treatments have been selected: 400 °C for 60 min, 450 °C for 60 min and 550 °C for 30 min. Samples are labeled respectively, M-400, M-450 and M-550. Table 2.1 justified the choice of these treatments. As seen in the table, a wire treated at 350 °C is not a good choice to be embedded into epoxy matrix because the transformation stress is too high. In fact, the rupture of epoxy matrix will occur before wire phase transformation.

Table 2.1. Some characteristics of NiTi wires subjected to different heat treatments

Alloy	Heat treatment	Plateau stress (MPa) at room temperature	Superelasticity	Shape memory effect
M- 600	600 (°C) for 30 min	100*	No	Yes
M- 550	550 (°C) for 30 min	100*	No	Yes
M- 500	500 (°C) for 60 min	120**	Yes	Yes
M- 450	450 (°C) for 60 min	140**	Yes	Yes
M- 400	400 (°C) for 60 min	250**	Yes	Yes
M- 350	350 (°C) for 60 min	400**	-	Yes

* Martensitic reorientation; ** Martensitic transformation.

Studied NiTi wires show the Austenite (B2) →R-phase→ Martensite (B19') transformation sequence on cooling and the B19'→B2 on heating. Fig. 2.1 shows the DSC results and table

2.2 details the transformation temperatures obtained after performing these heat treatments. As seen in this table, with decreasing the heat treatment temperature, the martensite start and finish (M_s, M_f) and the austenite start and finish (A_s, A_f) temperatures decrease and R_s and R_f (R-phase start and finish temperature) increase.

Table 2.2. Transformation temperatures (°C) of NiTi alloys after selected heat treatments

Alloy	Heat treatment	M_f (1)	M_s (1)	R_f (1)	R_s (1)	A_s (1)	A_f (1)
M- 550	550 (°C) for 30 min	18	34	34	41	54	77
M- 450	450 (°C) for 60 min	-21	2	41	52	49	65
M- 400	400 (°C) for 60 min	-70	-8	45	60	47	64

(1)- M_s, M_f, R_s, R_f, A_s and A_f are the Martensite, R-phase and Austenite start and finish temperatures respectively

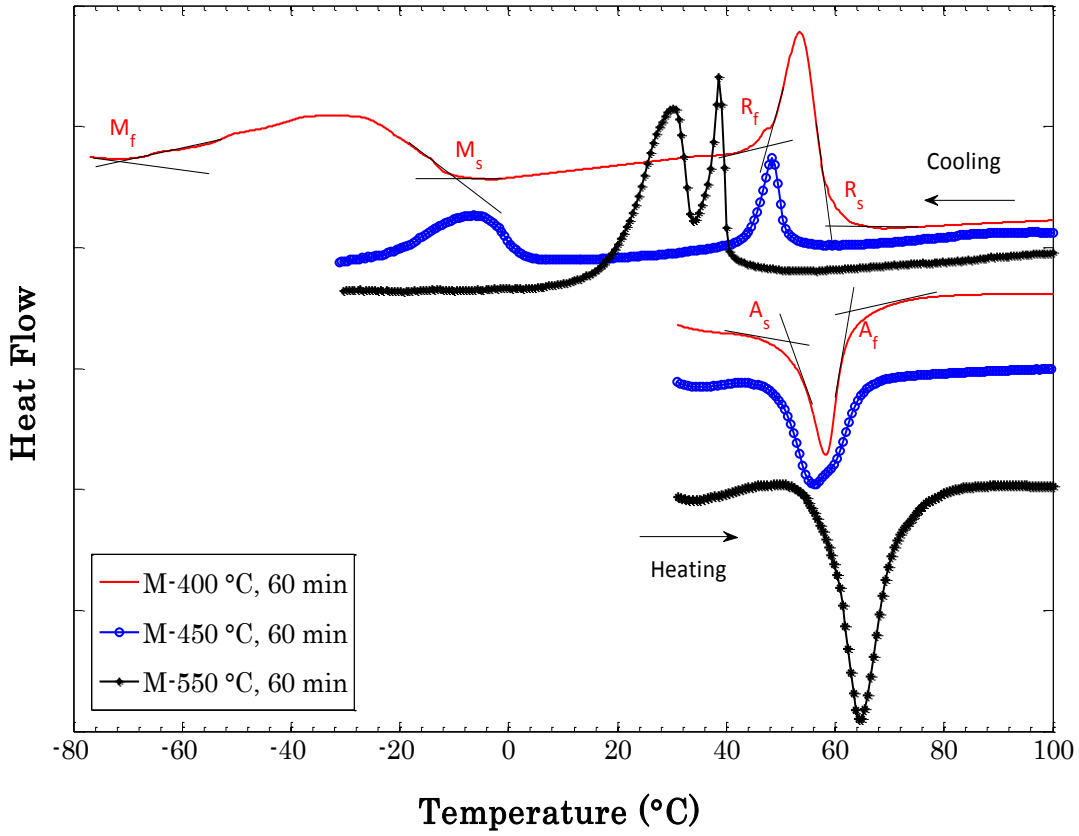

Fig. 2.1. DSC for M-550 and M450 with 5 K/min in Ar and M-400 wires with 10 K/min in He atmosphere

The wires were subjected to tensile test at room temperature using the test machine Zwick 1476 (load cell: 10kN) with an extensometer MultiXtens. The initial length (L_0) was fixed to 50 mm. At high temperature (80 and 90 °C) the tests were conducted in a thermal chamber with the use of test machine Zwick 1484 (load cell: 40kN) and an extensometer clip-on (L_0=20 mm, ΔL_{Max} = 10 mm). The crosshead speed was fixed to 0.5 mm/min in both cases.

The mechanical behaviors obtained at room temperature for M-550, M-450 and M-400 wires are shown in Fig. 2.2. According to table 2.2, at room temperature, the M-550 wires are martensitic and M-400 and M-450 wires are in the R-phase. Thus, by applying an external tensile stress, the martensitic reorientation occurs in M-550 whilst in M-450 and M-400, the reorientation of the R-phase occurs firstly (first plateau) and the martensitic transformation takes place later (second plateau, Fig. 2.2).

At room temperature, the stress at which the martensite reorients in the M-550 wires is about 100 MPa (F≈80 N). In M-450 wires the martensitic transformation occurs around 140 MPa (F≈110 N) and the M-400 wires transform under a stress about 250 MPa (F≈200 N) at the same temperature. In this work, these stresses/loads will be denoted by transformation stresses/loads.

To study the wires mechanical behavior at temperatures higher than A_f, the wires were subjected to tensile test at 80 and 90°C. In the present report, these temperatures are named as "high temperature". These temperatures were chosen to study the wires in austenitic state and to verify whether they present a superelastic effect. The mechanical behaviors of these wires at 80 and 90 °C are given in Fig. 2.3 and 2.4 respectively. As expected, the transformation stress increases with the test temperature. According to these figures, the M-450 and M-400 show a superelastic behavior at high temperature whilst there is no superelastic behavior for M-550 fiber (Fig. 2.3 and 2.4). It means that, after a treatment at 550 °C the recrystallization takes place in this wire which yields the dislocation density to become less than a certain value require for this effect. In fact, good shape memory effect and superelasticity are realized only after the alloy is subjected to proper thermo-mechanical treatment, because slip is easily introduced in solution-treated condition [Otsuka and Ren 2005]. The low critical stress for dislocation slip is assumed to be responsible for the limitation of superelastic recovery in solution-treated conditions [Sun et al. 2010]. Thus, when a sample is subjected to tensile test at a temperature above A_f slip can occur before that the stress-induced transformation begins, and thus the superelasticity does not appear.

It is known that stable superelasticity is often affected by a low critical stress for plastic deformation. Several strategies involving precipitation hardening or strain hardening have been developed to increase the dislocation slip threshold [Sun et al. 2010]. It is also reported that fine-grained microstructures could play critical roles in the improvement of superelastic properties, due to the large increase in the critical stress for the dislocation slip mechanism [Kim et al. 2006, Kim et al. 2006 Acta]. As a result, increasing in grain size due to the treatment at high temperature (550 °C) and possible recrystalization could be responsible for the limitation of superelastic effect.

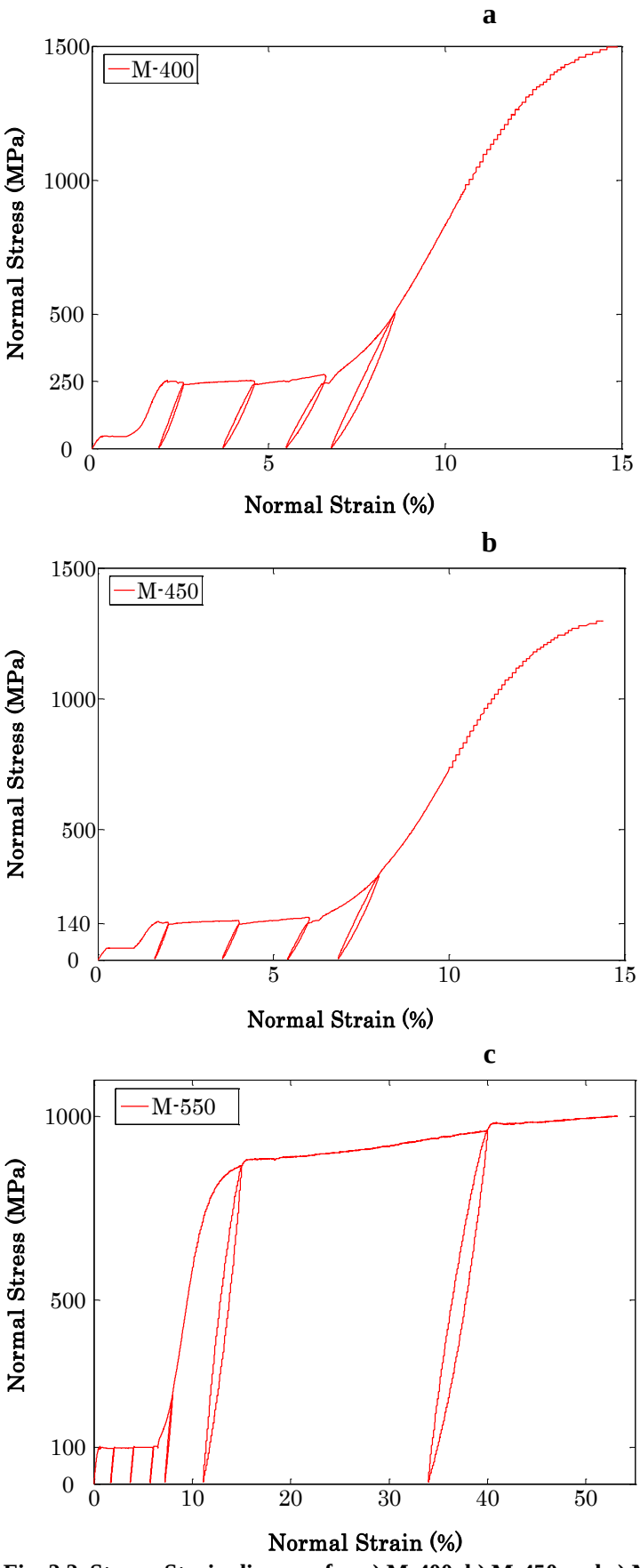

Fig. 2.2. Stress -Strain diagram for a) M-400, b) M-450 and c) M-550 wires at room temperature

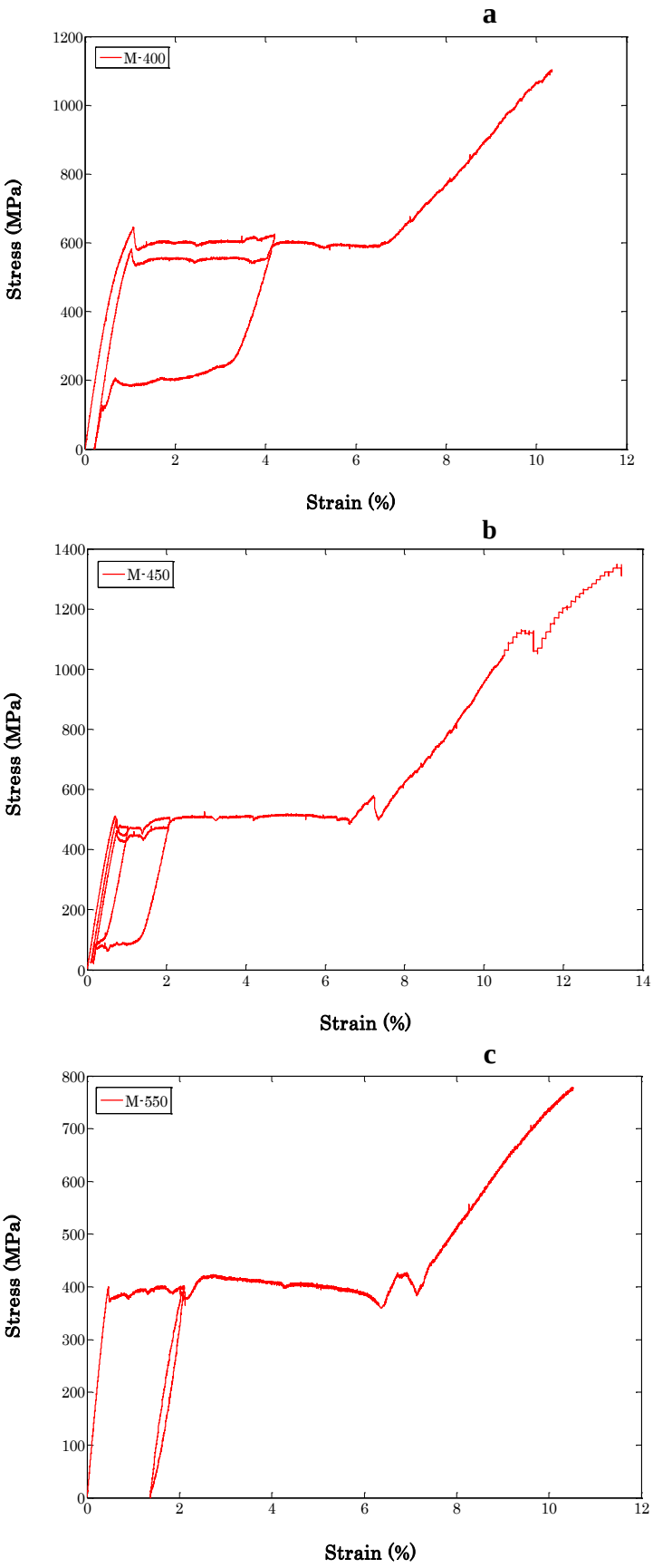

Fig. 2.3. Stress -Strain diagram for a) M-400, b) M-450 and c) M-550 wires at 80 °C

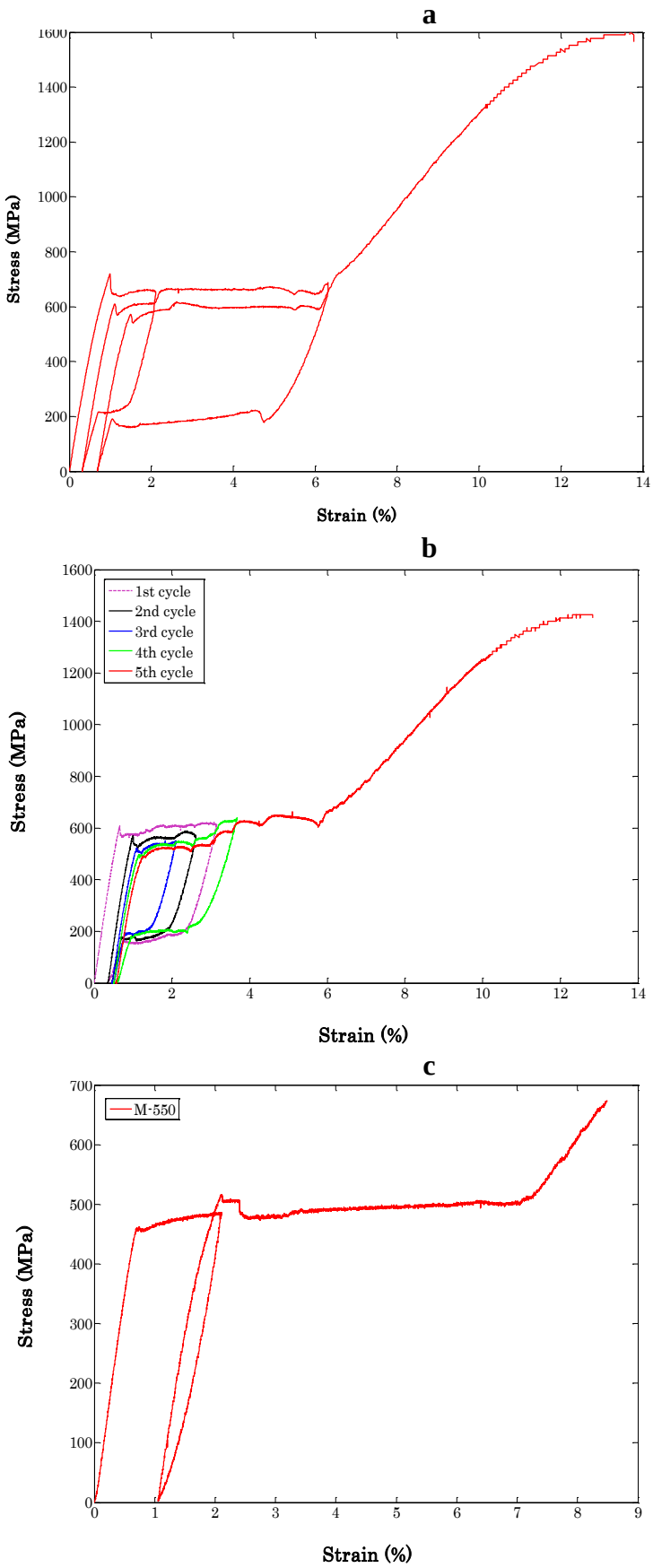

Fig. 2.4.Stress --Strain diagram for a) M-400, b) M-450 and c) M-550 wires at 90 °C

Fig. 2.3 and 2.4 illustrate that, the transformation stresses increase when the test temperature increases. The variations of the M_s under stress for all three wires are shown in Fig. 2.5 and detailed in table 2.3.

Table 2.3- The stress at which the transformation begins in the wires

wire	σ =0	T=20 °C	T=80 °C	T=90 °C	Relationship
	M_s (°C)	σ (MPa)			
M-550	34	100*	370	460	σ= 8.2 (T- M_s)
M-450	2	140	500	580	σ= 6.6 (T- M_s)
M-400	-8	250	600	670	σ= 6.7 (T- M_s)

* Martensitic reorientation occurs in M-550

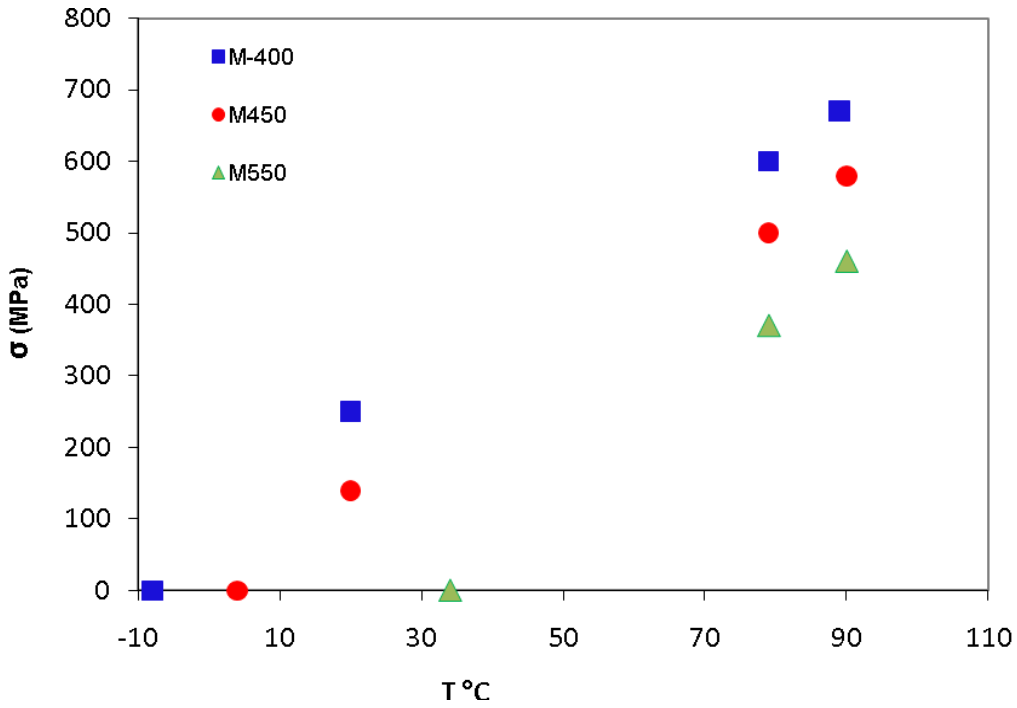

Fig. 2.5. Variation of M_s under stress for all three wires

It is well known that the transformation stress (σ) depends critically to the test temperature (T) [Miyazaki et al. 1981]. The relationship can be expressed by the following equation:

$$\sigma - \sigma_o = B\Delta T = B(T - T_o) \qquad (2.1)$$

where σ_o is the transformation stress at T_o, B is a constant and is about 7 MPa/°C for NiTi alloys. With comparing the stress-strain curves shown in Fig. 2.2, one understands that at the same temperature, the transformation stress increases when the M_s decreases. It is logic because the T must be increased or T_o must be decreased to have the same difference (ΔT). In other word, the ΔT increases when the test temperature increases or M_s decreases.

2.2.2. Epoxy matrix

The polymer matrix is an epoxy/amine mixture. The epoxy is D.E.R. 332 supplied by Sigma-Aldrich Chemie GmbH and amine is Lonzacure Detda 80 supplied by Lonza Ltd.

Liquid epoxy prepolymers are converted to thermoset materials by addition of a suitable hardener [Rodriguez et al. 2005]. Various hardeners are in use both at high temperature or room temperature. Major properties depend on the type of epoxy and the reinforcement [Ram 1997]. The most widely used epoxy resin is based on bis-phenol A and epichlorohydrin [Rodriguez et al. 2005, Ram 1997].

Amine-cured epoxies are used extensively in exterior coatings and polymer-fiber composites [Rezig 2006]. Epoxy resins have been widely used in many industrial applications because of their good heat and chemical resistance, superior mechanical and electrical properties and excellent process capabilities [Atta et al. 2005]. They are being used in fiber-reinforced polymer (FRP) composites for various applications, e.g. automobiles, ships, sport, aerospace, and windmill blades [Kanchanomai et al. 2005]. It is known that the tensile stress and yield stress of polymers are time dependent and the fracture properties of epoxy resin are also expected to be time dependent [Kanchanomai et al. 2005].

Kanchanomai (2005) and co-workers studied the influences of loading rate on fracture behavior and mechanism of thermoset epoxy resin with polyamine hardener. They found that under low loading rates ductile fracture occurs, while brittle fracture takes place in specimens tested under loading rate of 10 mm/min or higher [Kanchanomai et al. 2005].

Fracture toughness of an epoxy matrix composite has been investigated by Araki and co-workers [Araki et al. 2003], using Raman spectroscopic and the fractographical analysis. According to their study, a composite with a high T_g and a low fragility parameter, has a high fracture toughness [Araki et al. 2003].

The mechanical properties of the mixture depend critically to the resin/hardener ratio and to the curing conditions. As a general rule, use of a 1:1 stoichiometric ratio of amine to epoxy

will, when fully reacted, ensure maximum stability of the product [PCI, Burton 2001, Wisanrakkit 1990]. For some formulations, being either off-stoichiometry or not achieving full reaction, some properties change [Burton 2001, Burton 2001a]. Being off-stoichiometry and/or under-cured, can lead to higher modulus, greater hardness, more brittleness [Burton 2001] and a lower glass transition temperature [Carrega 1999]. Resistance to solvents or moisture may also be decreased [Burton 1993]. Therefore, depending on the application, a compromise should be made.

Formulating near a 1:1 stoichiometry of amine to epoxy, and sufficient curing, also helps ensure that the maximum obtainable T_g is achieved, while producing the maximum number of bonds, thus contributing to the strength. Although formulating away from a 1:1 stoichiometry will depress the T_g, provide more flexibility and, leave un-reacted groups in the system that can destabilize it over time. As an example, un-reacted epoxy groups can hydrolyze over time, leading to increased moisture sorption and related thermo-mechanical changes [Burton 2001, Burton 1993].

According to above discussion, the amine to epoxy ratio (r) in this work fixed to be 1 which means a 1:1 stoichiometric ratio.

$$r = \frac{\frac{m_A}{M_A}\frac{f_A}{f_E}}{\frac{m_E}{M_E}} = \frac{M_E}{M_A}\frac{f_A}{f_E}\frac{m_A}{m_E} \tag{2.2}$$

The molecular mass (M) and the number of function (f) for these components are given respectively as: M_E=356.12 g.mol^{-1}, f_E=2 (for Epoxy) and M_A=178.13 g.mol^{-1}, f_A=4 (for Amine), thus

$$\frac{m_E}{m_A} = 4r \tag{2.3}$$

where m_E and m_A are the mass of each constituents. A 1:1 stoichiometric ratio (r=1) corresponds to the mass ratio (m_E/m_A) equal to 4.

The epoxy resin was heated to a temperature about 50 °C and the hardener was added. The mixture was then agitated uniformly about 3 minutes with 500-700 rpm (depending on the volume of the mixture) while heating. To ensure good mechanical properties of the cured composite samples, a low viscosity is more suitable for wetting wire and filling the mould. In

such a case, the higher initial mix temperatures is required which results the lost of working time due to the faster reaction. Moreover, the amine-epoxy reaction is exothermic and during mixing large masses of materials considerable heat will release [PCI], and the reaction will proceed faster as the temperature increases. As a result molding must be done in a short time.

In this work, the temperature of epoxy-amine mixture was measured regularly. Just before casting, the temperature was about 70 °C. The fluidity of the mixture increases with increasing the temperature. At this temperature the liquid is fluid enough to fill the mould. The epoxy-amine mixture was cast into the mould and the curing process is done while the resin was still in the mould. Before starting the preparation of mixture, a released mould agent was applied on the internal surface of both pieces of the mould in order to release the cured samples easily. Once the surfaces became dry (after some hours) the mould was preheated to a temperature about 70 °C which leads the liquid to maintain its fluidity during casting. A curing process at 140 °C followed by a post curing one and cooling to room temperature.

The epoxy/amine mass ratio, released mould agent, post curing and cooling conditions were investigated in order to prepare the specimens without crack and with good mechanical properties together with high T_g. Three released mould agents were used namely, Lubrasec, Pulvegraph D 31A and QZ-13. The masse ratios of 4, 4.5 and 5 were tested. The samples were post cured at two temperatures (150 and 165 °C) for 4 or 5 hours. The glass transition temperature of the matrix determined using Differential Scanning Calorimeter (DSC). The results are shown in Fig. 2.6 and are detailed in table 2.4.

Table 2.4. The preparation and curing conditions and obtained glass transition temperatures (T_g ° C)

sample	Post curing temperature (°C)	Post curing time (h)	E/A ratio	T_g (°C)*
TR1	165	4	5	110
TR2	165	4	4	165
TR3	165	5	4	170
TR4	150	5	4	145
TR5	150	5	4.5	130

*Heating rate: 10 °C/min

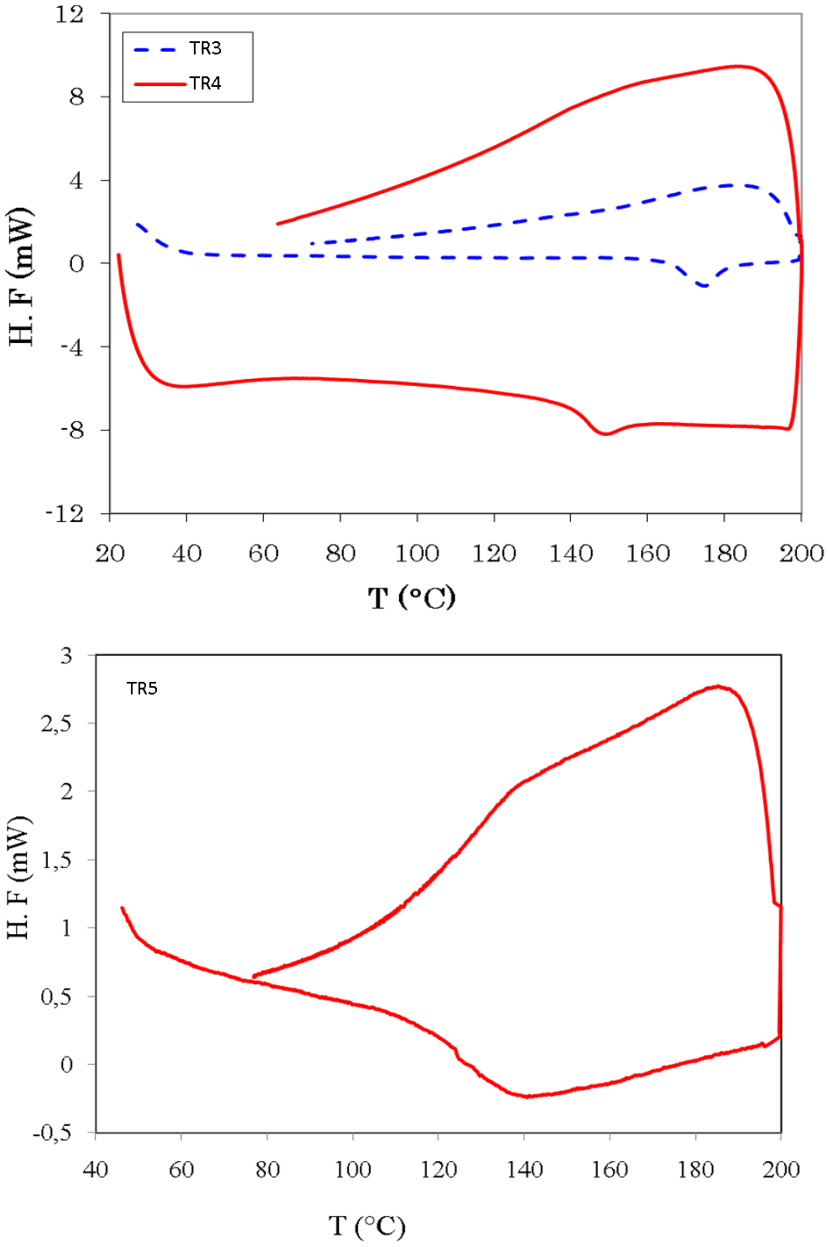

Fig.2.6. DSC results for TR3, TR4 and TR5, 10 K/min in air atmosphere

The samples were subjected to tensile test at 20 (RT), 80 and 90 °C to study the mechanical behavior of the matrix. For the tests performed at room temperature, the test machine Zwick 1476 (with 10kN load cell) with the extensometer MultiXtens was used. The initial length (L_0) of extensometer was fixed to 32 mm. At high temperature (80 and 90 °C) the tests were carried out with the use of a thermal chamber (Servathin: -70°C to 180°C). In this case, the test machine Zwick 1484 (with 40kN load cell) and an extensometer clip-on (L_0=20 mm, ΔL_{Max} = 10 mm) are utilized. The tests were conducted in air with a constant displacement rate of 0.5 mm/min.

The mechanical behavior of the resin matrix at room temperature is given in Fig. 2.7. This figure illustrates that the sample leaves no residual strain after unloading even with the non linear stress-strain behavior (after 2% imposed strain). The Fig. 2.8 shows the behavior of the epoxy resin at different temperatures. As seen, the slope of the stress-strain curve decreases with increasing the test temperature. The slope of the linear part of these curves is about 3300, 2800 and 2700 MPa at 20, 80 and 90 °C, respectively. It means by approaching to the T_g (about 150 °C) the material loses its rigidity. Fig. 2.9 illustrates that increasing the post curing temperature increases the Young modulus of the epoxy resin.

The results show that, selecting TR4 as a preparation conditions, QZ-13 as a released mould and cooling by turning off the furnace gives the best results. Composite specimens used in this study have been prepared under these conditions.

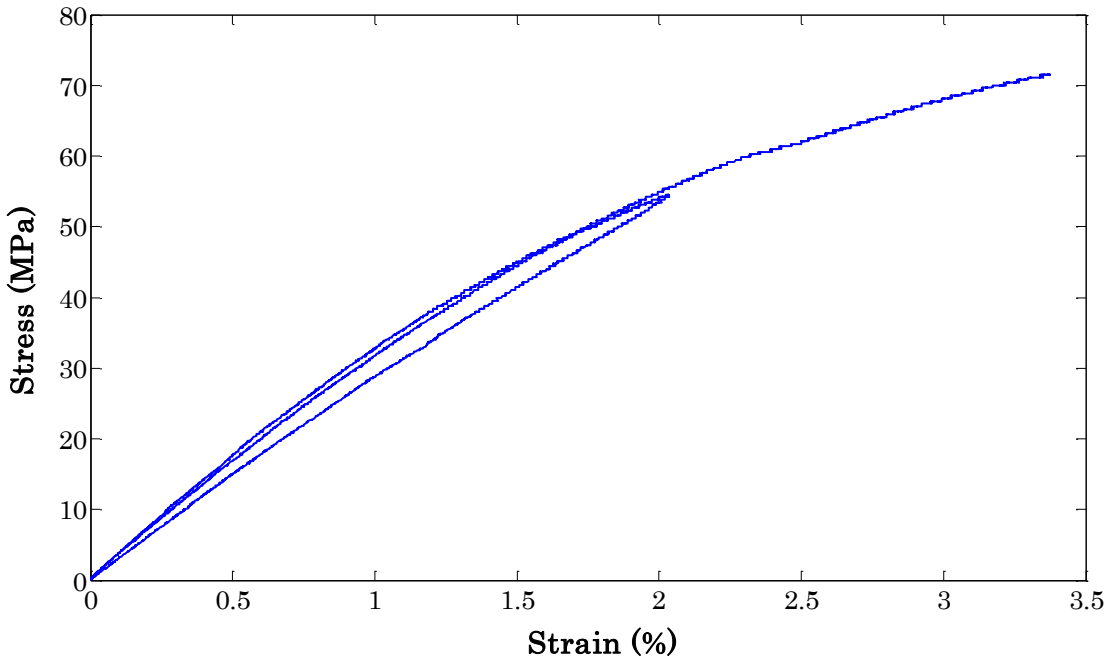

Fig. 2.7. Mechanical behavior of epoxy matrix at room temperature.

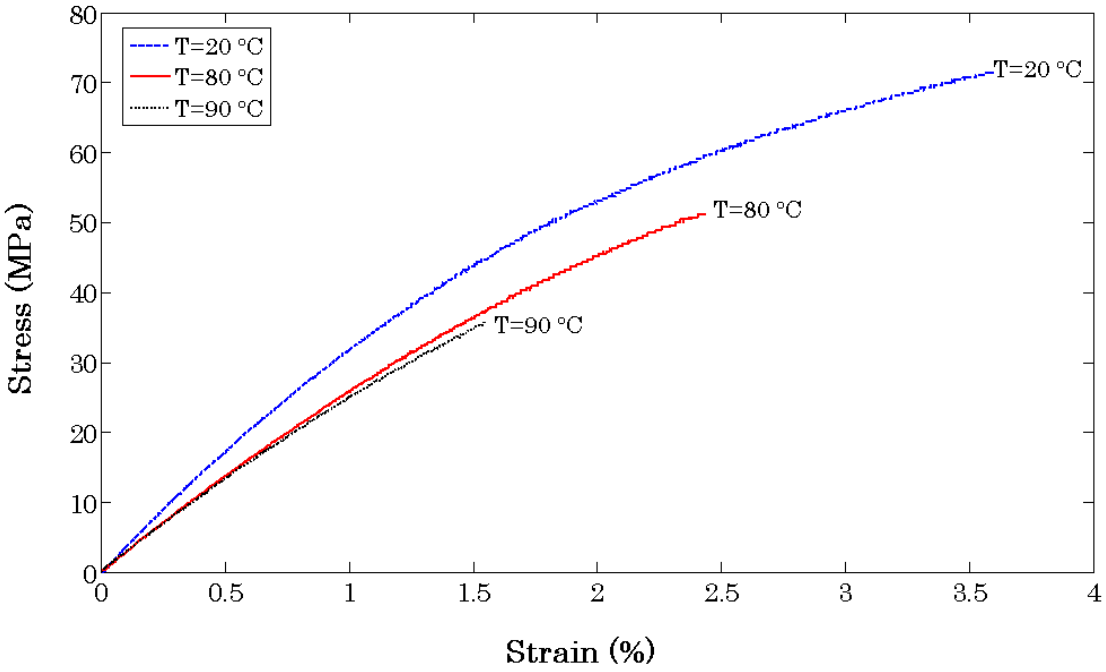

Fig. 2.8. Mechanical behavior of the epoxy matrix at different temperatures (TR4).

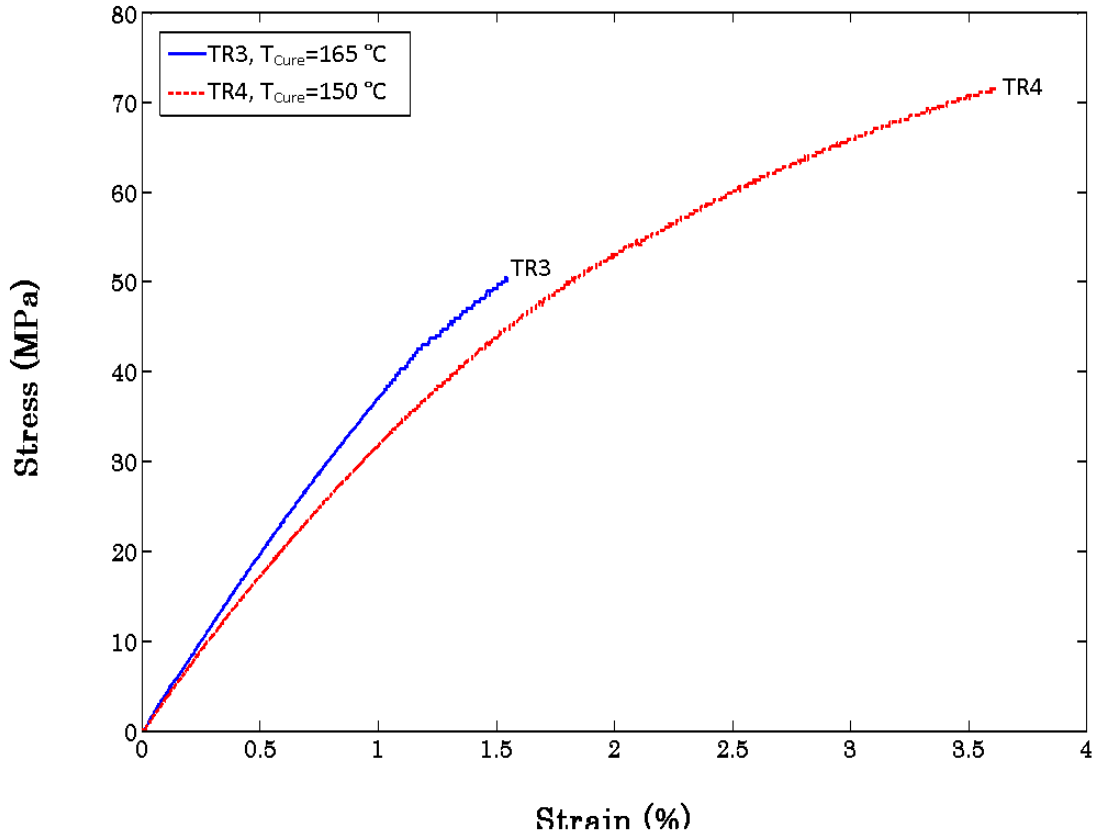

Fig. 2.9. Mechanical behavior of the epoxy matrix for two post curing temperatures (TR3 and TR4).

2.3. Preparation of composite sample

In this work, three types of samples were prepared namely pull-out samples, simple tensile test specimens and samples with complex geometry. These types of specimen were fabricated using two metallic moulds. The moulds were machined in two pieces and in each piece there were the grooves with 1 mm in diameter for positioning the wires.

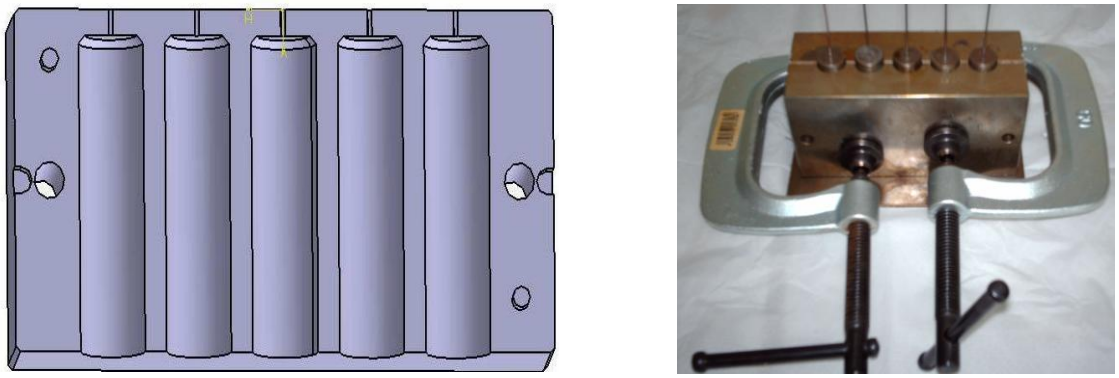

Fig.2.10. The mould for pull-out specimens

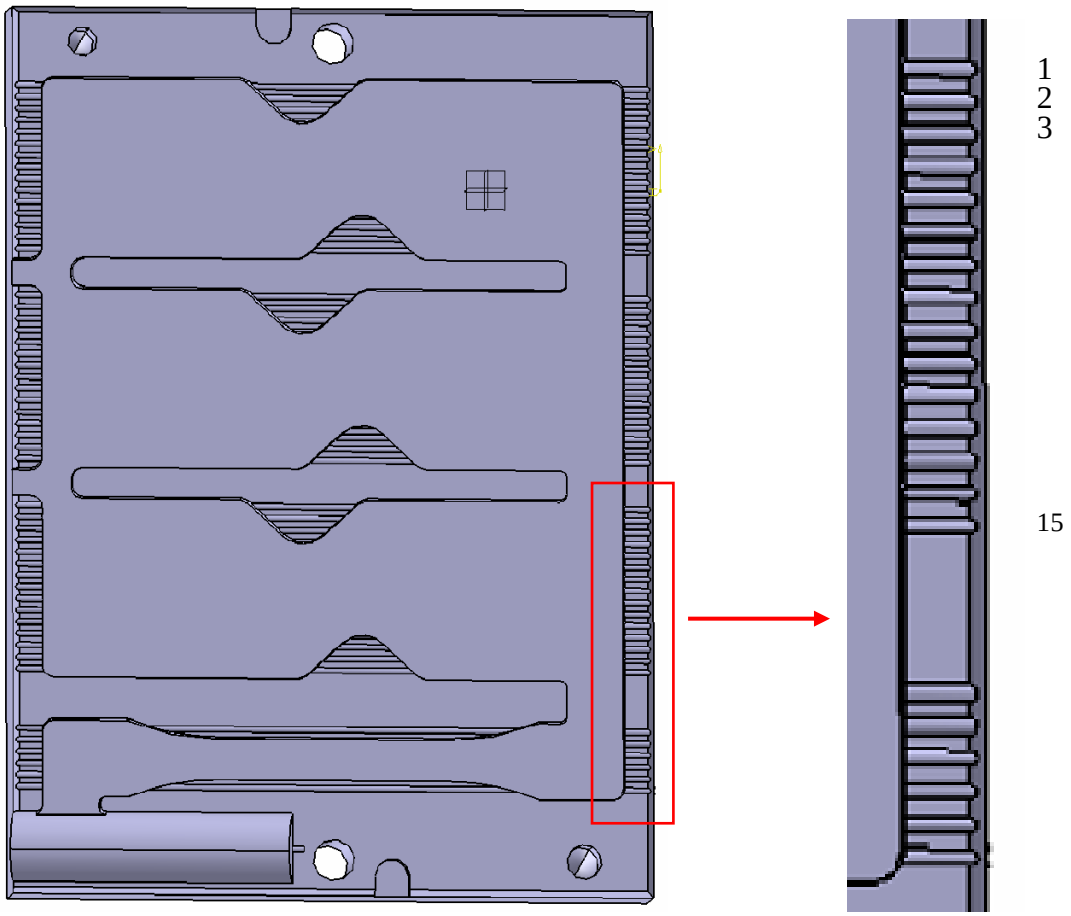

Fig. 2.11. The mould using to prepare the simple tensile samples and the specimens with complex geometry

The mould which was machined to prepare the pull out specimens is shown in Fig. 2.10. The other mould (Fig. 2.11) was designed for the simple tensile samples and also the specimens with complex geometry. In the later, the center to center distance between two next grooves are 2 mm. Depending on the defined wire volume fraction, the wires were positioned in the appropriate positions. For example, in the case of sample with complex geometry there were 15 grooves; the wires were located in the grooves with even number for the 5% wire volume fraction samples. In the case of samples with 3% volume fraction, the wires were positioned in the grooves with the following number: 2, 6, 10 and 14. By positioning the wire in all places, samples with 10% volume fraction were prepared.

It is well known that the coefficient of thermal expansion of the resin, wires and mould are different, so if the matrix is too brittle cracks can appear (Fig. 2.12) due to the residual thermal stress (Fig. 2.13). As the glass transition temperature (T_g) of the cured resin increases, the toughness and the ultimate strain of the polymer declines [Wisanrakkit 1990, Darragas et al. 1998]. Therefore, the formulations and curing conditions should be chosen in such a way to provide glass transition temperatures slightly higher than the expected service temperature. This is done in order to maintain rigidity together with toughness. Choosing a much higher T_g than necessary for this purpose tends to decrease the toughness [PCI] and the material could be susceptible to cracks.

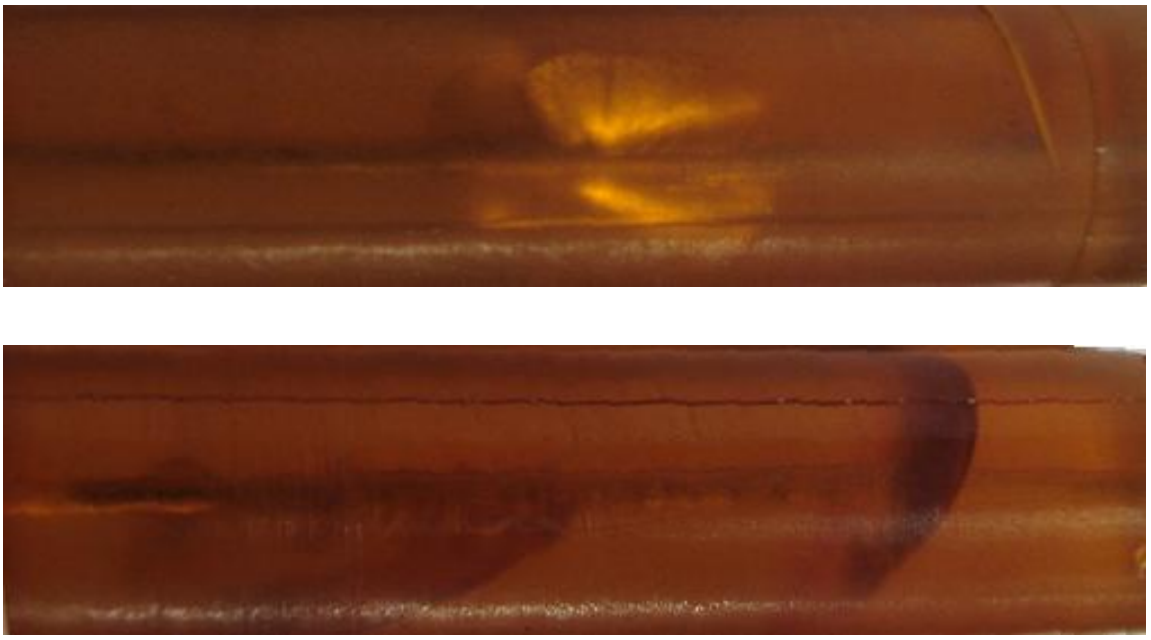

Fig. 2.12. Macroscopic cracks existing in the samples fabricated with a brittle matrix

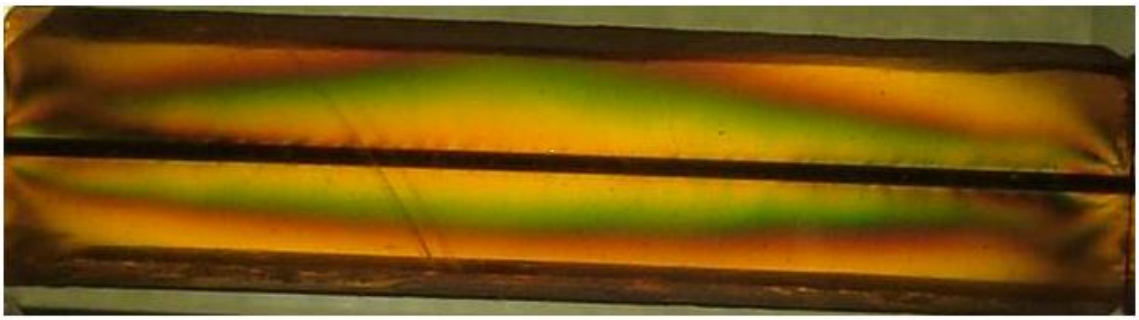

Fig.2.13. Residual thermal stress for a M-550 NiTi wire epoxy matrix composite using photoelasticity

The goal is to prepare the samples with maximum ductility and high T_g. A certain amount of ductility is required in the matrix to obtain composite specimens without cracks and to allow taking place the wire phase transformation when a composite sample is subjected to the tensile load. In the case of brittle matrix, the rupture occurs at low strain levels and the phase transformation will not occur in the embedded wires. Moreover, to test the composite samples at a temperature higher than A_f, the matrix should have the good mechanical properties. Therefore, the maximum mechanical properties for the matrix at room temperature and high test temperatures (about 100 °C) are needed which results to choose a high T_g. Decreasing the post curing temperature or time increases the matrix ductility but the glass transition temperature decreases. Thus, a balance should be obtained.

As mentioned in section 2.2.2, the best results is obtained by choosing a masse ratio of 4, post curing at 150 °C for 5 hours, and using QZ-13 as a released mould (TR4 in table 2.4). Therefore, the epoxy-amine with masse ratio of 4 was prepared using the procedure explained in section 2.2.2. The QZ-13 released mould agent was applied and after about two hours the wires were located in the mould.

Since, fiber misalignment is an important microstructural defect in multi-wire composite, the mould (with wires) was preheated to about 90 °C and then was tightened. The tightening at a temperature higher than A_f avoid the wires to be distorted because the wires elongate freely. Moreover, preheating the mould has also a positive influence on the casting process by increasing the fluidity of the epoxy-amine mixture.

The composite samples were cured at 140 °C for one hour, post cured at 150 °C for five hours and cooled to room temperature by turning off the furnace.

2.4. Pull-out test

Failure in composite materials usually occurs by debonding between matrix and fiber. Investigation of the interfacial properties is then important for composite characterization. The pull-out test has been well accepted as one of the most important test methods investigating the wire/matrix interfacial properties [Fu et al. 2000, Gao and Zhou 1999, Yue et

al. 1995, Bannister et al. 1995]. In these tests, the embedded length is usually small and the interfacial shear strength can be estimated by dividing the maximum force to the lateral surface assuming that the shear stress is uniformly distributed along the embedded length. In order to study the effect of martensitic transformation on the debonding initiation and propagation, a long embedded length is required. In this case, the common formula can not be used to calculate the interfacial shear strength. Therefore, another method should be employed for this purpose.

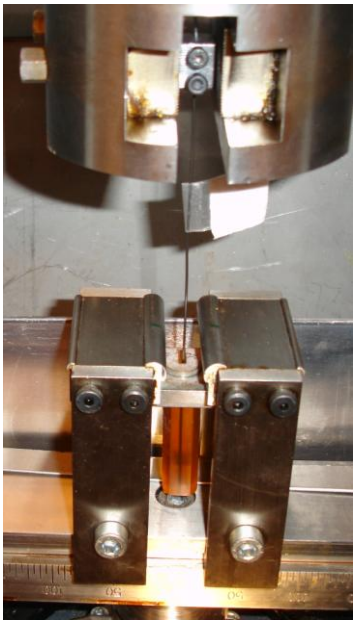

Fig.2.14. Experimental set-up

Single wire specimens with a long embedded length were subjected to pull-out test. The composite specimen was a cylinder with diameter and length of 15 and 50 mm, respectively. The embedded wire length, L, was 50 mm which corresponded to a wire aspect ratio of L/2a ≈ 50. The nominal wire volume fraction was about 0. 44 %. It is worth noting that the diameter ratio (matrix to wire) equals to 15 which is large enough to minimize the scale effect in the tested specimen.

To observe the wire/matrix interface the samples were polished slightly to achieve a surface parallel to the wire axis. The composite specimen was put under a metallic holder (Fig. 2.14), which had a 3 mm diameter hole at the centre; this diameter is 3 times larger than the wire diameter. The centre of the wire was placed at the centre of the hole in order to allow the wire to be pulled out freely from the specimen. The pull-out test was conducted in air at room temperature (20 °C) by fixing the holder and applying a tensile load to the free end of the wire. The tests were performed using MTS/1M test machine (5 kN load cell) at a constant displacement rate of 0.5 and sometimes 0.1 mm/min for comparison. The experimental set-up was shown in Fig. 2.15 schematically.

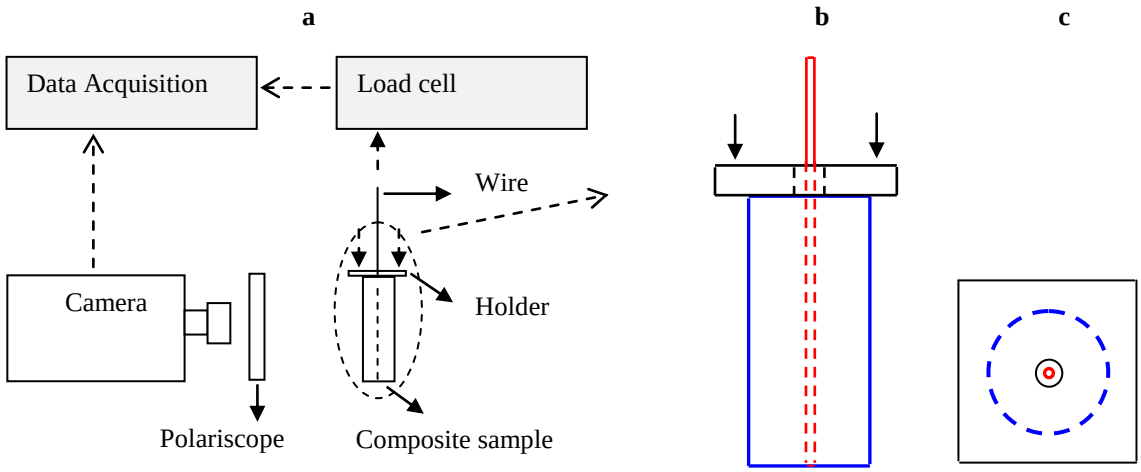

Fig.2.15 (a) Experimental set-up (b) side section (c) up view

The in-situ observations of the interface debonding and sliding behavior during the pull-out test were carried out using a digital camera which has been located in the back of a polariscope. Several pictures have been taken during the experiment. The time, load, displacement, debonding onset and also the position of debonding are known for each picture. The debonding rate was calculated for different samples. This process has been repeated two times for all three NiTi wires and two displacement rate.

For comparison, several samples were fabricated using a steel wire with a diameter of 1 mm. In these cases, at least three tests were carried out to obtain two comparable curves.

It should be noted that, before fabricating the pull-out samples, the oxide layer was removed from the wire surface by abrading the original surface with 600-grit papers. The wire was then cleaned and dried at room temperature. In order to verify the effect of oxide layer, some specimens were prepared without removing the oxide layer. As a result, a significant difference has not been observed.

2.5. Uniaxial tensile test

The mechanical behavior of the composite samples with three different NiTi wires at three test temperatures, and for three wire volume fractions have been determined using the uniaxial tensile test.

The tests were performed in air with an imposed constant displacement rate. Three temperatures were investigated: 20, 80 and 90 °C. The test details (equipments, initial length) mentioned in section 2.2.2. The dimensions of the specimen are shown in Fig. 2.16. The wire volume fractions studied in this work are 0, 6 and 12%.

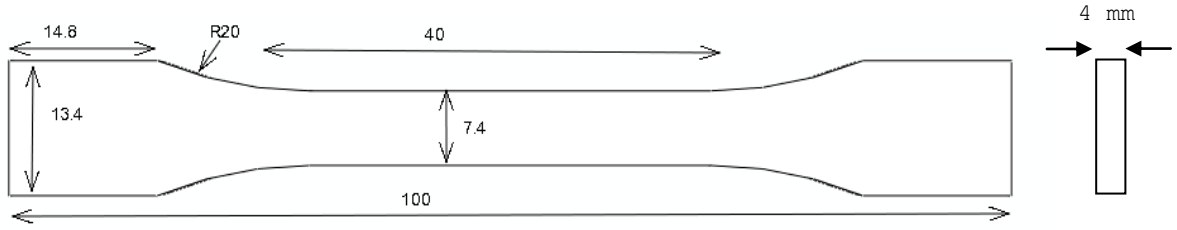

Fig. 2.16. The simple tensile test specimen

2.6. Heterogeneous test

By performing uniaxial tensile test, one may obtain the material properties in the load direction. For example in the case of elasticity, the Young modulus will be obtained from a tensile test. This is useful for isotropic material. However, for the orthotropic materials such as composites, several tests must be carried out to determine the material properties in longitudinal and transverse directions for example. To estimate the elastic properties of the composite material in these two directions, samples with complex geometry were required in order to induce a heterogeneous strain field inside the sample. The aim is to determine the material constants simultaneously from a single tensile test. For this meaning, some specimen's geometries were numerically analyzed, namely L, T, Y-type and Meuwissen [Meuwissen 1998] geometry. According to the numerical results (Fig. 2.17), Meuwissen sample seems to be suitable to induce heterogeneous strain field in unidirectional wire composite. In this work, a finite element analysis was performed to optimize the Meuwissen sample geometry.

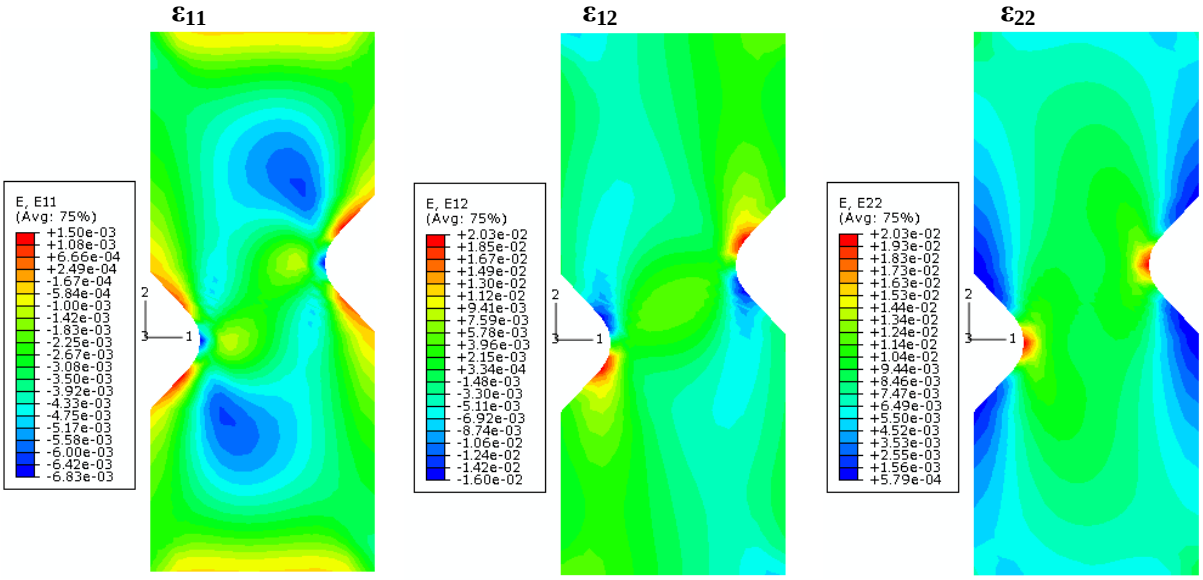

Fig. 2.17. Heterogeneous strain fields generated in Meuwissen-type sample, applied displacement: 0.6 mm

Using this type of geometry allows estimating simultaneously the elastic properties of the composite material in two directions (perpendicular and parallel to the wire axis). Applying a tensile load will generate the heterogeneous displacement/strain fields in samples. These fields could be determined by a digital image correlation (DIC) method. In this work, two software were used for this purpose: the Correli Q4 software developed by François Hild [Hild et al. 2008] and VIC2D [Doumalin 2000] software.

A schematic representation of the heterogeneous test specimen is shown in Fig. 2.18. Several samples with wire volume fraction of 0, 3, 5 and 10% were fabricated using the procedure explained in section 2.3.

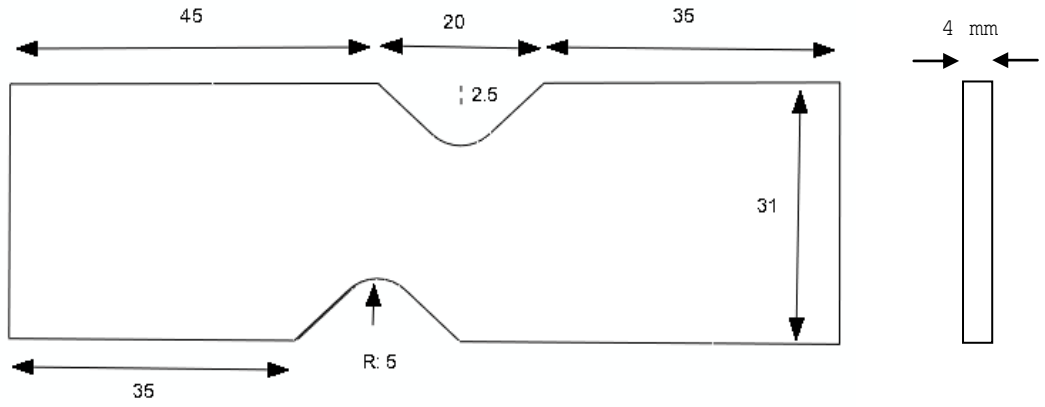

Fig. 2.18. The Heterogeneous test specimen

The tests were performed in air with crosshead speed of 0.5 mm/min at 20, 80 and 90 °C. The test equipments, initial length of extensometers were mentioned in section 2.2.2. Fig. 2.19 shows the experimental set-up.

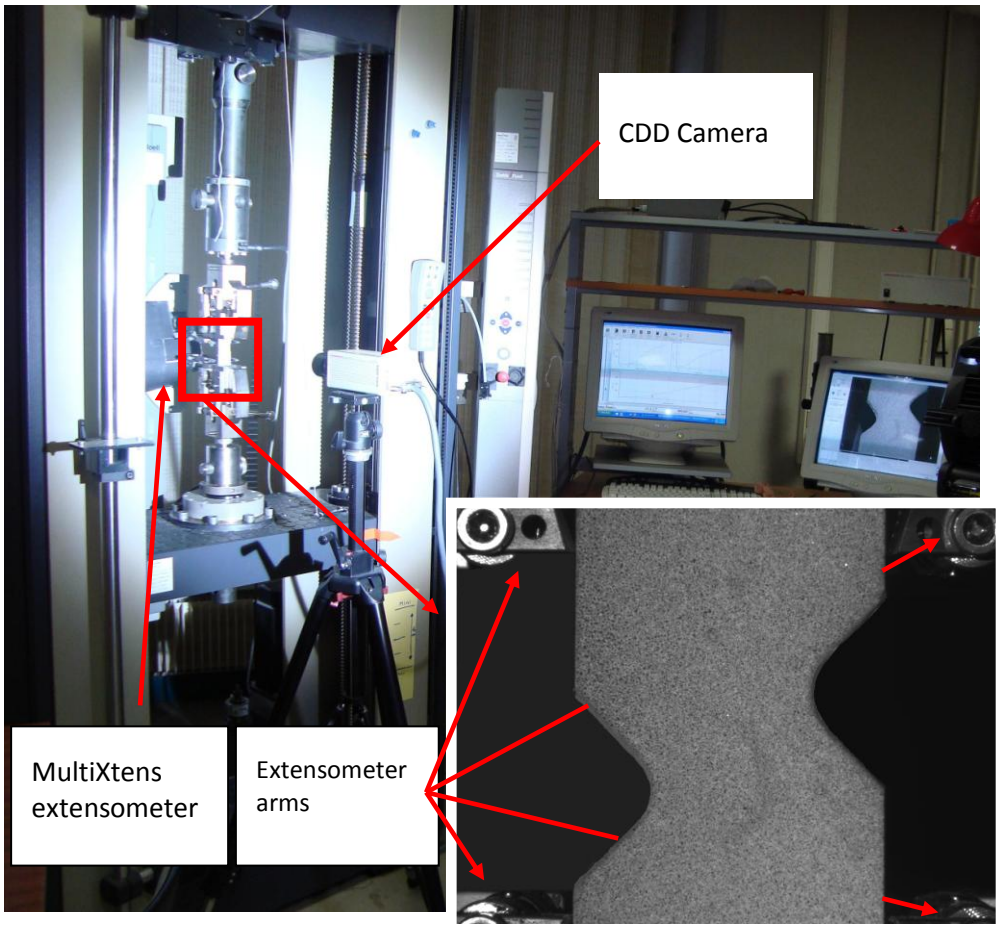

Fig. 2.19. The experimental set-up with a Meuwissen sample. View of the random speckle pattern.

References

[Araki et al. 2003] W. Araki, T. Adachi, A. Yamaji. Fracture Toughnesses of Bisphenol a Type Epoxy Resin and Silica Particulate-Filled Epoxy Composite. JSME International Journal, Series A: Solid Mechanics and Material Engineering 46 (2) (2003), p. 163–169.

[Atta et al. 2005] A. M. Atta, R. Mansour, M. I. Abdou, A. M. El-Sayed. Synthesis and Characterization of Tetra-Functional Epoxy Resins from Rosin. Journal of Polymer Research 12 (2005), p. 127–138.

[Bannister et al. 1995] DJ. Bannister, MC. Andrews, AJ. Cervenka, RJ. Young, Analysis of the single-fiber pull-out test by means of Raman spectroscopy. Part II: Micromechanics of deformation for an aramid-epoxy system. Composites Science and Technology 53 (1995), p. 41l-421.

[Burton 1993] BL. Burton, The Thermooxidative Stability of Cured Epoxy Resins. J. Appl. Polym. Sci. 47 (1993), p. 1821-1837.

[Burton 2001a] BL. Burton, Amine-blushing problems? No sweat! Huntsman Corp., presented at the Epoxy Resin Formulators' meeting, The Society of the Plastics Industry, fall 2001 (Baltimore, MD).

[Burton 2001] BL. Burton, Blushing of Amine cured Epoxy Resins, Huntsman Corp., presented at the Epoxy Resin Formulators' meeting, The Society of the Plastics Industry, fall 2001. (Baltimore, MD).

[Carrega 1999] M. Carrega, Les polymers : de la molécule à l'objet, EDP Science 1999, Courtaboeuf, France.

[Christian 1965] JW. Christian, The theory of transformations in metals and alloys. Oxford: Pergamon Press; 1965. p. 815.

[Darragas et al. 1998] K.F. Darragas, HP. Klein, Water-Reducible Coatings via Epoxy Resin Modification, International Waterborne, High-Solids and Powder Coatings Symposium, 1998, New Orleans, LA.

[Doumalin 2000] P. Doumalin, Microextensométrie locale par corrélation d'images numériques-Application aux études micromécaniques par microscopie électronique à balayage, PhD thesis, Ecole Polytechnique (LMS, France) 2000.

[Fu et al. 2000] Fu SY, Yue CY, Hu X, Mai YW. Analyses of the micromechanics of stress transfer in single- and multi-fibre pull-out tests. Composites Science and Technology 60 (2000), p. 569-79.

[Gao and Zhou 1999] YC. Gao, LM. Zhou, Energy release rate for interface debonding with prestress and friction. Theoretical and Applied Fracture Mechanics 32 (1999), p. 203-207.

[Hild et al. 2008] F. Hild, S. Roux, CORRELI-Q4: A software for "Finite-element" displacement field measurements by digital image correlation. Internal report No. 269, ENS Cachan, 2008, LMT Cachan, France.

[Kanchanomai et al. 2005]. C. Kanchanomai, S. Rattananon, M. Soni. Effects of loading rate on fracture behavior and mechanism of thermoset epoxy resin. Polymer Testing 24 (2005), p. 886–892.

[Kim et al. 2006 Acta] H.Y. Kim, T. Sasaki, J.I. Kim, T. Inamura, H. Hosoda and S. Miyazaki, Texture and shape memory behavior of Ti–22Nb–6Ta alloy, Acta Mater. 54 (2006), p. 423-433.

[Kim et al. 2006] H.Y. Kim, J.I. Kim, T. Inamura, H. Hosoda and S. Miyazaki, Effect of thermo-mechanical treatment on mechanical properties and shape memory behavior of Ti–(26–28) at. % Nb alloys, Mater. Sci. Eng. A 438–440 (2006), p. 839-843.

[Meuwissen 1998] Meuwissen MHH, Oomens CWJ, Baaijens FPT, Petterson R, Janssen JD. Determination of the elasto-plastic properties of aluminium using a mixed numerical-experimental method, Journal of Materials Processing Technology 75 (1998), p. 204–211

[Miyazaki et al. 1981] S. Miyazaki, K. Otsuka and Y. Suzuki, Transformation pseudoelasticity and deformation behavior in a Ti-50.6at%Ni alloy, Scripta Metall 15 (1981), p. 287-292.

[Otsuka and Ren 2005] K. Otsuka and X. Ren. Physical metallurgy of Ti–Ni-based shape memory alloys. Progress in Materials Science 50 (2005), p. 511–678.

[PCI] Painting & coatings industry (PCI), Amine Curing of Epoxy Resins: Options and Key Formulation Considerations, Available at:

http://www.pcimag.com/Articles/Feature_Article/4f50be4a7bdeb010VgnVCM100000f932a8c0

[Ram 1997] Arie Ram, Fundamentals of polymer engineering, Plenum press, Ney York, 1997.

[Rezig 2006] Aziz Rezig, Tinh Nguyen, David Martin, Lipiin Sung, Xiaohong Gu, Joan Jasmin, and Jonathan W. Martin. Relationship Between Chemical Degradation And Thickness Loss of an Amine-Cured Epoxy Coating Exposed to Different UV Environments. JCT Research, Vol. 3, No. 3, July 2006.

[Rodriguez et al. 2005] M.T. Rodriguez, S.J. Garcia, R. Cabello and J.J. Suay. Effect of Plasticizer on the Thermal, Mechanical and Anticorrosion Properties of an Epoxy Primer. JCT Research, Vol. 2, No. 7, July 2005.

[Sun et al. 2010] F. Sun, S. Nowak, T. Gloriant, P. Laheurte, A. Eberhardt and F. Prima, Influence of a short thermal treatment on the superelastic properties of a titanium-based alloy; Scripta Materialia 63 (11) (2010), p. 1053-1056.

[Wisanrakkit 1990] Wisanrakkit, G., and Gillham, J. K., Glass Transition Temperature (T_g) as an Index of Chemical Conversion for a High-T_g Amine/Epoxy System's Chemical and Diffusion-Controlled Reaction Kinetics, J. Appl. Polym. Sci., 41(11-12), 1990, p. 2885-2929.

[Yue et al. 1995] Yue CY, Looi HC, Quek MY. Assessment of wire-matrix adhesion and interfacial properties using the pull-out test. Int J Adhesion and Adhesives 15 (1995), p. 73 - 80.

Chapter 3.

Characterization of the matrix/wire interface-influence of the martensitic transformation

3.1. Introduction

3.2. Analytical method

3.3. Effect of martensitic transformation on debonding initiation

3.4. Effect of martensitic transformation on debonding propagation

3.5. Conclusion

References

3.1. Introduction

In a SMA-reinforced composite structure, strain recovery of an embedded SMA wire induces a high interfacial stress between wire and matrix [Poon et al. 2005]. It can generate the interfacial debonding. The interface can also be debonded during the mechanical test because the properties of the matrix and wire are different. Thus it is essential to know the interfacial shear strength between the SMA wire and the surrounding matrix for the evaluation of mechanical response and the development of well designed interfaces. In order to study the interface, the single wire composite samples with NiTi or steel wire were subjected to the pull-out test. The NiTi wires were heat treated at different conditions in order to obtain different transformation characteristics. The steel wire was taken as reference because it undergoes no phase transformation. In-situ observations of the interfacial debonding and sliding behavior were carried out.

Pull-out test has been well accepted as one of the most important test methods developed as a means of investigating the interfacial adhesion quality and interfacial properties between fibers and matrix [Fu et al. 2000, Gao et al. 1999, Yue et al. 1995, Bannister et al. 1995]. This test has been extensively used for this meaning in a SMA wire composite as studied in several works [Paine and Rogers 1993, Poon et al. 2004, Smith et al. 2004, Jang and Kishi 2005, Wang and Hu 2005, Neuking et al. 2008, Rossi et al. 2008, Sadrnezhaad et al. 2009].

In the pull-out tests, the embedded length is usually small and the interfacial shear strength (IFSS) can be estimated by dividing the maximum force to the lateral surface assuming that the shear stress is uniformly distributed [Rossi et al. 2008] along the embedded length.

It has been shown that the shear stress depends critically to the position in the embedded length [Fu et al. 2000]. Moreover, it is shown in this work that the debonding starts before the force reaches the maximum value [Payandeh et al. 2010]. From Zhou et al. [Zhou et al. 1992] the difference in the debonding and pull-out stresses increases with increasing embedded fibre length. Therefore, the common method ($F_{max}/2\pi rl$) can not be used in all cases, especially for the shape memory wire, because of martensitic transformation occuring in the wire.

However, for evaluating the phase transformation effect, a long embedded length is required. In this case, a new method should be developed in order to estimate the IFSS. In the present study a new method, based on the Fu's work [Fu et al. 2000], has been developed for the long embedded wire length samples. The IFSS was determined by implementing the experimental results into the model. It has been observed that the debonding stress for NiTi wire is significantly less than that for steel wire. It can be associated with the difference between the elastic modulus of the wires. The interfacial shear strength was then determined for these systems. It has been experimentally found that, when there is no phase transformation the IFSS is about 9 MPa while it is about 14 MPa when the martensitic transformation/ reorientation occurs in the reinforced wire.

3.2. Analytical method

When pulling-out a single wire, the shear stress reaches its maximum value at the wire entry point [Payandeh et al. 2010, Rodriguez et al. 2007] from where the debonding starts. The Maximum Interfacial Shear Stress (denoted hereafter by MISS) increases with increasing the normal applied stress. When the MISS increases and reaches the interfacial shear strength (IFSS or τ_i), interfacial debonding will start immediately. The debonding propagates while the load is applied. With propagation of debonding, the MISS will be at the debonded/ undebonded transition zone. In other word, the position of maximum shear stress varies with propagation of the debonding process.

From above discussion, a two-stage evolution of the MISS versus the applied stress σ_p can be considered. The first and second stage of this evolution can be expressed, respectively, as:

$$\tau^F_{max} = \beta.\ \sigma_p \qquad \text{for } \sigma_p < \sigma_p^* \qquad (3.1)$$

$$\tau^F_{max} = \tau_i \qquad \text{for } \sigma_p \geq \sigma_p^* \qquad (3.2)$$

σ_p^* is the applied stress at the beginning of debonding (debonding stress). The evolution of the MISS is shown in Fig. 3.1 schematically supposing that β is independent of the applied stress. In order to determine the parameter β, it is necessary to know the interfacial shear stress as a function of position *x*.

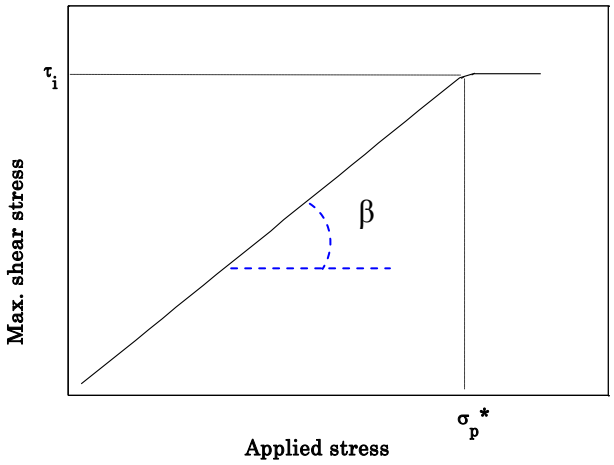

Fig. 3.1- Maximum shear stress vs. applied stress, τ_i and σ_p^* are interfacial shear strength and debonding stress, respectively

According to single-wire pull-out model by Fu et al. [Fu et al. 2000], the shear stress in the wire/matrix interface is calculated as below:

$$\tau^F(x) = \frac{a}{2}\alpha\left(C_{11}\cosh(\alpha x) + C_{12}\sinh(\alpha x)\right) \qquad (3.3)$$

where,

$C_{11} = \sigma_p [1- (A_{13} / A_{12}) + [(A_{13} \cosh(\alpha.l)) / A_{12}]] / \sinh(\alpha l)$

$C_{12} = - \sigma_p A_{13} / A_{12}$

$A_{11} = ab^2 [2 b^2 \ln(b/a) - (b^2-a^2)] / 2 (b^2-a^2)^2 - a/4$

$A_{12} = 2 G_m [(a^2 / (b^2-a^2)) + E_m / E_f] / (a.E_m.A_{11})$

$A_{13} = 2 G_m . a / [(b^2-a^2) . E_m . A_{11}]$

$\alpha = \sqrt{A_{12}}$

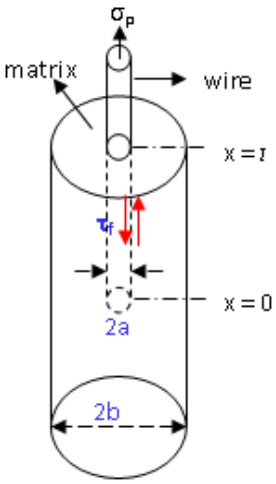

Where a and b are the radius of wire and matrix, σ_p is the applied stress. G_m, E_m and E_f are, respectively, the matrix shear modulus and Young's modulus of the matrix and wire. Table 3.1 lists the parameters C_{11}, C_{12}, A_{11}, A_{12} and A_{13} which are calculated for different wire's lengths and Young's moduli.

Reformulation of equation 3.3, and doing some mathematical works, gives:

$$\tau^F(x) = \frac{\gamma}{2}\left(B\sinh(\frac{\gamma x}{a}) + C\cosh(\frac{\gamma x}{a}) \right)\sigma_p \qquad (3.4)$$

where γ, A, B and C are written as bellow:

$$\gamma = \sqrt{\frac{1}{A(1+\nu_m)}(\frac{S_f}{S_m} + \frac{E_m}{E_f})}$$

$$A = -0.25 + b^2 \frac{2b^2 \ln\frac{b}{a} - b^2 + a^2}{2(b^2 - a^2)^2}$$

$$B = -\frac{S_f E_f}{S_f E_f + S_m E_m}$$

$$C = csch(2\gamma s) - B\tanh(\gamma s)$$

where $S_f = \pi a^2$, $S_m = \pi (b^2 - a^2)$, E_m and E_f are, respectively, the Young's modulus of the matrix and wire, b is the radius of the matrix, s is the wire's aspect ratio and ν_m is the matrix Poisson's ratio. The calculated values for dimensionless constants A, B, C and γ are listed in table 3.2, for different wire lengths and Young's moduli.

As discussed above, the shear stress has the maximum value at the wire entry point where x is equal to l. Thus, replacing x by l in equation 3.4, gives the MISS value. Therefore,

$$\tau^F_{Max} = \left[\gamma\sinh(\gamma s)\left(B\cosh(\gamma s) + C\sinh(\gamma s)\right) + \frac{C\gamma}{2} \right]\sigma_p \qquad (3.5)$$

Comparing equation 3.1 and 3.5 gives β as [Payandeh et al. 2010]:

$$\beta = \gamma s\sinh(\gamma s)\left(B\cosh(\gamma s) + C\sinh(\gamma s)\right) + \frac{C\gamma}{2} \tag{3.6}$$

Table 3.1. Variation of the parameters in the model of Fu [Fu et al. 2000] for different wire lengths and Young's moduli using a = 0.5 mm, b = 7.5 mm, σ_p = 100 MPa

	E_f = 27 (GPa)		E_f = 33 (GPa)		E_f = 210 (GPa)	
	l = 10 mm	l = 50 mm	l = 10 mm	l = 50 mm	l = 10 mm	l = 50 mm
A_{11} (mm)	0.99	0.99	0.99	0.99	0.99	0.99
A_{12} (mm^{-2})	0.1704	0.1704	0.1406	0.1406	0.0276	0.0276
A_{13} (mm^{-2})	0.0066	0.0066	0.0066	0.0066	0.0066	0.0066
C_{11} (MPa)	6.9633	3.8627	9.1714	4.6809	55.556	23.847
C_{12} (MPa)	-3.863	-3.863	-4.681	-4.681	-23.81	-23.81

Table 3.2. The calculated model dimensionless constants for different wire lengths and Young's moduli using a = 0.5 mm, b = 7.5 mm

	E_f = 27 (GPa)		E_f = 33 (GPa)		E_f = 210 (GPa)	
	l = 10 mm	l=50mm	l = 10mm	l = 50 mm	l = 10 mm	l = 50 mm
A	1.98	1.98	1.98	1.98	1.98	1.98
B	–0.039	–0.039	–0.047	–0.047	–0.238	–0.238
C	0.0696	0.0386	0.0917	0.0468	0.5556	0.2385
γ	0.2064	0.2064	0.1875	0.1875	0.0831	0.0831
β	0.0994	0.0992	0.0897	0.0894	0.0379	0.0317

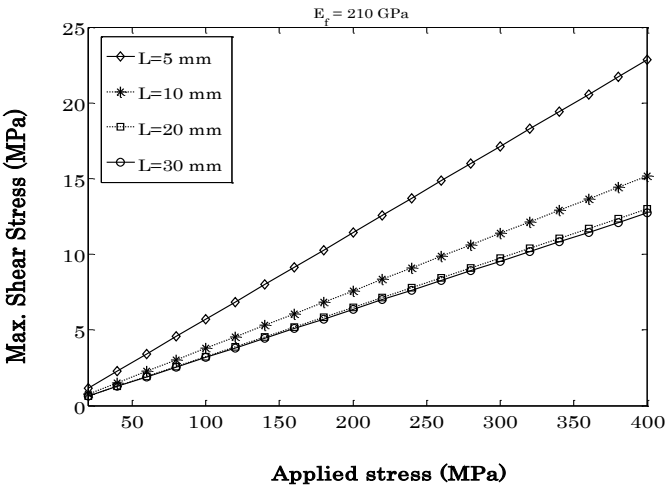

Fig. 3.2. Maximum shear stress vs. applied stress for different embedded wire lengths

From equation 3.1 and 3.6, β seems to be independent of applied stress, thus the maximum shear stress varies linearly with applied stress as it is shown in Fig.3.2. This figure illustrates

the variation of maximum shear stress versus applied stress for different embedded wire lengths. As it is seen, for steel wire the change of the MISS becomes small for the wire lengths greater than 20 mm. The wire length of 20 mm can be considered theoretically as a critical embedded length for steel wire. For the embedded lengths greater than the critical one, the MISS becomes independent of the embedded length.

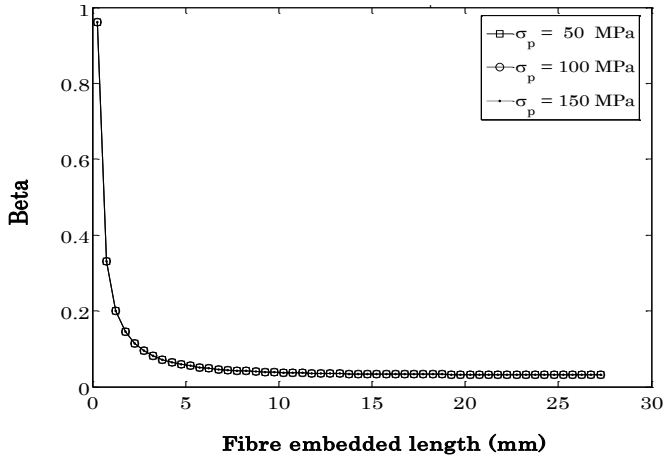

Fig3.3- Beta vs. embedded wire length for different applied stresses

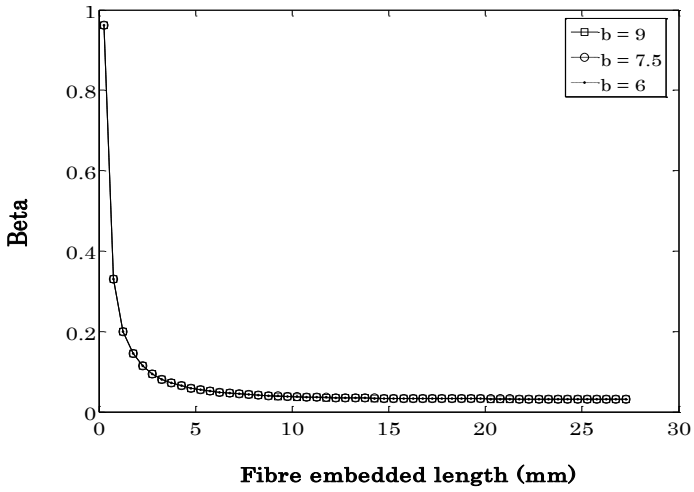

Fig. 3.4- Beta vs. embedded wire length for different specimen diameters

According to equation 3.1, the MISS varies only with the variation of the parameter β for a constant applied stress. Therefore, this parameter needs to be investigated. The parameter β shows to be independent of some parameters such as applied stress (Fig. 3.3) and matrix diameter (Fig. 3.4). In contrary, it depends on the Young's modulus of wire (Fig. 3.5). It is also dependent on embedded length and the wire diameter (Fig. 3.6) for the lengths smaller

than 20 mm (for steel wire). Therefore, the parameter β depends only on the Young's modulus of wire for the embedded length greater than a certain value.

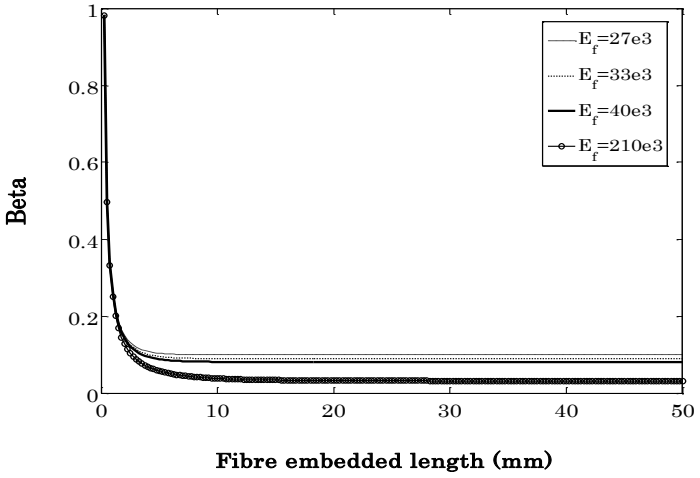

Fig. 3.5- Beta vs. embedded wire length for different wire's Young moduli

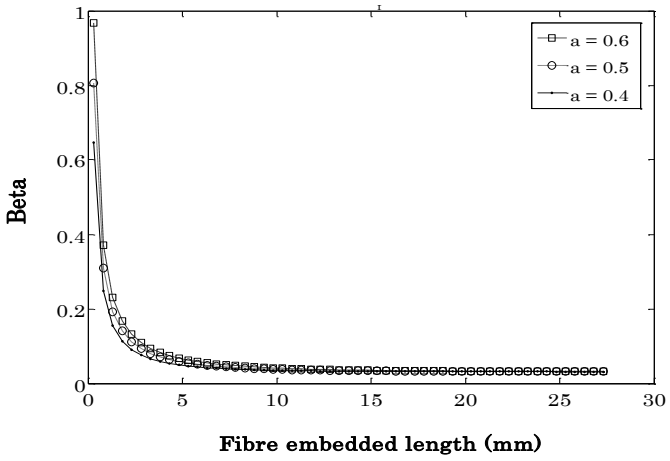

Fig3.6- Beta vs. embedded wire length for different wire radius

Since β is independent of applied stress, as discussed before, the MISS increases linearly with applied stress and remains constant as soon as the MISS is equal to τ_i.

3.3. Effect of martensitic transformation on the debonding initiation

Fig. 3.7 shows the debonding propagation in NiTi and steel wire samples. The arrows show the debonding position. As shown in the figure the debonding starts from the wire entry point and proceeds to the embedded end. This process occurs slowly and when the undebonded length reaches the critical length value, critical length, the debonding phenomenon proceeds so rapidly (see section 3.4 for more details). The wire is then pulled out of the resin matrix by

a frictional pull-out process. The results are shown in the Fig. 3.8 and 3.9. The debonding onset is indicated in each figure.

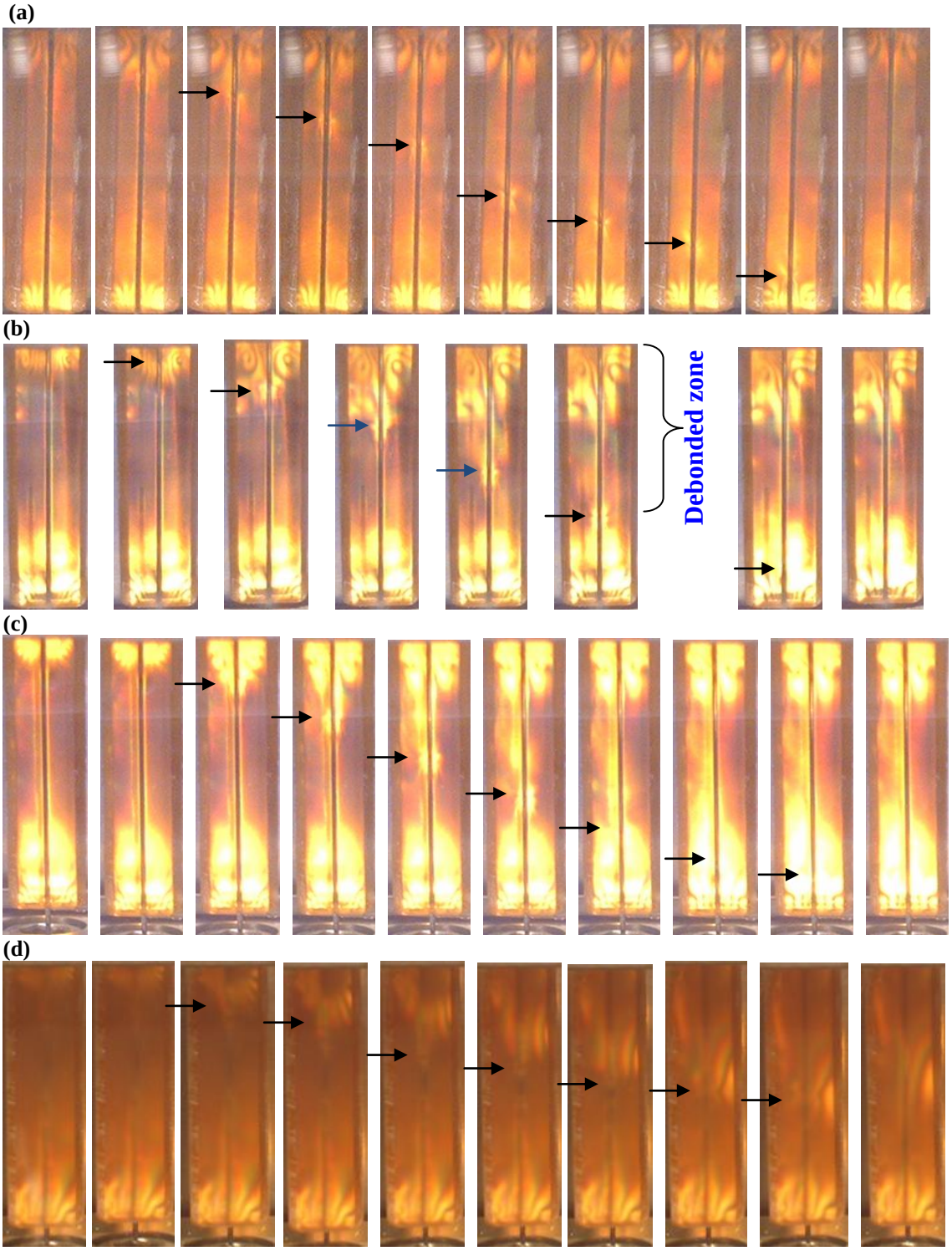

Fig. 3.7- Debonding process along the wire embedded length during the test. (a) M550, (b) M450, (c) M400 and (d) Steel wire. In all cases, the first image (left hand side) was taken before test and in the first case the last one was taken just after completed debonding. The arrows show the position of debonding.

In comparison with the NiTi wires, the steel wires are debonded more rapidly and the critical length is significantly greater than that of the NiTi wires. In contrary, the load at which the debonding process starts (debonding load) is more than that for the NiTi one. In other word, the interfacial failure for the steel wires starts in greater values of load, proceeds faster and reaches the critical length more rapidly in comparison with the NiTi wires. The critical length for NiTi wires is small (table 3.3). In the cases of M550 and M450 the debonding begins after martensitic reorientation/ transformation of the free part of wires. In other words, the stresses in which the debonding occurs (debonding stress) are greater than the stresses in which the phase transformation takes place (transformation stress). In these cases, critical length is very small (say less than 5 mm) in comparison with the steel wire specimens.

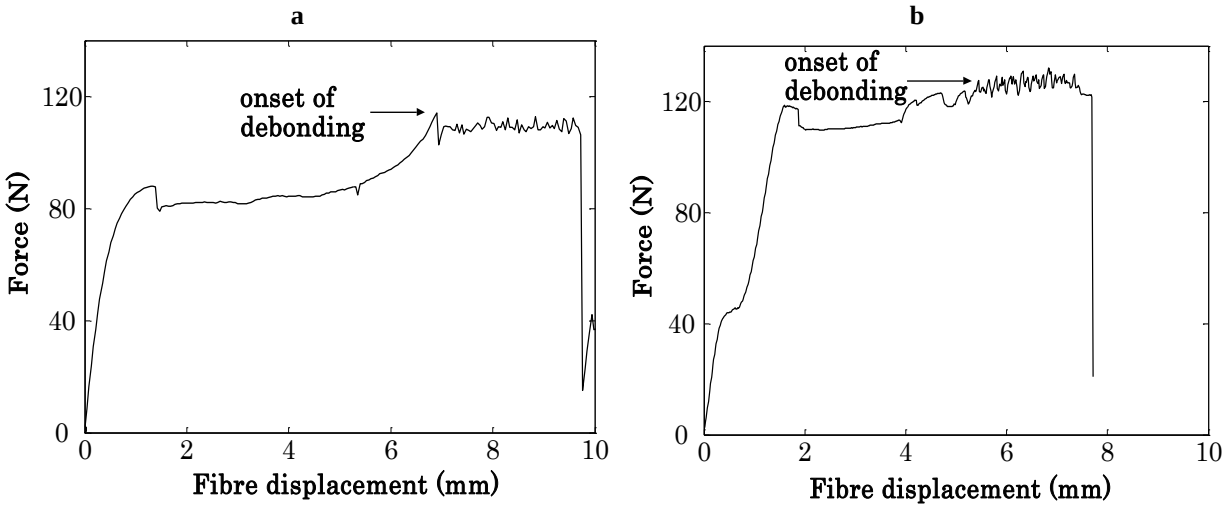

Fig. 3.8- Force - Displacement diagram for the specimens with (a) M550 and (b) M450 wire

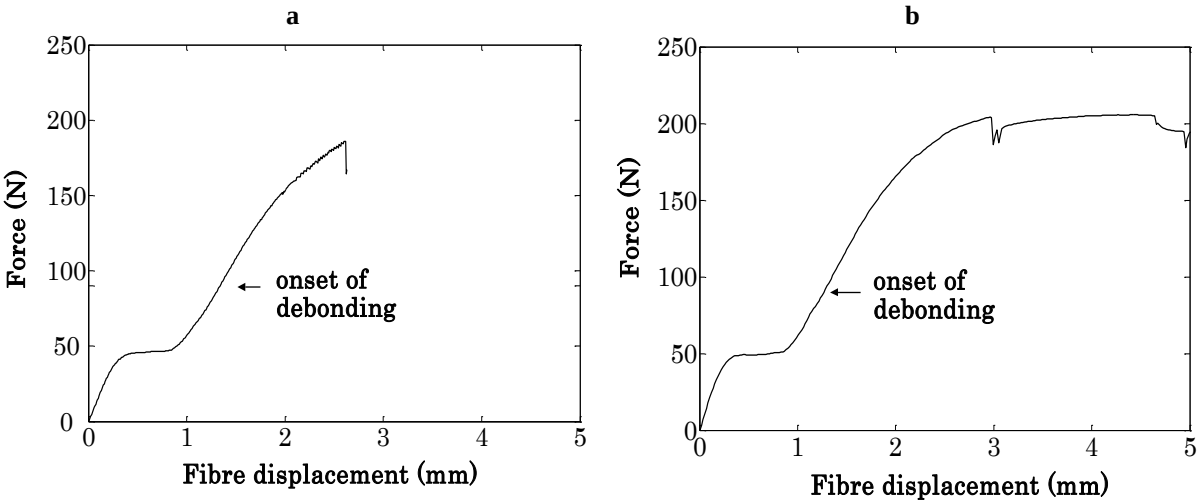

Fig. 3.9- Force - Displacement diagram for the specimens with M400 wire (a) without and (b) with transformation

The reported values of Young's modulus vary from 26 to 70 GPa for martensite and 30 to 70 GPa for austenitic NiTi [Ostachowicz et al. 2000, Hamada et al. 1998, Sittner et al. 2006, Liu and Xiang 1998, Niemczura et al. 2006, Sadrnezhaad et al. 2009b]. The variation of the measurements is too large to be accounted for experimental errors. The failure in determining the elastic modulus by mechanical testing is ascribed to stress-induced martensitic transformation or martensite reorientation, depending on the starting structure [Liu and Xiang 1998]. In this work, the apparent value of the Young's modulus for M550 wire has been determined experimentally to be 27 GPa. For M450 the values of 33 GPa has been determined for apparent Young's modulus. Since the wire displacement plays an important role in debonding process, it seems better to use the apparent Young's modulus, instead of the real one. For the parameter β, by using the apparent modulu for NiTi wires, the values of 0.032, 0.081, 0.089 and 0.099 are calculated for steel, M400, M450 and M550, respectively (Table 3.3). It should be noted that these values correspond to the wire embedded length greater than the critical one.

Table 3.3. Results summary

	Deformation mode	E_f (GPa)	β	F (N)	σ_p^* (MPa)	τ_i (MPa)	Critical length(mm)
M550	M. Reorientation	27 [(a)]	0.0992	110	140	13.9	< 5
M450	M. Transformation	33 [(a)]	0.0894	125	160	14.3	< 5
M400	-	40 [(a)]	0.0808	90	115	9.3	≈ 5
Steel	-	210	0.0317	225	286	9.1	≈ 15

(a). Apparent modulus.

By determining the interfacial shear strength for these systems one will be able to understand the effect of martensitic transformation on the debonding initiation. As it was noted before, when the MISS reaches the τ_i, the debonding starts. At this time the applied stress is equal to the debonding stress σ_p^*, thus:

$$\tau_i = \beta \sigma_p^* \tag{3.7}$$

The interfacial shear strength, τ_i, is calculated when the debonding stress is known. From experimental results (table 3.3), the debonding stress is 140 MPa (F ≈110 N) for M550 (Fig. 3.8- a), 160 MPa (F ≈ 125 N) for M450 (Fig. 3.8-b), 115 MPa (F ≈ 90 N) for M400 (Fig. 3.9) and 285 MPa (F ≈225 N) for steel/ epoxy (Fig. 3.10) systems. The difference between the debonding stresses is associated with the difference between the elastic modulus of the wires. By substituting these values into equation 3.7 the interfacial shear strength are obtained. The results are shown in table 3.3. From table 3.3, the τ_i is about 14 MPa for the samples with M550 and M450 wires (with martensitic transformation/reorientation). It is about 9 MPa for

steel and M400 specimens (no transformation) which is identical for different two kinds of wire (e.g. steel and M400) but the same matrix (Fig. 3.11). According to Rossi et al. [Rossi et al. 2008], the interfacial shear strength for martensitic NiTi wire/epoxy system has been reported to be equal to 13 MPa using common method and a embedded length about 5 mm.

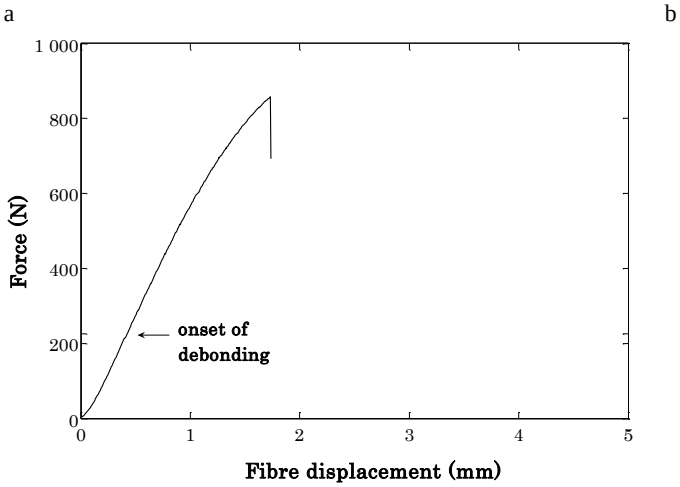

Fig. 3.10 - Force - Displacement diagram for the specimens with steel wire

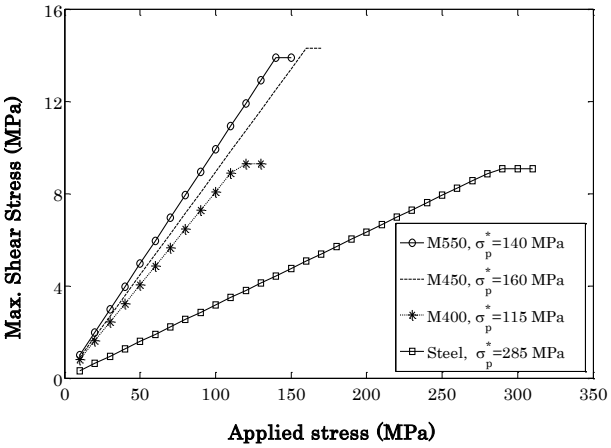

Fig. 3.11- Maximum shear stress vs. applied stress for different wire's Young moduli

As it was mentioned before, the interfacial shear strength is about 9 MPa when there is no phase transformation; and it is about 14 MPa when the wires exhibit martensitic transformation/reorientation which gives a rise about 50 percent of this parameter.

According to above discussion, the interfacial shear strength is, likely, independent of the kind of wire, but it seems to be dependent on the occurrence of martensitic transformation (MT)/reorientation in the wire.

The interfacial shear strength, τ_i, is a parameter that can be expressed in terms of matrix shear strength, τ^m_y. It is well known that, for a perfect adhesion, when the maximum shear stress at the interface is equal to the matrix shear strength (τ^m_y), the debonding will begin, but when the adhesion is imperfect, one introduces a non-dimensional parameter, λ, which can not exceed unity; at the debonding point we make τ_i equal to $\lambda\ \tau^m_y$ rather than τ^m_y [Piggott 1980], thus:

$$\lambda = \tau_i / \tau^m_y \qquad (3.8)$$

The parameter, λ, acts as the adhesion coefficient. For identifying this parameter, both τ_i and τ^m_y should be known. The matrix shear strength, τ^m_y, is determined directly by mechanical tests or from matrix yield stress and using the yielding criterion.

The composite with large τ_i has high strength due to effective stress transfer from the matrix to the wires. According to equation 3.8**,** the τ^m_y or λ must be increased in order to have the high values of τ_i. The former can be increased likely with increasing the curing time or temperature (as discussed in chapter 2) and the later should be dependent on some parameters such as the microscopic wire's surface condition, matrix shrinkage pressure. Following Rossi et al. [Rossi et al. 2008], the τ_i increases with macroscopic surface treatment of the wires.

3.4. Effect of martensitic transformation on the debonding propagation

The mechanical behavior of the wires was shown in chapter 2. The martensitic reorientation occurs in the M550 wires when subjected to the tensile load at room temperature. In the case of M400 and M450 wires, the reorientation of the R-phase followed by the martensitic transformation takes place.

The stresses/loads at which the martensite reorients in the M550 wires or martensitic transformation occurs in M450/M400 wires are denoted by transformation stresses/loads.

The results of pull-out test were shown in the Fig. 3.8 – 3.10. The debonding onset is indicated in each figure. The load at which the debonding begins is denoted by debonding load. Fig. 3.8 illustrates that in samples with M550 and M450 wires, the martensitic reorientation/ transformation of the free part of wires occurs before that debonding begins. In M400 wire specimens the martensitic transformation does not occur before the debonding onset (Fig. 3.9). In other word, the transformation load for M550 and M450 wires is less than debonding load whilst in M400 wire the debonding load is less than transformation one.

It is useful to note that for M550 and M450 samples, the load remains constant during debonding propagation (Fig. 3.8) while it increases during propagation of debonding in the specimens with M400 or steel wires. As it is shown in Fig. 3.9-b, the load remains constant as soon as it becomes more than the transformation load (≈200 N) which is discussed later.

It is useful to note that for M550 and M450 samples, the load remains constant during debonding propagation (Fig. 3.8) while it increases during propagation of debonding in the specimens with M400 or steel wires. As it is shown in Fig. 3.9-b, the load remains constant as soon as it becomes more than the transformation load (≈200 N) which will be discussed later.

According to in-situ observation, the debonding process occurs slowly and in some specimens with a constant rate. When the undebonded length reaches a critical value, the debonding phenomenon continues so rapidly (Fig. 3.12).

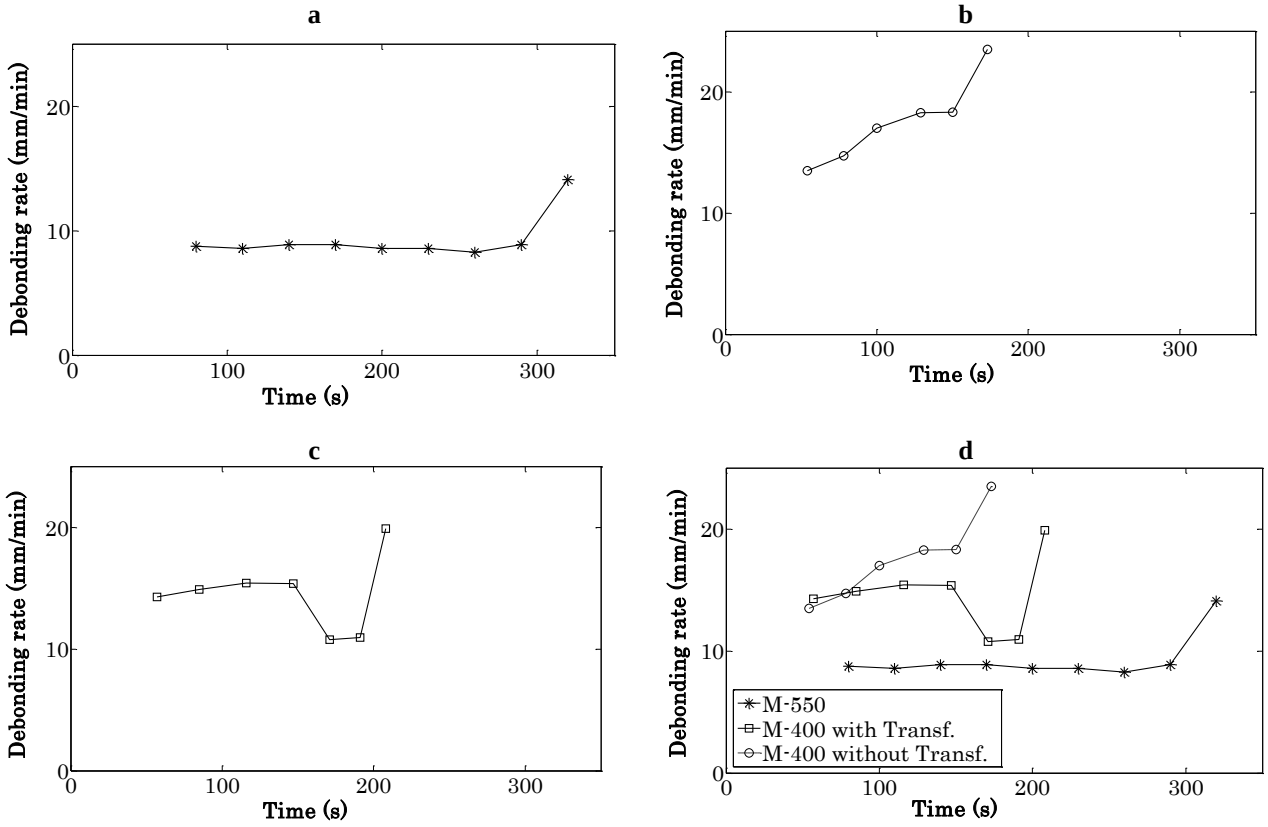

Fig. 3.12- Debonding rate for a specimen with a) M550, b) M400 and c) M400 wires d) a, b and c for comparison

Fig. 3.12-a shows the debonding rate versus time of debonding for the specimens with M550 wires. From this figure, apart from the last step, the debonding rate is constant and is about 8.5 mm/min. In the last part (critical length) the debonding propagates with the rate of 14.1 mm/min. The mean value is equal to 9.2 mm/ min. The average debonding rate for the other M550 samples varies between 8.3 and 9.3. The debonding rate for a sample with M400 wire is shown in Fig. 3.12-b. As shown, the debonding propagates in this specimen with the rate from 13.5 to 18.3, and 23.5 mm/min for the last part. The average debonding rate for the M400 samples varies between 14.4 and 17.3 mm/min. In the M400 samples with second plateau (e.g. Fig. 3.9-b), the average debonding rates are close to the lower value (14.4) and the average debonding rates which are close to the upper one (17.3) correspond to the M400

samples without second plateau (e.g. Fig. 3.9-a). In the case of M450 wire composite samples, the debonding propagates with an average rate which varies between 10.6 and 11.3 for different specimens. The discrepancy in debonding rates for three types of samples can be associated with the martensitic reorientation/ transformation occurring in the M550/ M450 wires during loading. In other words, due to increasing the length during martensitic reorientation/ transformation in M550/ M450 wires, the debonding rate in these specimens is small in comparison to the samples with M400 wires. In some specimens with M400 wire, the phase transformation occurs before that the interface is debonded entirely (Fig. 3.9-b). Fig. 3.12-c shows the debonding rate versus time for this specimen. As illustrated in Fig. 3.12-c, the interface debonds with the rate of about 15 mm/min and after about 150 seconds the rate decreases to 10.8 and 10.9 mm/min. This phenomenon was repeated in some other samples (with M400 wire) and can not be considered as experimental errors. In these specimens, the embedded length is a little more than the embedded length in the other samples with M400 wires, thus the debonding duration is a little more than the others. In the last few seconds, the load becomes more than transformation load (≈ 200 N) and the phase transformation begins just before that the interface debonds completely. As a result, the debonding rate decreases (Fig. 3.9-b and 3.12-c). In Fig. 3.13 the load is normalized by dividing to the transformation load. As shown in this figure, the debonding rate decreases as soon as the normalized load becomes more than 1. It means that the debonding propagation rate decreases when the martensitic transformation begins in the embedded part of wires.

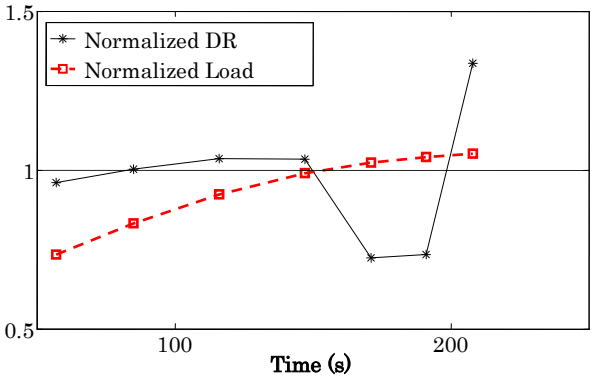

Fig. 3.13- Normalized force and debonding rate (DR) for the specimen of Fig. 3.9-b and 3.12-c, the force is divided by transformational load and the DR is divided by the average rate.

Therefore, it can be claimed that the length changes during martensitic reorientation in M550 or martensitic transformation in M450 or sometimes in M400, is the sole reason of decreasing in debonding rate [Payandeh et al. 2009]. In the specimens with M400, because there is no phase transformation, the interface debonds fast.

It is worth to note that when an embedded stress free SMA wire is subjected to the tensile load during pull-out test, the wire phase transformation/reorientation can not occur before interfacial debonding, because the phase transformation/reorientation is accompanied by a large inelastic strain [Payandeh et al. 2009]. But the transformation occurs immediately after partial debonding; and the length change during phase transformation causes the load to remain constant while debonding propagates (Fig. 3.8 and 3.9-b). It also leads the rate of debonding to decrease because the test is displacement controlled.

As discussed above, in the case of M450 and M550, the debonding begins after transformation of the free part of wires. Therefore, just before the interfacial debonding the displacement rate at the wire entry point will be equal to imposed displacement rate (V_i= 0.5 mm/min). After partial debonding, the debonded part will transform immediately. The displacement rate at the bonded-debonded transition zone (debonding front) will be equal to V_i; because the debonded part moves freely and the effect of friction will be negligible. The debonding propagates and the process will be repeated in the next parts. In order to simplify, we divide the embedded length (ℓ) to n imaginary parts supposing that the debonding occurs step by step and at each time increment (Δt) the debonding propagation length $\Delta\ell_t$ will be equal to ℓ/n mm. At the end of each step, the displacement rate at the debonding front is equal to V_i. Moreover, the interface debonds with the constant rate of v_d in (n-m) first parts (the m last parts refer to the critical embedded length). To find the relationship between the V_i, v_d and the transformation strain, ε^{tr}, consider 2 imaginary points, A and B, on the wire and at the wire matrix interface with the initial distance of $\Delta\ell_t$. At time t, the point A is located on the debonding front. At time t+Δt the debonding arrives to the point B and the part of wire between A and B with the length of $\Delta\ell_t$ (= $X_A - X_B$) transforms. Therefore, due to the length change during phase transformation/reorientation, the point A will displace about $\Delta\ell_t.\varepsilon^{tr}$ and the initial distance ($X_A - X_B$) increases to $\Delta l_{t+\Delta t}$ which is equal to $\Delta\ell_t + \Delta\ell_t.\varepsilon^{tr}$. Thus:

At t:

$$X_A - X_B = \Delta\ell_t \qquad (3.9)$$

At t+Δt:

$$X_A - X_B = \Delta\ell_{t+\Delta t} = \Delta\ell_t + \Delta\ell_t.\,\varepsilon^{tr} \qquad (3.10)$$

During the time increment Δt, because of wire phase transformation/reorientation, the point A displaces. At the same time, the debonding propagation length will be equal to $v_d.\,\Delta t$; thus:

$$\Delta l_t = v_d\,.\,\Delta t \qquad (3.11)$$

$$X_A\big|_{t+\Delta t} - X_A\big|_t = \Delta\ell_t.\,\varepsilon^{tr} \qquad (3.12)$$

Moreover, the displacement of the point A is related to the displacement rate as:

$$X_A\big|_{t+\Delta t} - X_A\big|_t = V_i\,.\,\Delta t \qquad (3.13)$$

Comparing the equations 3.12 and 3.13 gives:

$$V_i * \Delta t = \Delta \ell_t . \varepsilon^{tr} \quad (3.14)$$

With substituting Δl_t from equation 3.11 into equation 3.14, one obtains:

$$V_i . \Delta t = v_d . \Delta t . \varepsilon^{tr} \quad (3.15)$$

$$V_i = v_d . \varepsilon^{tr} \quad (3.16)$$

The debonding rate, v_d, and transformation strain, ε^{tr}, for each type of specimen has been measured from experimental data and the results are shown in Table 3.4 [Payandeh et al. 2009]. The equation 3.16 can be validated by comparing the last two columns.

Table 3.4- Debonding rate, v_d, displacement rate V_i (mm/min) and ε^{tr} and their relationship

Sample	Deformation mode	ε^{tr} (average)(1)	v_d (mm/min)	v_d (average)(1) (mm/min)	$\varepsilon^{tr}. v_d$	V_i
M550	M. Reorientation	0.056	8.3-9.3	8.84	0.495	0.5
M450	M. Transformation	0.045	10.6-11.3	10.95	0.493	0.5
M400 with MT	M. Transformation	0.044	10.8-11.4	11.25	0.495	0.5
M400 without MT	-	-	15.7 -17.3	16.58	-	0.5
M550	M. Reorientation	0.056	1.9- 1.98	1.95	0.109	0.1

(1)- The average ε^{tr} and v_d were calculated using several samples.

According to above discussion, the martensitic transformation (MT)/reorientation reduces the debonding rate. As discussed in section 3.3, this phenomenon (MT) increases the interfacial shear strength. Therefore, the martensitic transformation/ reorientation affects not only the debonding initiation but also the debonding propagation [Payandeh et al. 2010].

3.5. Conclusion

In the this chapter, the effect of martensitic transformation on the debonding initiation and propagation in single shape memory NiTi wire epoxy matrix composite was studied through an in-situ observation. The interfacial shear strength, τ_i, in NiTi wire epoxy matrix composite was estimated by coupling an analytical method and the experimental results.

From in-situ observations, the debonding starts from the wire entry point and proceeds to the embedded end along the interface until the entire wire is debonded.

It is proposed that the maximum interfacial shear stress (MISS) exhibits a linear variation as a function of applied stress: $\tau^F_{max} = \beta . \sigma_p$. The MISS reaches the τ_i, at the onset of debonding. The material parameter β has been calculated analytically for different wires on the basis of geometrical and mechanical characteristics of the wire and matrix.

From experimental data, the debonding stress for NiTi wire (in both martensitic and R phase) is significantly less than that for steel wire. The debonding stress for M550, M450, M400

SMA and steel wire/ epoxy systems are equal to 140, 160, 115 and 285 MPa, respectively. It has been shown that the debonding stress depends strongly on the wire's Young modulus.

According to experimental results, the interfacial shear strength is about 9 MPa when no phase transformation occurs (M400 SMA and steel wires); however, it is about 14 MPa when martensitic transformation/reorientation takes place in the wires (M550 and M450).

The present study is a contribution enabling investigation of the effect of MT on the debonding initiation in the SMA wire composites. It could be useful to estimate the interfacial shear strength for composites with long embedded wire length.

The wire phase transformation/reorientation in the embedded part can not occur before interfacial debonding, because the phase transformation/reorientation is accompanied by a large inelastic strain.

In both samples with M550 and M450 wires the martensitic reorientation/ transformation of the free part of wires occurs before that debonding begins. In M400 wire specimens, the martensitic transformation does not occur before the debonding onset.

The average debonding rate for the M550 samples varies between 8.3 and 9.3 mm/min for different specimens. In the case of M450 wire composite samples, the debonding propagates with an average rate that varies between 10.6 and 11.3 mm/min for different specimens. The debonding rate for a sample with M400 wire is different and varies between 14.4 and 17.3 mm/min.

In both samples with M550 and M450 wires the debonding propagates with a constant rate.

It could be claimed that the length changes during martensitic reorientation in M550 or martensitic transformation in M450 or sometimes in M400, is the sole reason of decreasing of the debonding rate. In the specimens with M400, because there is no phase transformation, the interface debonds fast.

The debonding rate depends on the displacement rate as well as the transformation strain. The equation $v_d = V_i / \varepsilon^{tr}$ was proposed to relate these three parameters.

References:

[Bannister et al. 1995] Bannister DJ, Andrews MC, Cervenka AJ, Young RJ. Analysis of the single-fibre pull-out test by means of Raman spectroscopy. Part II: Micromechanics of deformation for an aramid-epoxy system. Composites Science and Technology 1995; 53: 41l-421.

[Fu et al. 2000] Fu SY, Yue CY, Hu X, Mai YW. Analyses of the micromechanics of stress transfer in single- and multi-fibre pull-out tests. Composites Science and Technology 2000; 60: 569-579.

[Gao et al. 1999] Gao YC, Zhou LM. Energy release rate for interface debonding with prestress and friction. Theoretical and Applied Fracture Mechanics 1999; 32: 203-207.

[Hamada et al. 1998] Hamada K, Lee JH, Mizuuchi K, Taya M, Inoue K. Thermomechanical behaviour of TiNi shape memory wire reinforced 6061 aluminium matrix composite. Metallurgical and Materials Transactions A 1998; 29A: 1127 –1135.

[Jang and Kishi 2005] Jang BK, Kishi T. Adhesive strength between TiNi fibers embedded in CFRP composites. Materials Letters, 2005; 59, 11: 1338-1341.

[Liu and Xiang 1998] Liu Y, Xiang H. Apparent modulus of elasticity of near-equiatomic NiTi. Journal of Alloys and Compounds 1998; 270: 154–159.

[Neuking et al. 2008] Neuking K, Abu-Zarifa A, Eggeler G. Surface engineering of shape memory alloy/polymer-composites: Improvement of the adhesion between polymers and pseudoelastic shape memory alloys. Materials Science and Engineering A, 2008; 481-482: 606-611.

[Niemczura et al. 2006] Niemczura J, Ravi-Chandar K. Dynamics of propagating phase boundaries in NiTi. Journal of the Mechanics and Physics of Solids 2006; 54: 2136–2161.

[Ostachowicz et al. 2000] Ostachowicz W, Krawczuk M, Zak A. Dynamics and buckling of a multilayer composite plate with embedded SMA wires. Composite Structures 2000; 48: 163-167.

[Paine and Rogers 1993] Paine JSN., Rogers CA. Characterization of interfacial shear strength between SMA actuators and host composite material in adaptive composite material systems, in: Carman GP, Garcia E, editors, Adaptive Structures and Material Systems, New York: ASME; 1993; AD-35: 63-70.

[Payandeh et al. 2009] Payandeh Y., Meraghni F., Patoor E., Eberhardt A., Effect of Martensitic Transformation on the Debonding Propagation in NiTi Shape Memory Wire Composite, Materials Science and Engineering 2009; A 518: 35-40.

[Payandeh et al. 2010] Payandeh Y., Meraghni F., Patoor E., Eberhardt A., Debonding Initiation in NiTi Shape Memory Wire Composite, Influence of Martensitic Transformation, Materials and Design 2010; 31: 1077–1084.

[Piggott 1980] Piggott MR. Load Bearing Fibre composites. Canada: Pergamon International Library, 1980.

[Poon et al. 2004] Poon CK, Zhou LM, Yam LH. Size effect on the optimum actuation condition for SMA-composites. Composite Structures 2004; 66 (1-4): 503-511.

[Poon et al. 2005] Poon CK, Lau K, Zhou LM. Design of pull-out stresses for prestrained SMA wire/polymer hybrid composites. Composites Part B: Engineering 2005; 36, 1: 25-31.

[Rodriguez et al. 2007] Vazquez-Rodriguez JM, Herrera-Franco PJ, Gonza´lez-Chi PI. Analysis of the interface between a thermoplastic wire and a thermosetting matrix using photoelasticity. Composites Part A 2007; 38: 819-827.

[Rossi et al. 2008] Rossi S, Deflorian F, Pegoretti A, D'Orazio D, Gialanella S. Chemical and mechanical treatments to improve the surface properties of shape memory NiTi wires. Surface & Coatings Technology 2008; 202: 2214–2222.

[Sadrnezhaad et al. 2009] Sadrnezhaad SK, Hassanzadeh Nemati N, Bagheri R. Improved adhesion of NiTi wire to silicone matrix for smart composite medical applications. Materials & Design 2009; 30 (9): 3667-3672.

[Sadrnezhaad et al. 2009b] Sadrnezhaad SK, Hosseini SA. Fabrication of porous NiTi-shape memory alloy objects by partially hydrided titanium powder for biomedical applications. Materials & Design 2009; 30 (10): 4483-4487

[Sittner et al. 2006] Sittner P, Landa M, Luka´s P, Nova´k V. R-phase transformation phenomena in thermomechanically loaded NiTi polycrystals. Mechanics of Materials 2006; 38: 475–492.

[Smith et al. 2004] Smith NA, Antoun GG, Ellis AB, Crone WC. Improved adhesion between nickel–titanium shape memory alloy and a polymer matrix via silane coupling agents. Compos. Part A Appl. S. 2004; 35: 1307–1312.

[Wang and Hu 2005] Wang X, Hu G. Stress transfer for a SMA fibre pulled out from an elastic matrix and related bridging effect. Composites Part A 2005; 36: 1142–1151.

[Yue et al. 1995] Yue CY, Looi HC, Quek MY. Assessment of wire-matrix adhesion and interfacial properties using the pull-out test. Int J Adhesion and Adhesives 1995; 15: 73 -80.

[Zhou et al. 1992] Zhou LM, Kim JK, Mai YW. On the single fibre pull-out problem: effect of loading Method; Composites Science and Technology 1992, 45, 2: 153-160.

Chapter 4.

Tensile properties: characterization and micro-mechanical modeling- influence of martensitic transformation

4. 1. Introduction

4. 2. Experimental results

4. 3. Micromechanical analysis

4.3.1. Model development

4.3.2. Numerical results

4.4. Discussion

4.4.1. Comparison of micromechanical and experimental results

4.4.2. Effect of martensitic transformation on the mechanical behavior of composite

4.4.3. Effect of martensitic transformation on the debonding mechanism

4.5. Conclusion

References

4. 1. Introduction

The SMA fibers are used to strengthen the matrix, to absorb strain energy and reduce the residual stress and thereby improve the creep or crack resistance by stress-induced martensitic transformations. The embedded SMA fibers are also used to improve the damping capacity, increase the impact damage resistance, giving rise to the stiffness, vibration frequency and amplitude, acoustic transmission or shape of the composite. Acoustic radiation and transmission control of SMA hybrid composite have been also investigated in some works. Shape memory alloy composites have been shown both by analytical simulations and experiments to be effective adaptive materials for active vibration and structural acoustics control.

A large numbers of SMA composite materials have been studied by researchers. The metallic matrices such as Al and Sn were used as well as the polymeric ones. Various kinds of smart hybrid composites can be designed by incorporating shape-memory material components with composite materials.

For shape memory material components, a well-bonded interface will constrain the martensitic transformations and hence sacrifice the shape-memory effect and other performance. However, the stress can not be transferred to the fiber if the interface is weak. Therefore, a compromise should be reached to achieve optimal overall performance of the composite system [Wei et al. 1998]. Moreover, under the constraint of a matrix, the embedded SMA fibers will demonstrate a different transformation behavior to that in the free condition [Zheng et al. 2000]. A hard constraint between matrix (e.g. Al) and the embedded TiNi fiber, leads to a widened transformation span with a slow transformation rate by the martensite deformation process. However, a weak constraint of matrix (e.g. resin) yields a relatively easy transformation, if there is a good interfacial bond [Li et al. 2001].

There are numerous systems consisting of an epoxy matrix in which SMA elements in the form of wires, ribbons or strips have been incorporated [Bollas et al. 2007] [Lau et al. 2002b] [Lau et al. 2002c] [Lau et al. 2002d] [Shimamoto and Taya 1997]. The integrity of the SMA–epoxy resin interface, the integrated SMA displacements, the development of stress contours along the SMA and the host deformation are some of the parameters that have been studied [Jonnalagadda et al. 1997], [Jonnalagadda et al. 1998], [Yamashita and Shimamoto 2004] and [Murusawa et al. 2004].

The reverse martensitic transformation characteristics of pre-strained TiNi shape memory alloy fibers embedded in an epoxy matrix were studied by Li et al. [Li et al. 2001] using differential scanning calorimeter (DSC) measurements. Bidaux et al. [Bidaux et al. 1997] used NiTi fibers to actively change the stiffness of an epoxy matrix composite beam. The constrained thermoelastic martensitic transformation of TiNiCu wires embedded in an epoxy matrix was studied by modulated differential scanning calorimetry (MDSC) [Zheng et al.

2003]. Marfia and Sacco developed a micromechanical model for the evaluation of the overall constitutive behavior of a composite material obtained embedding NiTi wires into an epoxy matrix [Marfia and Sacco 2005]. Zheng et al. [Zheng et al. 2005b] have studied the actuating ability and reliability of NiTiCu/epoxy matrix composites. The results showed that by selecting small hysteresis SMAs as NiTiCu alloys, SMA hybrid composites have a linear stress-temperature behavior, which is relatively easy to control. The mechanical properties of epoxy resin composites filled with NiTi alloy short fibers and particles under bending have been investigated by Zhang and co-workers [Zhang et al. 2007]. From their results, the flexural rigidity of SMA/epoxy composites increases owing to the addition of SMA fillers. They showed that the addition of 3.5% of NiTi fillers to epoxy resin resulted in a remarkable increment of storage modulus, which is six times as large as that of epoxy bulk [Zhang et al. 2007].

Shimamoto et al. [Shimamoto et al. 2004] developed a design concept consisting of TiNi/ epoxy that improves the material strength. Ju and Shimamoto [Ju and Shimamoto 1999] embedded TiNi fibers to an epoxy matrix in order to improve the damping capacity of a beam in free vibration. The analytical and measured results illustrate the effects of current on the damping and frequency values [Ju and Shimamoto 1999].

In general, for SMA composite pre-strained fibers were embedded into a matrix. System activation generates the stress in matrix which opposing the applied load and improves the damping and mechanical properties of SMA composite. However, by incorporating pre-strained wires it is not possible to study *independently* the martensitic transformation and its effect on the overall behavior of composite. In this work, NiTi wires were embedded without pre-strain to investigate the martensitic transformation.

In this chapter, the mechanical behavior of the NiTi-epoxy composites is investigated using the standard tensile test. Specimens elaborated using three different types of wire (M400, M450 and M550) were tested. Three wire volume fractions (0, 6, and 12%) and three tensile test temperatures (20, 80 and 90 °C) were investigated.

In order to interpret the role of SMA wire in the composite, in more details, a micromechanical model is developed on the basis of Piggott's model [Piggott 1980]. This model helps to understand the influence of the martensitic transformation on the global behavior of the composite specimens at different temperatures. As Piggott's model was developed for elastic composites several modifications should be done. The interfacial shear strengths obtained experimentally (chapter 3) were introduced in this model. Furthermore, the non linear behavior of matrix and SMA wires were taken into account by considering their experimental behaviors in model development. The micromechanical results have been compared with the experimental ones and discussed in the last section of this chapter.

4.2. Experimental results for standard tensile test

The stress-strain responses of the three wires considered in this study were presented in chapter 2. According to table 2.1, M550 wires are martensitic at room temperature (about 20 °C). In M400 and M450 wires, the stable phase is the R-phase at room temperature. Thus, by applying an external stress, the martensitic reorientation occurs in M550 whilst in M450 and M400, the reorientation of the R-phase occurs firstly and then stress-induced martensitic transformation takes place. At high temperature (80 and 90 °C), the martensitic transformation takes place in all three wires because the test temperature is higher than A_f. As mentioned before, only M400 and M450 wires exhibit a superelastic behavior at high temperature. However, there is no superelastic behavior for M550 wire at high temperature. In this section the thermo-mechanical behavior of the composite samples is presented. As could be noticed on Fig. 4.1, this behavior is rather brittle with ultimate strain varying from 2 to 6%. Due to this brittleness, many samples broke before any useful data can be obtained which results to reduce the size of our database.

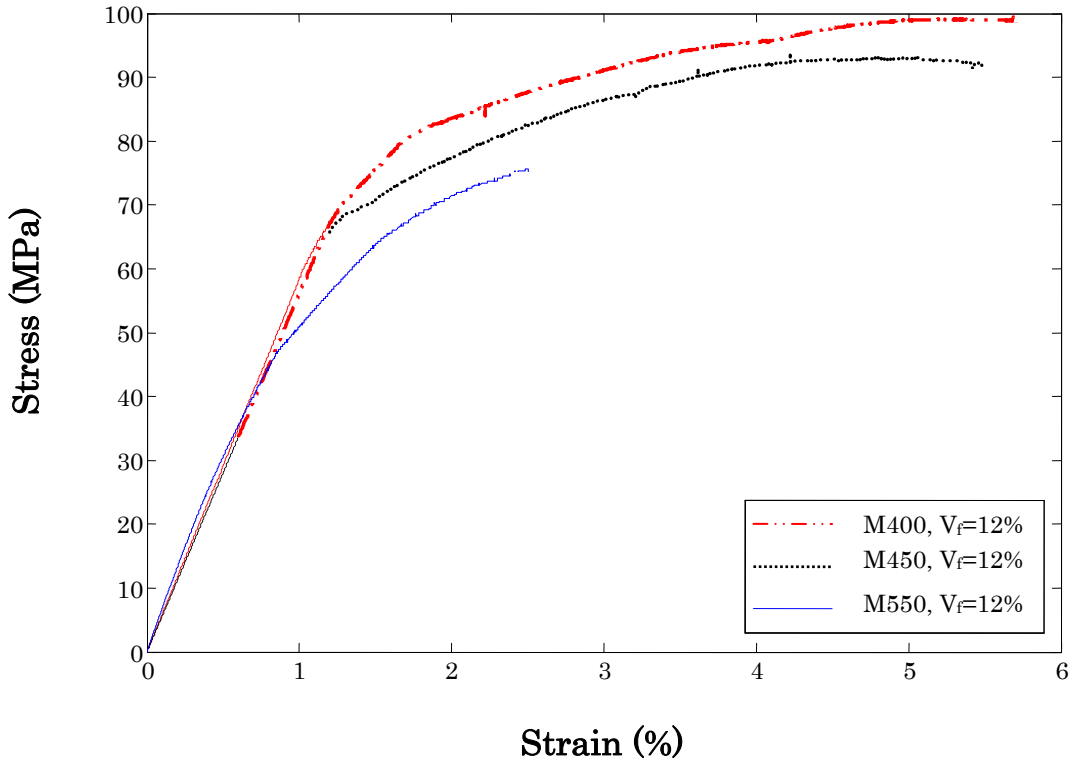

Fig. 4.1 Stress -Strain diagram for the composite samples with V_f =12% at 90 °C for three different wires.

The behavior of the composite materials elaborated using three different wires shows to be strongly affected by the wire characteristics (Fig. 4.1 and 4.2). These figures show that the wires who have the phase transformation under higher stress, improve mechanical properties

(tensile strength) of the composite specimens. In other words, by using a wire with higher transformation stress, the tensile strength of the composite samples increases which indicate the influence of the martensitic transformation on the overall behavior of the composite.

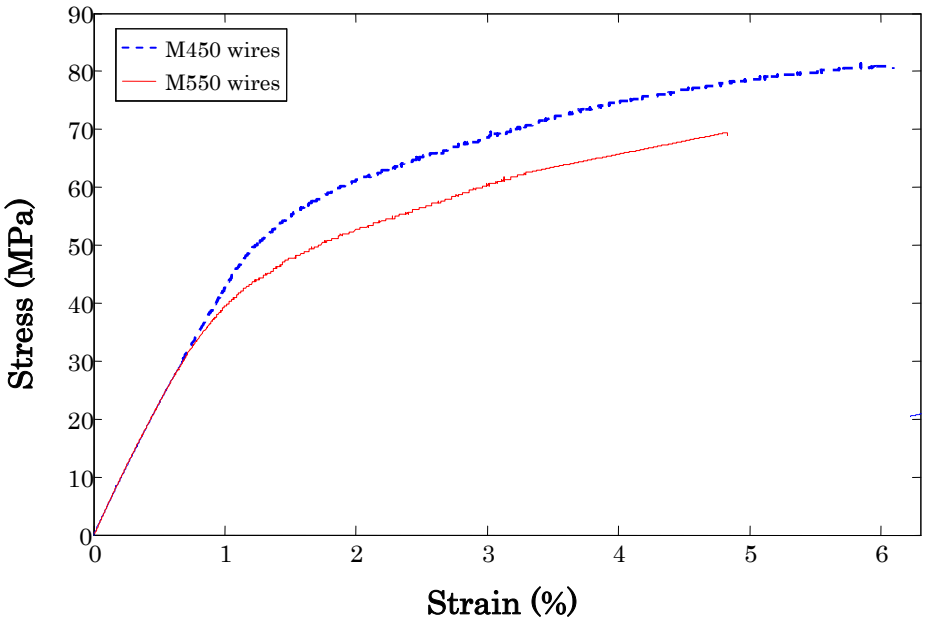

Fig. 4.2. Stress -Strain diagram for the composite samples with V_f=6% at 80 °C for two different wires.

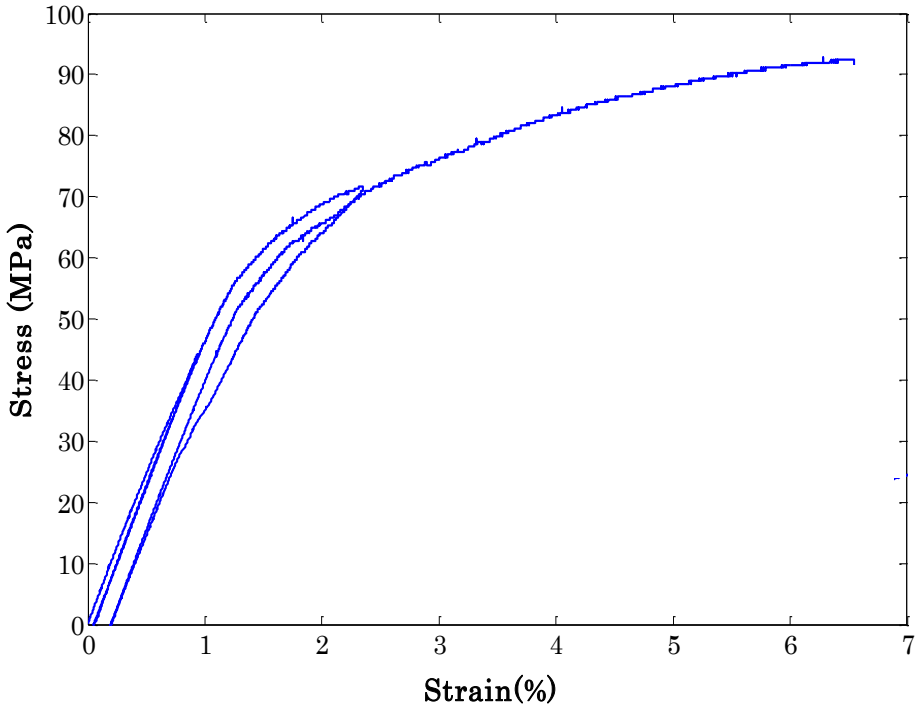

Fig. 4.3- Stress -Strain diagram for the composite samples with M450 wire, at 80 °C and with V_f=6%.

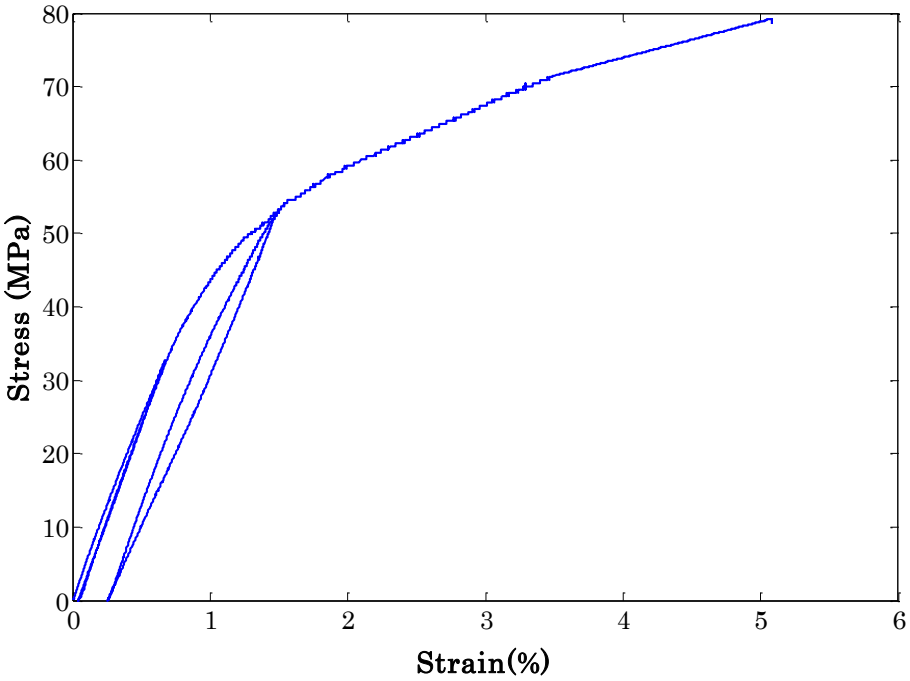

Fig. 4.4- Stress -Strain diagram for the composite samples with M550 wire, at 80 °C and with V_f=6%.

Fig. 4.3 – 4.4 show some representative results with loading-unloading curves at 80 °C. As shown in Fig. 4.3 the M450 wire composite sample exhibits the superelastic effect while the M550 wire specimens do not show this effect (Fig. 4.4).

As discussed in chapter 2, the transformation stresses (i.e. stresses at which the martensite reorientation/transformation occurs) increase when the test temperature increases. However, the tensile strength of the epoxy matrix decreases with increasing the temperature. Therefore, the mechanical behavior of the composite will be a compromise between these two factors depending on the test temperature and wire volume fraction.

The effect of wire volume fraction at 80 °C is shown in Fig. 4.5. As expected, the tensile strength of the composite increases with increasing the wire volume fraction.

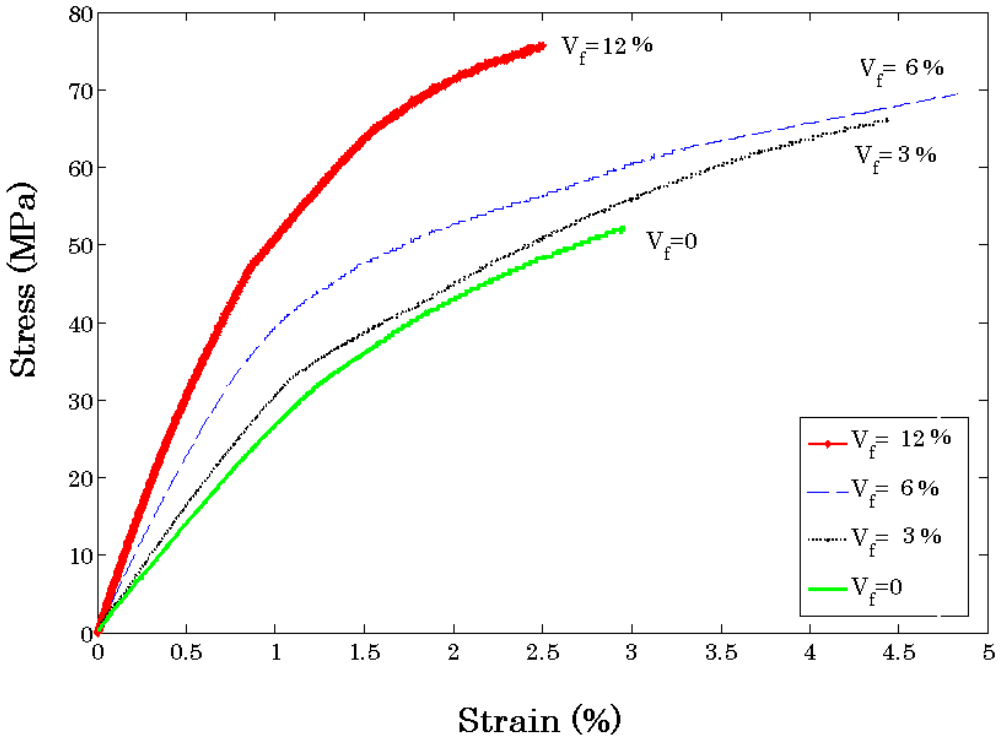

Fig. 4.5. Stress -Strain diagram for the composite samples with M550 wire at 80 °C for different wire volume fractions.

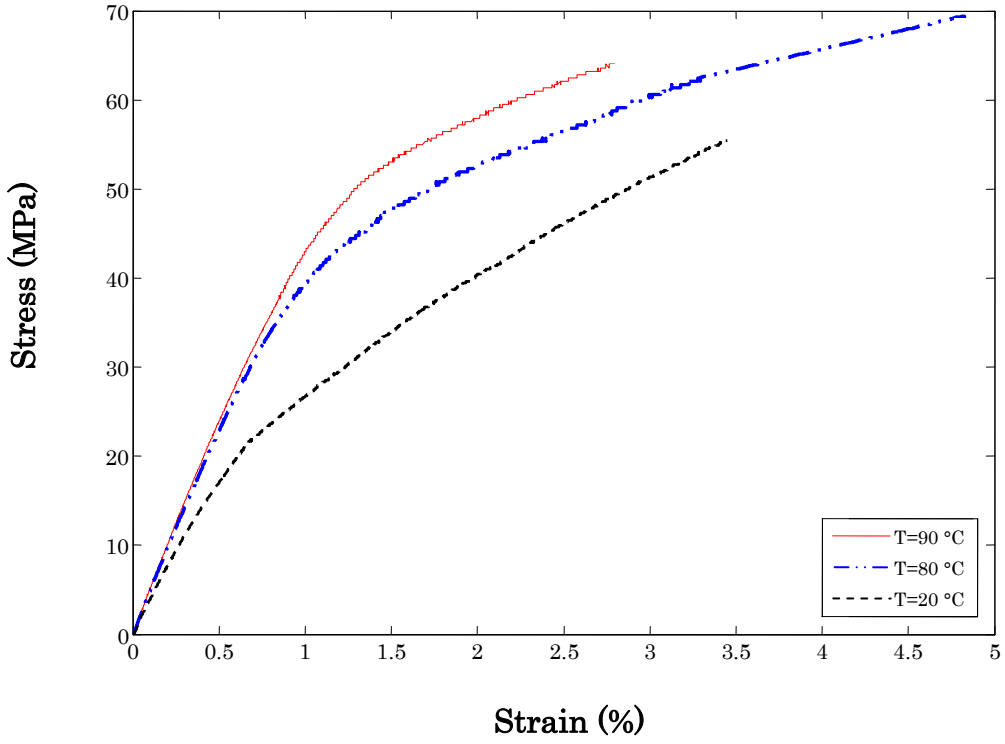

Fig. 4.6. Stress -Strain diagram for the composite samples with M550 wire with V_f=6%, at different temperatures.

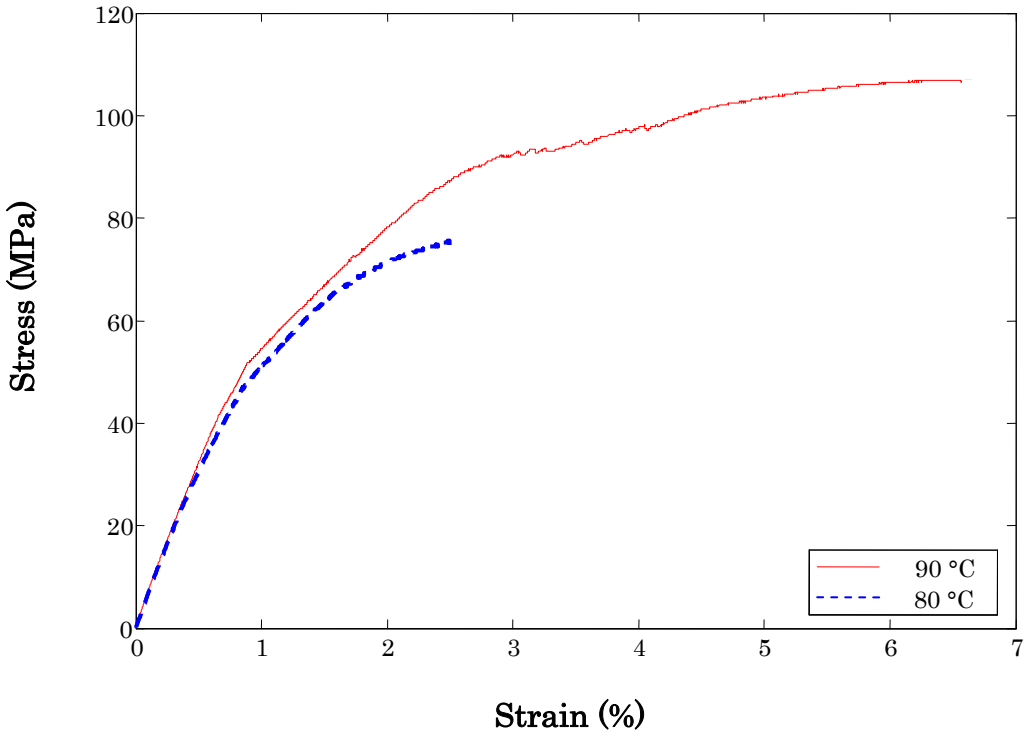

Fig. 4.7. Stress -Strain diagram for the composite samples with M550 wire with V_f=12%, at different temperatures.

Fig. 4.6 illustrates the effect of test temperature on the mechanical behavior of the M550 wire composite with 6% wire volume fraction. The elastic modulus of the composite samples increases slightly with temperature whilst an important enhancement in tensile strength is observable. This effect is also shown in Fig. 4.7 for the M550 wire composite with 12% volume fraction. It was shown in chapter 2 that with increasing the temperature the wire phase transformation takes place at higher stress. Therefore, the increase in tensile strength could be related to the martensitic reorientation/transformation occurring in the wires.

Table 4.1. Young modulus and stress at 2% strain for M550 wire composites at different temperatures

Volume fraction (V_f)	T = 20 °C		T = 80 °C		T = 90 °C	
	Young's modulus (MPa)	ε=2 (%) σ (MPa)	Young's modulus (MPa)	ε=2 (%) σ (MPa)	Young's modulus (MPa)	ε=2 (%) σ (MPa)
0	3300	50	2800	44	2700	42
6%	4200	40	4600	53	5000	58
12%	5300	52	6750	72	7300	78

The experimental behaviors of some composite samples were shown in Fig.4.3-4.4 as some representative results. The effects of wire volume fraction, test temperature and type of wire were presented as well. Table 4.1 lists some parameters such as Young modulus of the composite samples with three volume fractions at different temperatures. The strength of the specimens in a given strain (2%) is mentioned as well. It should be noted that this parameter can be used as a benchmark to compare the ultimate tensile strength of all samples in different conditions.

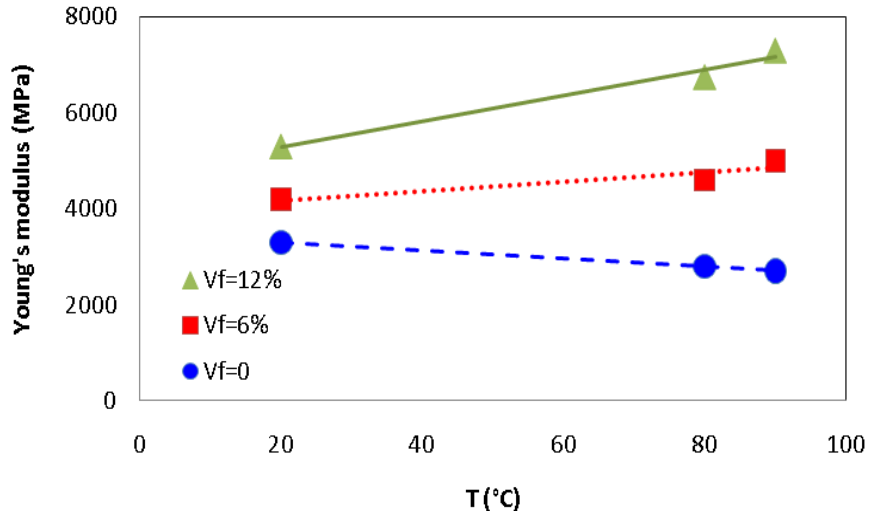

Fig. 4.8. Young modulus vs. temperature for three volume fractions (M550 wire samples)

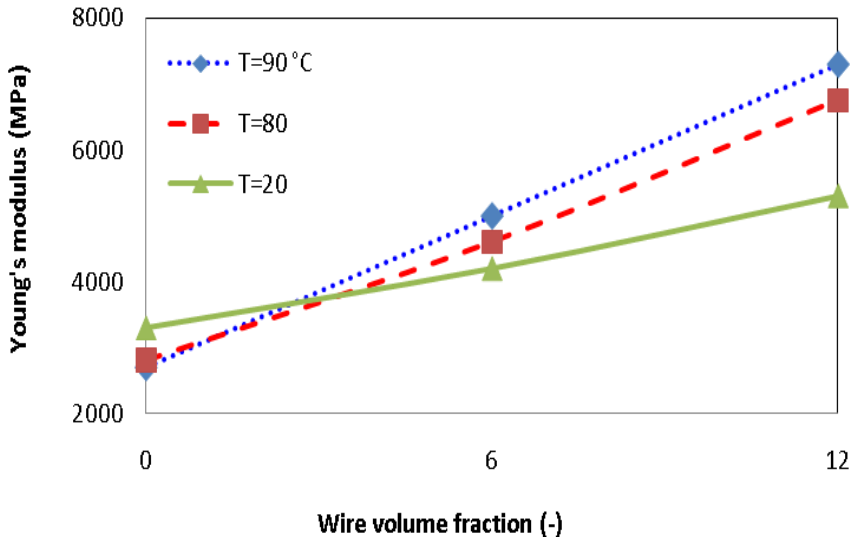

Fig. 4.9. Young modulus vs. volume fraction for three temperatures (M550 wire samples)

Fig. 4.8 shows the Young modulus as a function of temperature for 0, 6 and 12% volume fractions. The elastic modulus for the matrix (V_f=0) decreases with temperature whilst it increases slightly for the composite samples. The evolution of the Young modulus is more

visible when the volume fraction increases (Fig. 4.9). The same trends exist for the tensile strength which indicates the influence of wires on the overall behavior of the composites. As shown in Fig. 4.10 and 4.11, the tensile strengths increase with increasing the test temperature or volume fraction. The temperature effect is more evident for the larger volume fraction. In fact, increasing the volume fraction leads the drop of the matrix strength at higher temperature to be compensated more easily because of higher number of wire in the samples.

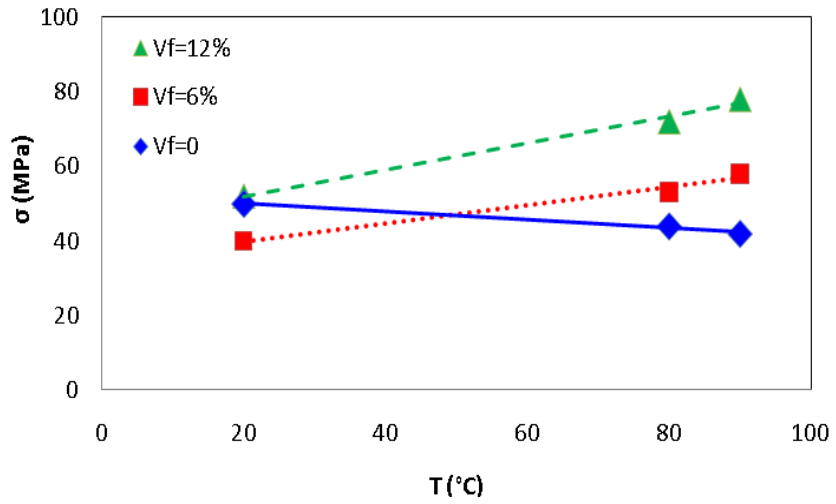

Fig. 4.10. Tensile strength (at ε =2%) vs. temperature for three volume fractions (M550 wire samples)

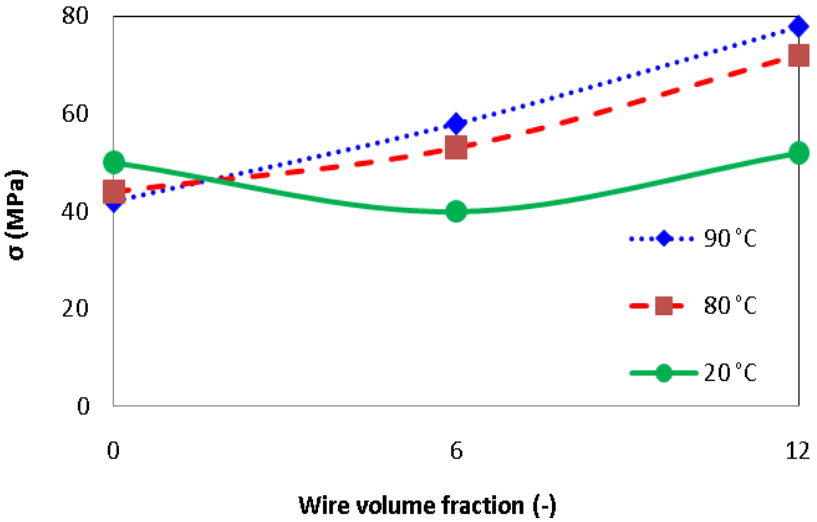

Fig. 4.11. Tensile strength (at ε =2%) vs. volume fraction for three temperatures (M550 wire samples)

The increase in tensile strength could be related to the martensitic transformation occurring in the wires. As discussed earlier, with increasing the temperature the wire phase transformation shifts to higher stress which results to increase the tensile strength of composite samples. Therefore, a larger strength could be expected by replacing the M550 wires by M450 or M400

due to the higher transformation stresses. Table 4.2 illustrates that composite specimens with M400 have larger strength that M450 or M550. Fig. 4.12 shows the tensile strength at 90 °C for three wires. As a result, by incorporating the wires in which the martensitic transformation takes place in higher stress, the tensile strength of composite increases. The same result is obtained by a temperature rise which increases the transformation stress.

Table 4. 2. Tensile strength at 2% strain for composites with different wires at 90 °C

Wire	V_f = 6%	V_f = 12%
	σ (MPa)	σ (MPa)
M550	58	72
M450	66	78
M400	-	84

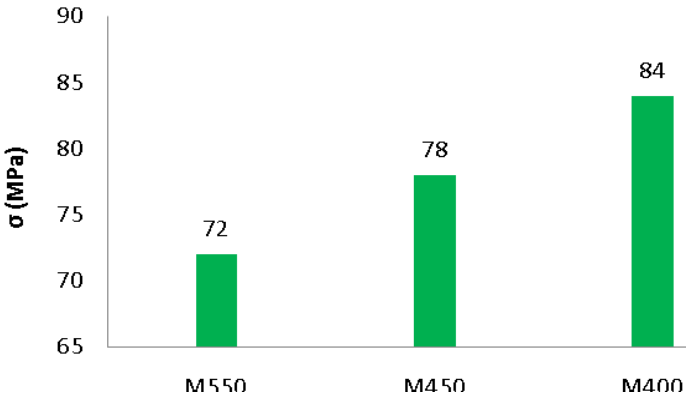

Fig. 4.12. Tensile strength (at ε =2%) for samples with three wires (V_f=12%) at 90 °C

From above discussion, the martensitic transformation occurring in the wire plays an important role in the composite properties.

More results are presented in appendix A (Fig. A.1 – A.6).

These different results establish that the behavior of NiTi/epoxy composite is strongly dependent to the martensitic transformation occurring within the wires. In order to interpret the role of wire phase transformation on the overall behavior of the composite, a micromechanical model was developed on the basis of the Piggott's model [Piggott 1980].

4.3. Micromechanical analysis

4.3.1. Model development

Cox [Cox 1952] proposed a micromechanical model for reinforced material with perfect interface. Piggott [Piggott 1980] has extended this model for weak interface with or without adhesion. Piggott considered that in polymeric matrix composites the interface is imperfect. He assumed that both wire and matrix behave elastically, and that the interface transfers the stress from wires to matrix. The matrix tensile strain, ε_m, is assumed to be equal to the composite tensile strain, ε_1. Fiber-fiber interactions are neglected in this approach. In these conditions the wire normal and shear stresses distribution are given as [Piggott 1980]:

$$\sigma_f = E_f \varepsilon_1 + B \sinh\left(\frac{nx}{a}\right) + D \cosh\left(\frac{nx}{a}\right) \quad (4\text{-}1)$$

$$\tau_f = -\frac{a}{2}\frac{d\sigma_f}{dx} \quad (4\text{-}2)$$

where B and D denote constants determined from the boundary conditions. Parameter *n* is defined as:

$$n = \sqrt{\frac{E_m}{E_f (1+\nu_m) \ln\left(R/a\right)}} \quad (4\text{-}3)$$

E_f and E_m are the Young modulus of wire and matrix, respectively. ν_m is the matrix Poisson ratio, R is the distance between two next wires, *a* is the radius of the wire and *x* is the position along the embedded wire.

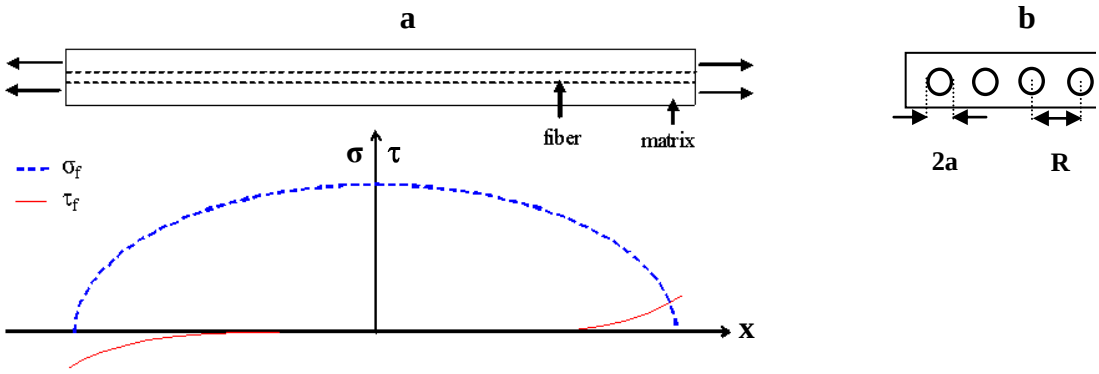

Fig. 4-13. Axial and shear stress distribution along an embedded wire

Assuming that no stress is transferred across the wire ends, $\sigma_f=0$ at $x=L$ and $x=-L$. therefore, the wire axial stress and the surface shear stress are given by:

$$\sigma_f = E_f \varepsilon_1 \left(1 - \frac{\cosh\left(\frac{nx}{a}\right)}{\cosh(ns)}\right) \tag{4-4}$$

$$\tau_f = \frac{1}{2} n E_f \varepsilon_1 \frac{\sinh\left(\frac{nx}{a}\right)}{\cosh(ns)} \tag{4-5}$$

s denotes the wire aspect ratio and equals to *L*/*a*. Fig. 4-13 shows the axial and shear stress distribution along the wire. Using the rule of mixture, the stress-strain relationship for the composite in the longitudinal direction is given by:

$$\sigma_1 = \left(V_f E_f \left(1 - \frac{\tanh(ns)}{ns}\right) + V_m E_m \right) \varepsilon_1 \tag{4-6}$$

where V_f and V_m are the volume fraction of the wire and matrix, respectively.

Sliding will occur between wires and matrix when the interfacial shear stress reaches a critical value. This will take place at wire ends, where the shear stress is maximum. For non-broken interface, stress distribution in the slip regions will be replaced by a constant shear stress equals to the shear yield stress of the matrix, τ_{my}. Due to the geometric and loading symmetry, the slip occurs over a length *mL* at both ends of wire (Fig. 4-14), where *m* is a dimensionless parameter that depends on the applied stress. For the center region, the boundary conditions are expressed as:

$$\sigma_f = \sigma_{fi} \quad \text{at} \quad x = \pm L(1-m) \tag{4-7}$$

where σ_{fi} is the stress transferred to the wire in the slip region [Pigott 1980]. For the center region

$$\sigma_{fc} = E_f \varepsilon_1 + (\sigma_{fi} - E_f \varepsilon_1) \frac{\cosh\left(\frac{nx}{a}\right)}{\cosh(n\bar{s})} \tag{4-8}$$

$$\tau_{fc} = \tau_{my} \frac{\sinh\left(\frac{nx}{a}\right)}{\cosh(ns)} \tag{4-9}$$

and in the slip regions:

$$\sigma_{fe} = 2\tau_{my} \frac{l - x}{a} \tag{4-10}$$

$$\tau_e = \tau_{my} \tag{4-11}$$

$$\sigma_{fi} = E_f \varepsilon_1 - 2\tau_{my} \frac{\coth(n\bar{s})}{n} \tag{4-12}$$

$$m = \frac{E_f \varepsilon_1}{2s\tau_{my}} - \frac{\coth(n\bar{s})}{ns} \tag{4-13}$$

This relationship allows determining the size of the debonded region with respect to the loading conditions and material and geometrical parameters.

$$\bar{s} = s(1-m) \tag{4-14}$$

In this case the stress-strain relationship for the composite is given by:

$$\sigma_1 \approx (V_f E_f + V_m E_m)\varepsilon_1 - \frac{V_f}{s}\left(\frac{\tau_{my}}{n^2} + \frac{E_f^2 \varepsilon_1^2}{4\tau_{my}}\right) \tag{4-15}$$

For broken interface, frictional slip takes place between wires and matrix, and a non-dimensional parameter, α, is introduced which is smaller than unity. At the slip point the τ^{max} now equates with $\alpha\tau_{my}$ rather than τ_{my} [Piggott 1980]. Therefore

$$\sigma_1 \approx (V_f E_f + V_m E_m)\varepsilon_1 - \frac{V_f}{s}\left(\frac{\alpha\tau_{my}}{n^2} + \frac{E_f^2 \varepsilon_1^2}{4\alpha\tau_{my}}\right) \tag{4-16}$$

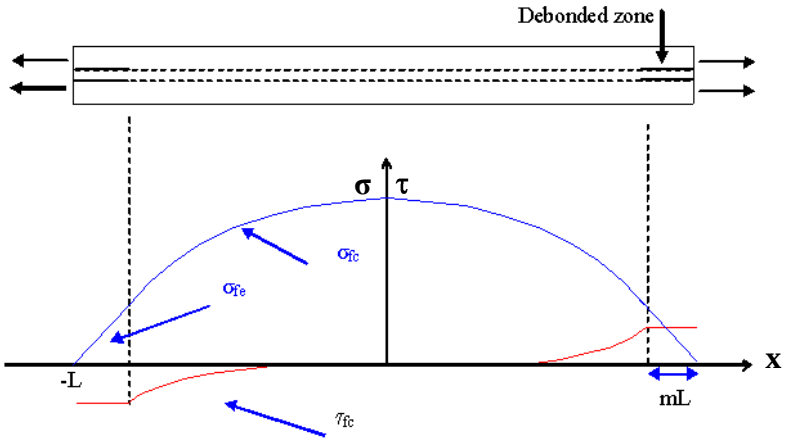

Fig. 4-14. Axial and shear stress distribution along an embedded wire

Application of this model to the NiTi composite samples

In order to apply this model to the real composite specimen used in this work, some modifications are required.

- ***Using the interfacial shear strength τ_i***

In chapter 3, the interfacial shear strength τ_i, has been determined. Thus, $\alpha\tau_{my}$ should be replaced by τ_i in equation 4-16. The following changes must be applied:

$$m = \frac{E_f \varepsilon_1}{2s\tau_i} - \frac{coth(\bar{n}s)}{ns} \tag{4-17}$$

From this equation, two cases can be considered. No debonding occurs when *m* is equal to zero, and two debonded zones (at both ends of wire) are observable when *m* is positive. In this case, with increasing the applied strain, the parameter *m* increases.

If *m*=0

In this case, the stress is transferred along all the length of wire. The wire shear and axial stress is directly obtained from equation 4-4 and 4-5 respectively. The composite normal stress can be calculated as follows:

$$\sigma_1 = V_m E_m \varepsilon_1 + \frac{V_f}{l}\int_0^l \sigma_f dx \tag{4-18}$$

If *m*>0

In undebonded region:

The axial and shear stress in the wire are now expressed as:

$$\sigma_{fe} = E_f \varepsilon_1 - \left(\frac{2\tau_i}{n\,sinh(\bar{n}s)}\right) cosh(\frac{nx}{a}) \tag{4-19}$$

$$\tau_{fe} = \tau_i \frac{sinh(\frac{nx}{a})}{sinh(\bar{n}s)} \tag{4-20}$$

In debonded region:

$$\sigma_{fc} = \left(\frac{E_f \varepsilon_1}{m} - \frac{2\tau_i}{nm} coth(\bar{n}s)\right)(1 - \frac{x}{l}) \tag{4-21}$$

$$\tau_{fc} = \tau_i \tag{4-22}$$

The composite normal stress can be determined using the following equation:

$$\sigma_1 = \frac{V_f}{l}\left(\int_0^{l(1-m)} \sigma_{fc}\,dx + \int_{l(1-m)}^{l} \sigma_{fe}\,dx\right) + V_m E_m \varepsilon_1 \qquad (4\text{-}23)$$

At each time increment, the strain value, ε_1, is known and the parameter *m* can be calculated. Depending on the *m* value, the composite normal stress will be determined using equation 4-18 or 4-23. The parameter *m* plays an important role in the model and can be considered as a normalized debonded length (L_d). For example, when *m* equals to 0.1, it means that debonded length is equal to10% of the embedded length.

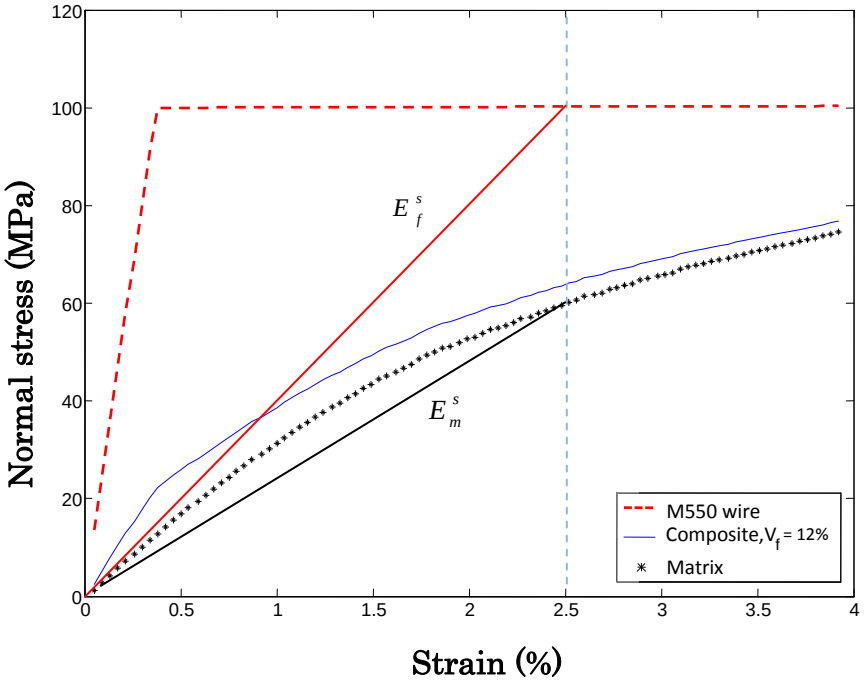

Fig. 4-15. Stress-strain behavior of the matrix, wire and composite at 20 °C

- ***Considering the non linear behavior***

Piggott's model was developed for elastic fiber and matrix. In the present study, both have a non linear behavior. The model must be modified to take into account these non linearities. As we consider only the loading case (no unloading) we will use a secant approach. The Young modulus for wire and matrix in the model has been replaced by the respective secant modulus. Using the secant modulus makes it possible to take into account the martensitic transformation occurring in the NiTi wires. In fact, the model considers only the elastic properties for the constituents whilst using the sequent modulus leads to extract the mechanical behavior of SMA composite in the conditions in which the wire transformation takes place. Moreover, the non linear behavior of the epoxy matrix will be brought into

consideration. In these circumstances the overall behavior of composite with different wires, wire volume fractions and at various test temperatures will be determined using the experimental stress-strain curves of the wires and matrix.

In Fig. 4.15 the stress-strain behavior of composite obtained using this approach is presented in relation with wire and matrix behaviors. Secant modulus for wire and matrix in ε_1=2.5% are shown in this figure.

4.3.2. Numerical results

The micromechanical results were shown in detail in Appendix A (figures A.7-A.15). Fig. 4.16-4.18 show respectively the effect of type of wire, test temperature and wire volume fraction on the mechanical behavior of the composite as some representative examples. In the next section, these results have been compared with the experimental ones.

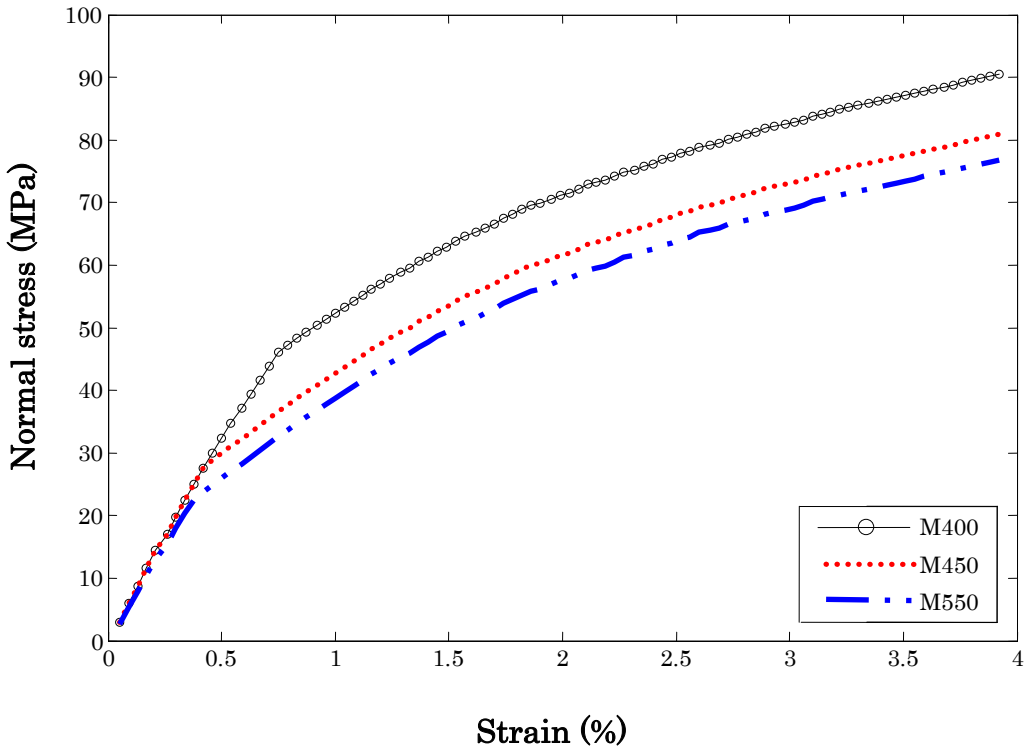

Fig. 4.16. Stress -Strain diagram for the composite samples with different wires at 20°C for V_f=12%.

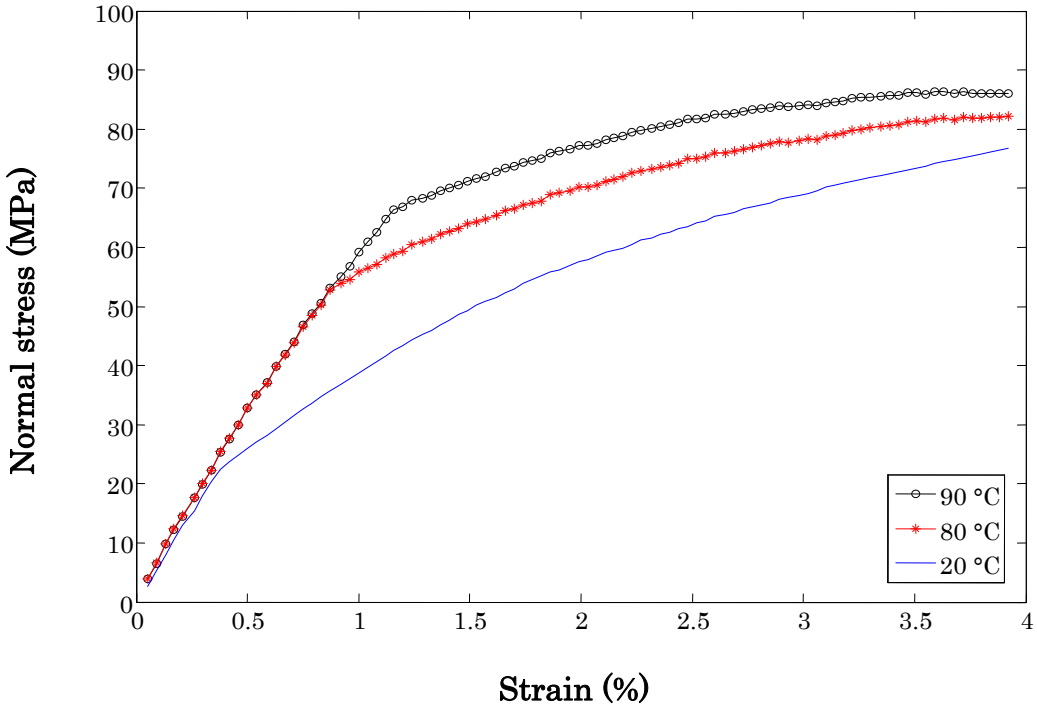

Fig. 4.17- Stress -Strain diagram of composite samples with M550 wire V_f=12% at three temperatures.

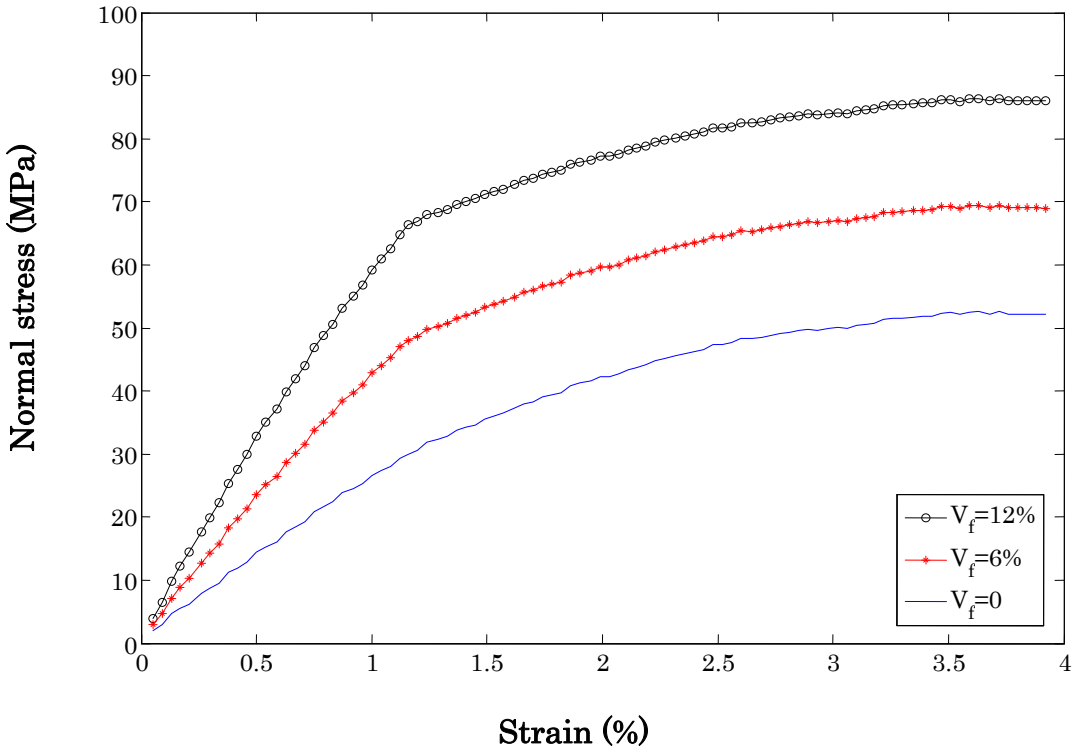

Fig. 4.18- Stress -Strain diagram for the composite samples with M550 wire at 90°C for three V_f.

4.4. Discussion

4.4.1. Comparison of the micromechanical and experimental results

The micromechanical results have been compared to the experimental ones (Fig. 4.19- 4.25). These figures show a relatively good correlation between the results. However, the numerical curves are always the upper ones. The following points should be considered when the numerical results are compared to the experimental ones.

As discussed in chapter 3, once the maximum interfacial stress reaches the interfacial shear strength, the debonding begins. The interfacial shear strength, τ_i, for these specimens might be different from that of the pull out samples. It should be noted that, in the pull out test the residual stress acts at the direction of applied stress which leads the interfacial debonding to begin sooner. But in the composite samples, the residual stress can delay the debonding to the higher values of applied stress. Moreover, the loading conditions are different in these tests. Therefore, using the τ_i for tensile test could be a source of error.

According to the experimental observation, the bedonding happens in the middle part of samples but from the model it is expected the debonding to occur at the wire ends. Moreover, reduction of the wire diameter due to the martensitic transformation has not been taken into account by the model.

The difference between the micromechanical and experimental results could be due to residual stress between wires and matrix and also between metallic mould and the matrix during curing process. It is known that the thermal expansion coefficient of these materials is different.

The transformation stress for the wire embedded in the matrix might be different with the case in which the wire transforms freely. Moreover, the martensitic transformation in a SMA wire starts in a point and propagates to the neighbor points, but when the wire is constrained by the surrounding matrix the transformation could start in several points at the same time (see section 4.4.3 for more details).

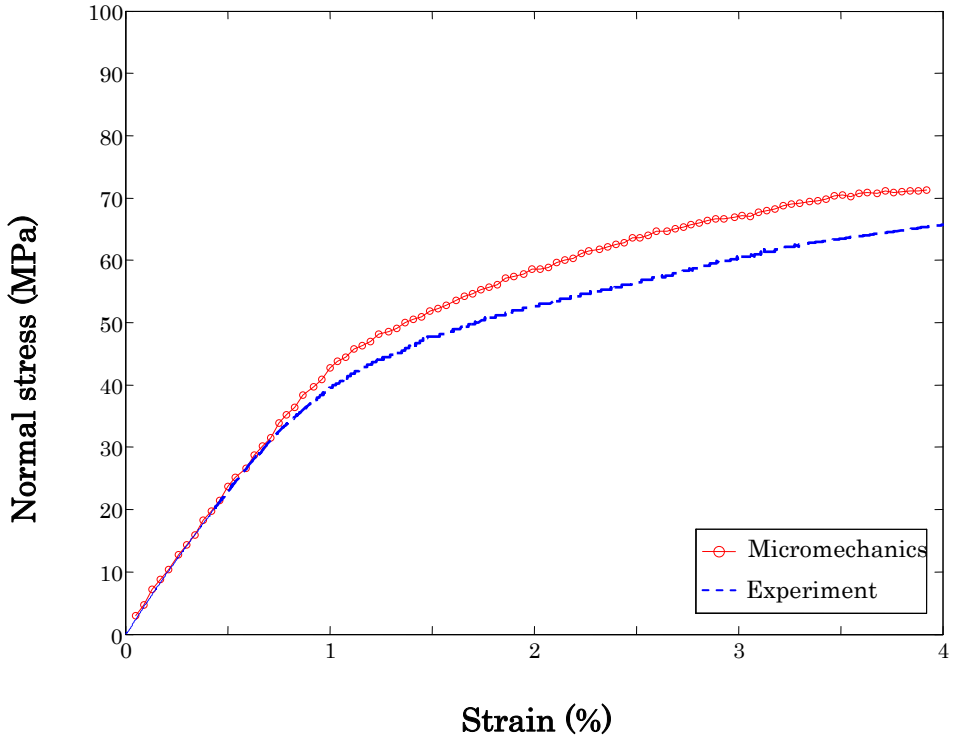

Fig. 4.19. Mechanical behavior of the M550 wire composite for V_f=6% at 80 °C

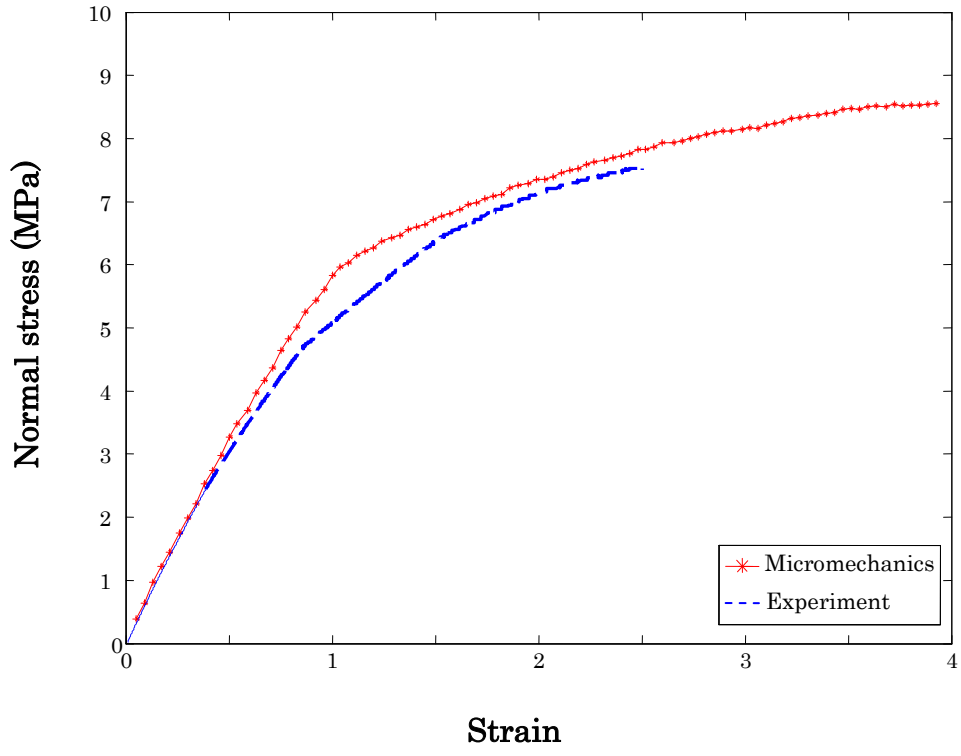

Fig. 4.20. Mechanical behavior of the M550 wire composite for V_f=12% at 80 °C

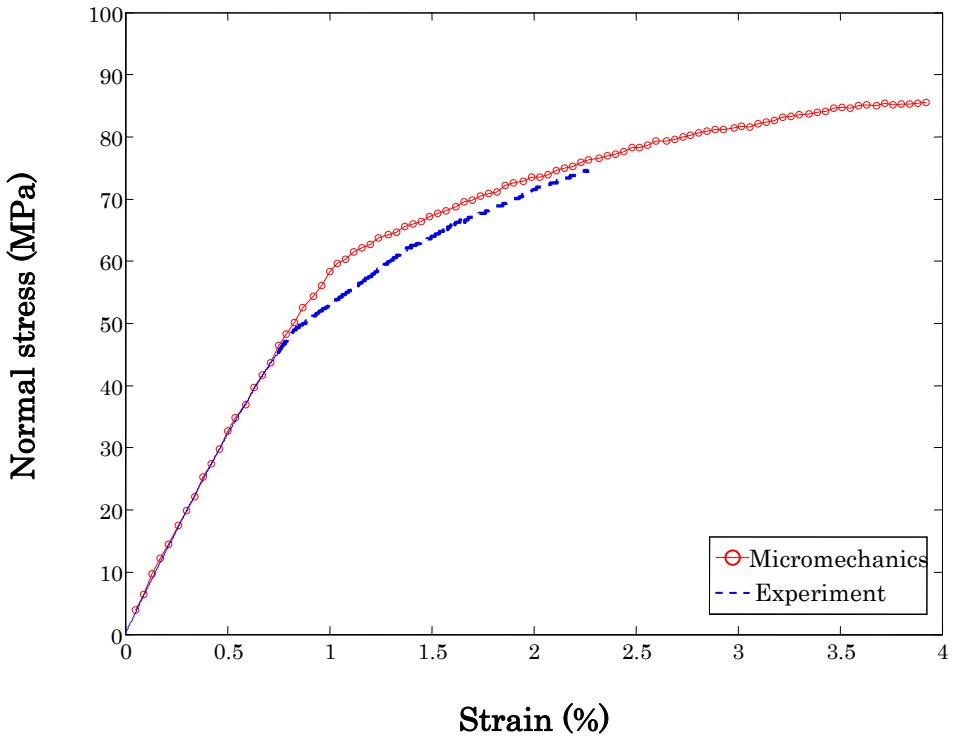

Fig. 4.21. Mechanical behavior of the M550 wire composite for V_f=12% at 80 °C

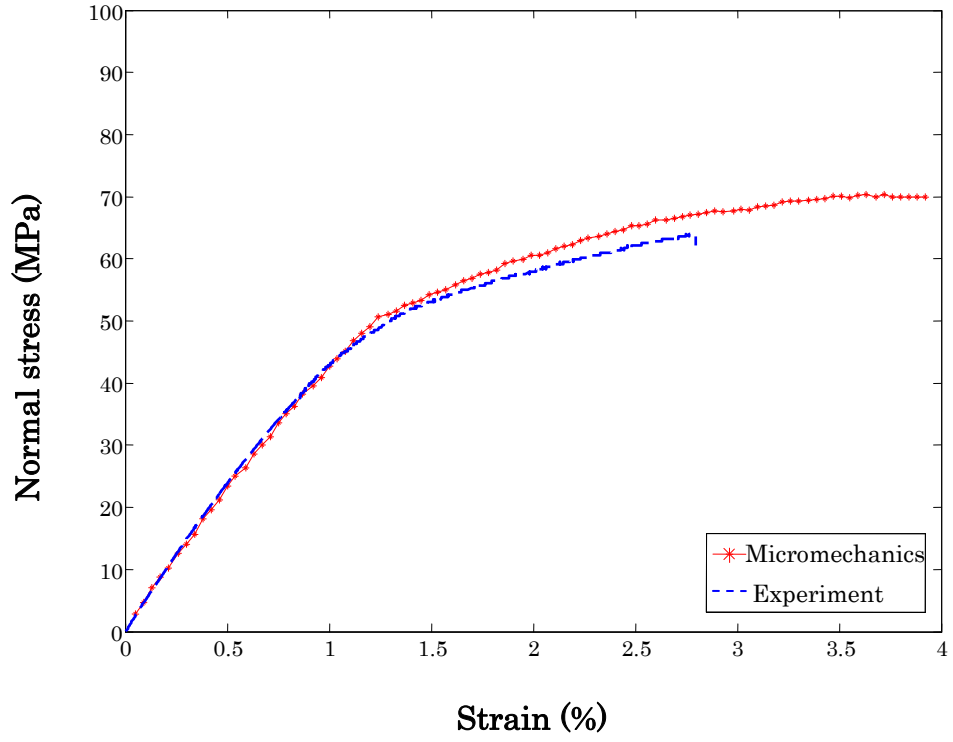

Fig. 4.22. Mechanical behavior of the M550 wire composite for V_f=6% at 90 °C

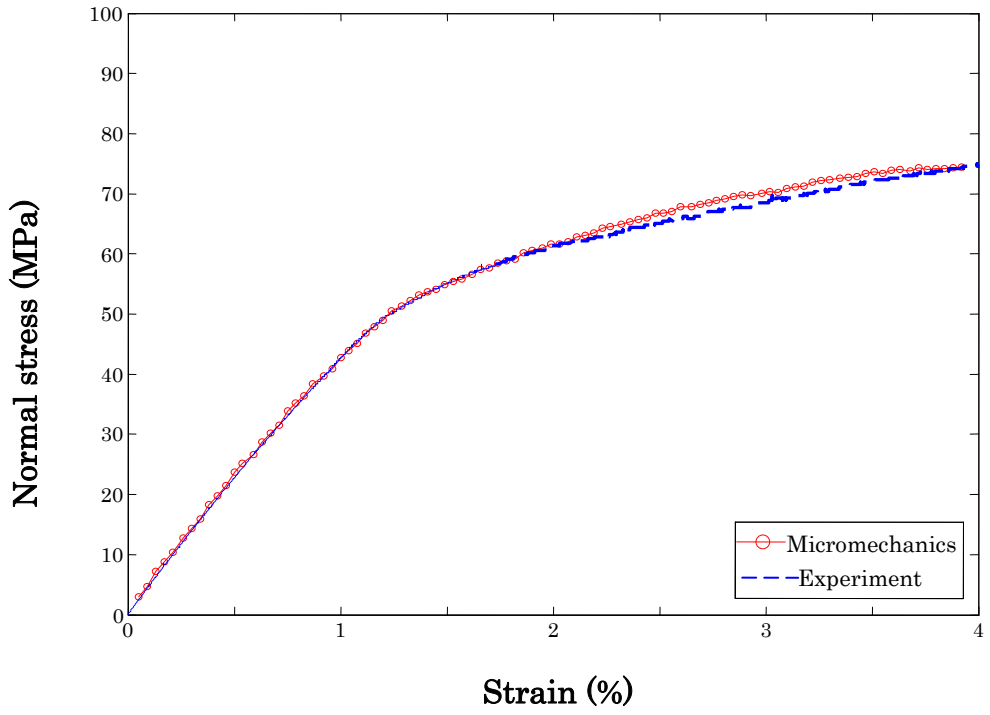

Fig. 4.23. Mechanical behavior of the M450 wire composite for V_f=6% at 80 °C

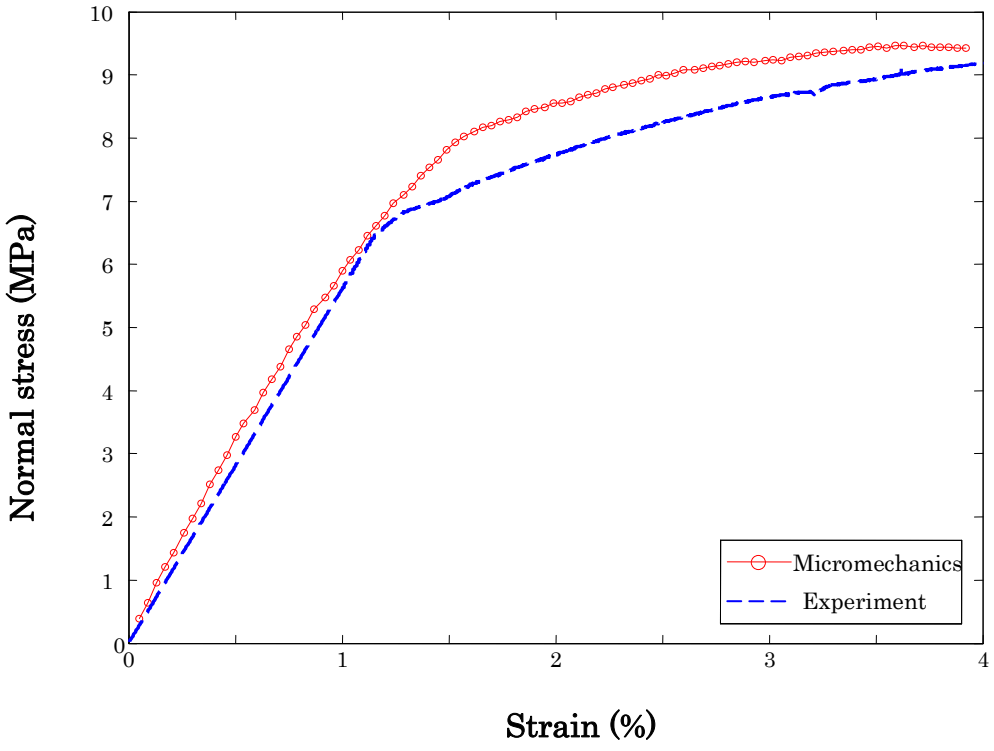

Fig. 4.24. Mechanical behavior of the M450 wire composite for V_f=12% at 90 °C

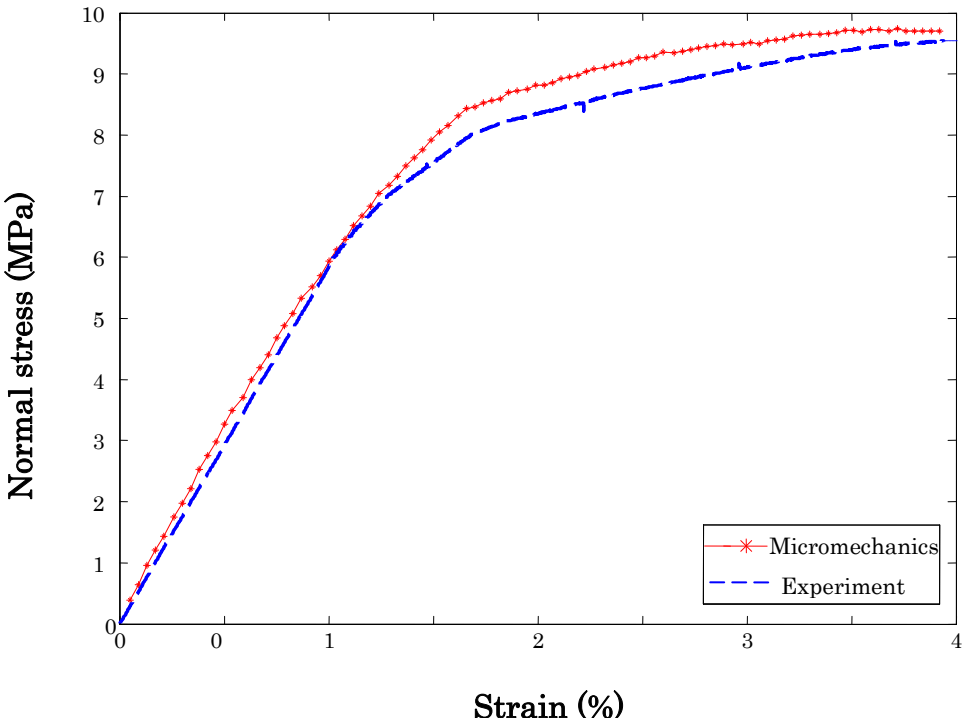

Fig. 4.25. Mechanical behavior of the M400 wire composite for V_f=12% at 90 °C

As discussed in chapter 3, the martensitic transformation affect on the debonding initiation and propagation. In the following paragraphs the martensitic transformation and its effect on the debonding is discussed using the micromechanical model. As mentioned in the previous section, the experimental behavior of the wire and matrix has been used by the model by introducing the secant modulus. Thus the transformation has been considered indirectly.

The variation of Normalized debonded length L_d (or *m*) as a function of applied strain is shown in Fig. 4.26. As shown, the debonded length increases with increasing the applied strain. Fig. 4.27 illustrates that for a given strain (0.5%) the L_d for steel wire composite is large and decreases respectively when M400, M450 and M550 are used. It means that the debonding will begin earlier in steel wire specimens. It can be associated to the Young modulus of the steel wire which leads the shear stress to increase rapidly in the interface and reach the interfacial shear strength (τ_i) very fast. Moreover, the τ_i in this system is less that that of the NiTi wire composites. Therefore, the debonding in steel wire samples will begin earlier and propagates faster compared to the NiTi wire specimens resulting in a large debonded length for a given strain. In the case of NiTi wires, the martensitic transformation plays an important role in delaying the debonding initiation and also altering its propagation [Payandeh et al. 2009 and 2010]. Very short debonded length for M550 can be due to the high τ_i and also a smaller transformation stress which lead the transformation to begin sooner.

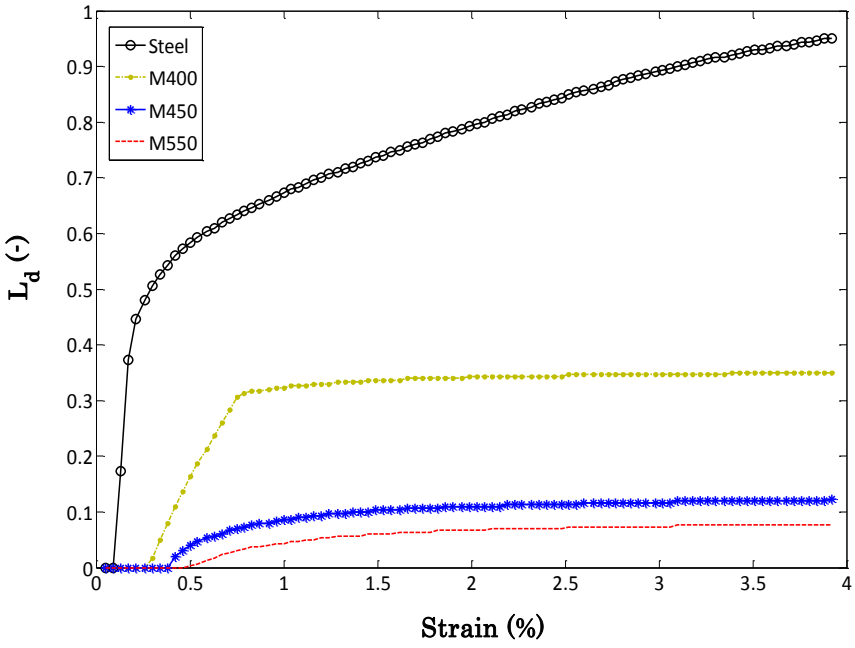

Fig. 4.26. Normalized debonded length (L_d) vs. applied strain for different wires at 20 °C.

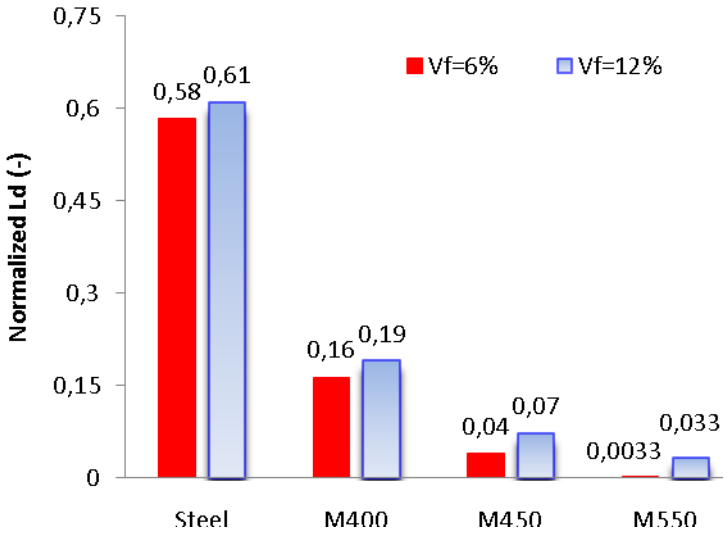

Fig. 4.27. Normalized debonded length (L_d) at 0. 5% applied strain for different wires at 20 °C.

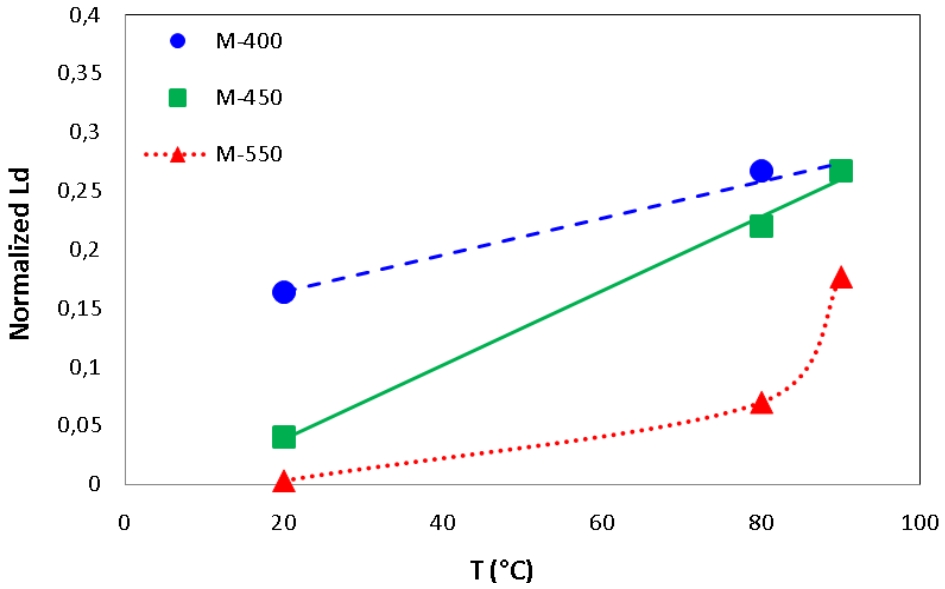

Fig. 4.28. Normalized debonded length (L_d) at 0. 5% applied strain for NiTi wires vs. temperature.

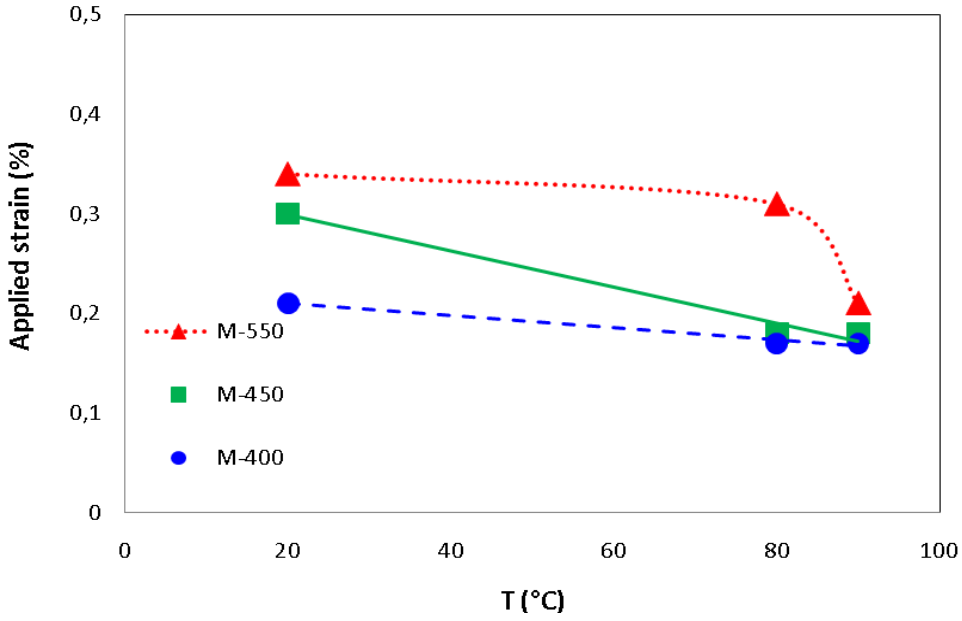

Fig. 4.29. Applied strain at which the debonding begins vs. temperature for NiTi wire samples

Fig. 4.28 shows the L_d as a function of test temperature for three NiTi wires. From this figure, the L_d increases with increasing the temperature from 20 to 80 °C and remains constant with subsequent heating to 90 °C. The increase in the debonded length can be justified by the fact that increasing the temperature delays the martensitic transformation and shifts it to the higher stress and then the conditions will approach to the cases in which no transformation occurs. Moreover, the Young modulus of the wires increases with temperature. In such conditions the

debonding will takes place earlier. Fig. 4.29 shows the debonding onset for all NiTi wires as a function of temperature. This figure illustrates that the debonding begins in a lower value of strain when the temperature increases. It means that the debonding starts sooner when the temperature increases.

In the micromechanical model, the effect of martensitic transformation has been taken into account by entering the experimental stress-strain of the wire in different conditions. This results considering the transformation indirectly as an effective and key parameter which yields a good correlation in experimental and micromechanical results. However, the interfacial shear stress generated after martensitic transformation remains still unsolved which needs to be studied.

The Piggott model can be applied for the ordinary composite materials in which the reinforcements behave elastically. From the model it is expected the debonding to occur at the wire ends where the interfacial shear stress is maximum (Fig. 4.30). The debonding increases with imposed strain. Similar result is obtained for NiTi composite (Fig. 4.31). In this case the debonded length is significantly smaller at given strain.

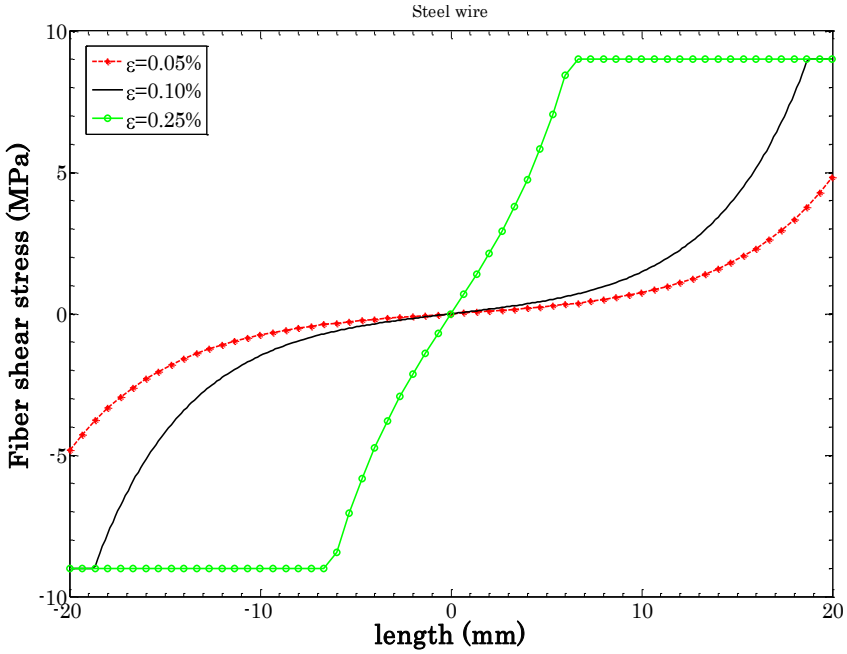

Fig. 4.30- Interfacial shear stress vs. length for steel wire at three strain levels (0.05, 0.1 and 0.25%).

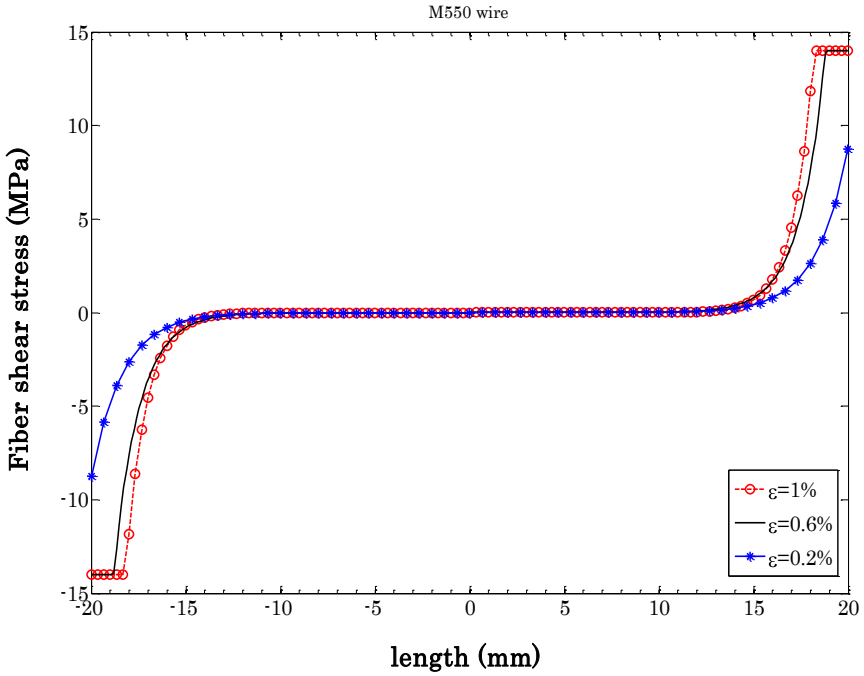

Fig. 4.31- Interfacial shear stress vs. length for M550 wire at three strain levels (0.2, 0.6 and 1%).

4.4.2. Effect of martensitic transformation on the mechanical behavior of composite

As discussed earlier, the tensile strength of the composite samples increases when the transformation stress of the embedded wires increases either by increasing the test temperature or by changing the type of wire (e.g. from M550 to M450). It illustrates that the MT has an influence on the behavior of the composite. If we consider a stress-strain diagram with a linear part followed by a non linear one, the MT should affect the second part. In other words, since increase in the transformation stress leads to increase the tensile strength, the MT should begin and intervene in the second part.

In all experimental stress-strain curves obtained for composite samples two different trends are observable (Fig. A.1-A.5): a quasi-linear part followed by a non-linear one. Fig. 4.5 shows this phenomenon for a non-zero volume fraction ($V_f \neq 0$). These two trends are also observable in all micromechanical results (Fig. A.6-A.14). Such a trend change, however, was not seen in the stress-strain curve for the epoxy matrix (Fig.4.5 for $V_f=0$ or Fig. 2.7). Hence, this phenomenon takes place only in the composite. Moreover, the stress corresponding to the change, increases when the transformation stresses in the wires increase. Table 4.3 shows that the change of trend in stress-strain curve for the M550 wire specimens increases with temperature. Changing the type of wire from M550 to M450 or M400 has the same effect and shifts the trend change to the higher stress (Table 4.4). Therefore, it could be related to the martensitic transformation which takes place in the embedded wires during the test. It seems that the second part begins as soon as the transformation takes place in the wires. In other word, the first part (linear) is a product of two linear behaviors, but the second part (curve) is

produced when a curve (for the matrix) and plateau (for the wire) combine. Therefore, the beginning of the second part is a sign of wire phase transformation. In Fig. 4.15 the stress-strain behavior of the matrix, wire and composite is compared. This figure shows the beginning of the stress plateau (for the wires) corresponds to the beginning of the second part in the behavior of the composite. As a conclusion, the MT affects the mechanical behavior of the composite.

Table 4. 3. Change of trend in stress-strain curve at different temperature for M550 wire samples

Volume fraction (V_f)	T = 20 °C		T = 80 °C		T = 90 °C	
	σ (MPa)	ε (%)	σ (MPa)	ε (%)	σ (MPa)	ε (%)
0	-	-	-	-	-	-
6%	22	0,68	41	1.1	51	1.32
12%	33	0,62	48	0.89	53	0.95

Table 4. 4. Change of trend in stress-strain curve for composites with different wires at 90

Wire	V_f = 6%		V_f = 12%	
	σ (MPa)	ε (%)	σ (MPa)	ε (%)
M550	51	1,32	53	0.95
M450	52	1,1	66	1.2
M400	-	-	71	1.3

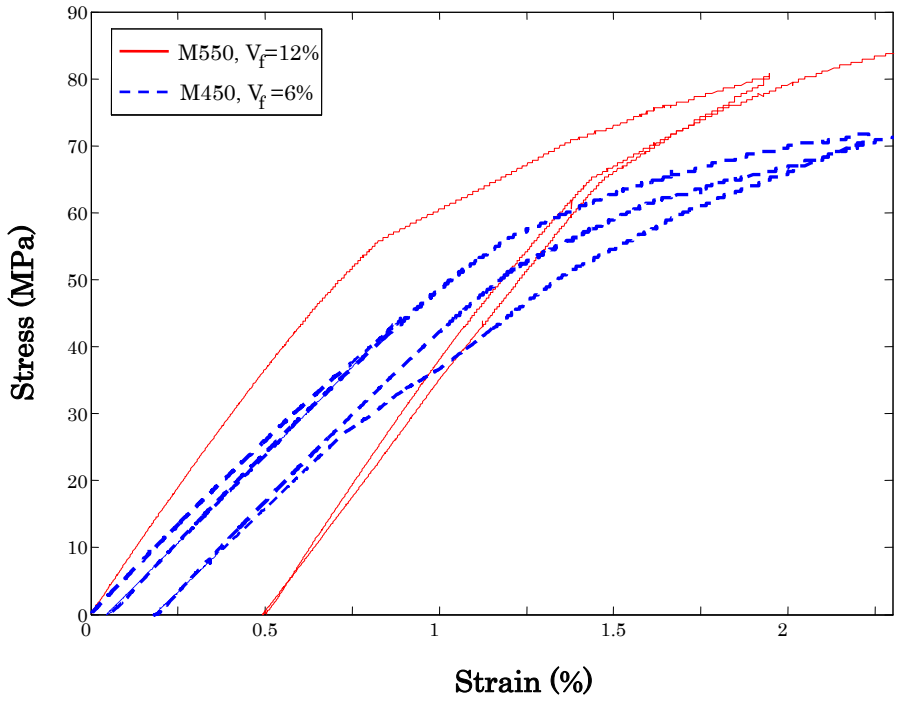

Fig. 4.32 Stress -Strain diagram for the composite samples with M450 and M550 wires, at 80 °C.

The M450 composite specimen is another example to show that the matrix follows the transformation occurring in the wires. As indicated before, the M450 wire sample exhibits a superelastic effect at 80 °C (Fig. 4.3). Whilst in the case of M550 wire composite, at the same temperature such a phenomenon is not observable (Fig. 4.4). As mentioned in chapter 2, at high temperature the M450 wires show the superelastic behavior whilst in the case of M550 there is no superelastic effect. In Fig. 4.32 the stress-strain curve for the specimens with M450 and M550 wires at 80 °C are compared.

It could be concluded that the martensitic transformation occurring in the wire, affects the overall behavior of the composite. Therefore, by doing an appropriate heat treatment on the wires, one can improve some mechanical properties such as tensile strength of the composite samples. It is also possible to have the composite exhibiting superelastic effect.

4.4.3. Effect of martensitic transformation on debonding mechanism

From micromechanical analysis, it is expected that the debonding happens in the wire ends due to the maximum interfacial shear stress. According to the experimental observation, however, the debonding happens in the center part of samples. Fig. 4.33 shows the debonding in NiTi composite samples. As shown, a regular debonded/undebonded pattern exist in the samples (the bright zones show the debonded parts). This phenomenon is more observable at high temperature, because the matrix is more ductile and undergoes a larger strain. As a conclusion, the debonding mode in SMA composite seems to be different in comparison to an ordinary composite (without MT). The main difference between these two kinds of composite is the MT taking place in the reinforced wire. Thus, different mode of debonding can be associated with the MT. This will be discussed in the following paragraphs.

As mentioned in chapter 3, during pull-out test, the martensitic transformation (MT) takes place just after partial interfacial debonding. In standard uniaxial tensile test, however, it could be different because loading conditions differs strongly. Both wire and matrix are loaded and both elongate in the same direction. In such conditions, the martensitic transformation could now occur within the embedded wire. Depending on the matrix elongation and on the interfacial strength, the MT can take place partially or completely. In fact, when the tensile strain in the matrix is larger than the transformational strain, ε^{tr}, the wire could experience a complete MT if the interface remains intact. When a composite sample is loaded, the load in the wire increases gradually and when it reaches the critical transformation load the MT begins. During the MT, the load remains almost constant in the wire. Increasing the applied displacement results to an increase in the transformed length. This phenomenon can continue until the embedded part transforms completely. It should be indicated that when the matrix is brittle, the debonding can take place before complete MT.

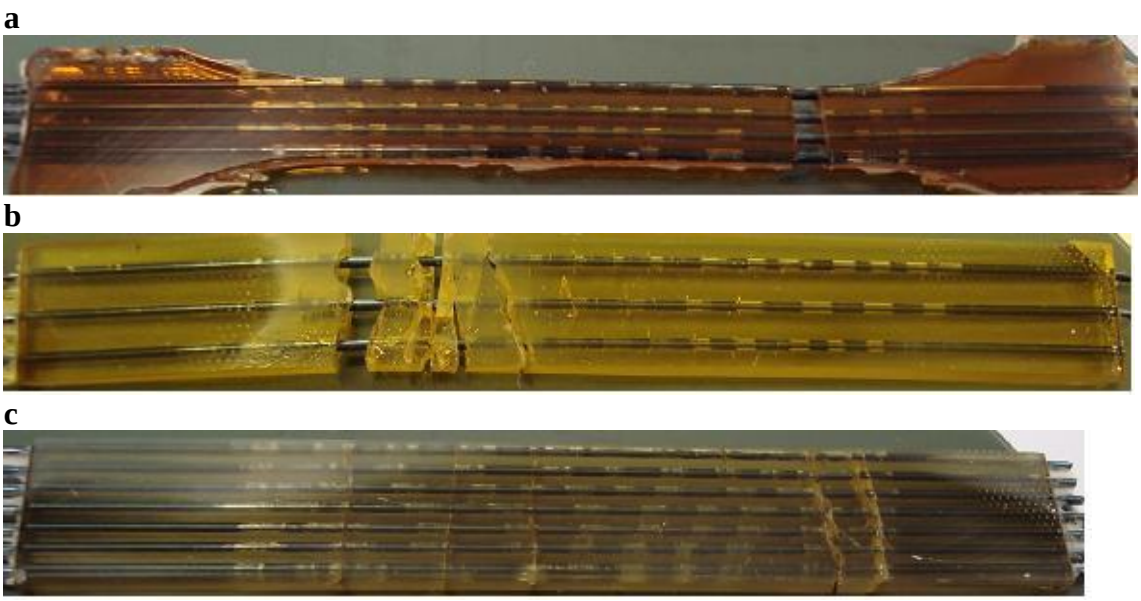

Fig. 4.33. Observation of the regular debonded/undebonded pattern taking place in NiTi wire composites a) Standard sample with M550, b) rectangular specimen with M550 and c) rectangular sample with M450, tested at 80°C (the bright zones show the debonded regions).

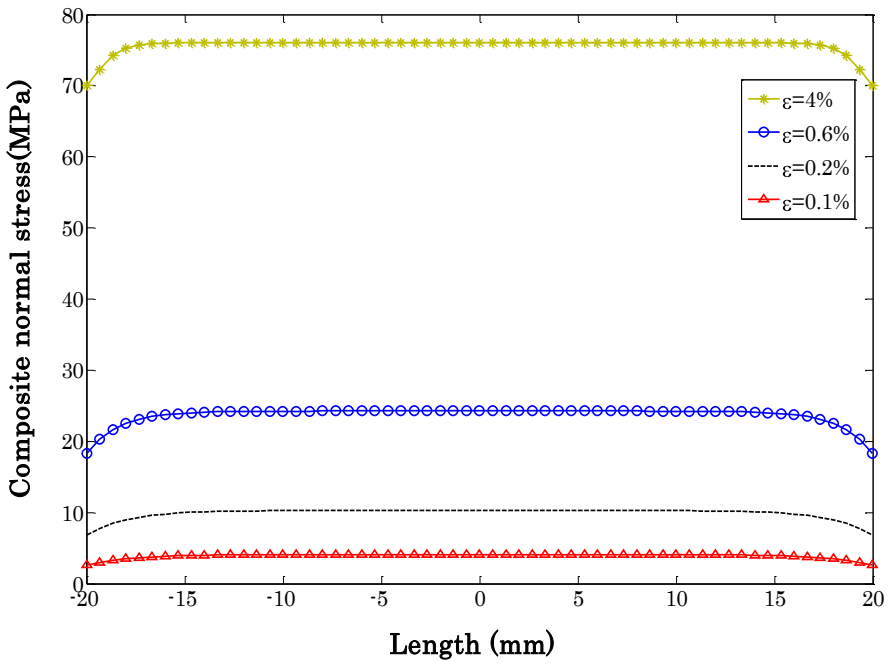

Fig. 4.34- longitudinal stress distribution for M550 wire composite samples in four strain levels (at 20°C, V_f=6%).

When a NiTi wire is subjected to the tensile load, the martesitic transformation starts from one end of the specimen and propagates to the other end [Otsuka and Ren 2005]; but when a wire is embedded in a matrix, the MT starts likely in several locations at the same time. It is known that the propagation of the stress-induced transformation is much easier compared to

nucleating martensite in untransformed region [Otsuka and Ren 2005]. Therefore, the number of points, from where the transformation begins, should be limited. In other words, on the constraint of the matrix, the martensitic transformation can start simultaneously at some limited number of points and propagates from these positions while the load is applied.

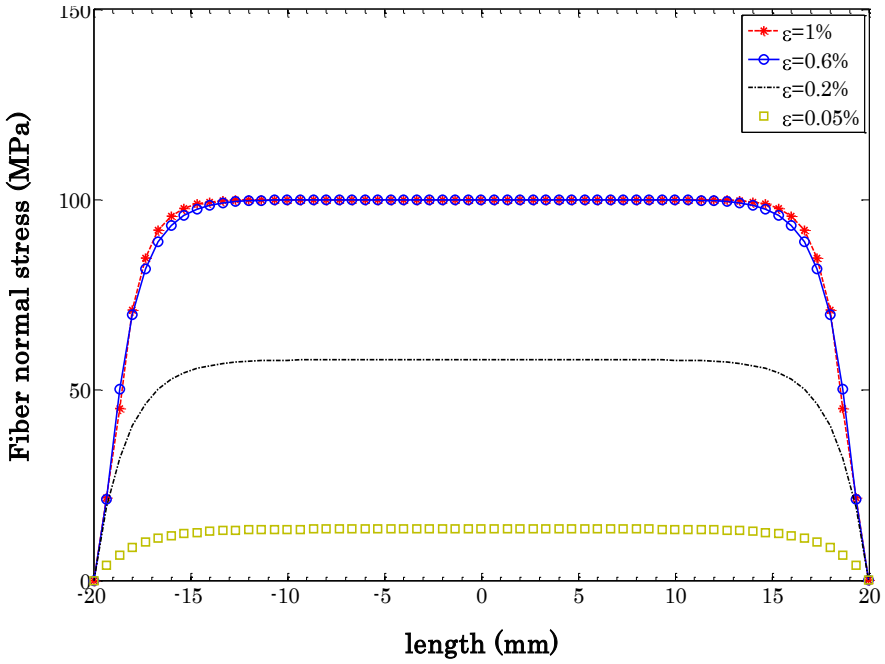

Fig. 4.35. Stress distribution in the embedded M550 wire with martensitic reorientation at T=20 °C

Since the wire and matrix have the same imposed strain level but different Young moduli, the loading condition will be different. In fact, by applying a load, in imposed displacement condition, the matrix and wire elongate as well but the load in the wire increases more rapidly in comparison to the matrix because the Young modulus of the wire is larger than that of the matrix. In such conditions, the load in the wires could reach to the transformation load and induce the martensitic transformation. For example in the case of M550 wire composite as shown in Fig. 4-34, the composite stress is about 25 MPa when applied strain equals to 0.6%. At this strain level, the stress in wires is about 100 MPa (Fig. 4.35) and remains constant. But in a steel wire (without transformation) the load increases even after debonding (Fig. 4.36). As mentioned before, the M550 wires reorient at 100 MPa applied stress which implies that the martensitic reorientation could potentially occur in a long part of the wire because the load in this part of wire is equal to the reorientation load. Fig. 4.37 shows the stress distribution in M450 wire samples. From this figure the stress in the wire remains constant when it reaches the transformation stress (140 MPa) at the 0.6% strain level. It is known that the martensitic transformation takes place as soon as the load reaches the transformation load. Since all of the uniform part of the sample elongates, the MT should occur in several points in the wire at the

same time to follow the matrix elongation. In other word, the wire is in contact to the matrix and they both undergo almost the same strain. Thus, the wire elongates as well as matrix and is forced to follow the matrix while the interface is intact. Therefore, the wire can not transform only in one point (like a wire in absence of matrix); it should elongate with matrix and in all the length embedded in the uniform part of specimen. Thus the wire transformation should occur simultaneously in all this part to have the same elongation as the matrix.

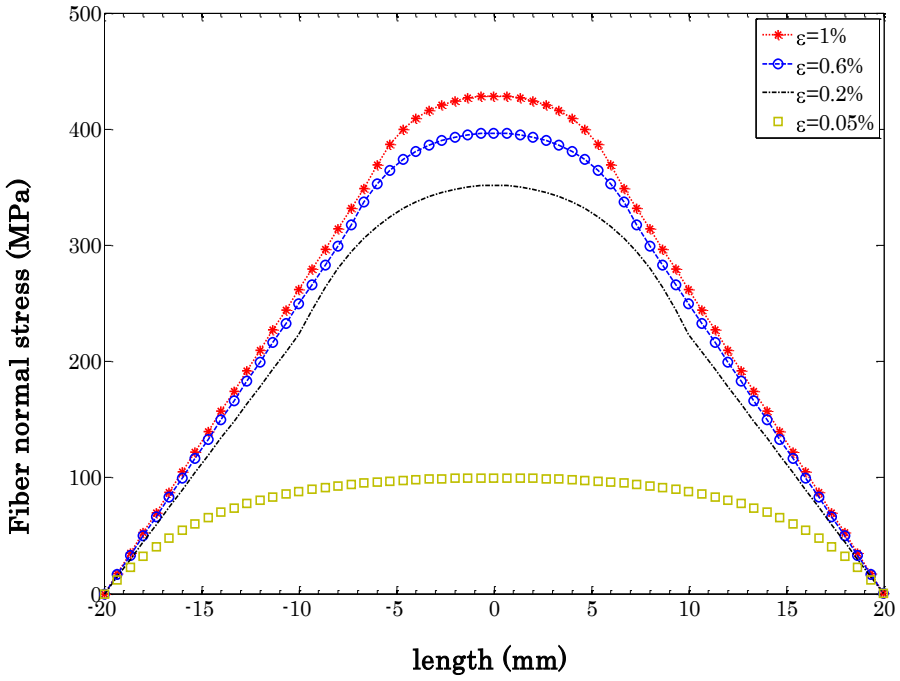

Fig. 4.36. Stress distribution in embedded steel wires (without MT) at 20 °C

From above discussion, on the constraint of the matrix the MT could take place partially and at some points to compensate the displacement applied by the matrix. While the load is applied, this phenomenon continues and the length of transformed parts increases. Once the length of the transformed part reaches a certain value, the loading conditions will change due to the fact that the wire diameter decreases because the phase transformation occurs at constant volume. In these conditions, the radial component of the load could accelerate the interfacial debonding initiation. And since the transformation takes place simultaneously in several points, the debonding could also happen in several points. These phenomena could result some numbers of debonding with a short length as shown in Fig. 4.33. When wires without phase transformation are embedded into a matrix, it is expected to have two long debonded parts at the wire ends because the interfacial shear stress has a maximum value at the wire ends (Fig. 4.31).

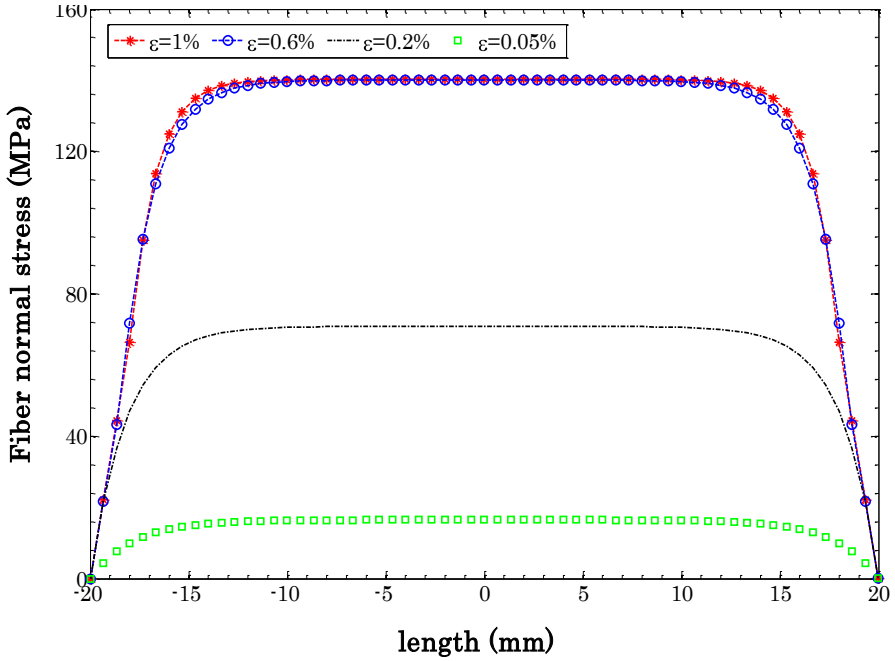

Fig. 4.37. Stress distribution in embedded M450 wires with MT at 20 °C

4. 5. Conclusion

In this chapter, the mechanical behavior of the NiTi-epoxy composite was investigated using standard tensile test. The effect of different types of wire, test temperature and wire volume fraction were studied as well. For this purpose, the specimens with three different wires (M400, M450 and M550) and also with three wire volume fractions (0, 6, and 12%) were subjected to the tensile load at 20, 80 and 90 °C.

As explained in details, with increasing the test temperature the mechanical behavior of the composite, such as tensile strength, is improved while the behavior of the matrix decreases when the test temperature increases. But the transformational stress in NiTi wires (in all three cases) increases with temperature.

The same effect were observed when the wires heat treated at higher temperature (e.g. M550) was replaced by the wires heat treated at lower temperature (say M450 or M400). In fact, the martensitic transformation takes place under higher stress in the wire which is heat treated at lower temperature; and due to the higher stress plateau, the overall behavior of the composite sample improved in this case.

As it was expected, increasing the wire volume fraction enhances the mechanical behavior of the composite specimens.

In order to interpret the role of wire in the composite, in more details, a micromechanical model was developed on the basis of Piggott's model. The micromechanical results are in good accordance with the experimental ones. It could be due to the fact that in the model, the experimental behavior of the wires and matrix at different temperature has been employed to extract the mechanical behavior of the composite at different wire volume fractions and test temperatures.

From the experimental or micromechanical results, two trends in the stress-strain behavior of the composite samples are observable. As concluded in the chapter, the beginning of the second part of the diagram is a sign of martensitic transformation taking place in the wires.

It was claimed that the martensitic transformation in the wire occurs simultaneously in several points so it can follow the displacement of the matrix as long as the interface remains intact.

It was also discussed that the M450 wire composites present a slight superelastic behavior at high temperature. This effect does not occur in M550 wire samples. It shows the influence of the wire on the behavior of composites.

The transformation stress for the wire on the constraint of the matrix might be different with the case in which the wire transforms freely. Moreover, the martensitic transformation in a SMA wire constrained by the matrix could start in several locations at the same time. Additional investigation will be necessary to better understand the influence of the martensitic

transformation in these points. The shear stress in the interface generated after transformation should be investigated as well. Moreover, reduction of the wire diameter due to the martensitic transformation has not been taken into account by the model. The transformation could play an important role in the particular debonded/undebonded pattern observed in the composite samples.

References

[Bidaux et al. 1997] J.E. Bidaux, J.A.E. Manson, R. Gotthardt. Active stiffening of composite materials by embedded shape-memory-alloy fibres, Mat. Res. Soc. Symp. Proc. 459 (1997), p. 107–117.

[Bollas et al. 2007] D. Bollas, P. Pappas, J. Parthenios, C. Galiotis, Stress generation by shape memory alloy wires embedded in polymer composites, Acta Materialia 55 (2007), p. 5489-5499.

[Cox 1952] H.L. Cox, The elasticity and strength of paper and other fibrous materials, British Journal of Applied Physics 3 (1952), p.72-79.

[Jonnalagadda et al. 1997] K.D. Jonnalagadda, G.E. Kline, N.R. Sottos, Local displacements and load transfer in shape memory alloy composites, Exp. Mech. 37 (1997), p. 78-86.

[Jonnalagadda et al. 1998] K.D. Jonnalagadda, N.R. Sottos, M.A. Qidwai, Lagoudas DC. Transformation of embedded shape memory alloy ribbons, J Intell Mater Syst Struct 9 (5) (1998), p. 379-390.

[Ju and Shimamoto 1999] D.Y. Ju, A. Shimamoto, Damping property of epoxy matrix composite beams with embedded shape memory alloy fibres. J Intel Mater Sys Struct 10 (1999), p. 514–520.

[Lau et al. 2002b] K.T. Lau, C.K. Poon, L.H. Yam, L.M. Zhou, Bonding behaviour at a NiTi/epoxy interface: SEM observation and theoretical study. Mater Sci Forum 394–395 (2002), p. 527–530.

[Lau et al. 2002c] K.T. Lau, W.L. Chan, S.Q. Shi, L.M. Zhou, Debond induced by strain recovery of an embedded NiTi wire at a NiTi/epoxy interface: micro-scale observation. Mater Des 23 (2002), p. 265–270.

[Lau et al. 2002d] K.T. Lau, W.Y. Tam, X.L. Meng, L.M. Zhou, Morphological study on twisted NiTi wires for smart composites systems, Mater Lett 57 (2002), pp. 364–368.

[Li et al. 2001] Y. Li, L. Cui, Y. Zheng, D. Yang, DSC study of the reverse martensitic transformation in prestrained TiNi shape memory alloy in different composites, Materials Letters 51(2001), p.73–77.

[Marfia and Sacco 2005] S. Marfia, E. Sacco, Micromechanics and homogenization of SMA-wire-reinforced materials, J. Appl. Mech. 72 (2) (2005), p. 259–268.

[Murasawa et al. 2004] G. Murasawa, K. Tohgo, H. Ishii, Deformation Behavior of NiTi/Polymer Shape Memory Alloy Composites- Experimental Verifications, J. Compos. Mater. 38 (2004), p. 399–416.

[Otsuka and Ren 2005] K. Otsuka, X. Ren, physical metallurgy of NiTi based shape memory alloys, Review Article, Progress in Materials Science 50 (5) (2005), p. 511-678.

[Payandeh et al. 2009] Y. Payandeh, F. Meraghni, E. Patoor, A. Eberhardt, Effect of Martensitic Transformation on the Debonding Propagation in NiTi Shape Memory Wire Composite, Materials Science and Engineering A 518 (2009), p. 35-40.

[Payandeh et al. 2010] Y. Payandeh, F. Meraghni, E. Patoor, A. Eberhardt, Debonding Initiation in NiTi Shape Memory Wire Composite, Influence of Martensitic Transformation, Materials and Design 31 (2010), p. 1077–1084.

[Piggott 1980] M.R. Piggott, Load Bearing Fibre composites. Pergamon International Library, Canada, 1980.

[Shimamoto and Taya 1997] A. Shimamoto, M. Taya, Reduction in K_I by shape memory effect in a TiNi shape-memory fiber-reinforced epoxy matrix composite. Trans. JSME Part A 63 605 (1997), p. 26–31.

[Shimamoto et al. 2004] A. Shimamoto, H. Ohkawara, F. Nogata, Enhancement of mechanical strength by shape memory effect in TiNi fiber-reinforced composites, Eng. Fract. Mech. 71 (2004), p. 737-746.

[Wei et al. 1998] Z.G.Wei, R. Sandstrom, S. Miyazaki, Review Shape-memory materials and hybrid composites for smart systems, Part II Shape-memory hybrid composites. Journal Of Materials Science 33 (1998), p. 3763-3783.

[Yamashita and Shimamoto 2004] K. Yamashita, A. Shimamoto. Effect of Temperature Caused for Mechanical Characteristics and Crack Closure Effect of Shape-Memory Alloy Fiber Reinforced Composite, Key Eng Mater 270–273 (2004), p. 2179-2186.

[Zhang et al. 2007] R Zhang, Q.Q. Ni, T. Natsuki, M. Iwamoto, Mechanical properties of composites filled with SMA particles and short fibers, Composite Structures 79 (2007) p. 90–96.

[Zheng et al. 2000] Y.J. Zheng, L.S. Cui, D. Zhu, D. Yang, The constrained phase transformation of prestrained TiNi fibers embedded in metal matrix smart composite, Materials Letters 43 (3) (2000), p. 91-96.

[Zheng et al. 2003] Y.J. Zheng, J. Schrooten, L.S. Cui, J. Van Humbeeck. Constrained thermoelastic martensitic transformation studied by modulated DSC, Acta Mater 51 (2003), p. 5467-5475.

[Zheng et al. 2005b] Y.J. Zheng, L.S. Cui, J. Schrooten, Basic design guidelines for SQMA-Epoxy smart composites, Materials Science and Engineering A 390 (2005), p. 139-143.

Chapter 5.

Parameters identification of NiTi/epoxy composite

5.1. Introduction

5.2. Inverse Method

Identification algorithm

Cost function

Optimization algorithms

a- Gauss-Newton method

b- Levenberg-Marquardt

Determination of the sensitivity matrix

Stop criteria

5.3. Application to the NiTi wire composite

5.3.1. Convergence and stability analysis

5.3.1.1. Convergence test

Influence of the experimental database

Influence of the number of element and mesh size

Influence of the initial estimation

Influence of the regularization parameter (μ)

5.3.1.2. Stability analysis

5.3.2. Application for experimental strain fields

Correli-Q4 software

Vic2D software

Applied displacement

5.4. Identification results

5.4.1. Identification results using Correli-Q4

5.4.2. Identification results using Vic2D

5.5. Conclusion

References

5.1. Introduction

The mechanical behavior of the studied material, through tensile test, was discussed in chapter 4. Performing standard tensile tests is the most common way to identify the stress–strain behavior of a material. This can be an adequate procedure for isotropic materials, but in the case of anisotropic material, such as composites material, several standard tests are required to identify the material parameters in different directions. For this purpose, a heterogeneous test has been carried out. Such complex tests can be obtained by using complex test geometries [Cooreman et al. 2007] and applying simple load by means of universal tension- compression test machine. This kind of tests allows the simultaneous identification of different parameters. Several configurations for heterogeneous tests were proposed recently [Lecompte et al 2007, Endelt and Nielsen 2005, Kajberg and Lindkvist 2004, Ghouati and Gelin 2001, Ghouati and Gelin 1998, Meuwissen et al. 1998].

The main problem is to measure the heterogeneous displacement fields generated during these types of tests. In recent years, some optical techniques such as digital image correlation (DIC) have been developed in the field of optical full-field measurement. DIC allows measuring the heterogeneous strain components on flat or curved surface. However, for heterogeneous tests there is no explicit relationship between displacement and applied load. This yields the fact that the stress tensor would be unknown. Therefore, an inverse method is required to extract the material parameters.

The identification by inverse analysis allows determining the parameters of constitutive equations for different materials. It has been used to identify the parameters of metallic materials, polymers, ceramics and composite. Gavrus et al. [Gavrus et al. 1996] formulated an inverse problem to identify the parameter of AG5 aluminum during torsion test. Meuwissen et al. [Meuwissen et al. 1998] used this method to identify the elasto-plastic behavior of aluminum samples through tensile test. Kajberg and Lindkvist [Kajberg and Lindkvist 2004] have identified the parameters of hot-rolled steels with taking into account the work hardening. Gavrus et al. [Gavrus et al. 2008] proposed to use the inverse analysis principle to identify the rheological parameters of DC03 sheet steel alloy directly from the Erichsen test. Mohammad Sadeghi [Mohammad Sadeghi 2010] developed a method to identify the parameters of TRIP steel and 304 stainless steel. Inverse analysis has been employed by Tillier [Tillier 1998] for identification of the mechanical behavior of thermoplastic polymers. The elastic properties of a ceramic material (silicon carbide) were evaluated during a biaxial flexure test (on disk specimen) by Furgiuele [Furgiuele et al. 1997]. Lecompte et al. [Lecompte et al 2007] identified the elastic parameters of the orthotropic composite material by performing a biaxial tensile test on a cruciform test samples. Genovese et al. [Genovese et al. 2004] have determined the in-plane elastic properties of an orthotropic composite material (woven fiberglass-epoxy) subjected to some loading condition, by means of an inverse

method. This method has been used by Nouri [Nouri 2009, Nouri 2009a, Nouri 2010] for identification of damage parameters of a reinforced thermoplastic subjected to fatigue. Hoc et al. [Hoc et al. 2003] has employed an inverse procedure for identifying the plastic behavior of single crystals.

The principle of identification method is to compare an experimental strain field with a numerical one determined using estimated parameters. The inverse problem will be solved iteratively by updating the parameters in the FE model in such a way that the numerically computed strain field matches the experimentally measured field.

In this work, the identification method is developed to identify the four independent elastic constants E_{11}, E_{22}, G_{12} and ν_{12} of an orthotropic composite material. The studied material is NiTi wire epoxy matrix composite. The method is based on the surface measurements of specimens. For this purpose, specimens with complex geometry (Meuwissen-type) were subjected to the tensile load. The strain fields are measured and treated using the Correli-Q4 [Hild and Roux 2008] and Vic2D software on the basis of digital image correlation. A finite element model, using ABAQUS standard, serves as numerical counterpart for the experimental set-up.

It should be noted that, the quality of the images for the specimens tested at high temperature was not satisfying because the camera were located outside of the heating chamber. Therefore, only the results obtained for the samples tested at room temperature were analyzed.

5.2. Inverse Method

Identification algorithm

The identification algorithm requires the following steps:

- Definition of a cost function
- Choosing an optimization algorithm
- Determination of the sensitivity matrix
- Choosing a stop criterion
- Construction of an experimental database
- Construction of a finite element model
- Estimation of initial parameters

The simulation results based on the finite element calculation are compared to the experimental database. During each iteration, a new set of parameters is proposed according to the minimization algorithm. The new calculated strain field is again compared to the

experimental one. This procedure will be repeated until the cost function becomes small and reaches a predefined value (10^{-8} in this work) used as the stop criterion.

Cost function

The cost function (objective function) expresses the least squared difference between the experimental and the computed response for the studied system. By minimizing this function during the inverse calculation, the material parameters will be extracted by solving the appropriate equation. The cost function is written generally in quadratic form as below:

$$F(P) = \sum_{i=0}^{m} \beta_i \left[M_i^{Exp} - M_i^{Num}(P) \right]^2 \qquad P = < P_1, P_2, \dots, P_n > \qquad (5.1)$$

where β_i are the weighting coefficients, M_i^{Exp} describe the experimental measurements (experimental database) used for identification (strain, force, ...), M_i^{Num} are the values calculated numerically by the model (numerical database), P_1, P_2, … P_n are the material parameters which will be identified, *n* is the number of material parameters and *m* indicates the number of measurement points.

The cost function should satisfy the following conditions:

F must be positive-definite (which requires $\beta_i > 0$),

F=0 if and only if $M_i^{Exp} = M_i^{Num}$

Optimization algorithms

In order to update the parameters, an increment (ΔP) is calculated at each iteration:

$$p_{k+1} = p_k + \Delta p_k \qquad (5.2)$$

In this way, different methods can be used such as Conjugate gradient, Gauss-Newton type methods or Marquardt type algorithms [Gavrus et al 1999]. The optimization algorithm used in this work is Levenberg-Marquardt [Levenberg 1944, Marquardt 1963] based on Gauss-Newton method.

a- Gauss-Newton method

The Gauss Newton method is based on the development (in Taylor series) of the gradient of the cost function:

$$\frac{dF}{dp}(p + \Delta p) = \frac{dF}{dp}(p) + \Delta p \ \frac{d^2F}{dp^2}(p) + o(\Delta p^2) \qquad (5.3)$$

The cost function has an extremum, if:

$$\frac{dF}{dp}(p + \Delta p) = 0 \tag{5.4}$$

Thus, an approximation of the variation Δp is obtained by solving the following linear system:

$$\Delta p \ \frac{d^2F}{dp^2}(p) + \frac{dF}{dp}(p) = 0 \tag{5.5}$$

Rewriting the equation 5.5 gives:

$$A\Delta P + B = 0$$

where A is $\frac{d^2F}{dp^2}(p)$, called the Hessian of F and B is $\frac{dF}{dp}(p)$ and is called the gradient of F.

From equation 5.3, we obtain the following terms for the matrices A and B:

$$B_i = \frac{dF}{dp_i}(p) = 2\sum_{k=1}^{m} \beta_k \left[M_k^{Num} - M_k^{Exp}\right]\frac{dM_k^{Num}}{dp_i} = 2\sum_{k=1}^{m} \beta_k \left[M_k^{Num} - M_k^{Exp}\right]S_{ki} \tag{5.6}$$

$$A_{ij} = \frac{d^2F}{dp_i dp_j}(p) = 2\sum_{k=1}^{m} \beta_k \left[M_k^{Num} - M_k^{Exp}\right]\frac{d^2M_k^{Num}}{dp_i dp_j} + 2\sum_{k=1}^{m} \beta_k \frac{dM_k^{Num}}{dp_i}S_{kj} \tag{5.7}$$

The term S_{ij} denoted the sensitivity matrix. It is also called Jacobian matrix whose components reflect the sensitivity of measurements to the identification parameters. The components of S are expressed by:

$$S_{ij} = \frac{dM_i^{Num}}{dp_j} \tag{5.8}$$

The Gauss-Newton proposes to neglect the second-order derivatives of the data calculated by the direct model. Then, A is obtained as:

$$A_{ij} \approx 2\sum_{k=1}^{m} \beta_k \frac{dM_k^{Num}}{dp_i}S_{kj} \approx 2\sum_{k=1}^{m} \beta_k S_{ki}S_{kj} \tag{5.9}$$

The calculation of S makes it possible to solve the equation (5.5) to estimate Δp. This can be written as follows, depending on the sensitivity matrix:

$$\Delta p = [S^T W S]^{-1}[S^T W]\Delta M \tag{5.10}$$

where the weighting term *W* is a diagonal matrix whose components are given by:

$$W_{ii} = \beta_i \tag{5.11}$$

and ΔM is the deviation vector and is expressed by:

$$\Delta M_i = \left[M_i^{Num} - M_i^{Exp}\right] \tag{5.12}$$

The approximation of A becomes more accurate when approaching the solution and the cost function tends to zero. If one or more parameters do not have direct influence on the observed magnitude, the eigenvalues of the matrix A would be equal to zero. As a result, there is not a solution for the inverse problem because the matrix is not inversible. In this case, it will be necessary to redefine the problem by choosing different parameters or another database.

b- Levenberg-Marquardt algorithm

The Gauss Newton algorithm is applied for solving the inverse problem. As mentioned before, this algorithm is sometimes difficult to converge. This is mainly due to the fact that there are ill-conditioned (ill-posed) problems. Implementing regularization algorithms may lead to stabilize the algorithm and to avoid the convergence difficulties. One of these algorithms is that of the Levenberg-Marquardt (LMA) [Levenberg 1944, Marquardt 1963] on the basis of Gauss-Newton. The algorithm was first published by Kenneth Levenberg on 1944, and was rediscovered by Donald Marquardt on 1963 [Wikipedia].

The LMA interpolates between the Gauss-Newton algorithm (GNA) and the method of gradient descent. The LMA is more robust than the GNA, which means that in many cases it finds a solution even if it starts very far away from the final minimum [Gavrus 1996]. This algorithm introduces a regularization parameter noted μ. Variation of this parameter will affect the convergence of the algorithm.

The linear system (equation 5.5) to be solved will be written as below:

$$\begin{cases} (H + \mu I)\Delta p = -\nabla F \\ H = \nabla^2 F \end{cases} \quad (5.13)$$

∇F is Gradient of F

H is the Hessian matrix of F

I is the identity matrix.

The equation 5.10 can be rewritten as below:

$$\Delta p = [S^T W S + \mu I]^{-1}[S^T W]\Delta M \quad (5.14)$$

Consequently, when μI is quite more than H ($\mu I >> H$), the equation takes the following form:

$$\mu \Delta p \approx -\nabla F \quad (5\text{-}15)$$

and then it will approach to a gradient descent method, which is known to converge quickly when it is away from the solution. When μI will be negligible in comparison to H ($\mu I << H$), we have:

$$H \Delta p \approx -\nabla F \quad (5.16)$$

This corresponds to the Newton method which converges rapidly around the solution. The initial value of μ should be between 10^{-1} and 10^{-10}. During the solution, the Levenberg-Marquardt coefficient, μ, changes regularly. In practice, if the cost function calculated at iteration *k+1* is less than that of the iteration *k*, the coefficient μ changes to become smaller and is given by:

$$\mu_{k+1} = 0.1\ \mu_k \tag{5.17}$$

In contrary, if the cost function increases at iteration *k+1*, a new evaluation of the cost function F_{k+1} is obtained after adjusting the parameter μ. At this time μ is given by:

$$\mu_{k+1} = 10\ \mu_k \tag{5.18}$$

or:

$$\begin{cases} if\ F_{k+1} < F_k\ \ then\ \ \mu_{k+1} = 0.1\mu_k \\ if\ F_{k+1} > F_k\ \ then\ \ \mu_{k+1} = 10\mu_k \end{cases} \tag{5.19}$$

Determination of the sensitivity matrix

Calculation of the sensitivity matrix is essential to solving the inverse problem. This matrix expresses the sensitivity of the measured quantities with regard to the variation of the identification parameters. This matrix is calculated during each iteration and can be determined in two main ways. The straightforward one is the finite difference method [Ghouati and Gelin 1998, Ghouati and Gelin 2001, Meuwissen et al. 1998, Mohammad Sadeghi 2010, Nouri 2009, Meuwissen et al. 1997], but it can also be computationally expensive [Ghouati and Gelin 2001]. Another way is to use an analytical method [Cooreman et al. 2007, Lecompte et al 2007, Gavrus et al. 1996, Merzouki 2008, Lecompte et al. 2005]. The analytical method is widely used in cases where the explicit relationship between the data and identification parameters is known. However, the analytical method requires to adapt the formulation allows the calculation of S_{ij}. The finite difference method is relatively easy to implement [Ghouati and Gelin 2001]. In this work, this matrix is calculated using the direct differentiation method which could be very accurate [Vidal et al. 1991]. To construct the sensitivity matrix, the parameters were perturbed one by one. The effect of the perturbation on the numerical data was calculated by the model. Once all the parameters are perturbed, all the components of sensitivity matrix are known.

$$S_{ij} = \frac{dM_i^{Num}}{dp_j} \approx \frac{\left[M_i^{Num}(p_j + \delta p_j) - M_i^{Num}(p_j)\right]}{\delta p_j} \tag{5.20}$$

where δp_j is the perturbation of the parameter p_j. Mathematically, the precision of the calculation increases when δp_j tends to zero. Therefore, the perturbation value should be as small as possible and should satisfy the following condition [Gavrus 1996]:

$$10^{-5}.|p_i| \leq \delta p_i \leq 10^{-3}.|p_i| \tag{5.21}$$

As an example, in the case of a problem with two parameters and from *m* measurement points, S_{ij} is written as follow:

$$\begin{pmatrix} \frac{M_1^{Num}(p_1+\delta p_1,p_2)-M_1^{Num}(p_1,p_2)}{\delta p_1} & \frac{M_1^{Num}(p_1,p_2+\delta p_2)-M_1^{Num}(p_1,p_2)}{\delta p_2} \\ \frac{M_2^{Num}(p_1+\delta p_1,p_2)-M_2^{Num}(p_1,p_2)}{\delta p_1} & \frac{M_2^{Num}(p_1,p_2+\delta p_2)-M_2^{Num}(p_1,p_2)}{\delta p_2} \\ \frac{M_3^{Num}(p_1+\delta p_1,p_2)-M_3^{Num}(p_1,p_2)}{\delta p_1} & \frac{M_3^{Num}(p_1,p_2+\delta p_2)-M_3^{Num}(p_1,p_2)}{\delta p_2} \\ \vdots & \vdots \\ \frac{M_m^{Num}(p_1+\delta p_1,p_2)-M_m^{Num}(p_1,p_2)}{\delta p_1} & \frac{M_m^{Num}(p_1,p_2+\delta p_2)-M_m^{Num}(p_1,p_2)}{\delta p_2} \end{pmatrix} \quad (5.22)$$

Stop criteria

The identification algorithm is stopped when one of the following conditions is satisfied:

- The cost function reaches a predetermined threshold. In this work the threshold was chosen as10^{-8}.
- The cost function reaches a stationary level and does not decrease further. This is called the stationary condition or stagnation. When the difference between the cost functions of last two iterations is too small, that threshold is reached so far. One can conclude that it eventually reaches a local minimum. It can also be expressed that ΔP tends to 0.

5.3. Application to the NiTi wire composite

In the present work, a method is proposed for the identification of the four independent elastic in-plane engineering constants E_{11}, E_{22}, G_{12} and ν_{12} of an orthotropic composite material. Fig. 5.1 describes the identification algorithm. The studied material is NiTi wire epoxy matrix composite. The method is based on the surface measurements of a sample with complex geometry (Fig. 2.18). For this meaning, the specimens with a random speckle pattern were subjected to the tensile load. Several images were taken during the test with a constant step time. The images were processed using the Correli-Q4 and VIC2D software on the basis of digital image correlation. As a result, the surface displacements are measured. Strains are subsequently calculated, on the basis of spatial derivation of the measured displacement

fields. A finite element model, using ABAQUS standard, serves as numerical counterpart/ matching part for the experimental set-up.

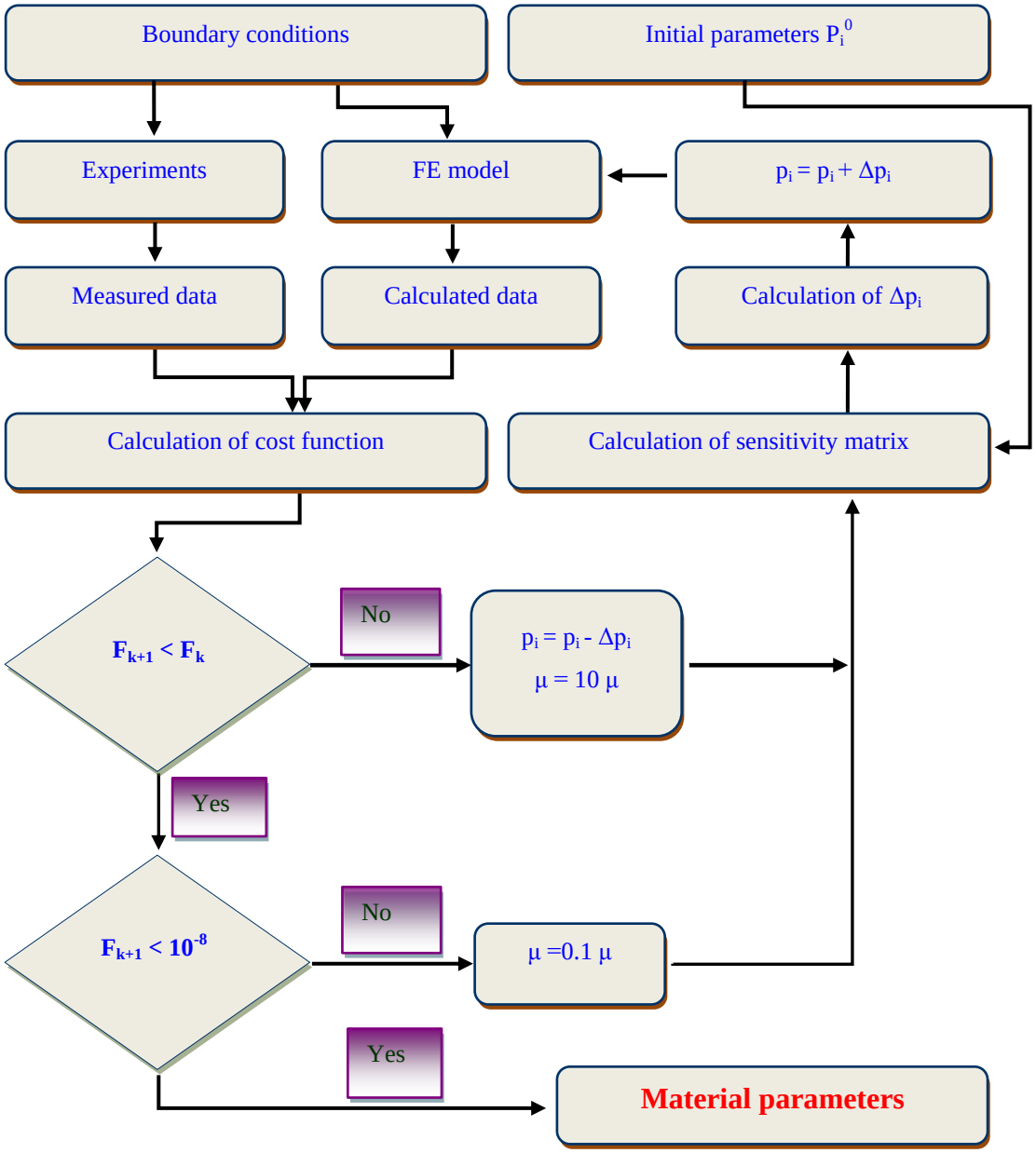

Fig. 5.1. Identification method

The cost function in this work is formulated on the basis of strain components (ε_{11}, ε_{22} and ε_{12}) and applied load (f). The load was taken into account to avoid a known ill-conditioned problem which could be introduced in elastic case. Entering this term will regularize the inverse method.

$$F(P) = \frac{1}{2}\left(\frac{\sum_{i=0}^{m}\left[\varepsilon_{1,i}^{Exp} - \varepsilon_{1,i}^{Num}\right]^2}{\sum_{i=0}^{m}\left[\varepsilon_{1,i}^{Exp}\right]^2} + \frac{\sum_{i=0}^{m}\left[\varepsilon_{2,i}^{Exp} - \varepsilon_{2,i}^{Num}\right]^2}{\sum_{i=0}^{m}\left[\varepsilon_{2,i}^{Exp}\right]^2} + \frac{\sum_{i=0}^{m}\left[\gamma_{12,i}^{Exp} - \gamma_{12,i}^{Num}\right]^2}{\sum_{i=0}^{m}\left[\gamma_{12,i}^{Exp}\right]^2}\right) + \frac{1}{2}\frac{\left[f^{Exp} - f^{Num}\right]^2}{\left[f^{Exp}\right]^2} \quad (5.23)$$

Comparing to equation 5.1, the weighting coefficients can be expressed as:

$$\beta_i = \frac{1}{\sum_{i=0}^{m}\left[\varepsilon_{ii}^{Exp}\right]^2}$$

The quadratic difference between the experimental and numerical database is minimized by updating the four independent elastic moduli: E_{11}, E_{22}, G_{12} and ν_{12}.

The sensitivity matrix was calculated by the direct differentiation method for each iteration with perturbing the four parameters (equation 5.24). These parameters were perturbed one by one and the responses of the system were recorded to calculate the sensitivities using equation 5.22 or 5.24. Fig. 5.2 shows the calculation of the sensitivity matrix schematically. Once the sensitivity matrix was obtained the ΔP could be calculated with the use of equation 5.14.

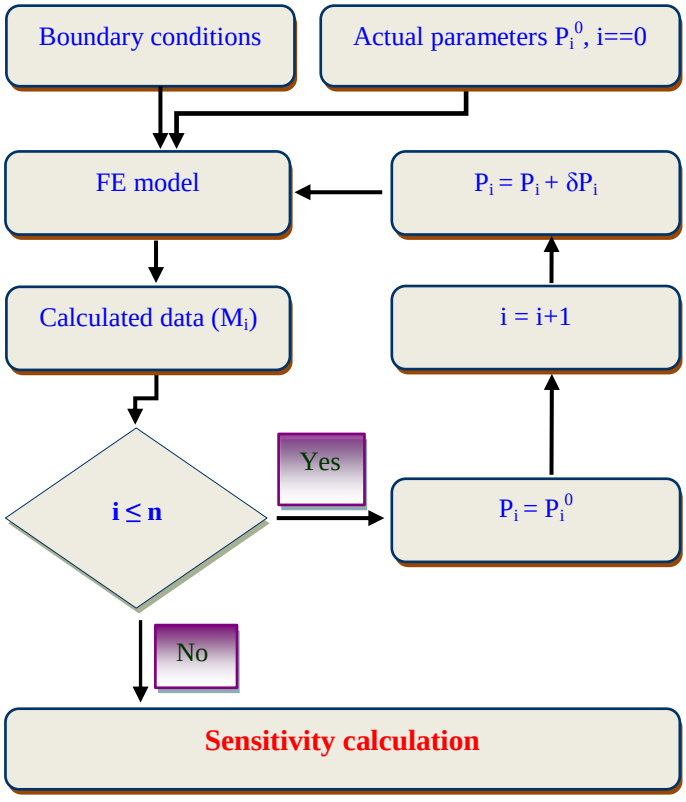

Fig. 5.2. Calculation of sensitivity matrix for *n* parameters

$$S_{ij} = \begin{bmatrix} \left(\frac{\partial \varepsilon_{11}}{\partial E_{11}}\right)_1 & \left(\frac{\partial \varepsilon_{11}}{\partial E_{22}}\right)_1 & \left(\frac{\partial \varepsilon_{11}}{\partial \nu_{12}}\right)_1 & \left(\frac{\partial \varepsilon_{11}}{\partial G_{12}}\right)_1 \\ \left(\frac{\partial \varepsilon_{22}}{\partial E_{11}}\right)_1 & \left(\frac{\partial \varepsilon_{22}}{\partial E_{22}}\right)_1 & \left(\frac{\partial \varepsilon_{22}}{\partial \nu_{12}}\right)_1 & \left(\frac{\partial \varepsilon_{22}}{\partial G_{12}}\right)_1 \\ \left(\frac{\partial \varepsilon_{12}}{\partial E_{11}}\right)_1 & \left(\frac{\partial \varepsilon_{12}}{\partial E_{22}}\right)_1 & \left(\frac{\partial \varepsilon_{12}}{\partial \nu_{12}}\right)_1 & \left(\frac{\partial \varepsilon_{12}}{\partial G_{12}}\right)_1 \\ \left(\frac{\partial \varepsilon_{11}}{\partial E_{11}}\right)_2 & \left(\frac{\partial \varepsilon_{11}}{\partial E_{22}}\right)_2 & \left(\frac{\partial \varepsilon_{11}}{\partial \nu_{12}}\right)_1 & \left(\frac{\partial \varepsilon_{11}}{\partial G_{12}}\right)_2 \\ \left(\frac{\partial \varepsilon_{22}}{\partial E_{11}}\right)_2 & \left(\frac{\partial \varepsilon_{22}}{\partial E_{22}}\right)_2 & \left(\frac{\partial \varepsilon_{22}}{\partial \nu_{12}}\right)_2 & \left(\frac{\partial \varepsilon_{22}}{\partial G_{12}}\right)_2 \\ \left(\frac{\partial \varepsilon_{12}}{\partial E_{11}}\right)_2 & \left(\frac{\partial \varepsilon_{12}}{\partial E_{22}}\right)_2 & \left(\frac{\partial \varepsilon_{12}}{\partial \nu_{12}}\right)_2 & \left(\frac{\partial \varepsilon_{12}}{\partial G_{12}}\right)_2 \\ & & \vdots & \\ \left(\frac{\partial \varepsilon_{11}}{\partial E_{11}}\right)_m & \left(\frac{\partial \varepsilon_{11}}{\partial E_{22}}\right)_m & \left(\frac{\partial \varepsilon_{11}}{\partial \nu_{12}}\right)_m & \left(\frac{\partial \varepsilon_{11}}{\partial G_{12}}\right)_m \\ \left(\frac{\partial \varepsilon_{22}}{\partial E_{11}}\right)_m & \left(\frac{\partial \varepsilon_{22}}{\partial E_{22}}\right)_m & \left(\frac{\partial \varepsilon_{22}}{\partial \nu_{12}}\right)_m & \left(\frac{\partial \varepsilon_{22}}{\partial G_{12}}\right)_m \\ \left(\frac{\partial \varepsilon_{12}}{\partial E_{11}}\right)_m & \left(\frac{\partial \varepsilon_{12}}{\partial E_{22}}\right)_m & \left(\frac{\partial \varepsilon_{12}}{\partial \nu_{12}}\right)_m & \left(\frac{\partial \varepsilon_{12}}{\partial G_{12}}\right)_m \\ \left(\frac{\partial f}{\partial E_{11}}\right) & \left(\frac{\partial f}{\partial E_{22}}\right) & \left(\frac{\partial f}{\partial \nu_{12}}\right) & \left(\frac{\partial f}{\partial G_{12}}\right) \end{bmatrix} \quad (5.24)$$

5.3.1. Convergence and stability analysis

The identification method has been verified with the use of calculated strain fields (artificial experimental database) before using the strain fields measured experimentally (real experimental database). In fact, for given material parameters (reference parameters), a strain field was created and used as an experimental strain field. Sets of initial parameters different to the reference ones were selected and the identified parameters compared to the reference values. In this way, two verifications have been achieved in order to examine the robustness of the method (convergence test) and its stability (stability analysis).

5.3.1.1. Convergence test

Influence of the experimental database

In order to verify the method's robustness, a numerical database has been constructed and used instead of the experimental database. This artificial experimental database has been generated using a set of parameters noted reference parameters. The parameters have been determined applying the developed algorithm to this numerical database. Less than 20 iterations was required to perform the identification. In each case, the obtained values are in very good agreement with those used to generate the numerical database. This procedure was repeated for different sets of reference parameters (table 5.1) in order to verify the identifiabiliy of the method for the samples with different wire volume fraction.

Moreover, since the fracture occurred at different strain levels for different samples, the effect of applied displacement was also studied. For this purpose several displacement values were applied using set 3 of reference parameters. Results are detailed in table 5.2. In all cases, the identification was successful.

Table 5.1. Identification results obtained using numerical database for three sets of reference parameters

		Set 1		**Set 2**		**Set 3**	
	Initial estimation	**Reference parameters**	Identified parameters	**Reference parameters**	Identified parameters	**Reference parameters**	Identified parameters
E_{11}	9000	3500	3500.9	3600	3601.0	3800	3801.3
E_{22}	9000	3500	3500.1	5000	5000.1	8000	8000.1
ν_{12}	0.45	0.35	0.3501	0.34	0.3401	0.24	0.24012
G_{12}	2000	1250	1250.1	1400	1400.1	1600	1600.2
Cost function		6.01e-9		6.44e-9		7.272e-9	
No. of iteration		16		19		19	

Table 5.2. Effect of applied displacement on the method's convergence, using 336-element set and set 3 of reference parameters

		Identified Parameters	
	Initial estimation	**applied displacement=0.6**	**applied displacement=1.2**
E_{11}	9000	3800.5	3800.7
E_{22}	9000	8000	8000.1
ν_{12}	0.45	0.24002	0.24003
G_{12}	2000	1600.1	1600.1
Cost function		3.04e-9	4.74e-9
No. of iteration		15	18

Influence of the number of element and mesh size

The effect of mesh size was verified choosing 66, 140, 336, 594 and 672 elements in a same zone. The results, presented in table 5.3, show that the parameters are identified in all cases. It is known that the element size has an important role in finite element model. Thus the response of the system should be compared in different cases in order to find the element size for which the response does not vary. In order to determine the best conditions, the effect of element size on the reaction force at the elements on the sample's frontier is shown in Fig. 5.3. The nominal parameters (reference) considered in this figure are 3800, 8000, 0.24 and

1600 and the applied displacement is 0.6 mm. As seen in the figure, the reaction force does not vary when the number of elements is larger than or equal to 336. Therefore, this mesh size is selected for the real experimental database.

In order to minimize the calculation time, it is necessary to find a zone of interest (ZOI) as small as possible. To this end, several zones with different number of elements (336, 400, and 656 with an identical mesh size) were tested (Fig. 5.4.). In all cases, the method converged and parameters were identified (table 5.4). From table 5.4, one finds that the iteration number increases with increasing the number of elements.

From above discussion, a system including a structured quadratic-dominated rectangular mesh with 714 nodes, 656 elements and a ZOI with 336 elements (Fig. 5.4-a) was selected to be applied for identification process.

Table 5.3. Effect of the mesh size on the identifiably of parameters, applied displacement=0.6 mm

		Identified Parameters				
	Initial estimation	**66-element set**	**140-element set**	**336-element set**	**594-element set**	**672-element set**
E_{11}	9000	3801	3800.7	3800.5	3800.4	3800.4
E_{22}	9000	8000.1	8000.1	8000	8000.1	8000.1
ν_{12}	0.45	0.24004	0.24003	0.24002	0.24002	0.24002
G_{12}	2000	1600.1	1600.1	1600.1	1600.1	1600.1
Cost function		3.11e-9	3.18e-9	3.04e-9	2.22e-9	2.69e-9
No. of iteration		16	15	15	16	15

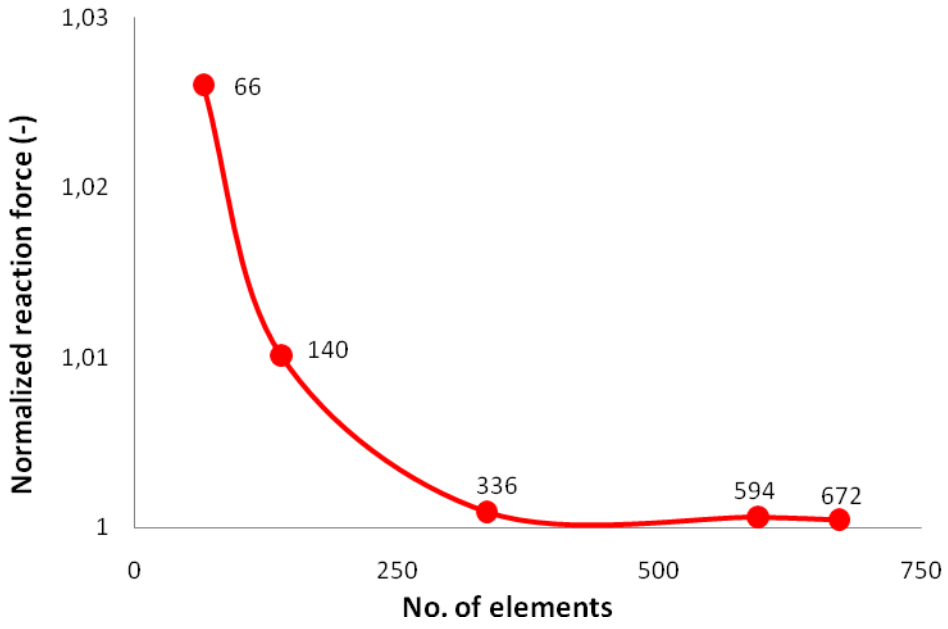

Fig. 5.3. Effect of mesh size on the reaction force

Table 5.4. Effect of the number of elements on method's convergence, applied displacement=1.2 mm

		Identified Parameters		
	Initial estimation	**336-element set***	**400-element set***	**656-element set***
E_{11}	9000	3800.7	3800.6	3800.7
E_{22}	9000	8000.1	8000.1	8000.1
ν_{12}	0.45	0.24003	0.24003	0.24003
G_{12}	2000	1600.1	1600.1	1600.1
Cost function		4.74e-9	3.67e-9	4.77e-9
No. of iteration		18	20	22

* These element sets are shown in Fig. 5.4.

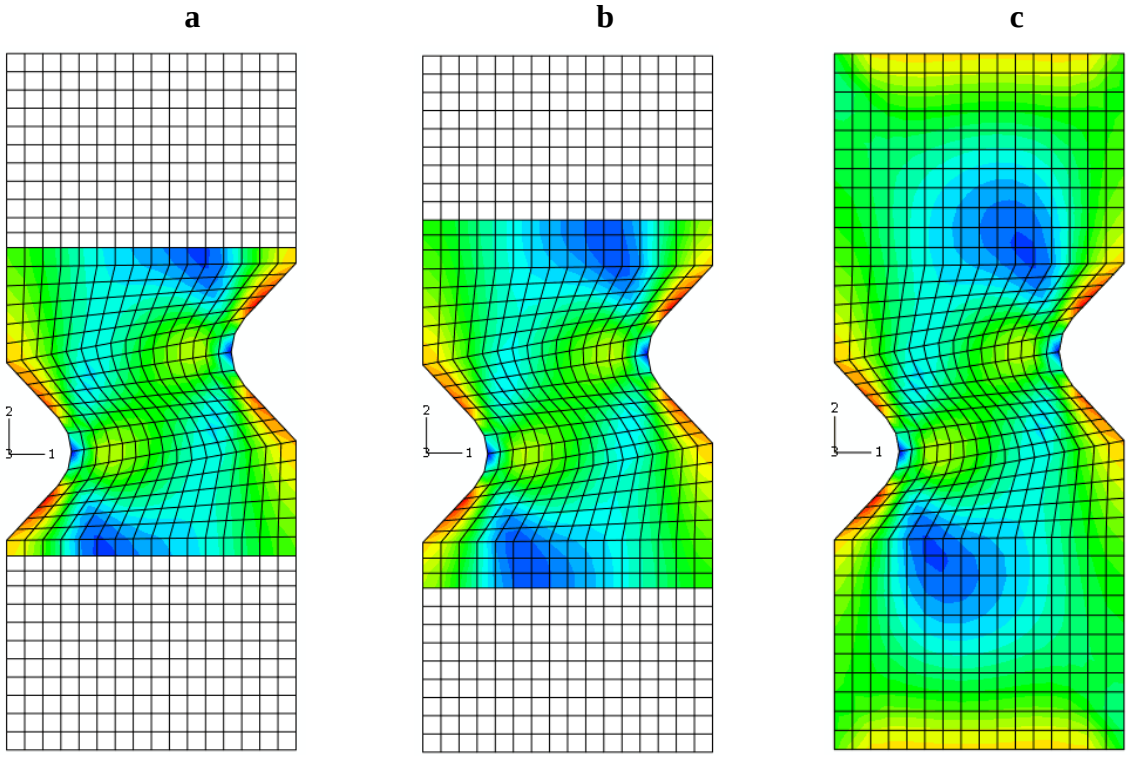

Fig. 5.4. The zones of interest (ZOI) with a) 336, b) 400, c) 656 elements

Influence of the initial estimation

Several initial parameters sets were tested. In all cases, the method converged and the same materials were identified. The results for three sets were listed in table 5.5. As shown in this table, when the initial parameters are the same as the reference ones, the material parameters are identified during the first iteration. However, when far away from the solution, the convergence will be obtained after some numbers of iteration. The evolutions of the cost function and parameters versus iteration number for three different sets of initial guess are shown in Fig. 5.5 - 5.7. These figures show that the method converges to the reference values starting from initial parameters smaller or larger than the reference ones.

Table 5.5. Identification results for three different sets of initial estimation

	Guess values 1		Guess values 2		Guess values 3	
	Initial estimation	Identified Parameters	Initial estimation	Identified Parameters	Initial estimation	Identified Parameters
E_{11}	3800	3800	6000	3801.2	10000	3801.3
E_{22}	8000	8000	2500	8000.1	12000	8000.1
ν_{12}	0.24	0.24	0.3	0.24011	0.45	0.24012
G_{12}	1600	1600	2150	1600.2	4500	1600.2
Cost function	0		6.545e-9		7.272e-9	
No. of iteration	1		20		19	

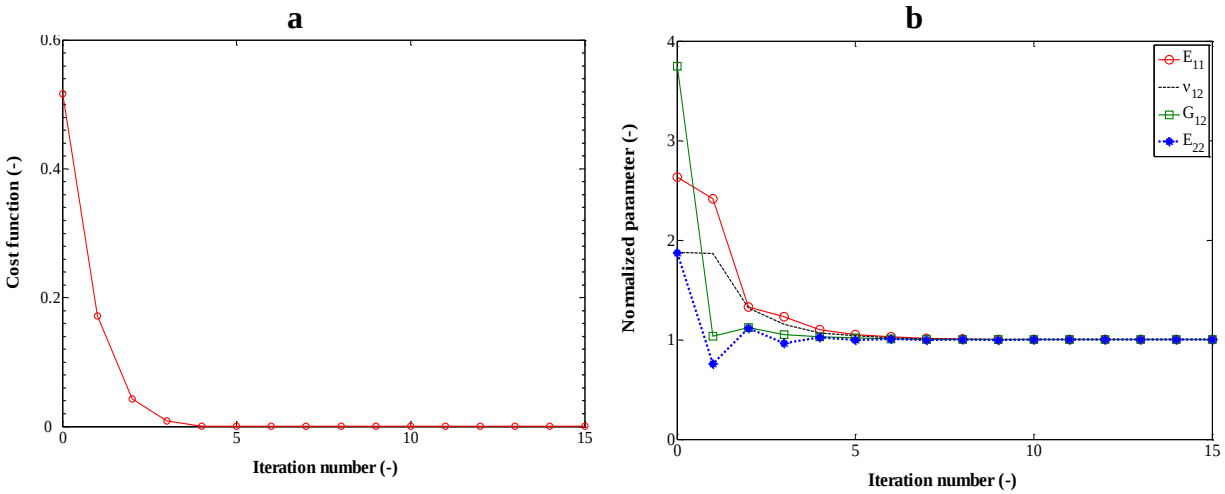

Fig. 5.5. Variation of a) the cost function and b) the parameters vs. iteration number for 336-element set and applied displacement=0.6 mm; convergence from the larger values

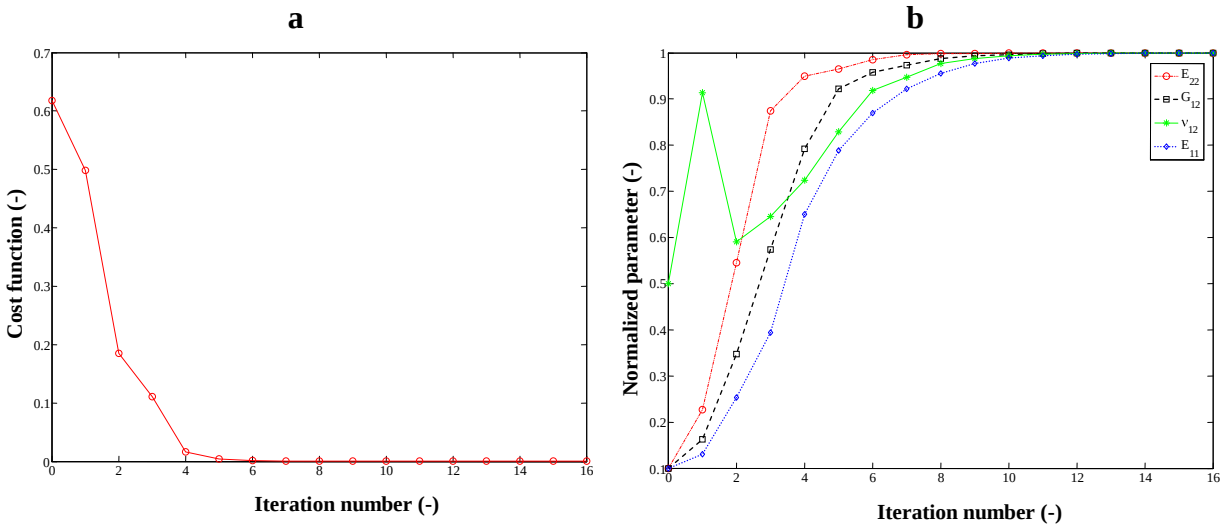

Fig. 5.6. Evolution of a) the cost function and b) the parameters versus iteration number for 336-element set and applied displacement=0.6 mm; convergence from the larger values

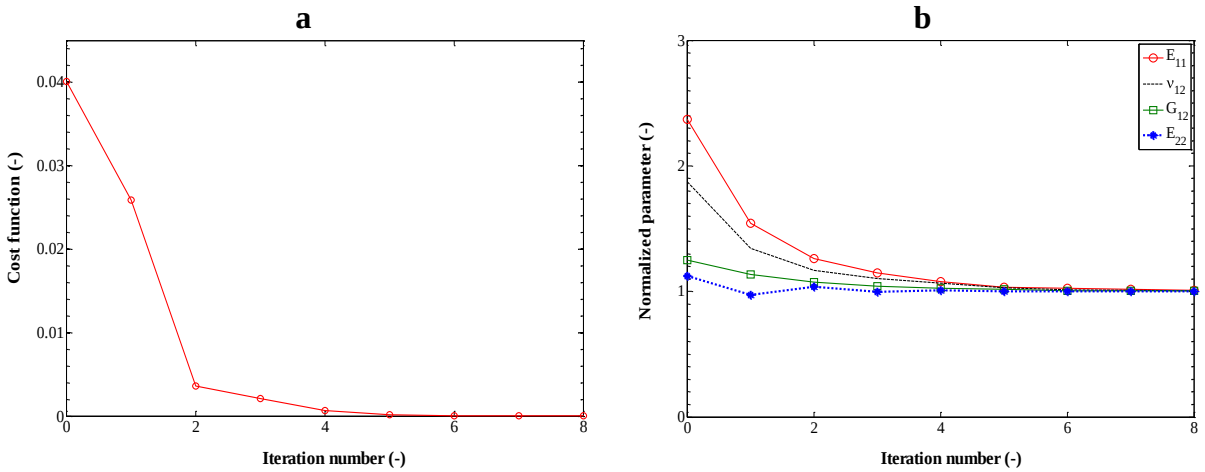

Fig. 5.7. Variation of a) the cost function and b) the parameters versus iteration number for 336-element set and applied displacement=0.6 mm; starting from the values close to the solution

Influence of the regularization parameter (μ)

The effect of the regularization parameter (μ) has been studied and several values have been tested (10^{-1}, 10^{-2} to 10^{-10}). In all cases, only the number of iteration was different and no relationship was found. But it seems better to choose a regularization parameter between 10^{-4} and 10^{-2}.

The identification results show that the nominal values are obtained in a few iterations with a very great accuracy which indicates the performance of the method (convergence test). It should be noted that in this work the convergence criteria is reached when the cost function becomes less than 1E-8 and generally this condition is satisfied beyond 10 iterations (Table 5.6). But in reality, the identified parameters are very close to the reference ones when the cost function decreases to a value about 1E-5 and after about five iterations.

Table 5.6. Variation of the cost function and the parameters with iteration number.

Iteration No.	E_{11}	E_{22}	ν_{12}	G_{12}	Cost Function (CF)	Average discrepancy (%)
0	9000	9000	0.45	2000	3.04E-002	65.5
1	6641.8	7789.1	0.36092	1828.0	1.634E-002	34.1
2	4997.3	8272.7	0.29563	1741.8	3.988E-003	16.7
3	4430.6	8026.1	0.26652	1677.1	1.278E-003	8.2
4	4107.9	8059.9	0.25610	1647.5	4.332E-004	4.6
5	3920.3	8000.7	0.24669	1622.7	8.173E-005	1.8
6	3870.5	8013.2	0.24214	1610.0	2.936E-005	0.9
7	3838.2	8005.4	0.24149	1606.1	6.152E-006	0.5
8	3815.5	8001.0	0.24042	1602.8	2.429E-006	0.2
9	3807.8	8001.0	0.24033	1601.1	2.281E-007	0.1
10	3805.1	8000.7	0.24020	1600.6	1.01E-007	0.07
11	3802.4	8000.2	0.24008	1600.4	3.873E-008	0.03
12	3801.5	8000.3	0.24006	1600.2	8.949E-009	0.02
13	3800.9	8000.0	0.24003	1600.1	6.362E-009	0.01

From above discussion, it can be concluded that the method converges in all cases and the reference parameters can be identified. Thus, the convergence test is satisfied and the method can be applied for the actual experimental strain fields if it satisfies the stability test.

5.3.1.2. Stability analysis

Since the experimental strain fields are generally affected by the errors, the stability analysis has been done to verify the influence of the errors. In other words, the stability study shows the ability of the method to identify the parameters at presence of errors. Accordingly, a perturbed database with systematic errors has been created numerically. For generating this type of database, 5% or 10% of the average values were added to all the components of the artificial experimental database (bias errors):

$M_p^{ex} = M_{i,j}^{ex} + e_i$ for i = 1, 2, 3 and j=1, m

where M_p^{ex} and M^{ex} are respectively the perturbed and artificial experimental database, *m* is the number of measured points and *e* represents the uncertainty (error):

$$e_1 = \frac{a}{m}\sum_{i=0}^{m}\varepsilon_{11,i}^{Exp} \quad e_2 = \frac{a}{m}\sum_{i=0}^{m}\varepsilon_{22,i}^{Exp} \quad e_3 = \frac{a}{m}\sum_{i=0}^{m}\varepsilon_{12,i}^{Exp} \qquad a = 0.05 \text{ or } 0.10.$$

In the case of perturbed data (table 5.7), a 5% error leads to the small error about 1.8% (E_{11}: 1.25%, E_{22}: 0.2, ν_{12}: 4.3, G_{12}: 1.29%) in the identification values. For a 10% error, the identified parameters deviate about 3.3% (E_{11}: 2%, E_{22}: 0.66, ν_{12}: 8.49, G_{12}: 1.97%). This analysis demonstrates the stability of the inverse algorithm and consequently the capability of the method to extract the right values even from noisy strain fields. Fig. 5.8 and 5.9 illustrate the evolutions of the cost function and parameters versus iteration number for 5% and 10% error, respectively. These results show that the parameter ν_{12} is sensitive to the perturbation level.

The parameters identified with the use of the perturbed strain fields are in the same order of the reference parameters. The results demonstrate that the method is stable enough to be applied for actual experimental test because it is able to provide good results from a noisy database.

Table 5.7. Identification results using perturbed experimental database (stability study)

			Identified Parameters (*)			
	Initial estimation	Reference parameters	**database with 5% error**		**database with 10% error**	
				Error (%)		Error (%)
E_{11}	9000	3800	3847	1.2	3877	2.02
E_{22}	9000	8000	7987	0.2	7947	0.66
ν_{12}	0.45	0.24	0.2503	4.3	0.2604	8.5
G_{12}	2000	1600	1621	1.3	1631	1.97
CF			3.51e-3		1.34e-2	
No. of iteration			15		12	
Relative error (%)			1.8		3.3	

(*) using 336-element set with an applied displacement=0.6 mm

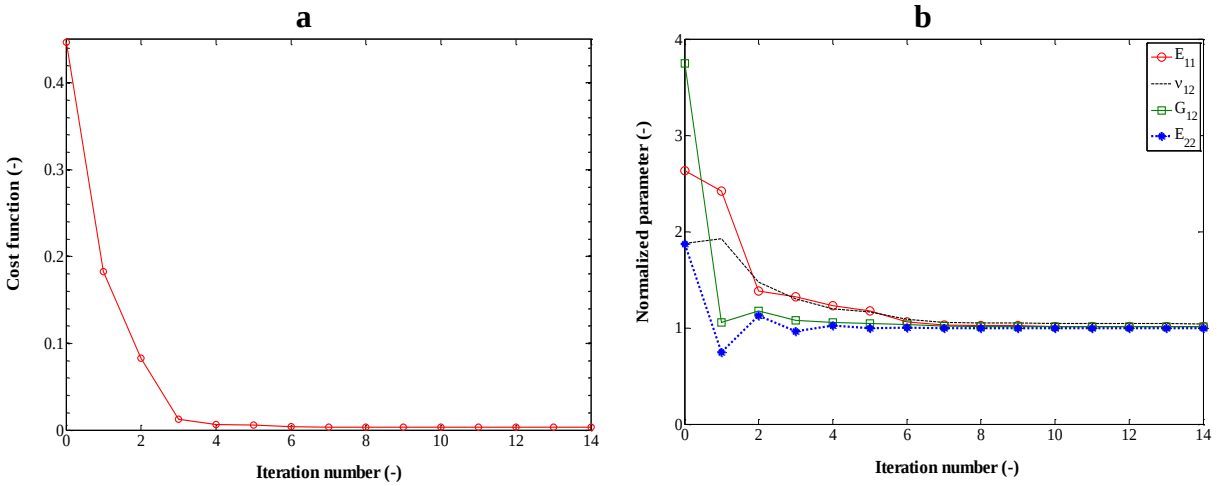

Fig. 5.8. Evolution of a) the cost function and b) the parameters vs. iteration number for 5% error (336-element set and applied displacement=0.6 mm)

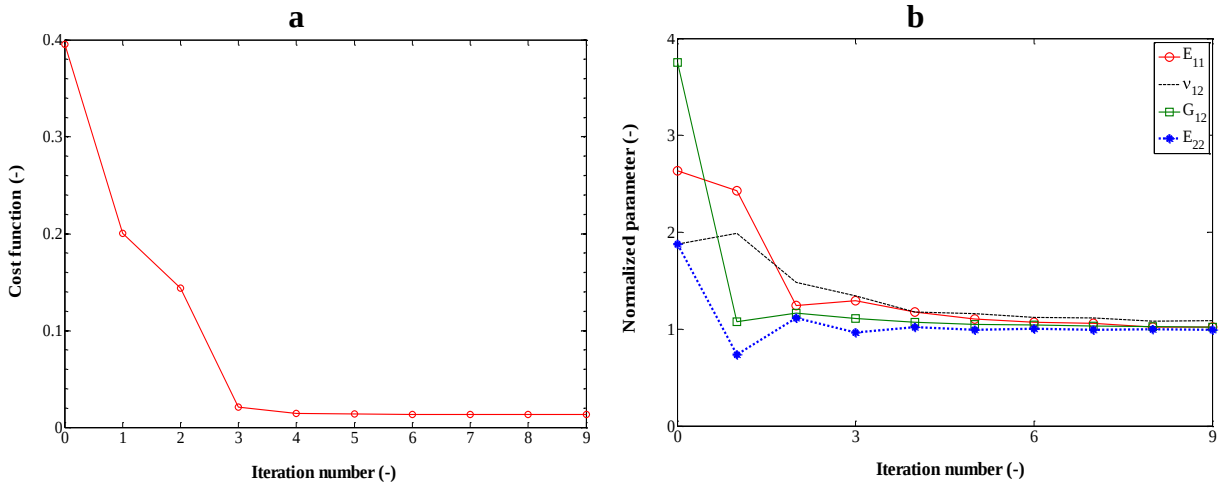

Fig. 5.9. Variation of a) the cost function and b) the parameters vs. iteration number for 10% error (336-element set and applied displacement=0.6 mm); the initial parameters are the same as

5.3.2. Application for experimental strain fields

Actual experimental strain fields are obtained from the heterogeneous test of the composite specimens with different wire volume fractions at room temperature. To determine the experimental strain fields, as mentioned before, two software were used and the results are compared.

Correli-Q4 software

To construct an experimental database, the images were processed using the Correli-Q4 software. During the process, the ZOI are meshed and the ε_{11}, ε_{22} and ε_{12} are extracted for the 16x16(pixels)-sub-image (0.65x0.65 mm). It should be noted that it was not possible, in some

samples, to find the strain values in all elements. In these cases, the element size increased. The other problem was to find the values for the elements located on the sample's border (frontier). For this purpose, a new sub-routine was developed to extract the values for points corresponding to the center of elements in the FE model. The input is hence the output of the Correli-Q4 software. In the case where there is no data for an element, the routine can not continue any more. Therefore, several calculations were run to approach to the frontier and reduce the element size. These calculations were very time-consuming (Computation time could exceed five hours using a double core processor). Among the 20 tested samples at room temperature, the results were obtained only for 4 specimens. Because, the failure strain in some specimens were not high enough to overcome the noise. The element size and number in FE and the sub-image location in experiment are compared in Fig. 5.10.

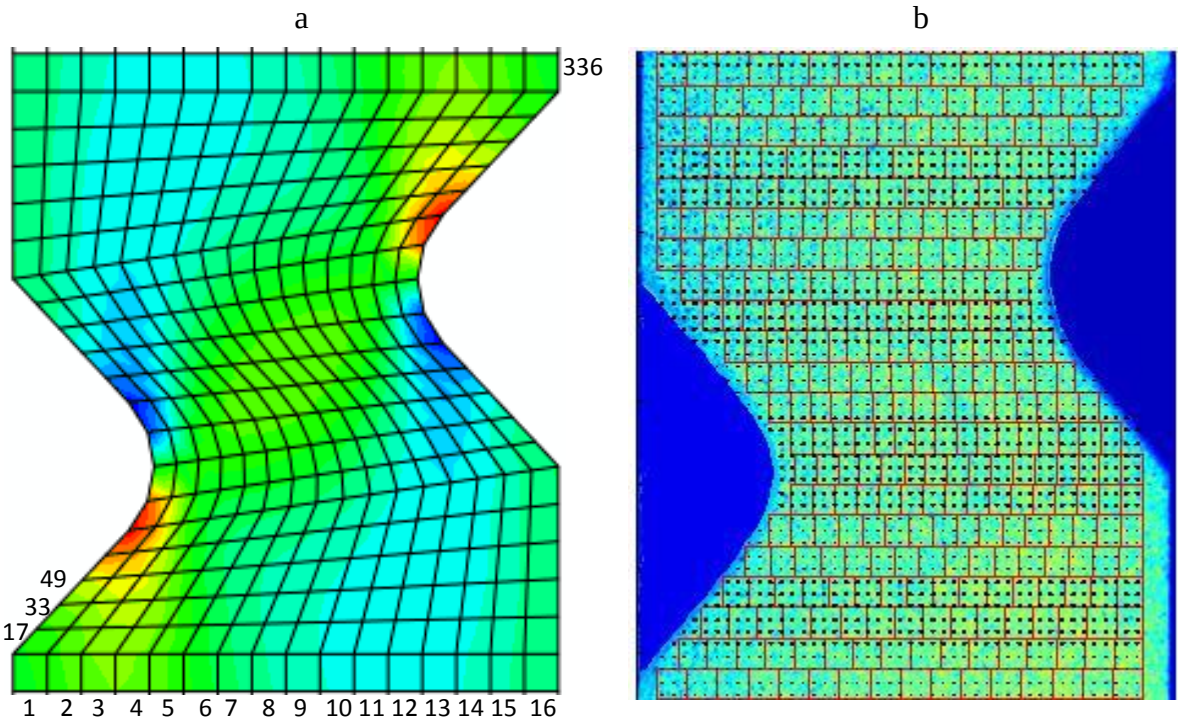

Fig. 5.10. The element size and the sub-image location in a) FE and b) experimental studied areas (the numbers in the FE zone show the element number)

Vic2D software

As mentioned, the calculations with the Correli-Q4 are very time-consuming. Moreover, with this software the strain fields were extracted for a few numbers of samples. In order to overcome the problems when using the Correli-Q4 software and verify the results obtained by this software, the images were processed using other software. The new software called Vic2D seems to be more adopted in comparison to the Correli-Q4. The specimens were analyzed and the strain fields were determined for most of the samples. In this case, the strain

components were extracted for the elements coordinates in the numerical part after correction of the starting point. In other words, using this software allows extracting directly the strain for the points used in the FEM.

5.4. Identification results

5.4.1. Identification results using Correli-Q4

Table 5.8 details the identification results which were obtained using the Correli-Q4 software. For each sample, several calculations were performed starting from different initial guess values. This table shows that when the fiber volume fraction increases the parameters E_{11}, E_{22} and G_{12} increase but the Poisson's ratio decreases.

Table 5.8- Identification results, the experimental database created using Correli-Q4 software

V_f	E_{11} (MPa)	E_{22} (MPa)*	ν_{12}	G_{12} (MPa)	CF
0	3360±100	3575±20	0.35±0.01	1455±20	0.1100
0.03	3495±60	4575±10	0.33±0.005	1770±10	0.1090
0.03	3535±100	4505±20	0.33±0.005	1785±20	0.0845
0.10	3880±100	6555±90	0.25±0.01	2055±70	0.35

* Direction 22 is the loading direction and is parallel to the wire axis

The strains (ε_{11}, ε_{22} and ε_{12}) in each element obtained experimentally are compared to the numerical ones in Fig. 5.11-5.13. The numerical database was obtained using the identified parameters. A good correlation is observed in these figures.

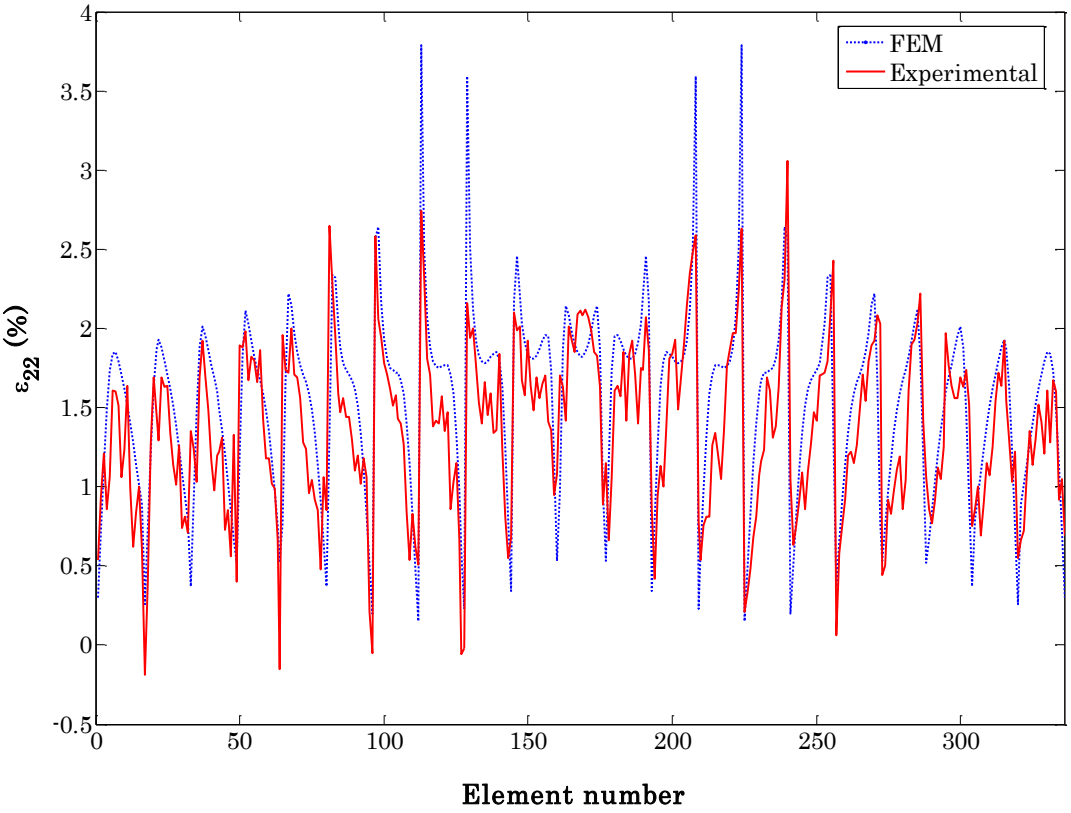

Fig.5.11- Strain ε_{22} calculated numerically in each element (noted in Fig. 5.10) using the identified parameters compared to the experimental values, direction 22 is the loading direction which is parallel to the wire axis

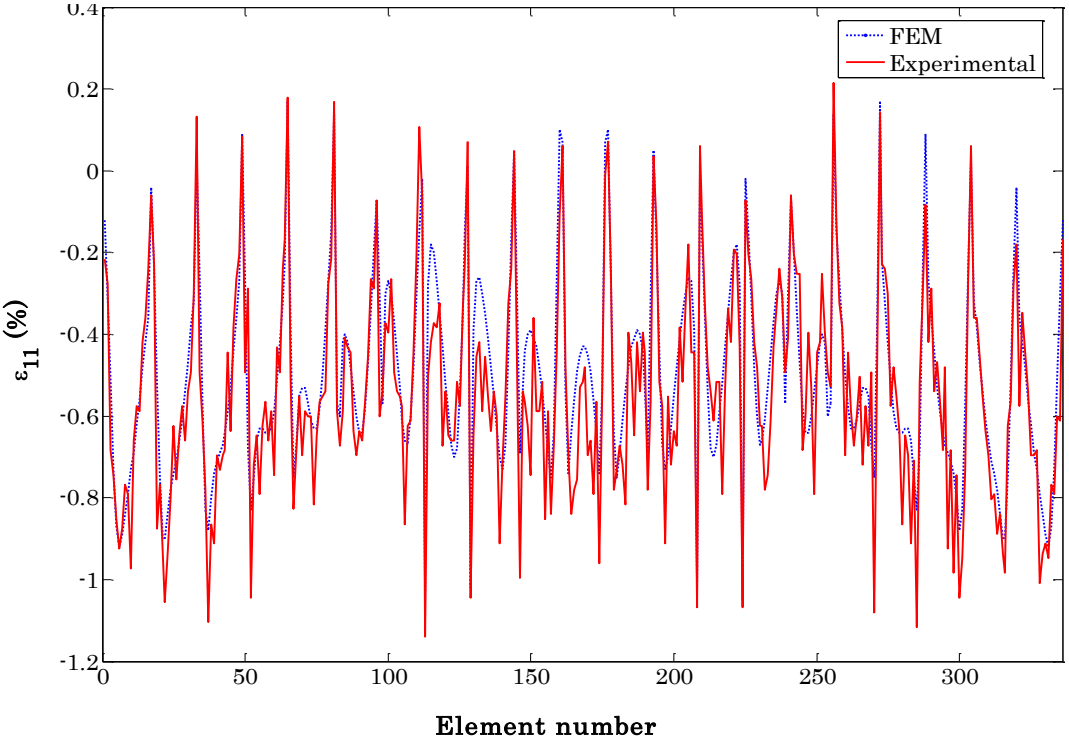

Fig.5.12- Strain ε_{11} calculated numerically in each element (noted in Fig. 5.10) using the identified parameters compared to the experimental values

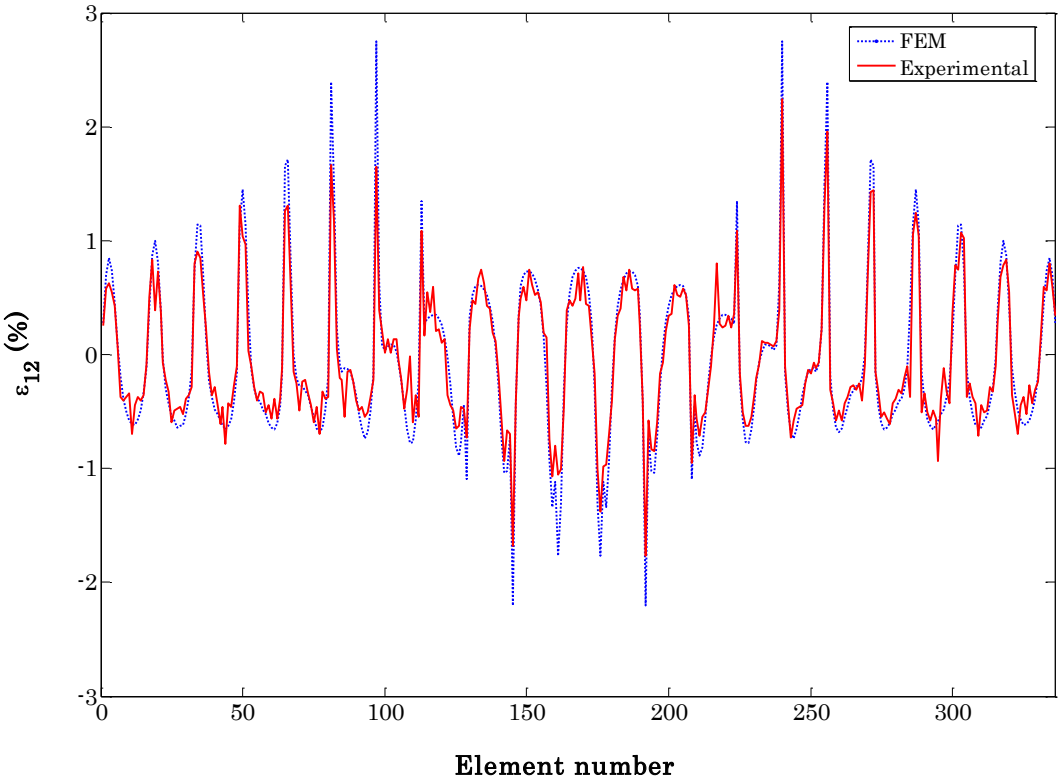

Fig.5.13- Strain ε_{12} calculated numerically in each element (noted in Fig. 5.10) using the identified parameters compared to the experimental values

5.4.2. Identification results using Vic2D

The identified parameters using the experimental database extracted by Vic2D are detailed in table 5.9. A good correlation is found by comparing these results to the results detailed in table 5.8.

Table 5.9- Identification results, the experimental database created using Vic2D software

V_f	E_{11} (MPa)	E_{22} (MPa)*	ν_{12}	G_{12} (MPa)
0	3430±70	3550±20	0.345±0.005	1480±10
0.03	3470±80	4120±20	0.33±0.01	1650±20
0.05	3670±80	4760±20	0.305±0.005	1705±20
0.10	3980±50	6440±10	0.255±0.005	2230±10

* Direction 22 is the loading direction which is parallel to the wire axis

In Fig. 5.14 and 5.15 the displacement and strain fields determined experimentally using Vic2D are compared to the numerical ones. These figures show good correlations between experimental and numerical fields.

ε_{11}- Experimental

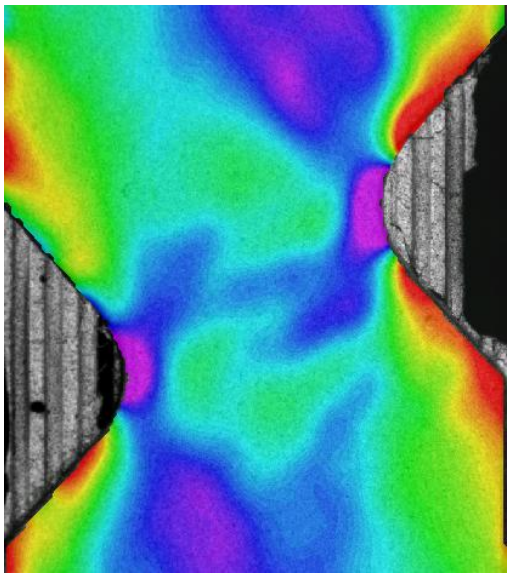

ε_{11}-Numerical

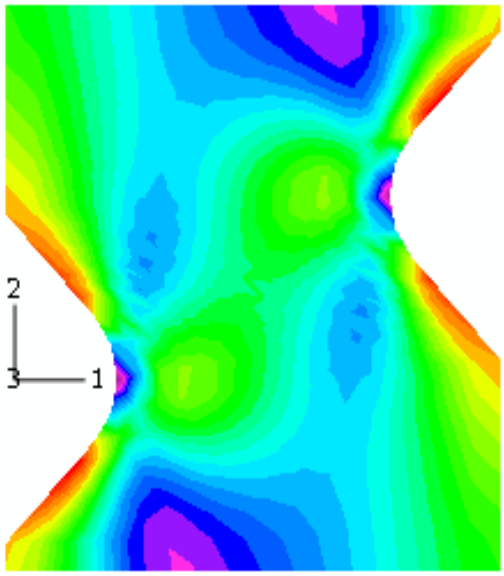

ε_{12}- Experimental

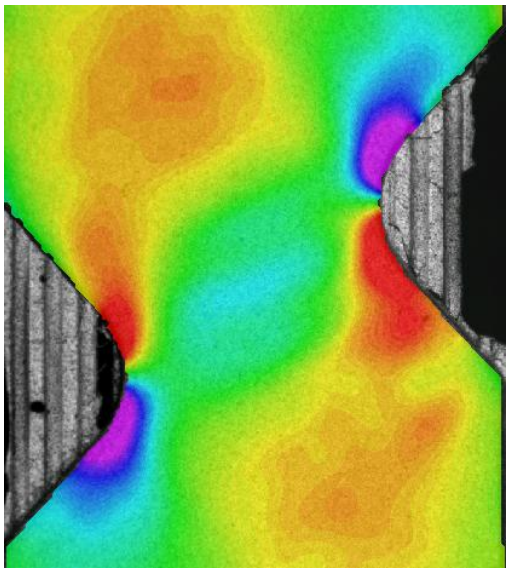

ε_{12}-Numerical

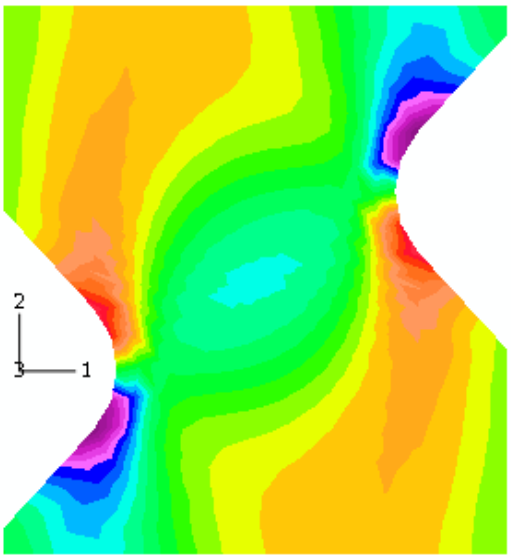

ε_{22}- Experimental

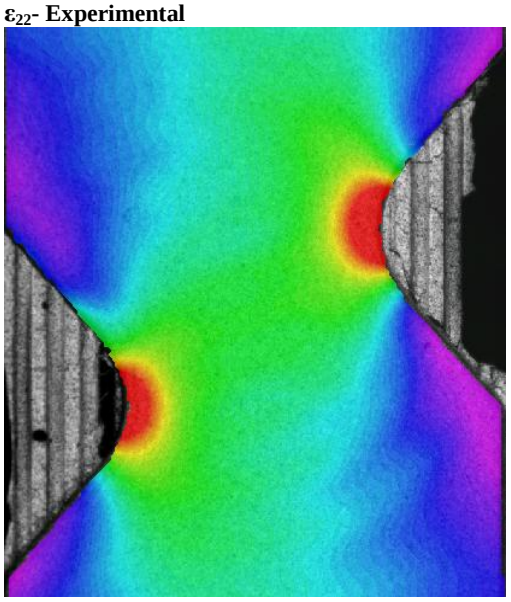

ε_{22}-Numerical

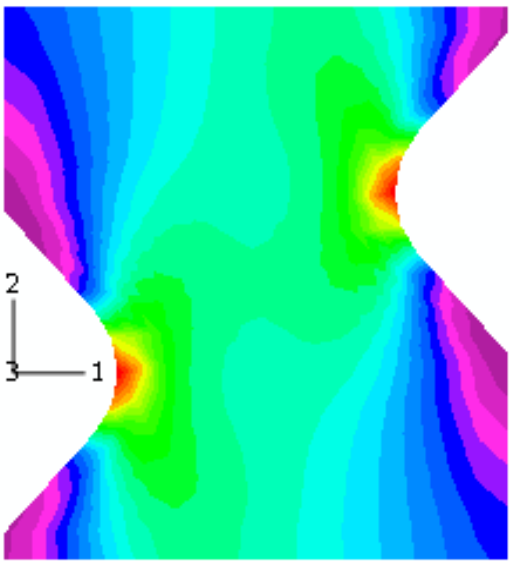

Fig. 5.14. Strain fields determined experimentally using Vic2D are compared to the numerical ones

obtained using the identified parameters

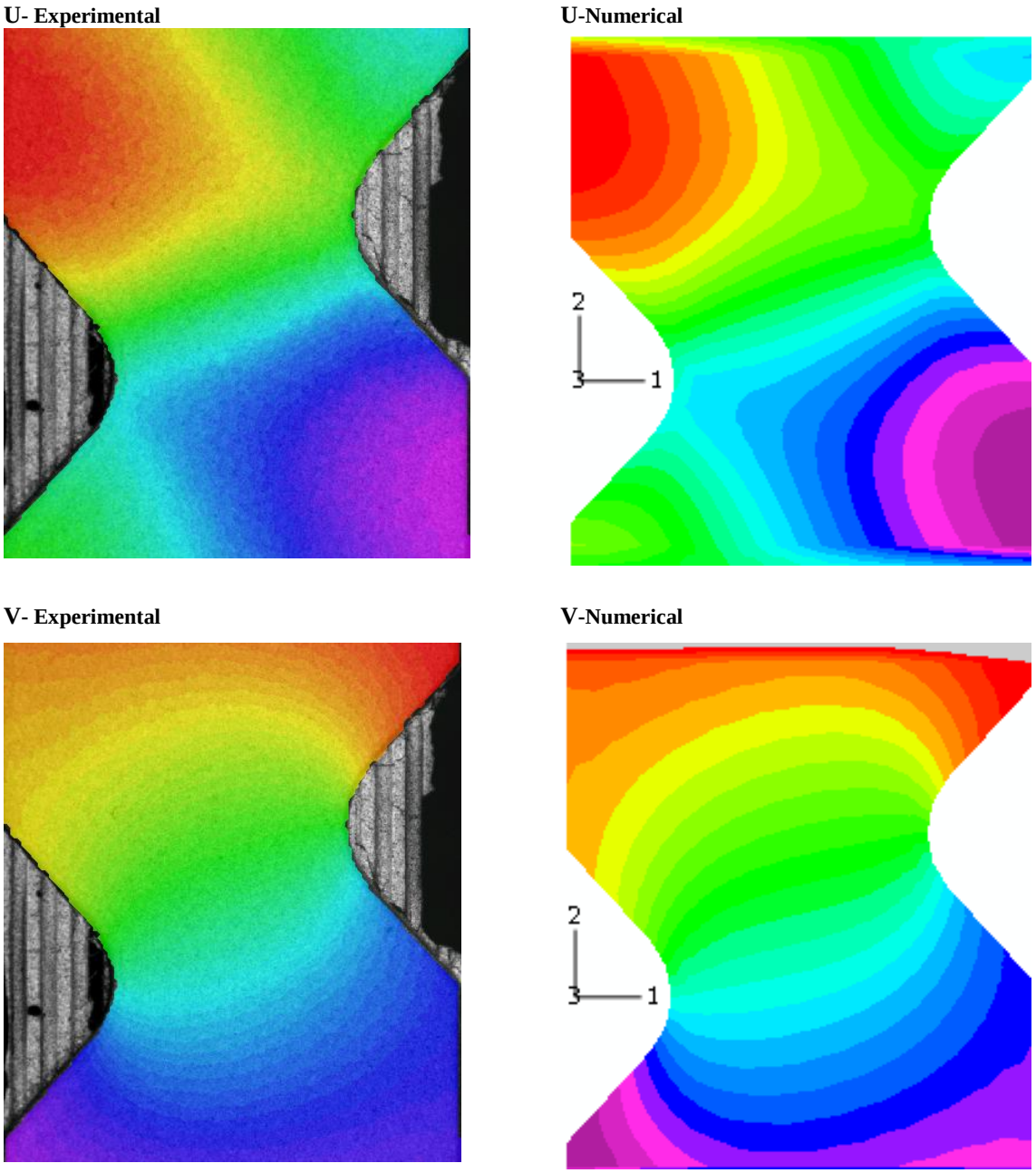

Fig. 5.15. Displacement fields determined experimentally using Vic2D are compared to the numerical ones obtained using the identified parameters

From experimental results, it is possible to validate the Young modulus in the load direction (E_{22}) for all samples. It is also possible to verify the E_{11} in the samples without fiber which could be identical to the E_{22} in the same specimen. From uniaxial tensile test results, the E_{22} is about 3300, 4200 and 5300 MPa for the samples with 0, 6 and 12% wire volume fraction. In Fig. 5.16 the identified E_{22} is compared to the results obtained from tensile test. It should be noted that the studied composite samples exhibit a non linear elastic behavior. The Young modulus from tensile test was obtained considering all of this non linear part which leads to

find values smaller than real ones. This could justify the difference between the identified E_{22} and the Young modulus obtained from tensile test.

Marfia and Sacco [Marfia and Sacco 2005] calculated analytically the stiffness tensor for NiTi wire polymer matrix composite. Some constants used in this work and also their results are listed in table 5.10. Jarali and co-workers [Jarali and Raja 2008] have done a similar work and obtained the same results. In Fig. 5.17 the results calculated by Marfia and Sacco are compared with VIC2D results.

Table 5.10. Material parameters and results obtained by Jarali et al. [Jarali and Raja 2008] and Marfia and Sacco [Marfia and Sacco 2005]

	E_m (MPa)	ν_m	E_f (MPa)	ν_f	G_f (MPa)	G_m(MPa)
Jarali et al. 2008	3450	0.35	70000	0.33	46550	1280
Marfia and Sacco, 2005	3600	0.305	70000	0.33	46550	
The results obtained for a wire volume fraction of 3.6%						
	E_{11} (MPa)	E_{22} (MPa)	G_{12}(MPa)	ν_{21}	ν_{12}	
	4456	6382	1542	0.44	0.307	

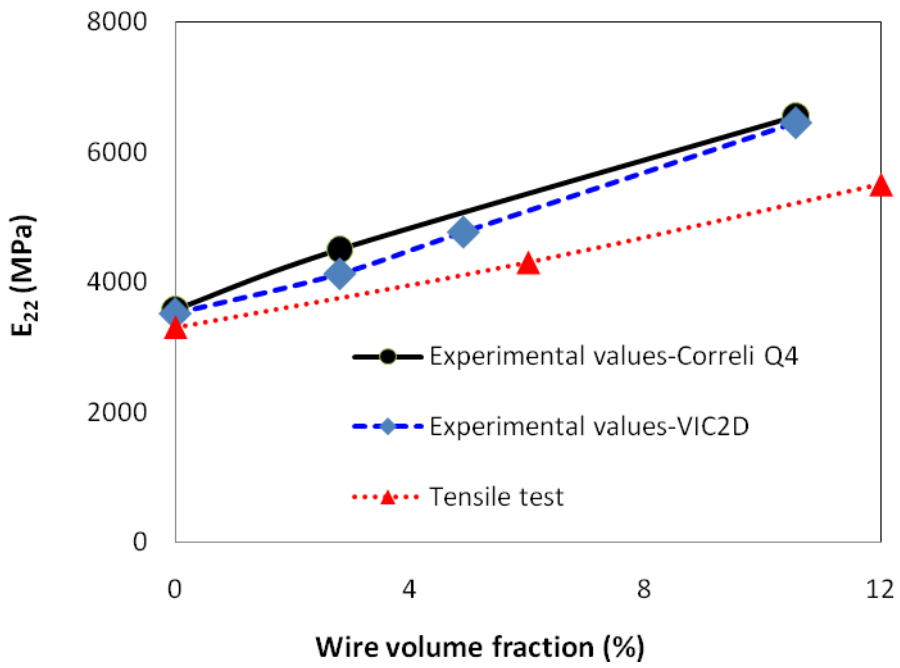

Fig. 5.16. Identified E_{22} (in the loading direction) compared to the results obtained from tensile test

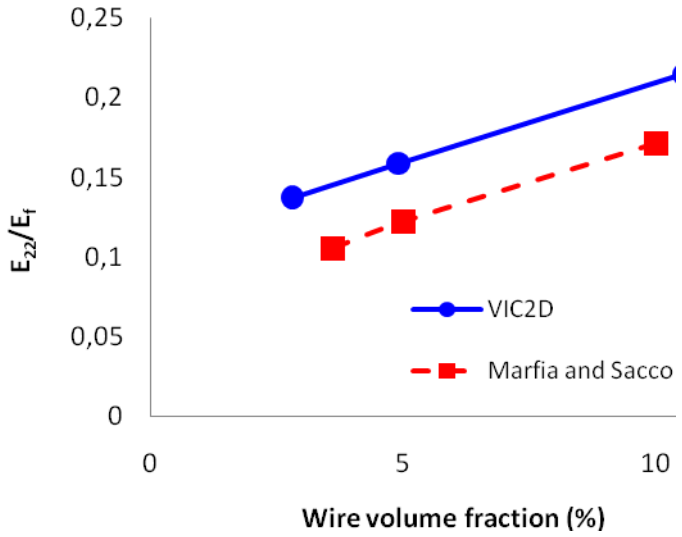

Fig. 5.17. Identification results compared to the results calculated by Marfia and Sacco [Marfia and Sacco 2005]

In order to verify the identified values, these parameters were calculated for different wire volume fraction using Sim-CEEC software. This software was developed by F. Meraghni on the basis of the Mori-Tanaka's model and the formulations were published elsewhere [Meraghni et al. 1996, Meraghni et al. 1995, Desrumaux et al. 2001]. The results are detailed in table 5.11. Comparing to the calculated parameters (Fig. 5.18), the identified results seem to be in good correlation with the expected values.

Table 5.11. Material parameters obtained using Mori-Tanaka's model (E_f=30000 MPa, ν_f=0.3)

V_f	E_{11} (MPa)	E_{22} (MPa)*	ν_{12}	G_{12} (MPa)
0.00	3500	3500	0.36	1287
0.03	3716	4284	0.31	1350
0.05	3854	4807	0.29	1394
0.10	4194	6116	0.24	1511

* Direction 22 is the loading direction which is parallel to the wire axis

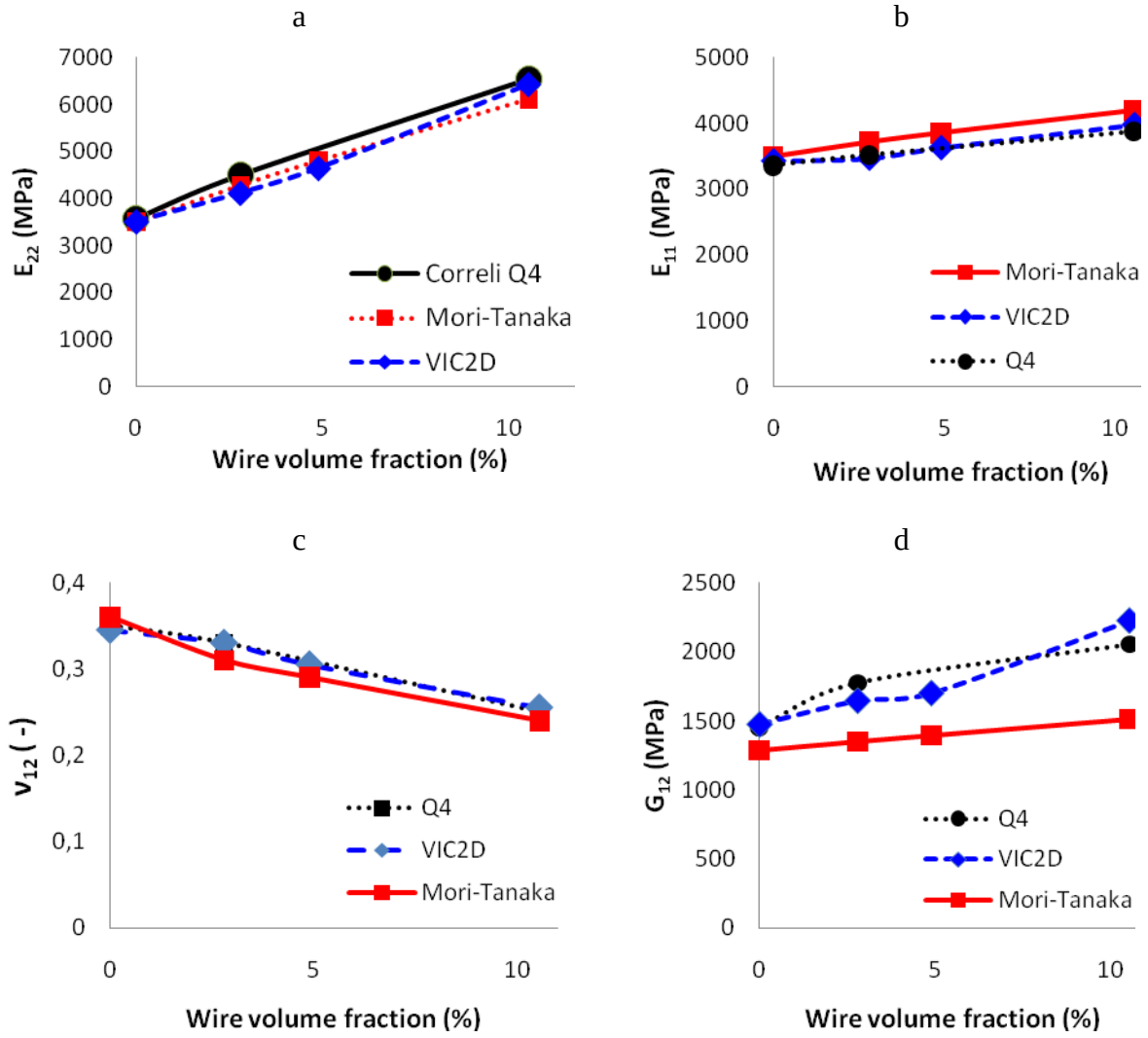

Fig. 5.18. Identification results compared to the results obtained using Mori-Tanaka's model

5.5. Conclusion

The identification method in this work was proposed to extract the four independent elastic constants E_{11}, E_{22}, G_{12} and ν_{12} of an orthotropic composite material. The studied material is NiTi wire epoxy matrix composite with four different fiber volume fractions.
The objective was to identify simultaneously the material parameters using the heterogeneous test. Thus, the samples with complex geometry were subjected to the tensile load. The surface displacements are measured and strains are subsequently calculated using the Correli-Q4 and Vic2D software. An inverse method was developed and the material parameters were identified.

During the inverse method the strain field measured experimentally was compared to the strain field computed numerically. A finite element model, using ABAQUS standard, served as numerical counterpart/match for the experimental set-up.

A cost function was constructed on the basis of strain components (ε_{11}, ε_{22} and ε_{12}) and the applied load (f). The inverse problem was solved iteratively by minimizing the cost function which shows the difference between the measured and computed values. In each iteration, the sensitivity matrix was calculated using finite difference method. This matrix expresses the sensitivity of the measured quantities (strains and load) to variation of the identification parameters. The material parameters in the FE model were changed on the basis of sensitivity calculation. By updating the four independent elastic moduli the difference between the experimental and numerical database was minimized and the material parameters were consequently identified.

The identification method was verified before using the experimental database. In this way, two verifications have been achieved: the convergence test (robustness of the method) and the stability analysis (effect of the experimental errors). The numerical study demonstrates the stability of the inverse method and its capability to be applied for the studied NiTi wire composite samples.

The experimental strain fields were extracted using Correli-Q4 and Vic2D software. The material parameters for the composite samples with four different wire volume fractions were identified and compared to each other. The identified parameters were also compared to those obtained using Mori-Tanaka's model. Moreover, the strain fields which were determined numerically using the identified parameters were compared to the experimental ones. Good correlations were found in all cases.

Additionally, since the method is validated, it could be applied to estimate the actual parameters of NiTi SMA wires. In fact, residual stress and the cooling under stress can change the transformation characteristics of NiTi wires. Furthermore, the transformation occurring on the constraint of matrix may be different from that of wire in absence of matrix. For this purpose, it is essential for the matrix to sustain a strain level about 7%.

References

[Cooreman et al. 2007] Cooreman S., Lecompte D., Sol H., Vantomme J., Debruyne D., Elasto-plastic material parameter identification by inverse methods: Calculation of the sensitivity matrix, International Journal of Solids and Structures 44 (2007), p. 4329–4341.

[Desrumaux et al. 2001] Desrumaux F, Meraghni F, Benzeggagh ML. "Generalised Mori-Tanaka scheme to model anisotropic damage using numerical Eshelby tensor", Journal of Composite Materials 35 (7) (2001), p. 603-624.

[Endelt and Nielsen 2005] Endelt, B. and Nielsen, KB. General framework for analytical sensitivity analysis for inverse identification of constitutive parameters. In: Proceedings of COMPLAS, 8th International Conference on Computational Plasticity. September 2005, Barcelona – Spain.

[Furgiuele et al. 1997] Furgiuele FM, Muzzupappa M, Pagnotta L. A full-field procedure for evaluating the elastic properties of advanced ceramics. Experimental Mechanics 37 (1997), p. 285–291.

[Gavrus 1996] Gavrus A. Identification automatique des paramètres rhéologiques par analyse inverse. PhD thesis, L'Ecole Nationale Supérieure des Mines de Paris, 1996.

[Gavrus et al 1999] Gavrus A, Massoni E, and Chenot JL. The rheological parameter identification formulates as an inverse finite element problem. Inverse Problem in Engineering 7 (1999), p. 1-41.

[Gavrus et al. 1996] Gavrus A, Massoni E., Chenot JL., An inverse analysis using a finite element model for identification of rheological parameters, Journal of Materials Processing Technology 60 (1996), p. 447-454.

[Gavrus et al. 2008] Gavrus A, Banu M, Ragneau E, Maier C, Oleksik V. An inverse analysis approach of the Erichsen test starting from a finite element model, Int J Mater Form Suppl 1 (2008), p. 5–8.

[Genovese et al. 2004] Genovese K, Lamberti L, Pappalettere C. A new hybrid technique for in-plane characterization of orthotropic materials. Experimental Mechanics 44 (2004), p. 584–592.

[Ghouati and Gelin 1998] Ghouati O and Gelin JC., Identification of material parameters directly from metal forming processes, Journal of Materials Processing Technology (1998), p. 560–564.

[Ghouati and Gelin 2001] Ghouati O and Gelin JC., A finite element-based identification method for complex metallic material behaviour, Computational Materials Science 21 (2001), p. 57–68.

[Hild and Roux 2008] Hild F, and Roux S. CORRELI-Q4: A software for “Finite-element” displacement field measurements by digital image correlation. Internal report No. 269, ENS Cachan, 2008, LMT Cachan, France.

[Hoc 2003] Hoc Th, Crepin J, Gelebart L, Zaoui A, A procedure for identifying the plastic behaviour of single crystals from the local response of polycrystals. Acta Mater, Vol 51 (2003), p. 5479-5490.

[Jarali and Raja 2008] Jarali CS and Raja S, Upadhya AR. Micro-mechanical behaviors of SMA composite materials under hygro-thermo-elastic strain fields, International Journal of Solids and Structures 45 (2008), p. 2399–2419.

[Kajberg and Lindkvist 2004] Kajberg J. and Lindkvist G., Characterization of materials subjected to large strains by inverse modelling based on in-plane displacement fields, International Journal of Solids and Structures 42 (2004), p. 3439–3459.

[Lecompte et al 2007] Lecompte D., Smits A., Sol H., Vantomme J., Van Hemelrijck D., Mixed numerical–experimental technique for orthotropic parameter identification using biaxial tensile tests on cruciform specimens, International Journal of Solids and Structures 44 (2007), p. 1643–1656.

[Lecompte et al. 2005] Lecompte D, Smits A, Sol H, Vantomme J, Van Hemelrijck D. Elastic orthotropic parameter identification by inverse modelling of biaxial tests using digital image correlation. In: Proceedings of the 8th European Mechanics of Materials Conference on Material and Structural Identification from Full-field Measurements., September 2005, Cachan, France, p. 53–61.

[Levenberg 1944] Levenberg K. A method for the solution of certain non-linear problems in least squares, Quarterly of Applied Mathematics 2 (1944), p. 164–168.

[Marfia and Sacco 2005] Marfia S and Sacco E. Micromechanics and homogenization of SMA-wire-reinforced materials, J. Appl. Mech. 72 (2) (2005), p. 259–268.

[Marquardt 1963] Marquardt DW. An algorithm for least-squares estimation of non-linear parameters. Journals on Applied Mathematics 11 (1963), p. 431-441.

[Meraghni et al. 1995] Meraghni F and Benzeggagh, ML. ‘Micromechanical Modelling of Matrix Degradation in Randomly Oriented Discontinuous Fibre Composites’, Composites Science and Technology 55 (1995), p. 171–186.

[Meraghni et al. 1996] Meraghni F, Blakeman CJ and Benzeggagh ML. ‘Effect of Interfacial Decohesion on Stiffness Reduction in a Random Discontinuous Fibre Composite Containing Matrix Microcracks’, Composites Science and Technology 56 (1996), p. 541–555.

[Merzouki 2008] Merzouki T. Identification expérimentale et modélisation du comportement d’un multicrista en alliage à mémoire de forme, PhD thesis, Arts et Metiers ParisTech, Metz, 2008.

[Meuwissen et al. 1997] Meuwissen M, Oomens C, Baaijens F, Petterson R and Janssen J. Determination of parameters in elasto-plastic models of aluminium. In: H. Sol and C.W.J. Oomens, Editors, Material Identification using Mixed Numerical Experimental Methods, Kluwer Academic Publishers, Dordrecht (1997), p. 71–80.

[Meuwissen et al. 1998] Meuwissen M, Oomens C, Baaijens F, Petterson R and Janssen J. Determination of the elasto-plastic properties of aluminium using a mixed numerical-experimental procedure, Journal of Materials Processing Technology 75 (1998), p. 204–211.

[Mohammad Sadeghi 2010] Mohammad Sadeghi B. Identification de lois de comportement à partir de mesures de champs cinématiques dans le cas de chargements complexes Application à la mise en forme des aciers TRIP, PhD thesis, Arts et Metiers ParisTech, Metz, 2010.

[Nouri 2009] Nouri H. Modélisation et identification de lois de comportement avec endommagement en fatigue polycyclique de matériaux composite à matrice thermoplastique, PhD thesis, Arts et Metiers ParisTech, Metz, 2009.

[Nouri 2009a] Nouri H., Meraghni F., Czarnota C., Lory P., Experimental Identification of Fatigue Damage Model for Short Glass Fibre Reinforced Thermoplastics. 7th International Conference on Composite Science and Technology (ICCST-7), January 2009.

[Nouri 2010] Nouri H., Meraghni F., Czarnota C., Lory P., Fatigue Damage Modelling for Short Glass Fibre Reinforced Polyamide (PA6-GF30): Experimental identification and validation using full-field strain measurements. ECCM-14, Budapest, June 2010.

[Tillier 1998] Tillier Y. Identification par analyse inverse du comportement mecanique des polymeres solides ; applications aux sollicitations multiaxiales et rapides, PhD thesis, L'Ecole Nationale Supérieure des Mines de Paris, 1998.

[Vidal et al. 1991] Vidal CA, Lee HS and Haber RB, The consistent tangent operator for design sensitivity analysis of history-dependent response. Comput. Syst. Eng. 2 (1991), p. 509–523.

[wikipedia] An article from Wikipedia:

http://en.wikipedia.org/w/index.php?title=Levenberg-arquardt_algorithm&oldid=113860862

Conclusion

In this work the influence of the martensitic transformation in a near equiatomic NiTi shape memory wire epoxy matrix composite was studied. The NiTi wire in as drawn condition was subjected to three heat treatments in order to prepare the wires with different transformation characteristics. The wires were labeled M550, M450 and M400. Three metallic moulds were designed to elaborate samples with different geometries, namely pull-out, simple traction and heterogeneous test specimens. The composite specimens were elaborated by casting followed by curing and post curing process. The mechanical characterization was conducted at three temperatures (20, 80 and 90 °C) and at a constant cross-head speed.

The effect of martensitic transformation on the debonding initiation and propagation in single wire composite was studied through an in-situ observation. The interfacial shear strength, τ_i, in composite was estimated by coupling an analytical method and experimental results.

According to experimental results, the interfacial shear strength is about 9 MPa when the phase transformation does not occur (M400 SMA and steel wires). However, it can reach a value of 14 MPa when martensitic transformation or reorientation takes place in the wires (M550 and M450).

In both samples with M550 and M450 wires the martensitic reorientation/ transformation of the free part of wires occurs before that the interfacial debonding begins. In M400 wire specimens, the martensitic transformation does not occur before the debonding onset.

From in-situ observations, the debonding starts from the wire entry point and proceeds to the embedded end along the interface until the entire wire is debonded. The average debonding rate for the M550 samples is about 9 mm/min for different specimens. In the case of M450 wire composite samples, the debonding propagates with an average rate of 11 mm/min for different specimens. The debonding rate for a sample with M400 wire is different and varies between 14.4 and 17.3 mm/min. In both samples with M550 and M450 wires the debonding propagates with a constant rate.

It was found that the martensitic reorientation/transformation occurring in M-550 or M-450 decreases the debonding rate. In the specimens with M-400, where no phase transformation takes place, the interface exhibits a fast debonding. It should be expressed that the debonding rate depends on the displacement rate as well as the transformation strain. A relationship between the cross-head speed, the debonding rate and the transformation strain was proposed to link these three parameters.

The effect of the martensitic transformation on the mechanical behavior of the NiTi-epoxy composite was investigated using standard tensile test. The effect of different types of wire, test temperature and wire volume fraction were studied as well. For this purpose, the

specimens with three different wires (M400, M450 and M550) and also with three wire volume fractions (0, 6, and 12%) were subjected to the tensile load at 20, 80 and 90 °C.

It is found that the martensitic transformation occurring in the wire affect the mechanical behavior of the composite specimens. In this way, using the wire with larger transformation stress enhances the composite tensile strength. This is achieved either by increasing the test temperature or by using the wires heat treated at lower temperatures.

As expected, it was established that increasing the wire volume fraction enhances the mechanical behavior of the composite specimens.

A micromechanical model was developed in order to investigate the role of the wire in the composite. The interfacial shear strength obtained from pull-out test was implemented into the model. Furthermore, the experimental behavior of the wires and matrix at different temperature has been taken into account by introducing the respective secant modulus. The micromechanical results are in good accordance with the experimental ones. The transformation was considered indirectly as an effective and key parameter which yields a good correlation in experimental and micromechanical results. However, the interfacial shear stress generated after martensitic transformation remains an issue which needs to be investigated.

In the experimental stress-strain behavior of the composite samples, two stages are observed: a quasi linear followed by a non linear. Such a trend was not observed in the stress-strain curve obtained for the epoxy matrix. The stress level associated to the transition from one stage to the other one increases as the test temperature increases. This transition can be associated with the martensitic transformation taking place in the wires.

It was claimed that on the constraint of matrix, the martensitic transformation occurs simultaneously in several points in the wire. Consequently, the debonding occurs in several zones and a very typical regular debonded/undebonded pattern takes place in NiTi wire composite.

The M450 wire composites present a slight superelastic behavior at high temperature. This effect does not occur in M550 wire samples.

The identification method in this work was proposed to extract the four independent elastic constants E_{11}, E_{22}, G_{12} and ν_{12} of an orthotropic composite material. The studied material is NiTi wire epoxy matrix composite with four different fiber volume fractions. The samples with complex geometry were subjected to the tensile load. The surface displacements are measured and strains are subsequently calculated using the Correli-Q4 and VIC2D softwares. An inverse method was developed and the material parameters were identified.

A cost function was constructed on the basis of measured strain components (ε_{11}, ε_{22} and ε_{12}) and the applied load (f). The inverse problem was solved iteratively by minimizing the cost

function involving the squared differences between the measured and computed values. In each iteration, the material parameters in the finite element model were changed in such a way to minimize the difference between experimental and numerical stain fields.

The identification method was assessed before using the experimental database. In this way, two verifications have been done: the convergence test (robustness of the method) and the stability analysis (effect of experimental errors). The numerical study has established the stability of the inverse method and its capability to be applied for the studied NiTi wire composite samples even with noisy data.

The identified parameters were compared to those obtained using Mori-Tanaka's model. Moreover, the strain fields determined numerically using the identified parameters were compared to the experimental ones. Good correlations were found in both cases.

Thermal residual stress and cooling under stress can affect the transformation characteristics of an embedded SMA wire. Furthermore, the transformation occurring in the wire on the constraint of matrix may be different from that of wire in absence of matrix. The identification method could be applied to estimate the actual parameters of NiTi wires in these conditions. For this purpose, it is necessary to use a matrix undergoing a strain level about 7%. This can be achieved either by changing the curing condition to prepare more ductile samples or testing at 80 °C (for instance). The latter requires using a specific image acquisition system at this temperature.

Several new and original results about the influence of the martensitic transformation on the mechanical response of NiTi/epoxy composites were obtained in this work:

- The interfacial shear strength is increased when MT takes place
- The debonding rate decreases when MT occurs
- An improvement of the overall behavior of the composite is observed:

  The tensile resistance is increased

  A quasi-linear elastic regime occurs at low strain regime.

  Super elastic behavior can be observed in some particular conditions.

- An identification method was proposed and validated to determine the four elastic constants for this composite.
- A very regular debonding/undebonded pattern was observed and related to the transformation mechanism of the NiTi wires.

The high brittleness of the matrix has strongly limited the amount of data available with this composite. A more ductile matrix is necessary to gain benefit of the influence of the MT of SMA wires in SMA/epoxy composites.

Appendix A.

Mechanical behavior of the composite samples

A.1. Experimental results

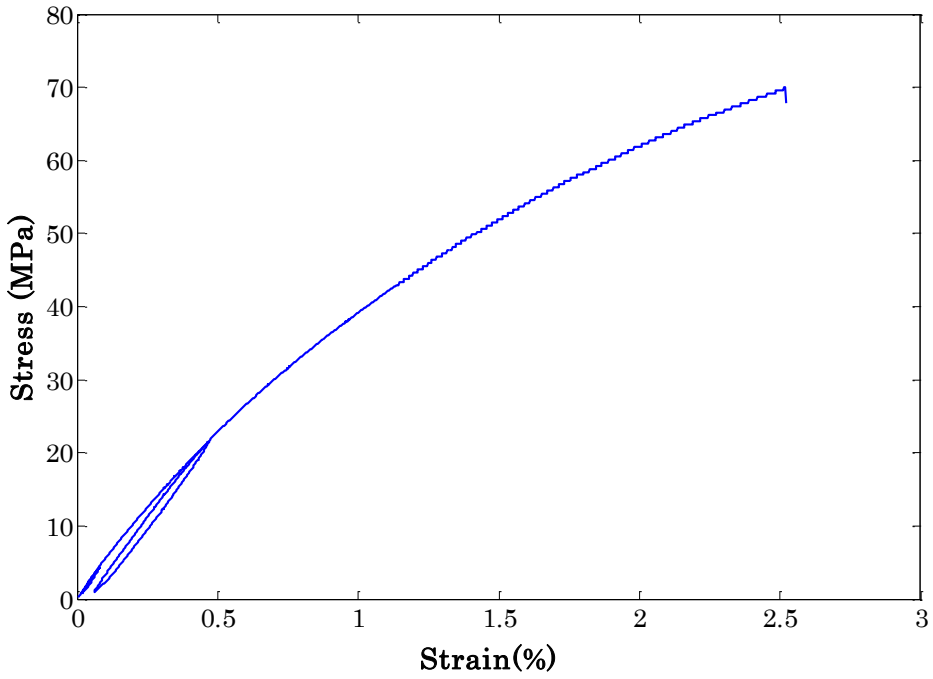

Fig. A.1- Stress -Strain diagram for the composite samples with M-550 wire, at 20 °C and with V_f=6%.

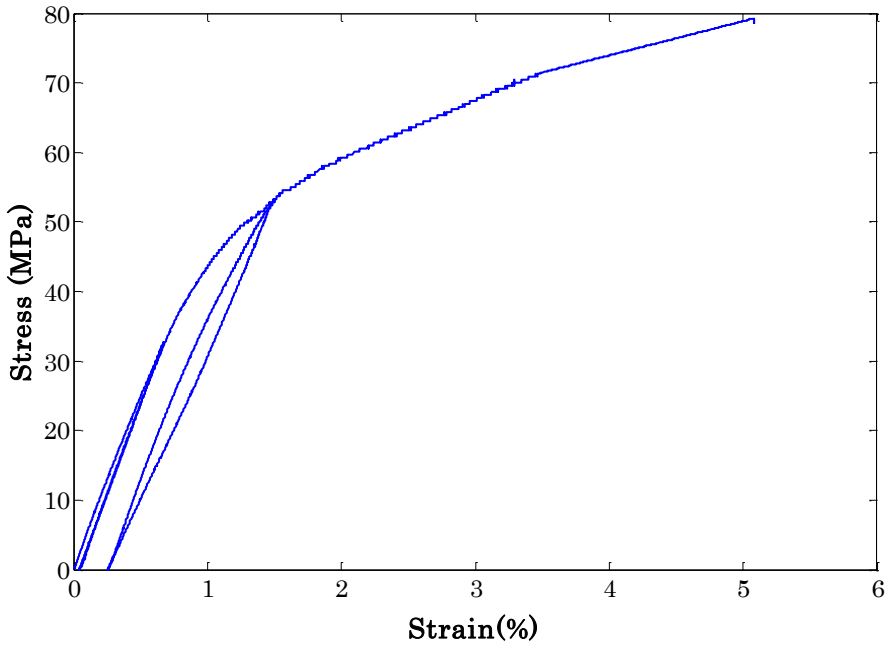

Fig. A.2- Stress -Strain diagram for the composite samples with M-550 wire, at 80 °C and with V_f=6%.

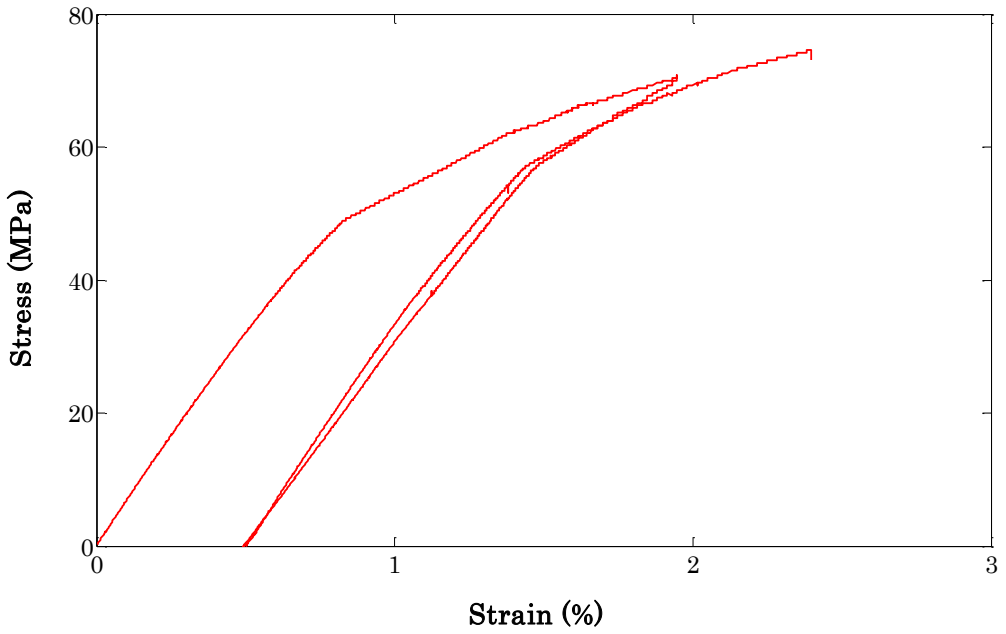

Fig. A.3- Stress -Strain diagram for the composite samples with M-550 wire, at 80 °C and with V_f=12%.

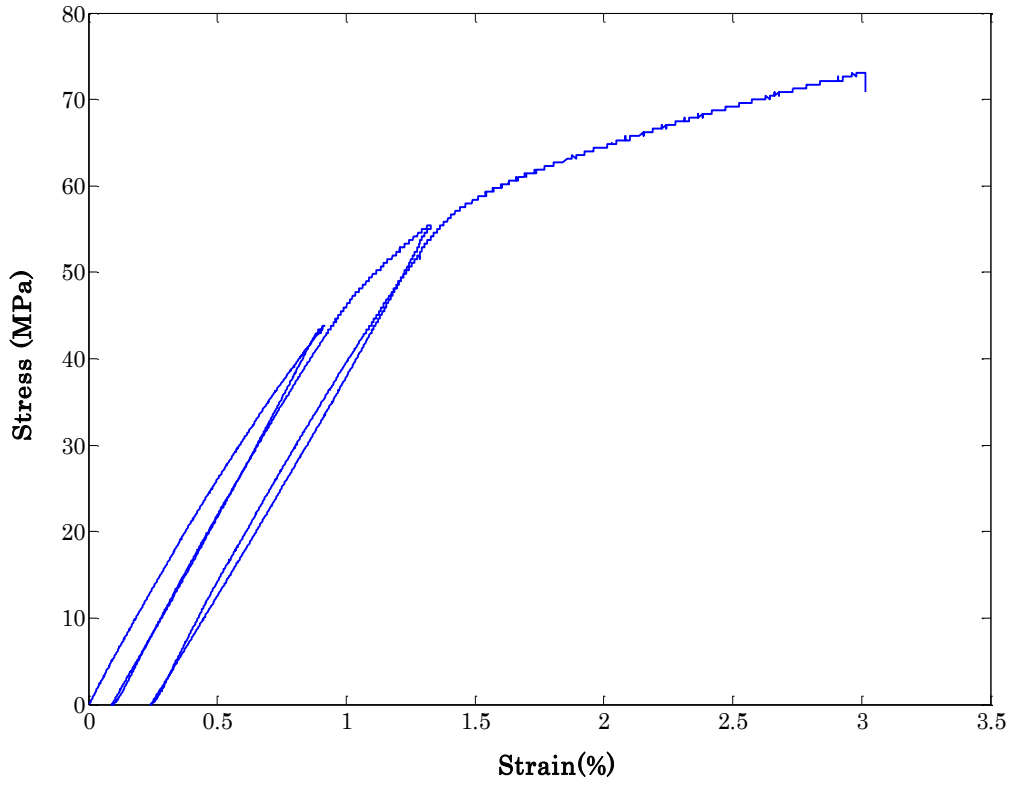

Fig. A.4- Stress -Strain diagram for the composite samples with M-550 wire, at 90 °C and with V_f=6%.

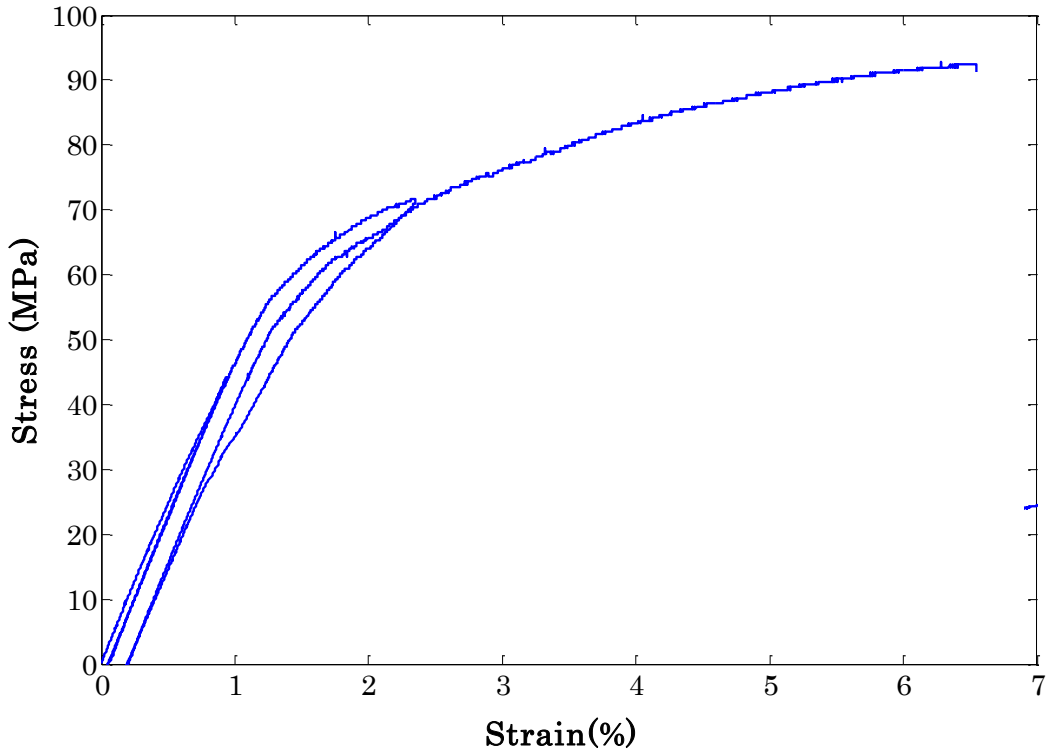

Fig. A.5- Stress -Strain diagram for the composite samples with M-450 wire, at 80 °C and with V_f=6%.

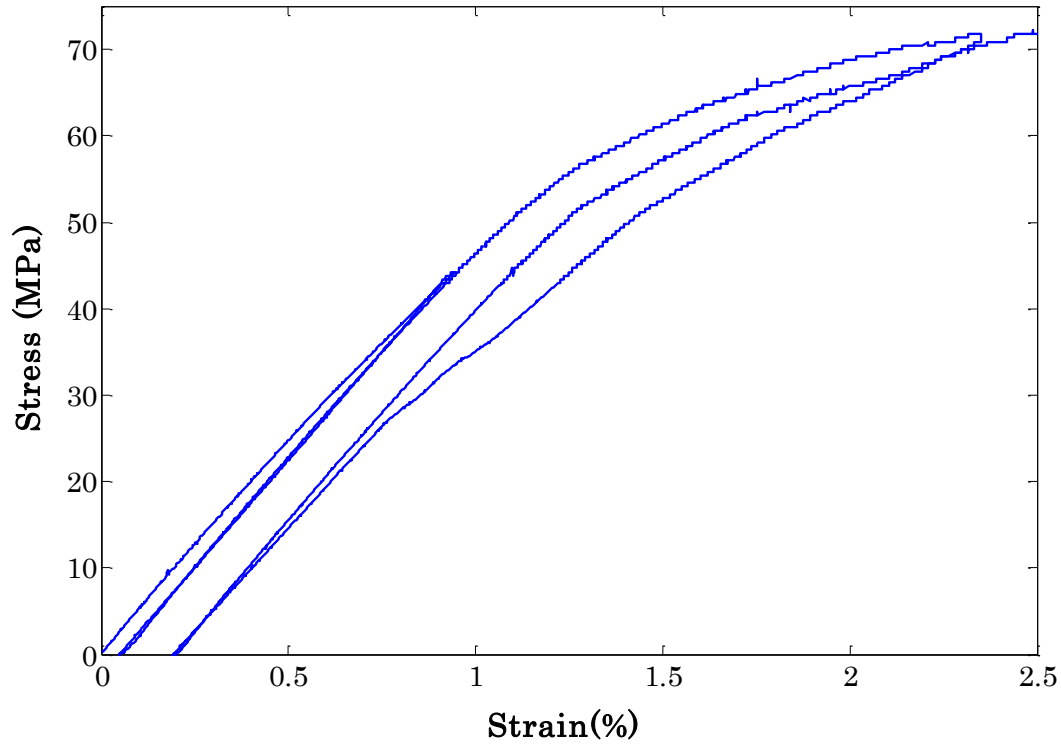

Fig. A.6- Stress -Strain diagram for the composite samples with M-450 wire, at 80 °C and with V_f=6%.

A.2. Micromechanical results

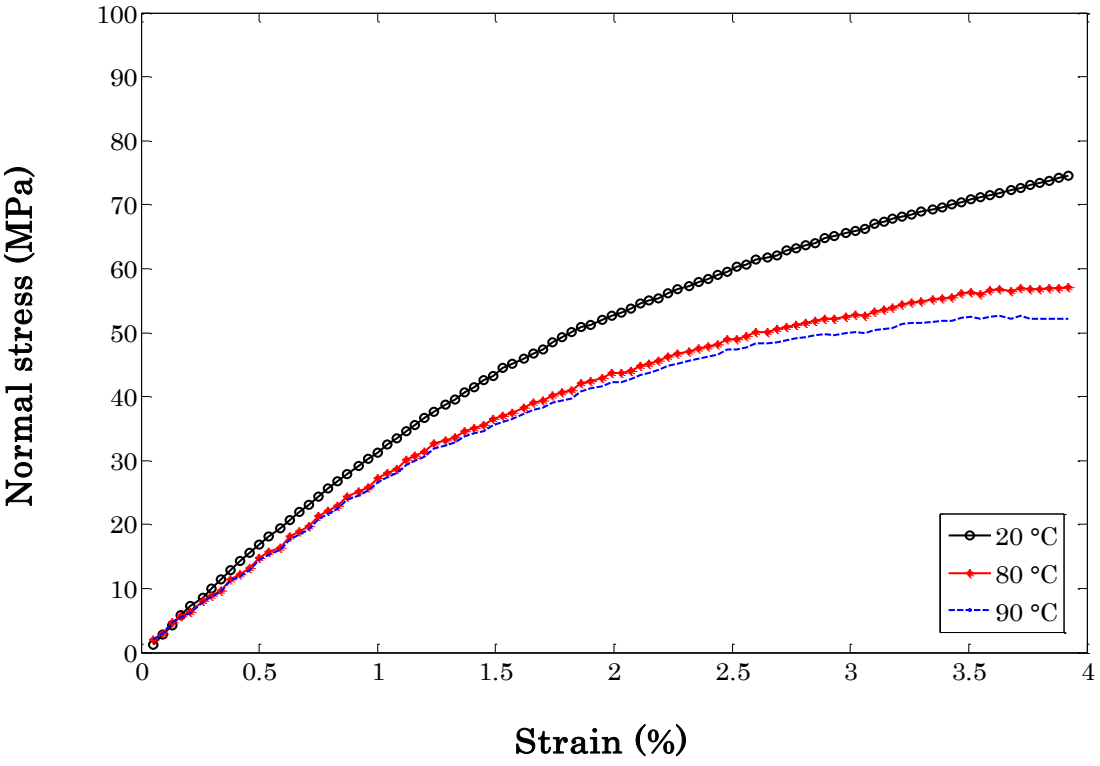

Fig. A.7- Stress -Strain diagram for the matrix samples at three temperatures.

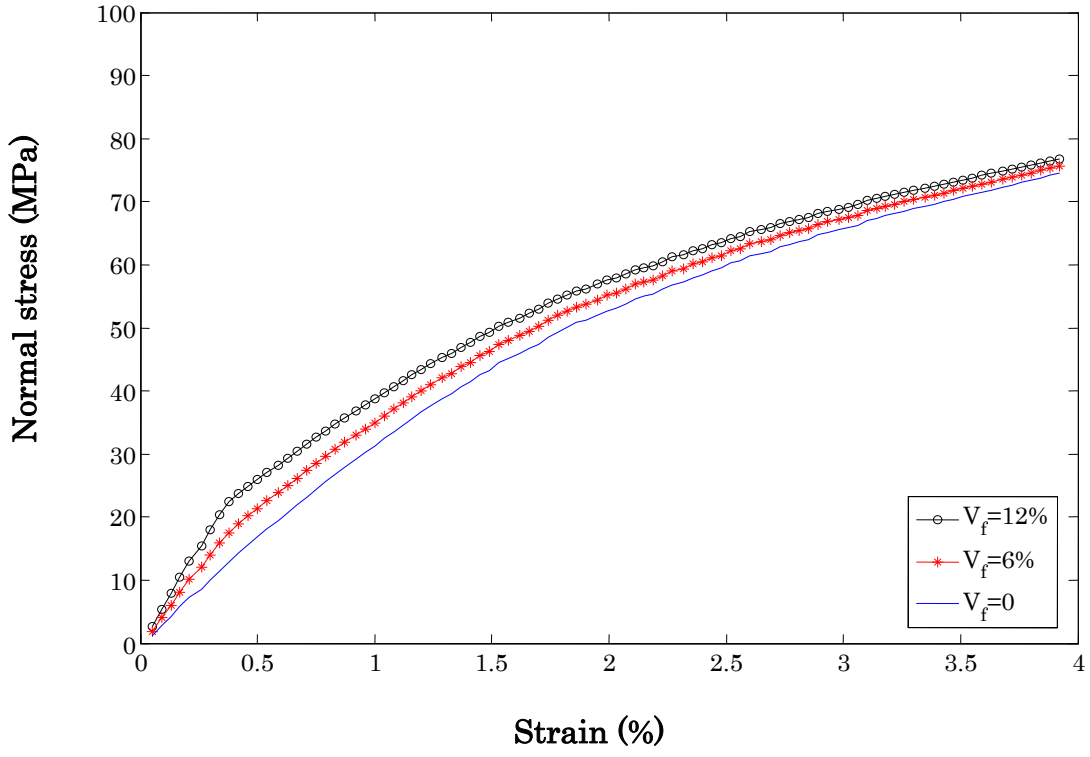

Fig. A.8- Stress -Strain diagram for the composite samples with M-550 wire at 20°C for three V_f.

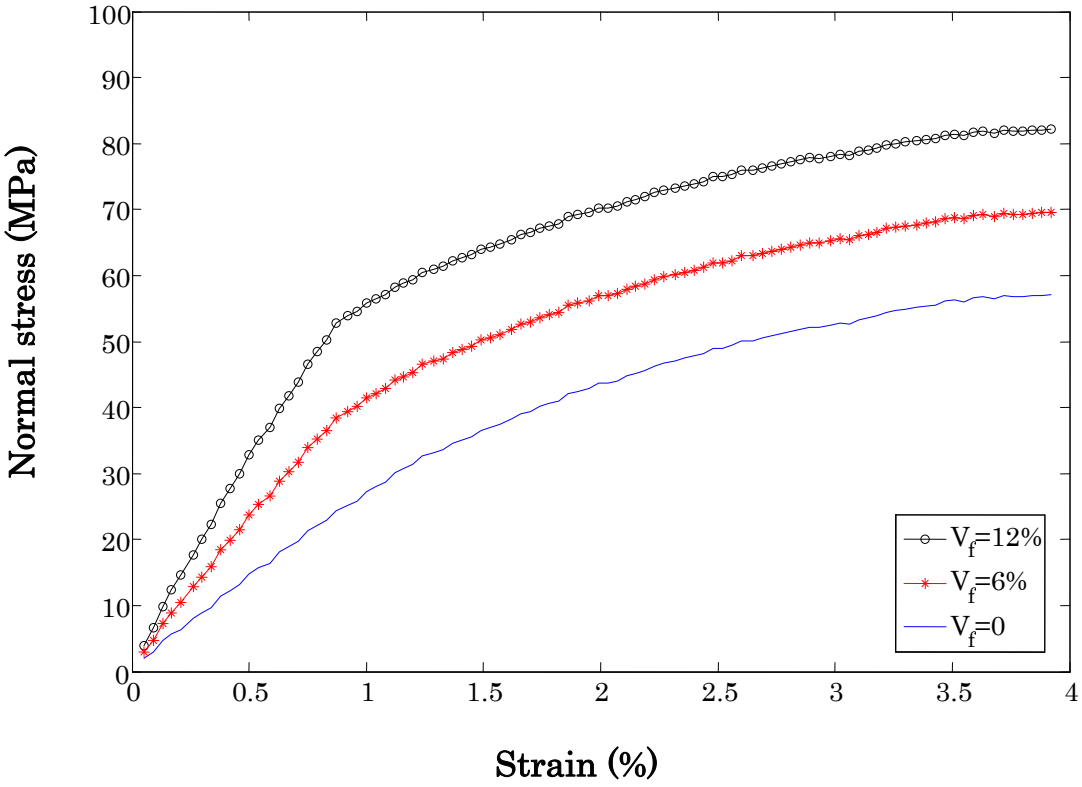

Fig. A.9- Stress -Strain diagram for the composite samples with M-550 wire at 80°C for three V_f.

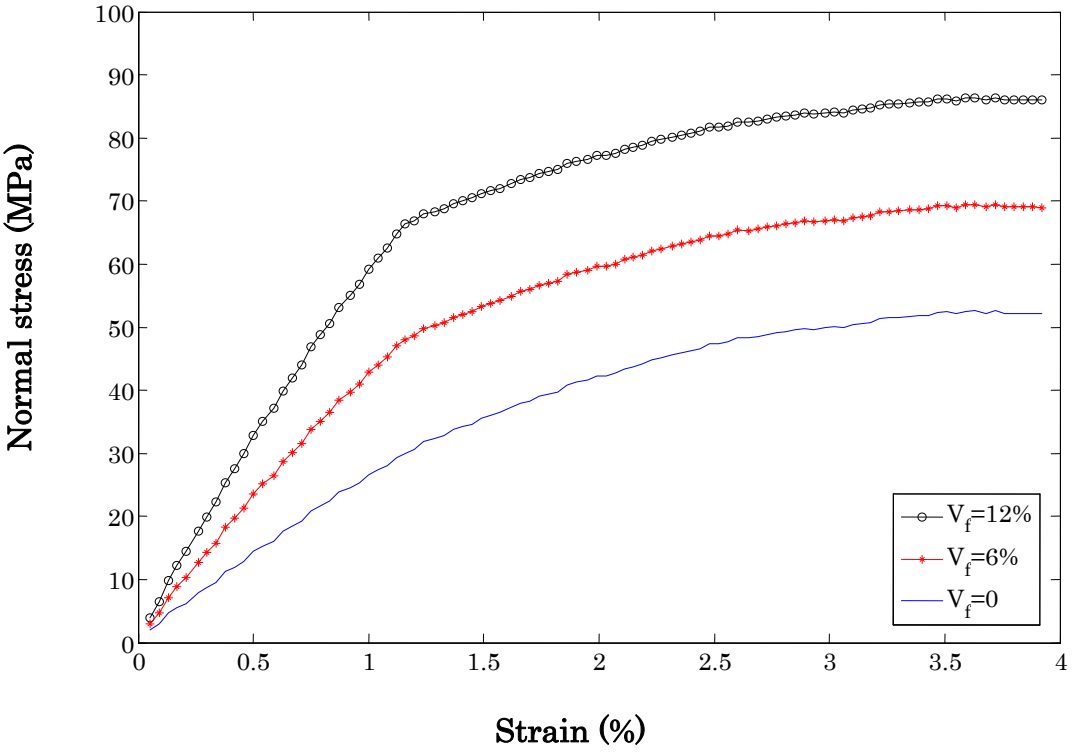

Fig. A.10- Stress -Strain diagram for the composite samples with M-550 wire at 90°C for three V_f.

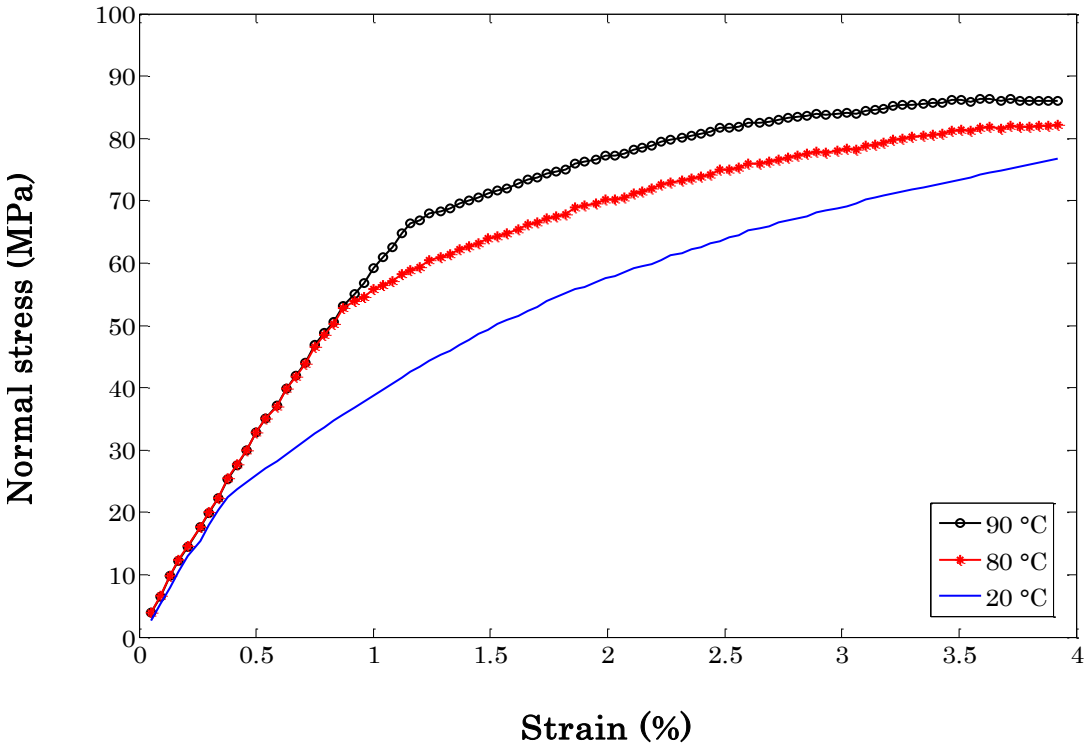

Fig. A.11- Stress -Strain diagram of composite samples with M-550 wire V_f=12% at three temperatures.

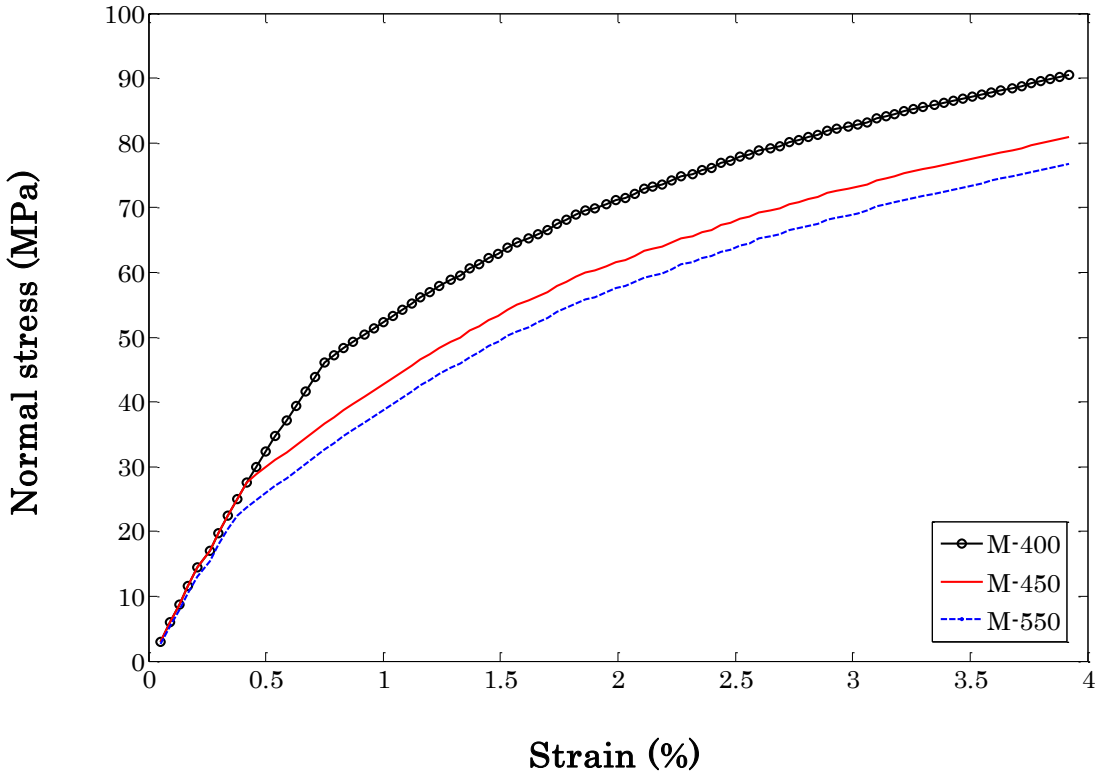

Fig. A.12- Stress -Strain diagram of composite samples with V_f=12% at 20 °C for three different wires.

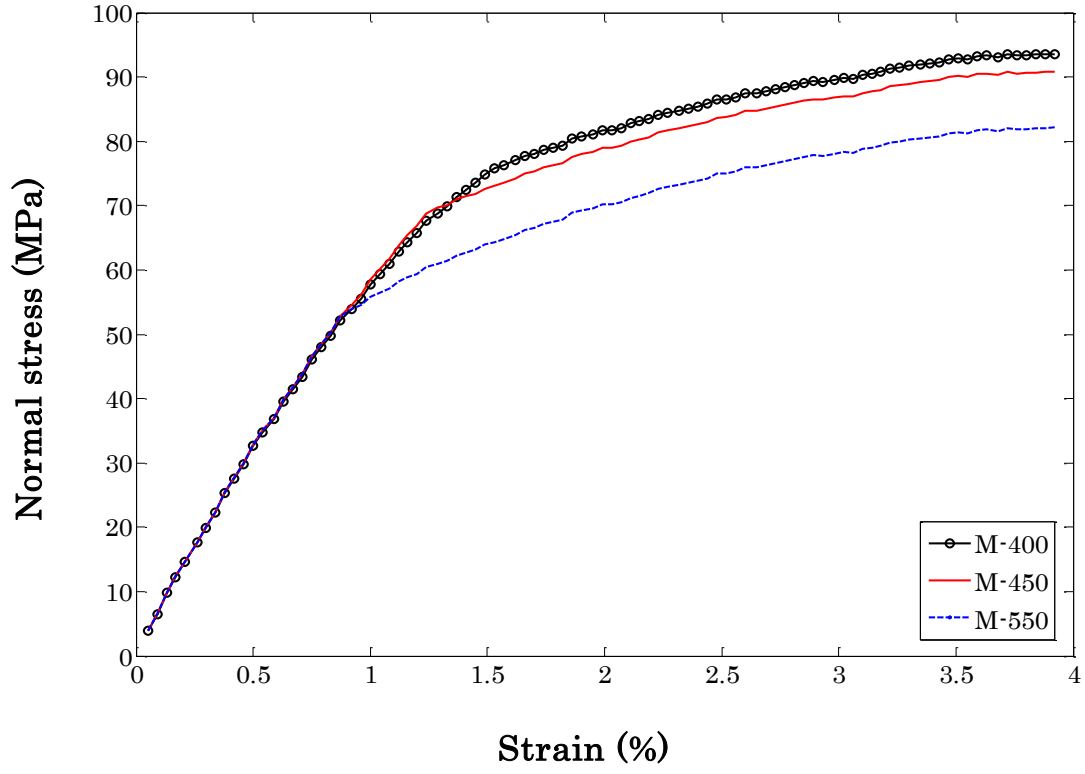

Fig. A.13- Stress -Strain diagram of composite samples with V_f=12% at 80 °C for three different wires.

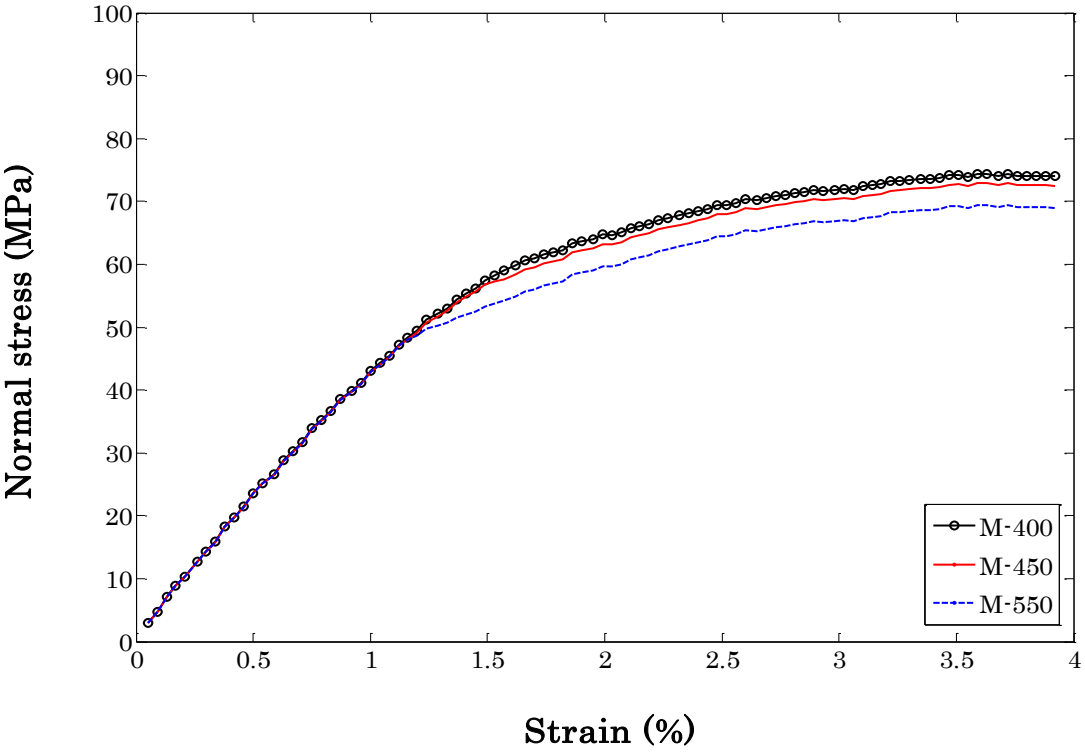

Fig. A.14- Stress -Strain diagram of composite samples with V_f=6% at 90 °C for three different wires.

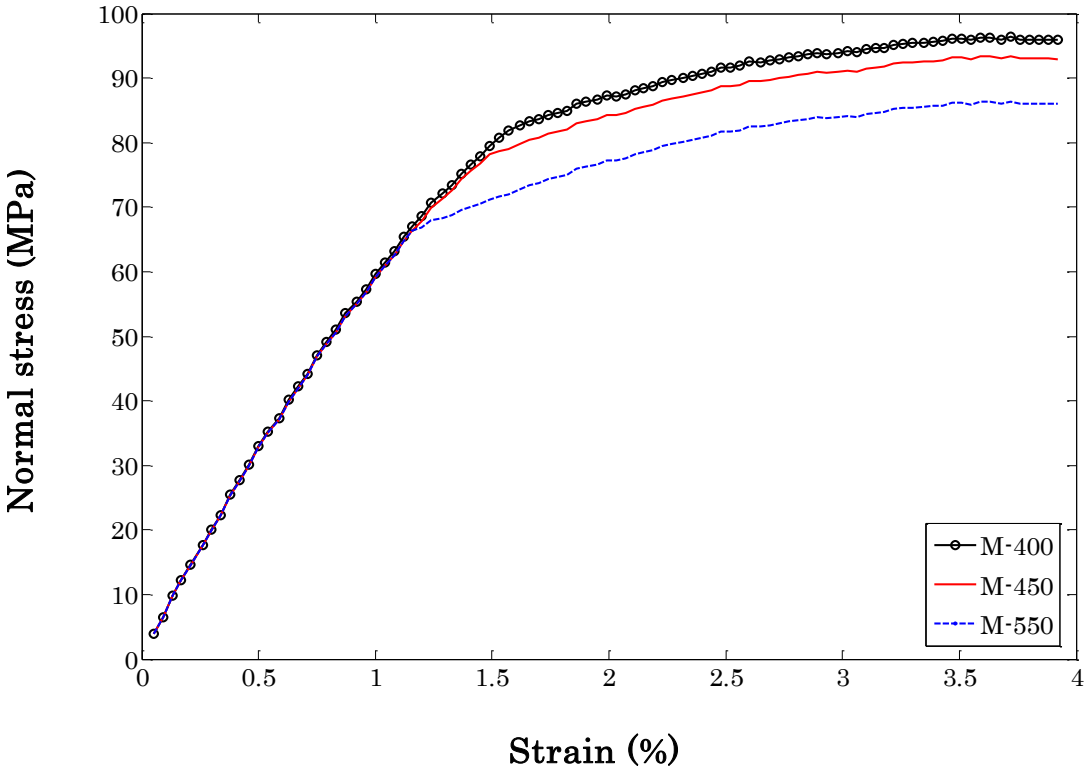

Fig. A.15- Stress -Strain diagram for the composite samples with V_f=12% at 90 °C for three different wires.

Part II:

Résumé étendu

Résumé

1. Introduction

2. Processus de fabrication et méthodologie de caractérisation

3. Caractérisation de l'interface matrice/ fils - Influence de la transformation martensitique

4. Propriétés en traction : caractérisation et modélisation micromécanique, influence de la transformation martensitique

5. Identification des paramètres

6. Conclusion

Résumé

Dans ce travail, nous avons élaboré et étudié un composite constitué d'une matrice en résine époxyde renforcée par des fils en alliage à mémoire de forme (AMF). Le fil, en NiTi écroui a été soumis à trois traitements thermiques afin d'obtenir des caractéristiques de transformation différentes. Trois types d'échantillons, nommés pull-out, traction simple et éprouvettes à géométrie complexe ont été réalisés. Les composites ont été fabriqués par moulage suivi d'une cuisson et d'une post-cuisson. Les tests ont été effectués dans l'air à trois températures (20, 80 et 90 °C) à vitesse constante.

Des échantillons mono-filaments ont été réalisés et soumis à un essai d'arrachement afin d'étudier l'effet de la transformation martensitique sur l'initiation et la propagation de la décohésion. Les observations in-situ de la décohésion interfaciale et de comportement au glissement ont été effectuées avec un polariscope.

Dans le test d'arrachement, la longueur noyée est généralement petite et la résistance de l'interface au cisaillement (IFSS) peut être estimée en divisant la force maximale par la surface latérale. En revanche, pour évaluer l'effet de la transformation de phase, une grande longueur noyée est nécessaire. Pour estimer l'IFSS, une nouvelle méthode fondée sur un modèle analytique a été développée. La résistance de l'interface au cisaillement a été déterminée pour ces systèmes. Il a été constaté expérimentalement que, lorsqu'il n'y a pas de transformation de phase l'IFSS est d'environ 9 MPa alors qu'elle est d'environ 14 MPa lorsque la transformation martensitique / réorientation se produit dans le fil.

L'effet de la transformation martensitique sur la propagation de la décohésion d'un composite mono-filament (fil NiTi) a également été étudié. D'après les observations in situ, la décohésion commence à partir du point d'entré des fils et continue vers la fin de la longueur noyée. Il est observé que lorsqu'il n'y a pas de transformation martensitique la décohésion se propage rapidement alors qu'elle est plus lente quand il y a transformation ou réorientation de la martensite. Dans le cas où la décohésion commence pour une contrainte appliquée inférieure à la contrainte de transformation, la vitesse de décohésion diminue dès que la transformation de phase commence. Il est constaté que la vitesse de décohésion dépend de la vitesse de déplacement ainsi que de la déformation de transformation.

Le comportement mécanique de la matrice de résine, l'effet de la température d'essai et de la fraction volumique de fil ont été déterminés en utilisant le test de traction simple. Les essais ont été conduits à trois températures. Comme prévu, la pente de la courbe contrainte-déformation pour la résine époxyde diminue avec l'augmentation de la température d'essai. Au contraire, le module d'élasticité des échantillons du composite augmente légèrement lorsque la température augmente. Il est constaté que la transformation martensitique se produisant dans le fil influe de manière significative le comportement mécanique des échantillons composites. De cette façon, en utilisant le fil avec une contrainte de transformation plus grande améliore la

résistance du composite à la traction. Ceci est réalisé soit en augmentant la température d'essai ou en faisant un traitement thermique à une température plus basse. La résistance à la traction augmente aussi en augmentant la fraction volumique de fil. Il est proposé que la transformation martensitique peut changer le mode de décohésion. En absence de matrice, quand un fil d'AMF est sollicité, la transformation commence à une des extrémités de fil et se propage vers l'autre extrémité. Cependant, en présence de la matrice la transformation se produit simultanément en plusieurs points. On observe alors, une intermittence de zones décollées et non décollées.

Un modèle micromécanique sur la base du modèle Piggott a été développé afin d'étudier le rôle de fil sur le comportement global du composite. Le comportement mécanique du fil et de la matrice déterminés expérimentalement a été mis en œuvre dans le modèle. Les résultats ont été comparés avec les résultats expérimentaux et un bon accord a été trouvé. Les résultats analytiques et expérimentaux montrent que le changement de la pente de la courbe contrainte-déformation est le signe de la présence de la transformation martensitique. L'essai de traction uniaxial permet d'identifier les paramètres d'un matériau isotrope. Pour les matériaux anisotropes, tels que le composite étudié, plusieurs tests de traction sont nécessaires pour identifier les paramètres du matériau dans des directions différentes. Dans ce cas, faire un test hétérogène peut réduire le nombre de tests et permet l'identification simultanée des paramètres du matériau. Dans ce travail, les échantillons à géométrie complexe ont été conçus et fabriqués afin d'estimer les propriétés élastiques du matériau composite dans deux directions (perpendiculaire et parallèle à l'axe du fil). Les spécimens avec un mouchetis aléatoire ont été soumis à un chargement simple à température ambiante et plusieurs photos ont été prises avec un pas de temps constant. Les champs hétérogènes de déplacement/ de déformation générés grâce à la géométrie complexe des échantillons composites ont été mesurées à l'aide du logiciel VIC2D et Correli Q4 par corrélation d'images numériques (CIN). Pour des tests hétérogènes, il n'y a pas de relation explicite entre le déplacement et la charge appliquée, le tenseur des contraintes est inconnu. Par conséquent, une méthode inverse a été développée et les paramètres du matériau ont été identifiés. Les résultats ont ensuite été comparés aux résultats obtenus par la méthode de Mori-Tanaka. Le champ de déformation obtenu numériquement, à partir des paramètres identifiés a été comparé à ceux obtenus expérimentalement. Une bonne corrélation a été trouvée dans les deux cas.

1. Introduction

Les alliages à mémoire de forme (AMF) présentent une grande déformation recouvrable (jusqu'à 8%) et la possibilité de reprendre leur forme initiale lorsqu'ils sont chauffés au-dessus de la température de transition. Un effort de recherche important est actuellement en cours, orientée vers l'utilisation des AMF dans les actionneurs pour des structures intelligentes, pour

contrôler la forme et les vibrations. Ils présentent également une très grande capacité d'amortissement en raison d'un effet pseudoélastique et superélastique. Cette propriété des AMF est extrêmement utile pour amortir les vibrations et réduire les dommages d'impact dans les structures.

Afin de garantir une rigidité et une résistance suffisante des éléments de structure et une grande durabilité, les AMF sont parfois intégrés dans une matrice plastique ou métallique. Ces composites sont utilisés en aéronautique, dans l'industrie de transport à grande vitesse et dans l'automobile. Néanmoins, certaines caractéristiques de la fibre changent au cours de la transformation de phase et peuvent affecter les propriétés interfaciales. Cette thèse étudie plusieurs aspects de ces composites.

Les fibres d'AMF sont utilisées pour renforcer la matrice, pour absorber l'énergie de déformation et réduire les contraintes résiduelles afin d'améliorer la résistance au fluage ou à la fissuration grâce à la transformation martensitique induite par la contrainte. Les fibres noyées sont également utilisés pour améliorer la capacité d'amortissement, augmenter la résistance à l'endommagement par impact, améliorer la rigidité, modifier la fréquence de résonance ou la forme des composites.

Un grand nombre de composites à base d'AMF sont étudiées dans la littérature. Des matrices métalliques telles qu'aluminium et étain et des matrices polymères sont utilisés.

Dans ce travail, des fils en NiTi ont été incorporés dans une matrice constituée de résine. La procédure expérimentale, le processus de fabrication, les essais mécaniques sur les fils AMF, sur la matrice époxyde et sur les échantillons composites sont détaillés dans le chapitre 2.

La reprise de la déformation de fil NiTi noyés dans la matrice génère une contrainte interfaciale élevée qui peut conduire à la décohésion interfaciale. Ainsi, il est nécessaire d'étudier l'interface fil/matrice afin d'évaluer la réponse mécanique du composite. La caractérisation de l'interface est développée dans le chapitre 3.

Le chapitre 4 traite du comportement thermomécanique des échantillons composites. Dans ce chapitre, les effets de la fraction volumique de fil, type de fil et de la température d'essai ont été étudiés en traction uniaxiale. Ainsi, des échantillons avec trois fils différents et avec trois fractions volumiques des fils (0, 6, et 12%) ont été étudiés à température ambiante (20), 80 et 90 °C. L'influence de la transformation martensitique dans les fils sur le comportement global des échantillons composites est discutée. Un modèle micromécanique est développé et utilisé afin de mieux comprendre le rôle des fils dans le composite.

Quand un matériau est isotrope, il est possible d'identifier les paramètres simplement en effectuant un test de traction standard. Pour un matériau anisotrope, tels que le matériau composite étudié, plusieurs tests standards sont nécessaires pour identifier les paramètres du matériau. Il est possible de remplacer ces différents essais par un essai hétérogène réalisé en

appliquant un chargement simple sur des échantillons à géométrie complexe. Ce type de tests permet l'identification simultanée des différents paramètres. Le problème principal est de mesurer les champs de déplacement/ de déformation hétérogènes générés au cours de ces types d'essai. Un autre problème lié aux essais hétérogènes est le fait qu'il n'y a pas de relation explicite entre le déplacement et la charge appliquée ce qui signifie que le tenseur des contraintes est inconnu. Par conséquent, une méthode inverse est nécessaire pour identifier les paramètres du matériau. Dans le chapitre 5, la procédure d'identification est expliquée. Cette stratégie est développée pour identifier les quatre constantes élastiques indépendantes E_{11}, E_{22}, G_{12} et ν_{12} des échantillons composites.

2. Processus de fabrication et méthodologie de caractérisation

2.1. Matériaux étudiés

Le matériau étudié est un composite à matrice époxyde renforcé par des fils en NiTi. Dans ce qui suit, les constituants sont décrits et les caractérisations mécaniques et physiques sont présentées.

2.1.1. Fil en AMF

Le fil de NiTi proche de la composition équiatomique, dans l'état écroui, de 1 mm de diamètre a été fourni par la société Nimesis Technologie. Ce matériau a été soumis à des traitements thermiques à différentes températures (350, 400, 450, 500, 550 et 600 °C), suivie par une trempe à l'eau. Les températures de transformation ont été déterminées par DSC. Ensuite, les fils ont été caractérisés en traction uniaxiale pour déterminer la contrainte la contrainte de transformation (tableau 1). Trois traitements thermiques ont été retenus : 400 °C pendant 60 min, 450 °C pendant 60 min et 550 °C pendant 30 min. Les échantillons sont désignés respectivement, M400, M450 et M550.

Tableau 1. Caractéristiques des fils NiTi soumis à différents traitements thermiques

Alliage	Traitement thermique	Contrainte (MPa) à l'ambiant	Superélasticité	Effet mémoire
M 600	600 (°C) pour 30 min	100*	Non	Oui
M 550	550 (°C) pour 30 min	100*	Non	Oui
M 500	500 (°C) pour 60 min	120**	Oui	Oui
M 450	450 (°C) pour 60 min	140**	Oui	Oui
M 400	400 (°C) pour 60 min	250**	Oui	Oui
M 350	350 (°C) pour 60 min	400**	-	Oui

* Réorientation de martensite; ** Transformation Martensitique.

Tableau 2. Températures de transformation (°C) des alliages NiTi après traitements thermiques

Alliage	Traitement thermique	M_f (1)	M_s (1)	R_f (1)	R_s (1)	A_s (1)	A_f (1)
M 550	550 (°C) pour 30 min	18	34	34	41	54	77
M 450	450 (°C) pour 60 min	-21	2	41	52	49	65
M 400	400 (°C) pour 60 min	-70	-8	45	60	47	64

(1)- M_s, M_f, R_s, R_f, A_s et A_f sont les températures de début et fin de transformation pour la Martensite, la phase R et l'Austénite respectivement

Les fils NiTi montrent pendant le refroidissement la transformation austénite (B2) →R-phase→ Martensite (B19') et au chauffage B19'→B2. Le tableau 2 détaille les températures de transformation obtenues après ces traitements thermiques.

Les variations de contrainte de transformation pour les trois fils sont présentées dans le tableau 3.

Tableau 3-Contrainte de transformation en fonction de la température.

Fil	σ =0	T=20 °C	T=80 °C	T=90 °C	Relationship
	M_s (°C)	σ (MPa)			
M550	34	100*	370	460	$\sigma = 8{,}2\ (T - M_s)$
M450	2	140	500	580	$\sigma = 6{,}6\ (T - M_s)$
M400	-8	250	600	670	$\sigma = 6{,}7\ (T - M_s)$

* la réorientation de la martensitique se produit dans l'échantillon M550

2.1.2. Matrice époxyde

La matrice polymère est un mélange époxyde / amine. Les propriétés mécaniques du mélange dépendent de façon critique du rapport résine / durcisseur et des conditions de cuisson. En règle générale, l'utilisation d'un rapport de 1:1 stœchiométrique, assure une stabilité maximale du produit. Dans ce travail nous adopterons ce rapport.

La résine époxyde a été chauffée à une température d'environ 50 °C et le durcisseur a été ajouté. Après homogénéisation, la température est de 70 °C et le liquide est suffisamment fluide pour être coulé dans un moule préchauffé à 70 °C et revêtu d'un agent démoulant. Le processus de cuisson se fait à 140 °C. Il est suivi d'une post-cuisson et d'un refroidissement lent jusqu'à température ambiante.

Le rapport l'époxyde /amine, agent démoulant, post-cuisson et des conditions de refroidissement ont été étudiés afin de préparer les échantillons sans fissure, avec de bonnes propriétés mécaniques et une T_g élevée. Les échantillons ont été post-cuits à deux températures (150 et 165 °C) pendant 4 ou 5 heures. La température de transition vitreuse de la matrice est déterminée à l'aide Calorimètre Différentiel à Balayage (DSC). Les résultats sont détaillés dans le tableau 4.

Tableau 4. Températures de transition vitreuse (Tg °C) en fonction des conditions de préparation.
Conditions de préparation et de cuisson

Échantillon	Température de post-cuisson (°C)	Durée de post-cuisson (h)	E/A	T_g (°C)*
TR1	165	4	5	110
TR2	165	4	4	165
TR3	165	5	4	170
TR4	150	5	4	145
TR5	150	5	4,5	130

*vitesse : 10 °C/min

2.2. Préparation de l'échantillon composite

Trois types d'éprouvettes ont été préparés, nommés respectivement échantillons pull-out, de traction simple et à géométrie complexe. Elles ont été fabriqués en utilisant deux moules métalliques (Fig. 1 et 2).

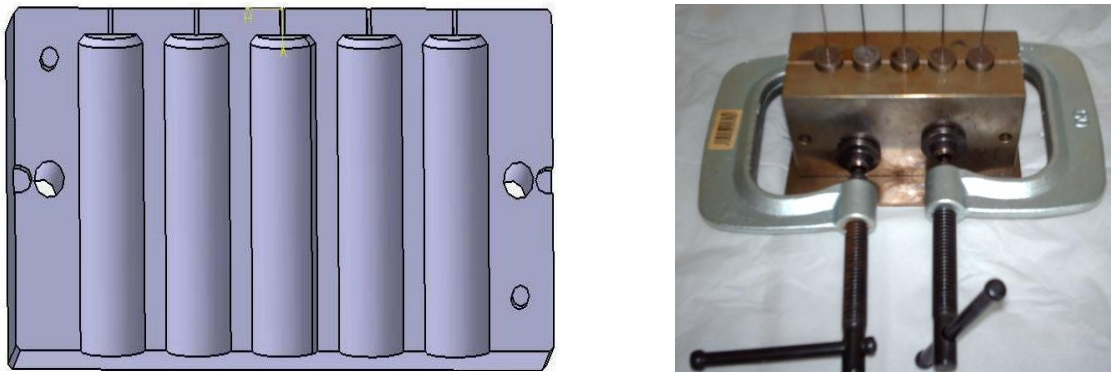

Fig.1. Moule pour échantillons pull-out

L'objectif est de préparer des échantillons avec une ductilité maximale et température de transition vitreuse T_g élevée. Une certaine ductilité de la matrice est cependant nécessaire pour obtenir des spécimens composites sans fissures et permettre la transformation de phase dans le fil pendant l'essai de traction. Dans le cas d'une matrice fragile, la rupture se produit à des déformations faibles et la transformation de phase ne se produit pas. En plus, pour tester les échantillons composites à une température supérieure à A_f, la matrice doit avoir de bonnes propriétés mécaniques. Par conséquent, les propriétés mécaniques maximales de la matrice à la température ambiante et à des températures d'essai élevées (environ 100 °C) sont nécessaires ce qui entraîne de choisir une T_g élevée. La diminution de la température ou le temps de la post-cuisson augmente la ductilité de la matrice mais baisse la température de transition vitreuse.

Comme mentionné dans la section 2.1.2 de la thèse, les meilleurs résultats est obtenu en choisissant un rapport de masse de 4, une cuisson à 140°C, une post-cuisson à 150 ° C pendant 5 heures, et en utilisant l'agent démoulant QZ-13 (TR4 dans le tableau 4).

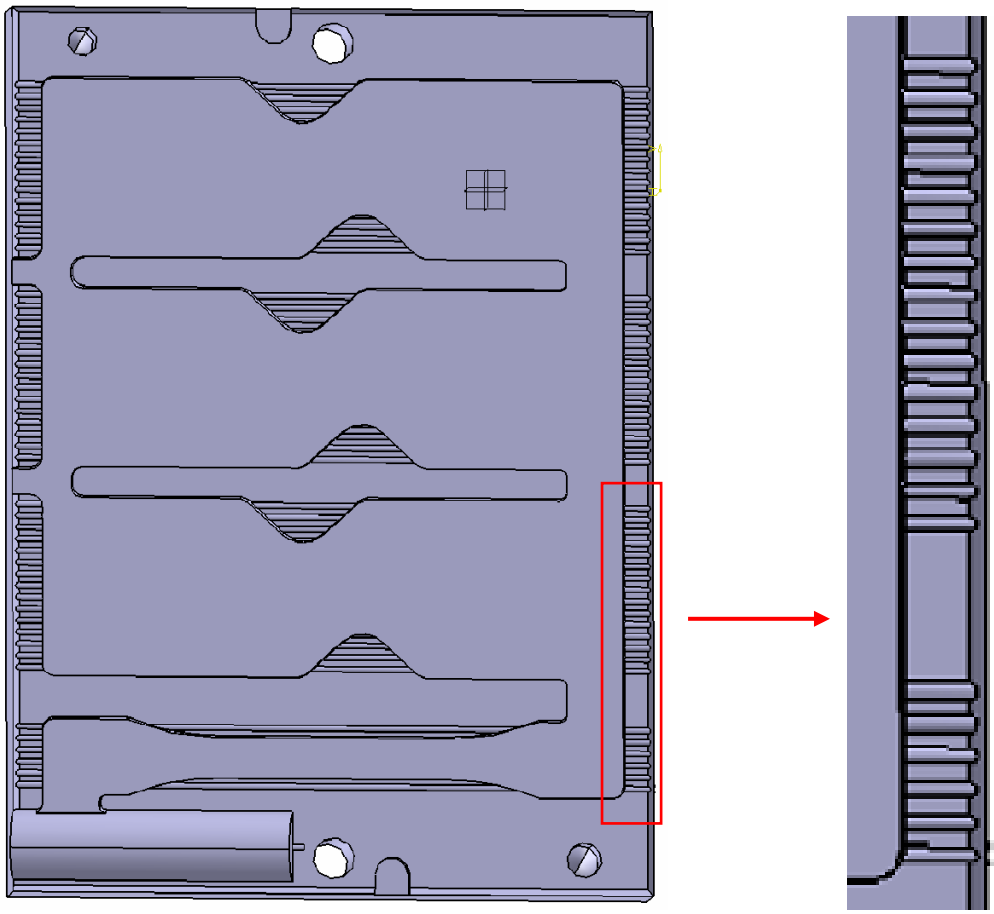

Fig. 2. Moule utilisé pour les échantillons de traction simple et les échantillons à géométrie complexe

2.3. Essai d'arrachement

Les éprouvettes mono-filaments ont été soumis à l'essai d'arrachement. L'échantillon composite est un cylindre de diamètre et de longueur 15 et 50 mm, respectivement. La longueur noyée de fil L est de 50 mm ce qui correspond à un rapport de forme de $L/2a \approx 50$. La fraction volumique nominale de fil est d'environ 0,44%. Le rapport de diamètre (matrice / fil) est égal à 15 qui est assez grand pour minimiser l'effet d'échelle dans l'échantillon.

Pour observer l'interface fil /matrice les échantillons ont été polis légèrement pour générer une surface plane parallèle à l'axe du fil. L'échantillon composite a été placé sur un support métallique percé d'un trou de 3 mm de diamètre en son centre pour le passage du fil. L'essai d'arrachement a été conduit dans l'air à la température ambiante (20 ° C). Les tests ont été

effectués sur une machine de traction MTS/1M (cellules 5 kN) à une vitesse constante de 0,5 mm / min. Le dispositif expérimental est schématisé dans la Fig. 3.

Les observations in-situ du glissement et de la décohésion de l'interface pendant l'essai d'arrachement ont été réalisées avec un appareil photo numérique situé à l'arrière d'un polariscope. Le temps, la charge, le déplacement et la position de la décohésion sont connus pour chaque image. La vitesse de décohésion a été calculée pour différents échantillons. Ce processus a été répété deux fois pour chacun des trois fils NiTi.

A titre de comparaison, plusieurs échantillons ont été fabriqués en utilisant un fil d'acier d'un diamètre de 1 mm.

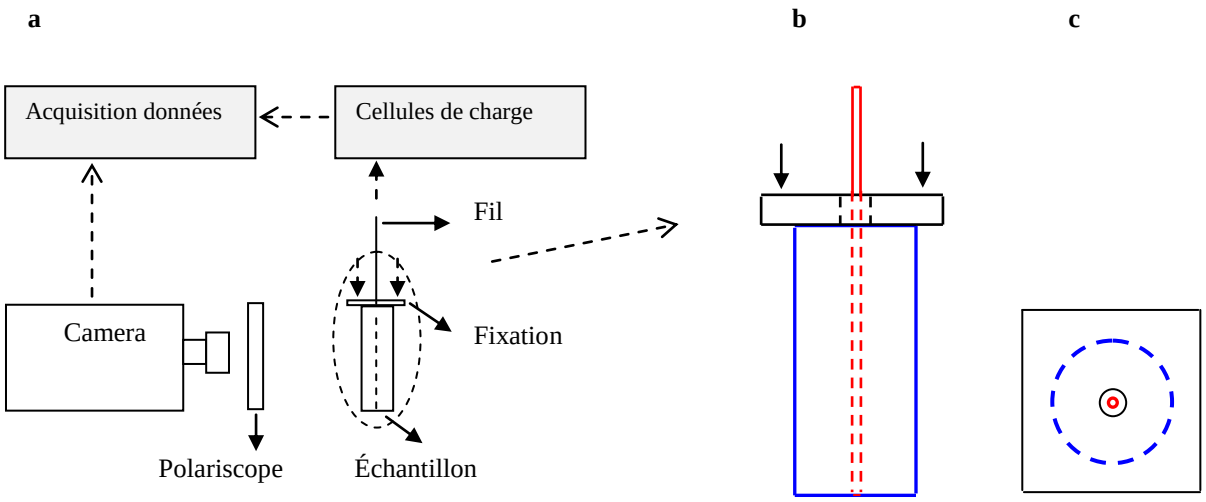

Fig.3. Dispositif expérimental (a) vue de face (b) vue de coté (c) vue de dessus

2.4. Essai de traction uniaxiale

Le comportement mécanique des échantillons composites avec trois fils différents de NiTi à trois températures d'essai, et pour trois fractions volumiques des fils ont été réalisés en utilisant le test de traction uniaxiale.

Les tests ont été effectués dans l'air avec une vitesse constante imposée. Trois températures ont été étudiées : 20, 80 et 90 °C. La procédure d'essai détails de test (équipements, la longueur initiale) est mentionné à section 2.1.2 de la thèse. Les fractions volumiques de fil étudiées sont 0, 6 et 12%.

2.5. Test hétérogènes

Par un l'essai de traction uniaxiale on peut obtenir les propriétés du matériau dans la direction de chargement. Par exemple dans le cas de l'élasticité, le module d'Young sera obtenu à partir

d'un essai de traction, ce qui est suffisant pour un matériau isotrope. Pour les matériaux orthotropes tels que les composites, plusieurs tests doivent être effectués pour déterminer les propriétés du matériau dans des directions longitudinale et transversale par exemple. Pour estimer les propriétés élastiques du matériau composite dans ces deux directions, des échantillons à géométrie complexe sont nécessaires pour induire un champ de contraintes hétérogènes à l'intérieur de l'échantillon. L'objectif est de déterminer simultanément les constantes du matériau à partir d'un seul test de traction. A cette fin, les géométries d'éprouvettes de type "L", "T", "Y" et "Meuwissen", ont été analysées numériquement. D'après les résultats numériques (Fig. 4), l'échantillon Meuwissen semble être susceptible d'induire champ de déformation hétérogène dans un composite unidirectionnel. Dans ce travail, une analyse par éléments finis a été réalisée afin d'optimiser la géométrie de l'échantillon Meuwissen.

L'utilisation de ce type de géométrie permet d'estimer simultanément les propriétés élastiques du matériau composite dans deux directions (perpendiculaire et parallèle à l'axe du fil). L'application d'une charge de traction va générer les champs de déplacement et de contraintes hétérogènes dans les échantillons. Ces champs peuvent être déterminés par une méthode fondée sur la corrélation d'image numérique (DIC). Dans ce travail, deux logiciels ont été utilisés à cet effet : Correli Q4 développé par François Hild et VIC2D. La Fig. 5 montre le dispositif expérimental avec un échantillon Meuwissen.

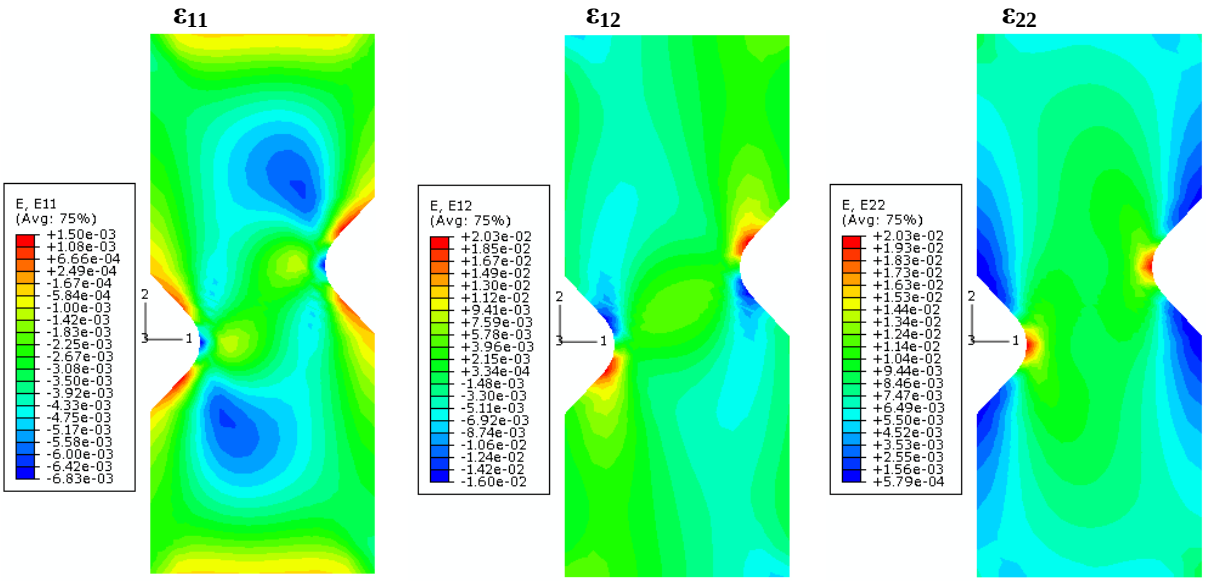

Fig. 4. Les champs de déformation hétérogène généré dans l'échantillon de type Meuwissen, déplacement imposé: 0.6 mm

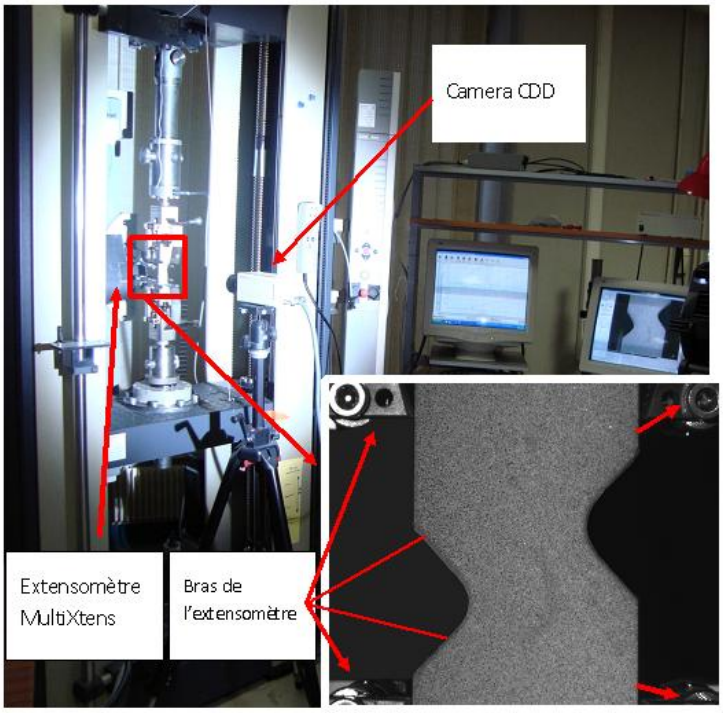

Fig. 5. Dispositif expérimental avec un échantillon Meuwissen. Vue du speckle aléatoire

3. Caractérisation de l'interface matrice/ fils - Influence de la transformation martensitique

L'essai d'arrachement est l'une des méthodes développées pour étudier la qualité de l'interface et les propriétés interfaciales. Ce test a été utilisé pour un composite à renfort en AMF.

Dans les tests d'arrachement, la longueur immergée est généralement petite et la résistance de l'interface au cisaillement (IFSS) peut être estimée en divisant la force maximale (F^{max}) par la surface latérale en supposant que la contrainte de cisaillement est distribuée uniformément dans toute la partie noyée.

Il a été montré que la contrainte de cisaillement dépend de la position sur la longueur noyée et que la décohésion commence avant que la force atteigne la valeur maximale. Selon Zhou et al.[1], la différence entre la contrainte de décohésion et d'arrachement augmente avec la longueur noyée de la fibre. Par conséquent, la méthode habituelle ($F^{max}/2\pi rl$) ne peut pas être utilisée dans tous les cas, en particulier pour le fil à mémoire de forme, en raison de la transformation martensitique qui se produit dans le fil.

Toutefois, pour évaluer l'effet de transformation de phase, une grande longueur intégrée est nécessaire. C'est pourquoi une nouvelle méthode doit être développée afin d'estimer l'IFSS.

[1] Zhou LM, Kim JK, Mai YW. On the single fibre pull-out problem: effect of loading Method; Composites Science and Technology 1992, 45, 2: 153-60.

Cette méthode, fondée sur les travaux du Fu[2], a été développée pour une grande longueur noyée de fil. L'IFSS a été déterminée par la mise en œuvre des résultats expérimentaux dans le modèle.

3.1. Méthode analytique

Lors de l'arrachement d'un fil unique, la contrainte de cisaillement atteint sa valeur maximale au point d'entrée du fil où la décohésion commence. La contrainte de cisaillement interfaciale maximum (notée ci-après MISS) augmente avec la contrainte normale appliquée. Lorsque la MISS augmente et atteint la résistance de l'interface au cisaillement (IFSS ou τ_i), la décohésion commence immédiatement et se propage lorsque que la charge est appliquée. Avec la propagation de la décohésion, la MISS est située à l'extrémité de la zone décollée /collée. En d'autres termes, la position de la contrainte de cisaillement maximale varie en fonction de la propagation du processus de décohésion.

On peut envisager de décomposer l'évolution de la MISS en deux étapes par rapport à la contrainte appliquée σ_p. Les deux phases de cette évolution peuvent être exprimées, respectivement, par[3] :

$$\tau^F_{max} = \beta . \sigma_p \qquad \text{pour } \sigma_p < \sigma_p^* \qquad (1)$$

$$\tau^F_{max} = \tau_i \qquad \text{pour } \sigma_p \geq \sigma_p^* \qquad (2)$$

σ_p^* est la contrainte appliquée au début de la décohésion (contrainte de décohésion). Afin de déterminer le paramètre β, il est nécessaire de connaître la contrainte de cisaillement interfaciale en fonction de la position x. Selon le modèle de Fu[2] et al. pour le test d'arrachement, la contrainte de cisaillement à l'interface fil / matrice est calculée.

$$\tau^F(x) = \frac{a}{2}\alpha\,[\,C_{11}\cosh(\alpha x) + C_{12}\sinh(\alpha x)\,] \qquad (3)$$

Et en reformulation de l'équation 3.3:

$$\tau^F(x) = \frac{\gamma}{2}\left(B\sinh(\frac{\gamma x}{a}) + C\cosh(\frac{\gamma x}{a})\right)\sigma_p \qquad (4)$$

où γ, A, B et C sont données par:

$$\gamma = \sqrt{\frac{1}{A(1+\nu_m)}(\frac{S_f}{S_m} + \frac{E_m}{E_f})}$$

[2] Fu SY, Yue CY, Hu X, Mai YW. Analyses of the micromechanics of stress transfer in single- and multi-fibre pull-out tests. Composites Science and Technology 2000; 60: 569-79.

[3] Y. Payandeh, F. Meraghni, E. Patoor, A. Eberhardt, Debonding Initiation in NiTi Shape Memory Wire Composite, Influence of Martensitic Transformation, Materials and Design 31 (2010) 1077–1084.

$$A = -0.25 + b^2 \frac{2b^2 \ln\frac{b}{a} - b^2 + a^2}{2(b^2 - a^2)^2}$$

$$B = -\frac{S_f E_f}{S_f E_f + S_m E_m}$$

$$C = \operatorname{csch}(2\gamma s) - B\tanh(\gamma s)$$

où $S_f = \pi a^2$, $S_m = \pi (b^2 - a^2)$, E_m et E_f sont, respectivement, le module d'Young de la matrice et du fil, b est le rayon de la matrice, s est rapport d'aspect du fil et ν_m est coefficient de Poisson de la matrice. Les valeurs calculées pour les constantes sans dimension A, B, C et γ sont données dans le tableau 5, pour différentes longueurs de fil et module de Young. La contrainte de cisaillement a une valeur maximale au point d'entrée de fil où x est égal à l. Donc, en remplacement de x par l dans l'équation 4, on obtient pour MISS:

$$\tau_{Max}^{F} = \left[\gamma \sinh(\gamma s)[B\cosh(\gamma s) + C\sinh(\gamma s)] + \frac{C\gamma}{2}\right]\sigma_p \quad (5)$$

en comparant avec l'equation 3.1 :

$$\beta = \gamma \sinh(\gamma s)[B\cosh(\gamma s) + C\sinh(\gamma s)] + \frac{C\gamma}{2} \quad (6)$$

Comme β est indépendant de la contrainte appliquée, la MISS augmente linéairement avec la contrainte appliquée et reste constante dès que la MISS est égal à τ_i.

Tableau 5. Constantes sans dimension calculées pour différentes longueurs de fil et module de Young (a = 0,5 mm, b = 7,5 mm)

	E_f = 27 (GPa)		E_f = 33 (GPa)		E_f = 210 (GPa)	
	l = 10 mm	l=50mm	l = 10mm	l = 50 mm	l = 10 mm	l = 50 mm
A	1,98	1,98	1,98	1,98	1,98	1,98
B	–0,039	–0,039	–0,047	–0,047	–0,238	–0,238
C	0,0696	0,0386	0,0917	0,0468	0,5556	0,2385
γ	0,2064	0,2064	0,1875	0,1875	0,0831	0,0831
β	0,0994	0,0992	0,0897	0,0894	0,0379	0,0317

3.2. Effet de la transformation martensitique sur la propagation de la décohésion

La Fig. 6 montre la propagation de décohésion dans les fils en NiTi et d'acier. Les flèches indiquent la position de décohésion. On remarque que la décohésion commence à partir du point d'entrée de fil et se propage vers la fin de la longueur noyée. Ce processus se déroule lentement et lorsque la longueur collée atteint une valeur critique, le phénomène de

décohésion se produit très rapidement (voir la section 3.4 pour plus de détails). Le fil est ensuite extrait de la matrice de résine par frottement. Les résultats sont présentés dans les Fig. 7 et 8. La position de la décohésion est indiquée sur chaque figure par une flèche.

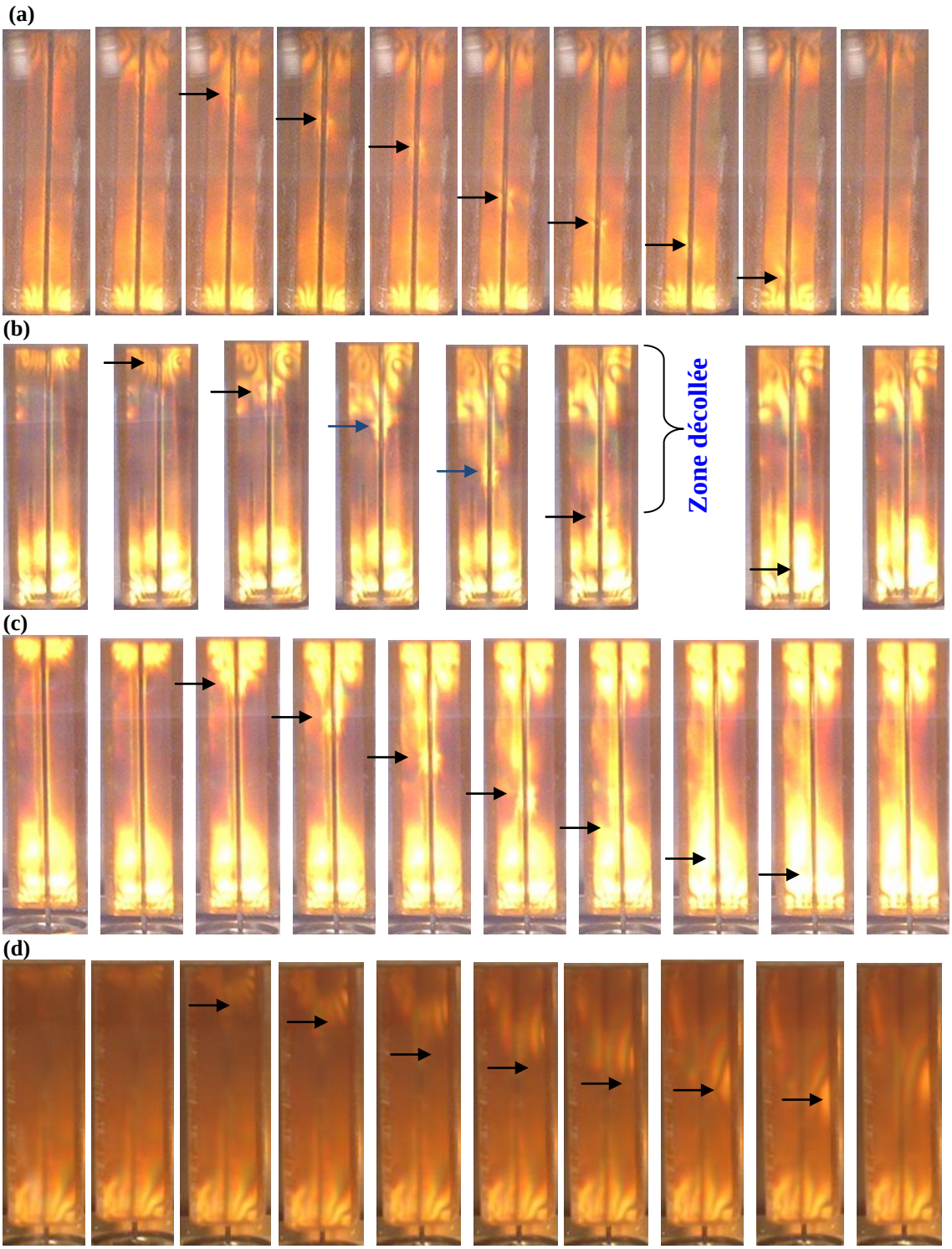

Fig. 6. Processus de décohésion le long du fil pendant l'essai. (a) M550, (b) M450, (c) M400 et (d) fil d'acier. Dans tous les cas, la première image (à gauche) a été prise avant l'essai et dans le premier cas, la dernière a été prise juste après la fin de la décohésion. Les flèches indiquent la position de la décohésion

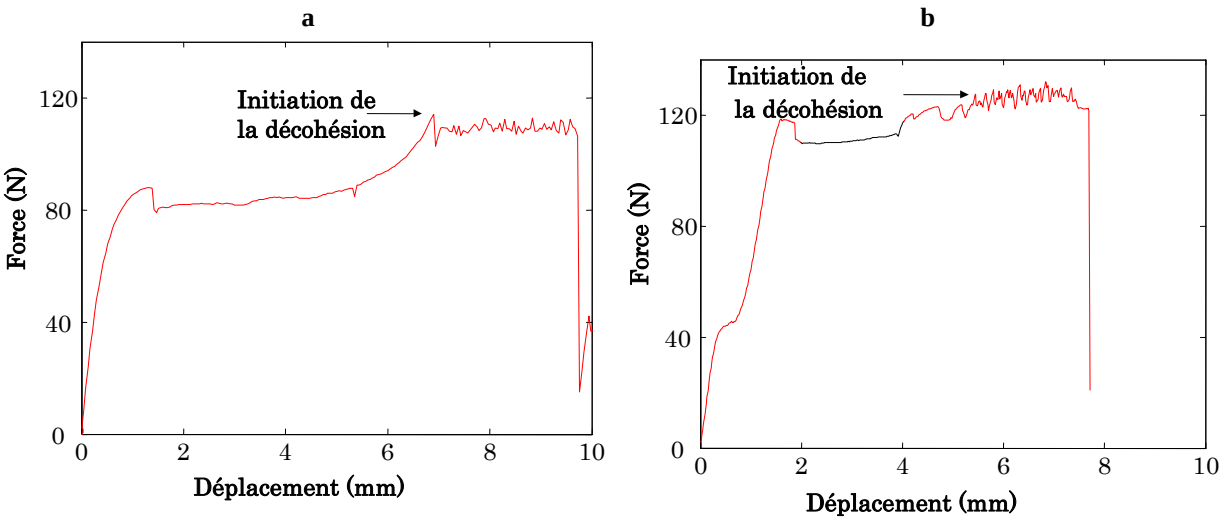

Fig. 7. Force - déplacement pour les échantillons avec (a) M550 et le fil M450 (b)

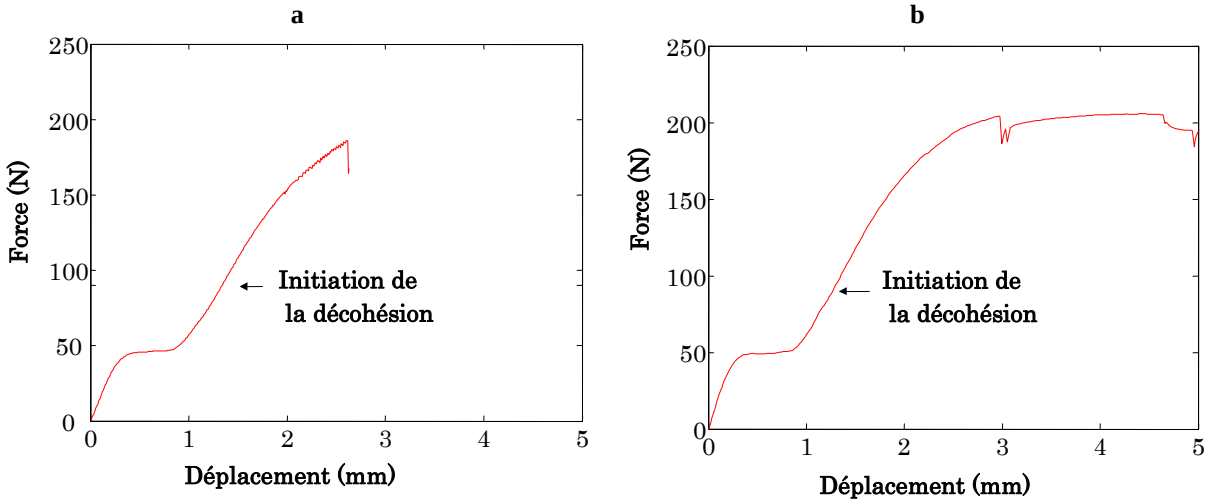

Fig. 8. Force - déplacement pour les échantillons avec le fil M400 (a) sans et (b) avec la transformation

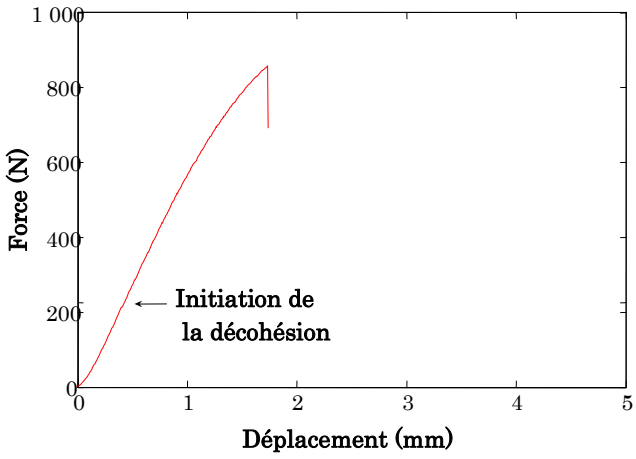

Fig. 9. Force - déplacement pour les échantillons avec le fil d'acier

En comparaison avec les fils NiTi, les fils d'acier se décollent plus rapidement et la longueur critique est significativement supérieure à celle des fils de NiTi. Au contraire, la charge à laquelle la décohésion commence (charge de décohésion) est plus grande que celle des fils NiTi. En d'autres termes, la décohésion interfaciale pour les fils d'acier commence pour des valeurs plus importante de la charge, se propage plus rapidement et atteint la longueur critique plus rapidement que pour les fils de NiTi. La longueur critique pour les fils NiTi est faible (tableau 6). Dans les échantillons M550 et M450 la décohésion commence après la réorientation/ transformation martensitique de la partie libre de fils. La contrainte de décohésion est plus importante que la contrainte de transformation de phase. Dans ces cas, la longueur critique est très faible (par exemple inférieure à 5 mm) par comparaison aux échantillons de fil d'acier.

Table 6. Résumé des résultats

	Mode de déformation	E_f (GPa)	β	F (N)	σ_p^* (MPa)	τ_i (MPa)	Longueur Critique(mm)
M550	Réorientation	27 [(a)]	0,0992	110	140	13,9	< 5
M450	Transformation	33 [(a)]	0,0894	125	160	14,3	< 5
M400	-	40 [(a)]	0,0808	90	115	9,3	≈ 5
Steel	-	210	0,0317	225	286	9,1	≈ 15

(a). Module apparent.

Pour le paramètre β, les valeurs de 0,032, 0,081, 0,089 et 0,099 sont calculés pour l'acier, M400, M450 et M550, respectivement (tableau 6). Il convient de noter que ces valeurs correspondent à une longueur intégrée supérieure à la longueur critique.

En déterminant la résistance de l'interface au cisaillement pour ces systèmes, on est en mesure de comprendre l'effet de la transformation martensitique sur l'initiation de décohésion. Comme il a été noté précédemment, la décohésion commence lorsque le MISS atteint la valeur critique τ_i,. A ce moment la contrainte appliquée est égale à la contrainte de décohésion, σ_p^*, donc :

$$\tau_i = \beta \sigma_p^* \tag{7}$$

La résistance de l'interface au cisaillement τ_i, est calculée lorsque la contrainte de décohésion est connue. A partir des résultats expérimentaux (tableau 6), la contrainte σ_p^*est de 140 MPa pour les échantillons M550 (Fig. 7-a), 160 MPa pour les M450 (Fig. 7-b), 115 MPa pour les M400 (Fig. 8) et 285 MPa pour l'acier / époxyde (Fig. 9) systèmes. La différence entre la σ_p^*est associée à la différence entre le module élastique des fils. En substituant ces valeurs dans l'équation 7 la contrainte τ_i est obtenue. Les résultats sont présentés également dans le tableau 6. La contrainte τ_i est d'environ 14 MPa pour les échantillons M550 et M450 (avec réorientation/ transformation martensitique). Elle est d'environ 9 MPa pour l'acier et M400

(pas de transformation), identique pour deux types différents de fil (par exemple acier et M400), avec la même matrice. Selon Rossi et al[4], la contrainte τ_i pour le composite constitué du fil NiTi martensitique et de la matrice époxyde est de 13 MPa en utilisant la méthode habituelle et d'une longueur intégrée d'environ 5 mm.

Comme mentionné précédemment, la résistance de l'interface au cisaillement est d'environ 9 MPa lorsqu'il n'y a pas de transformation de phase, et il est d'environ 14 MPa lorsque les fils présentent la transformation martensitique. Cela donne une augmentation d'environ 50 pourcent de ce paramètre.

Selon la discussion ci-dessus, la résistance de l'interface au cisaillement est, probablement, indépendante du type de fil, mais semble dépendre de la transformation martensitique (MT) dans le fil.

3.3. Effet de la transformation martensitique sur la propagation de la décohésion

A partir des résultats expérimentaux, dans des échantillons avec des fils M550 et M450, la réorientation / transformation martensitique de la partie libre de fils se produit avant que la décohésion commence. Dans des échantillons avec le fil M400 la transformation martensitique ne se produit pas avant le début de décohésion. En d'autres termes, la charge de transformation de fils M550 et M450 est inférieure à la charge de décohésion alors que pour M400 la charge de décohésion est inférieure à celle de la contrainte de transformation.

Il est utile de noter que pour les échantillons M550 et M450, la charge reste constante au cours de la décohésion et de la propagation tandis qu'elle augmente lors de la propagation de la décohésion dans les échantillons avec des fils M400 ou en acier. Dans les échantillons de fil M400, la charge reste constante dès qu'elle devient plus grande que la charge de transformation (≈ 200 N).

Selon l'observation in situ, le processus de décohésion se produit lentement et, dans certains échantillons avec une vitesse constante. Lorsque la longueur collée atteint une valeur critique, le phénomène de décohésion se poursuit très rapidement.

Pour les échantillons avec M550, la vitesse de décohésion est constant, il est d'environ 8,5 mm / min. Dans la dernière partie (longueur critique) la décohésion se propage avec la vitesse de 14,1 mm / min (valeur moyenne de 9,2 mm / min). La vitesse moyenne de décohésion pour les autres échantillons avec le fil M550 varie entre 8,3 et 9,3. La décohésion se propage dans les échantillons avec le fil M400 à la vitesse de 13,5 à 18,3, et 23,5 mm / min pour la dernière

[4] Rossi S, Deflorian F, Pegoretti A, D'Orazio D, Gialanella S. Chemical and mechanical treatments to improve the surface properties of shape memory NiTi wires. Surface & Coatings Technology 2008; 202: 2214–22.

partie. La vitesse moyenne pour les échantillons avec le fil M400 varie entre 14,4 et 17,3 mm / min. Dans les échantillons avec le fil M400 et un second plateau (avec la transformation Fig. 8-b), les vitesses moyennes sont proches de la valeur la plus faible (14,4) et les vitesses moyennes qui sont proches de celle du haut (17,3) correspondent aux échantillons avec le fil M400 sans second plateau (sans transformation Fig. 8-a). Dans le cas des échantillons avec le fil M450, la décohésion se propage avec une vitesse moyenne qui varie entre 10,6 et 11,3 pour les différents spécimens. L'écart des vitesses de décohésion pour trois types d'échantillons peuvent être associés à la réorientation / transformation martensitique se produisant dans les fils M550 / M450 pendant le chargement. En d'autres termes, en raison de l'augmentation locale de la longueur lors de la réorientation / transformation martensitique pour les fils M550 / M450, la vitesse de décohésion de ces spécimens est faible comparée aux échantillons avec des fils M400. Dans certains spécimens avec le fil M400, la transformation de phase se produit avant que l'interface soit entièrement décollée. En conséquence, la vitesse de décohésion baisse. Cela signifie que la vitesse de propagation de décohésion diminue lorsque la transformation martensitique commence dans les fils.

On peut affirmer que les changements de longueur lors de la réorientation martensitique dans le fil M550 ou la transformation martensitique dans le fil M450 ou parfois dans le fil M400, est la seule raison de la baisse de la vitesse de décohésion. Dans les échantillons avec le fil M400 l'interface se décolle rapidement car il n'y a pas de transformation de phase.

Il est intéressant de noter que lors de l'essai d'arrachement, lorsqu'un fil en AMF est soumis à la charge de traction, la transformation de phase fil ne peut pas se produire avant la décohésion interfaciale. Ce comportement est dû au fait que la transformation martensitique s'accompagne d'une grande déformation inélastique. Mais la transformation se produit immédiatement après la décohésion partielle. L'augmentation de longueur lors de la transformation est à l'origine de la constance de la charge pendant la propagation de la décohésion. Cette augmentation de longueur diminue la vitesse de décohésion car le test est à déplacement imposé. L'équation suivante, développée dans le chapitre 3, a été proposée pour relier la vitesse de décohésion (v_d) à la vitesse de traverse (V_i) et la déformation de transformation (ε^{tr}) [5]:

$$V_i = v_d \cdot \varepsilon^{tr} \qquad (8)$$

La vitesse de décohésion v_d et la déformation de transformation ε^{tr} pour chaque type d'échantillon ont été mesurées à partir des données expérimentales et les résultats sont présentés dans le tableau 7. L'équation 8 peut être validée en comparant les deux dernières colonnes.

[5] Payandeh Y., Meraghni F., Patoor E., Eberhardt A., Effect of Martensitic Transformation on the Debonding Propagation in NiTi Shape Memory Wire Composite, Materials Science and Engineering A 518 (2009), 35-40.

Tableau 7-Vitesse de décohésion v_d, vitesse de déplacement V_i (mm / min) et ε^{tr}

Echantillon	Mode de déformation	ε^{tr} (moyenne)(1)	v_d (mm/min)	v_d (moyenne)(1) (mm/min)	ε^{tr}. v_d	V_i
M550	Réorientation	0,056	8,3-9,3	8,84	0,495	0,5
M450	Transformation	0,045	10,6-11,3	10,95	0,493	0,5
M400 avec MT	Transformation	0,044	10,8-11,4	11,25	0,495	0,5
M400 sans MT	-	-	15,7 -17,3	16,58	-	0,5
M550	Réorientation	0,056	1,9- 1,98	1,95	0,109	0,1

(1)- La déformation et la vitesse moyenne sont calculées en utilisant plusieurs échantillons.

On peut en conclure que la transformation martensitique (MT) réduit la vitesse de décohésion. Comme discuté dans la section 3, la transformation martensitique augmente la résistance de l'interface au cisaillement. Donc, la transformation martensitique affecte non seulement l'initiation de la décohésion, mais aussi la propagation de la décohésion.

4. Propriétés en traction : caractérisation et modélisation micromécanique, influence de la transformation martensitique.

Dans la plupart des travaux sur les composites à renforts en AMF, les fibres pré-déformées ont été intégrées dans une matrice. Le système génère une contrainte dans la matrice qui s'oppose à la charge appliquée et donc améliore les propriétés mécaniques et d'amortissement du composite. Cependant, en y incorporant des fils pré-déformés, il n'est pas possible d'étudier de manière indépendante la transformation martensitique et ses effets sur le comportement global du composite. Dans ce travail, des fils NiTi sans pré-déformation ont été intégrés à la matrice époxyde pour étudier la transformation martensitique.

Dans ce chapitre, le comportement mécanique des composites NiTi-époxyde est étudié en utilisant l'essai de traction uniaxiale. Les éprouvettes avec trois types de fils (M400, M450 et M550) sont testées et trois fractions volumiques des fils (0, 6, et 12%) ont été soumises à l'essai de traction à 20, 80 et 90 °C. Il est constaté que la transformation martensitique se produisant dans les fils influe sur le comportement mécanique du composite. De cette façon, en utilisant le fil avec une contrainte de transformation plus importante on peut améliorer la résistance du composite à la traction. Ce résultat est obtenu en augmentant la température d'essai, en faisant un traitement thermique sur les fils à des températures plus basses ou en augmentant la fraction volumique de fils. La transformation martensitique change le mode de décohésion. En présence de la matrice, la transformation commence simultanément en plusieurs points et par la suite entraîne la décohésion en ces points.

Pour interpréter le rôle du fil dans le composite, un modèle micromécanique est développé à partir du modèle Piggott[6]. Le comportement du fil et de la matrice à différentes températures a été utilisé pour en déduire le comportement mécanique du composite à différentes fractions volume des fils et différentes températures d'essai. Ce modèle permet de comprendre l'influence de la transformation martensitique de fils sur le comportement global des échantillons composites à des températures différentes.

Afin d'appliquer ce modèle au composite utilisés dans ce travail, certains paramètres doivent être modifiés.

• ***Utilisation de la résistance de l'interface au cisaillement*** τ_i

Dans le chapitre 3, la résistance de l'interface au cisaillement τ_i, a été déterminée. Donc, la τ_i est utilisée dans le modèle. Les modifications suivantes doivent être appliquées :

$$m = \frac{E_f \varepsilon_1}{2s\tau_i} - \frac{\coth(n\bar{s})}{ns} \qquad (9)$$

Cette relation permet de déterminer la longueur de la zone décollée. Deux cas peuvent être envisagés : aucun décollement ne se produit lorsque *m* est égal à zéro, et deux zones décollées (aux deux extrémités du fil) sont observables lorsque *m* est positif. Dans ce denier cas le paramètre *m* augmente avec l'augmentation du déplacement imposé.

Lorsque m = 0

La contrainte normale dans le composite s'écrit :

$$\sigma_1 = \frac{V_f}{l}\int_0^l \sigma_f dx + V_m E_m \varepsilon_1 \qquad (10)$$

Lorsque m>0

La contrainte normale dans le composite peut être déterminée en utilisant l'équation suivante :

$$\sigma_1 = \frac{V_f}{l}\left(\int_0^{l(1-m)} \sigma_{fc} dx + \int_{l(1-m)}^{l} \sigma_{fe} dx\right) + V_m E_m \varepsilon_1 \qquad (11)$$

Pour chaque incrément de temps, la valeur de la déformation est connue, et le paramètre *m* est calculé. Suivant la valeur de *m*, la contrainte normale dans le composite sera calculée en utilisant l'équation 10 ou 11. Le paramètre *m* joue un rôle important dans le modèle et peut

[6] Piggott MR. Load Bearing Fibre composites. Canada: Pergamon International Library, 1980.

être considéré comme une longueur décollée normalisée (L_d). Par exemple, lorsque *m* est égal à 0,1, cela signifie que la longueur décollée est égale à 10 % de la longueur noyée.

• Prise en compte du comportement non linéaire

Afin de se rapprocher du comportement expérimental du fil et de la matrice à différentes températures, on est amené à utiliser le module sécant pour le fil et la matrice. L'utilisation du module sécant permet de tenir compte de la transformation martensitique qui se produit dans les fils NiTi. En effet, le modèle ne considère que les propriétés élastiques des constituants mais l'utilisation du module sécant permet de prendre en compte le comportement mécanique des constituants du composite dans les conditions pour lesquelles la transformation du fil se produit. En plus, le comportement non linéaire de la matrice époxyde sera pris en considération. Dans ces conditions, le comportement global du composite avec des fils différents, des fractions volumique des fils et à des températures différentes de test sera déterminé en utilisant les courbes contrainte-déformation expérimentales des fils et de la matrice.

Les résultats micromécaniques ont été comparés à ceux obtenus expérimentalement, la corrélation est satisfaisante.

Résultats expérimentaux

Le tableau 8 présente le module de Young pour les échantillons avec des fractions volumiques de 0, 6 et 12% à trois températures. Le module d'élasticité de la matrice ($V_f = 0$) diminue avec la température et augmente légèrement pour les échantillons composites. L'évolution du module de Young est plus visible lorsque la fraction volumique de fil augmente. Cet effet traduit l'influence des fils sur le comportement global des composites.

La même tendance existe pour la résistance à la traction. Elle augmente avec la température d'essai et la fraction volumique. L'effet de la température est plus évident pour une fraction volumique plus élevée. En fait, l'augmentation de la fraction volumique compense la diminution de la résistance de la matrice plus efficacement.

Tableau 8. Module d'Young et contrainte à 2% de déformation pour les composites avec les fils M550 à différentes températures

Fraction volumique (V_f)	T = 20 °C		T = 80 °C		T = 90 °C	
	Module d'Young (MPa)	ε=2 (%) σ (MPa)	Module d'Young (MPa)	ε=2 (%) σ (MPa)	Module d'Young (MPa)	ε=2 (%) σ (MPa)
0	3300	50	2800	44	2700	42
6%	4200	40	4600	53	5000	58
12%	5300	52	6750	72	7300	78

Tableau 9. Contrainte à 2% de déformation pour les composites avec différents fils à 90 °C

Fil	V_f = 6%	V_f = 12%
	σ (MPa)	σ (MPa)
M550	58	72
M450	66	78
M400	-	84

L'augmentation de la résistance à la traction est liée à la transformation martensitique dans les fils. La contrainte de transformation dans les fils augmente avec de la température et se traduit par une augmentation de la résistance à la traction des échantillons composites. Par conséquent, une plus grande résistance est attendue par le remplacement des fils M550 par des fils M450. Le Tableau 9 illustre que les composites avec des fils M400 ont de plus grandes résistance que ceux comportant des fils M450 ou M550. En conséquence, en intégrant des fils avec une contrainte de transformation plus importante, la résistance à la traction du composite augmente. Le même résultat est obtenu par une élévation de température qui augmente la contrainte de transformation.

De la discussion ci-dessus on remarque que la transformation martensitique dans le fil joue un rôle déterminant dans les propriétés du composite.

Effet de la transformation martensitique sur le comportement mécanique des composites

Si on considère un diagramme contrainte-déformation constitué d'une partie linéaire suivie d'une autre non linéaire, la transformation martensitique devrait influer sur la deuxième partie. En d'autres termes, puisque augmentation de la contrainte de transformation conduit à augmenter la résistance à la traction, la MT doit commencer et d'intervenir dans la deuxième partie.

Tableau 10. Changement de tendance dans la courbe de contrainte-déformation à des températures différentes pour les échantillons avec le fil M550

Fraction volumique	T = 20 °C		T = 80 °C		T = 90 °C	
(V_f)	σ (MPa)	ε (%)	σ (MPa)	ε (%)	σ (MPa)	ε (%)
0	-	-	-	-	-	-
6%	22	0,68	41	1,1	51	1,32
12%	33	0,62	48	0,89	53	0,95

Tableau 11. Changement de tendance dans la courbe de contrainte-déformation pour les échantillons avec différents fils à 90 °C

Fil	V_f = 6%		V_f = 12%	
	σ (MPa)	ε (%)	σ (MPa)	ε (%)
M550	51	1,32	53	0,95
M450	52	1,1	66	1,2
M400	-	-	71	1,3

Dans toutes les courbes contrainte-déformation expérimentales obtenues pour les échantillons composites, deux tendances différentes ont été observées : une partie quasi-linéaire suivie d'une partie non-linéaire. Comme un tel changement de tendance n'a pas été observé pour la matrice époxyde, ce phénomène est dû à la présence des fils. En plus la contrainte correspondant à cette variation augmente avec la contrainte de transformation dans les fils (tableau 10 et 11). Ce changement de tendance, qui commence dès que la transformation a lieu dans les fils, est associé à la transformation martensitique dans les fils.

L'échantillon M450 est un autre exemple qui montre que la matrice suit la transformation se produisant dans les fils. En effet, les éprouvettes avec des fils M450 montrent un effet superélastique à 80 °C alors qu'avec des fils M550 à la même température un tel phénomène n'est pas observé. Comme mentionné au chapitre 2, à haute température les fils M450 montrent le comportement superélastique, alors que dans le cas des fils M550 il n'y a aucun effet superélastique.

En faisant un traitement thermique approprié sur les fils, on peut améliorer certaines propriétés mécaniques telles que résistance à la traction des échantillons du composite. Il est également possible d'avoir composite présentant un effet superélastique.

Effet de la transformation martensitique sur le mécanisme de la décohésion

L'analyse micromécanique prévoit que la décohésion se produit aux extrémités du fil là où la contrainte de cisaillement à l'interface est maximum. Expérimentalement, on observe que les décohésions se repartissent le long des échantillons, Fig. 10. Ce phénomène est plus significatif à haute température parce que la matrice, plus ductile, subit une grande déformation.

a

b

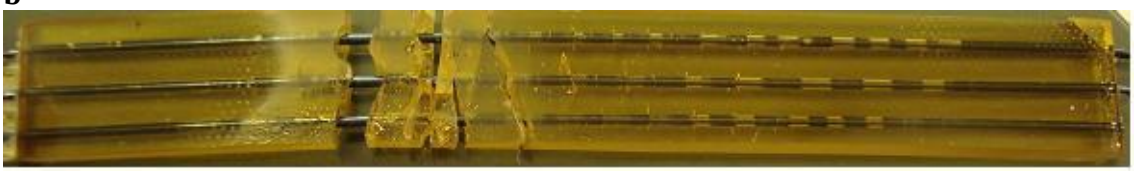

c

Fig. 10. Zones collées/décollées réparties le long des composites a) éprouvette standard avec M550, b) éprouvette rectangulaire avec M550 et c) éprouvette rectangulaire avec M450, testé à 80 ° C

Le mode de décohésion d'un composite à renfort AMF est différent de celui d'un composite ordinaire (sans MT). La différence principale est dûe à la transformation martensitique dans le renfort et permet d'expliquer l'apparition des différents modes de décohésion. Ceci sera discuté ci-après.

Comme mentionné au chapitre 3, lors de l'essai d'arrachement, la transformation martensitique a lieu juste après décohésion partielle de l'interface. Dans l'essai de traction uniaxial, cependant, l'ordre peut être différent parce que les conditions de chargement diffèrent fortement. Le fil et la matrice sont chargés et les deux s'allongent dans le même sens, contrairement à l'essai d'arrachement. Dans ces conditions, la transformation martensitique peut se produire dans le fil noyé et ceci avant la décohésion. Selon l'allongement de la matrice et la résistance de l'interface, on peut avoir une transformation partielle ou complète. En fait, lorsque la déformation de la matrice est plus grande que la déformation de transformation, ε^{tr}, le fil se transforme complètement si l'interface reste intacte. Quand un échantillon composite est chargé, la contrainte dans le fil augmente progressivement, quand elle atteint la contrainte critique (contrainte de transformation) la transformation commence et se poursuit à charge constante dans le fil. La longueur transformée augmente avec le déplacement imposé. Ce phénomène se poursuit jusqu'à ce que la partie noyée soit complètement transformée. Si la matrice est fragile ou si la cohésion de l'interface est trop faible, la décohésion peut avoir lieu avant la transformation complète.

Lorsque le fil de NiTi est soumis à la charge de traction, la transformation martensitique commence d'un côté du fil et se propage vers l'autre extrémité[7]. Mais lorsque le fil est noyé dans une matrice, la transformation commence en plusieurs points en même temps. Il est connu que la propagation de la transformation induite par la contrainte est beaucoup plus facile que la nucléation de la martensite dans la région non transformées[7]. Par conséquent, le nombre de points où la transformation commence, devrait être limité. En d'autres termes, en présence de la matrice, la transformation martensitique peut commencer en même temps à un certain nombre de points et se propage alors que la charge est appliquée.

Puisque le fil et la matrice ont la même déformation mais des modules d' Young différents, l'état de charge sera différent dans le deux composants. En effet dans un essai à déplacement imposé, le déplacement est le même dans le fil et la matrice, et par suit la charge dans le fil augmente plus rapidement que dans la matrice (le module d'Young du fil est supérieur à celui de la matrice). La charge dans le fil atteint la charge de transformation et autorise la transformation martensitique tout le long de l'échantillon. Par exemple dans le cas du composite avec un fil M550, la contrainte normale dans le composite est d'environ 25 MPa pour une déformation appliquée de 0,6%. La contrainte dans le fil est alors d'environ 100 MPa et reste constante lorsque la contrainte appliquée augmente. Dans un fil d'acier (sans transformation) la charge augmente même après la décohésion. Les fils M550 se déforment par réorientation à 100 MPa, ce qui implique que cette réorientation peut se produire tout le long du fil, car la contrainte dans cette partie du fil est égale à la contrainte de réorientation. La Fig. 11 montre la répartition des contraintes dans les échantillons avec le fil M450. La contrainte dans le fil reste constante quand elle atteint la contrainte de transformation (140 MPa) pour une déformation de 0,6%. Il est connu que la transformation martensitique a lieu dès que la charge atteint la charge de transformation. Comme toute la partie uniforme de l'échantillon s'allonge (et pas seulement en un point), la transformation doit se produire en plusieurs points en même temps dans le fil pour suivre l'allongement de la matrice. Lorsque le fil est en contact avec la matrice et ils subissent tous les deux la même déformation. Par conséquent, le fil ne peut pas se transformer en un seul point (comme c'est le cas pour un fil seul). Donc, la transformation de fil doit se produire simultanément dans toute la partie uniforme pour avoir la même élongation que la matrice.

En conclusion, en présence de la matrice la transformation peut avoir lieu à certains points pour compenser le déplacement appliqué par la matrice. Pendant que la charge est appliquée, ce phénomène se poursuit et la longueur transformée augmente. Une fois la longueur transformée atteint certaine valeur, l'état de contrainte va changer à cause du fait que le diamètre de fil après la transformation diminue. Dans ces conditions, la composante radiale de

[7] K. Otsuka, X. Ren, physical metallurgy of NiTi based shape memory alloys, Review Article, Progress in Materials Science 50 (5) (2005), p. 511-678.

la contrainte pourrait accélérer l'initiation de décohésion interfaciale. Et puisque la transformation est commencée simultanément en plusieurs points, la décohésion peut se produire en plusieurs points. Ces phénomènes pourraient créer certains nombres de décohésion avec une courte longueur comme le montre la Fig. 10. Lorsque les fils sans transformation de phase sont noyées dans une matrice, il est prévu de disposer de deux longues pièces décollée à deux extrémités de fils, car la contrainte de cisaillement interfaciale a une valeur maximale aux extrémités de fils.

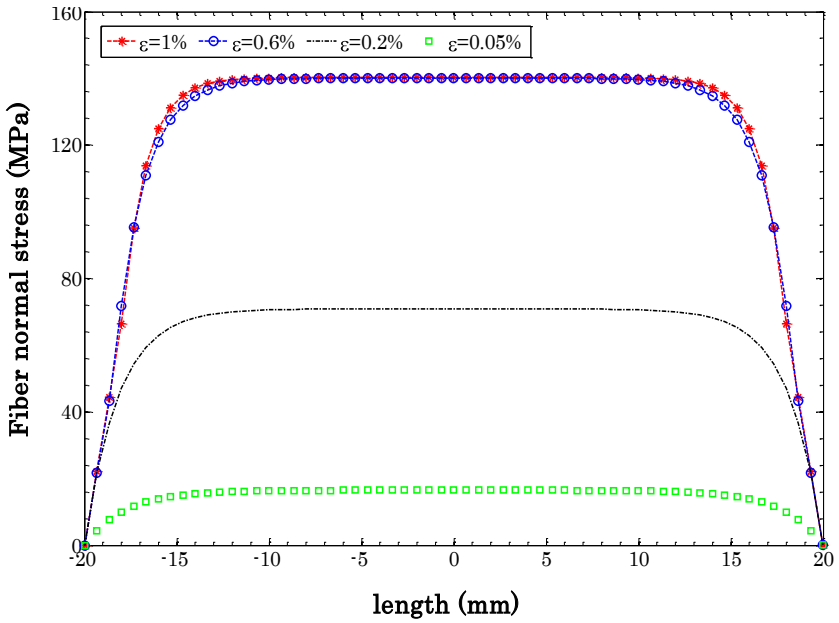

Fig. 11. Répartition des contraintes dans les échantillons avec le fil M450 à 20 °C

5. Identification des paramètres du composite NiTi/époxyde

L'essai de traction est la méthode la plus courante pour identifier le comportement mécanique d'un matériau isotrope. Il a été étudié dans le chapitre 4. Pour des matériaux anisotropes, tels que les matériaux composites étudiés, plusieurs essais sont nécessaires pour identifier les paramètres du matériau dans des directions différentes. L'alternative proposée est de réaliser un essai hétérogène à partir d'une éprouvette à géométrie complexe soumis à un chargement uniaxial. Ce type de tests permet l'identification simultanée des différents paramètres.

Le problème principal est de mesurer les champs de déplacement hétérogènes générés au cours de ce type de test. Ces dernières années, des techniques optiques tels que la corrélation d'image numérique (CIN) ont été développés pour mesurer des champs de déplacement hétérogènes et par suite la déformation. Toutefois, pour les essais hétérogènes, il n'y a pas de relation explicite entre le déplacement et la charge appliquée et par suite, le tenseur des

contraintes est inconnu. Une méthode inverse est alors nécessaire pour identifier les paramètres du matériau.

Le principe de la méthode d'identification est de comparer un champ de déformation expérimental avec un champ numérique. Le problème inverse sera résolu de manière itérative en mettant à jour les paramètres dans le modèle d'éléments finis de telle manière que le champ de déformation calculé numériquement corresponde au champ mesuré expérimentalement.

Dans ce travail, la méthode d'identification est développée pour identifier les quatre constantes élastiques indépendants E_{11}, E_{22}, G_{12} et ν_{12} d'un matériau composite orthotrope. Le matériau étudié est le composite époxyde-fils NiTi. La méthode est fondée sur les mesures de champs de déplacement en surface des échantillons. A cet effet, les échantillons à géométrie complexe (type Meuwissen) ont été soumis à une charge de traction. Les champs de déformation sont mesurés en utilisant les logiciels Correli-Q4 et VIC2D sur la base de la corrélation d'images numériques. La modélisation éléments finis est réalisée à l'aide d'ABAQUS.

La qualité des images pour les échantillons testés à haute température n'est pas satisfaisant car la caméra est située à l'extérieur de la chambre d'ambiance. Par conséquent, les résultats ont été obtenus pour les échantillons testés à la température ambiante.

Algorithme d'identification

Les étapes nécessaires pour résoudre le problème inverse sont :

- Construction d'une base expérimentale pertinente avec une condition de sensibilité des données expérimentales aux paramètres qu'on cherche à identifier ;
- Définition d'une fonction coût ;
- Choix de l'algorithme d'optimisation ;
- Calcul de la matrice de sensibilité ;
- Choix du critère d'arrêt.

Les résultats de simulation basés sur le calcul par éléments finis sont comparés à la base de données expérimentale (de référence). Au cours de chaque itération, une nouvelle série de paramètres est proposé. La nouvelle base de données est à nouveau calculée par rapport à la référence. La procédure sera répétée jusqu'à ce que la fonction coût devienne faible et atteigne une valeur prédéfinie (10^{-8} dans ce travail) utilisée comme critère d'arrêt.

Fonction coût

La fonction coût (fonction objectif) est égale au carré de la différence entre les résultats expérimentaux et la réponse calculée pour le système étudié. En minimisant cette fonction pendant le calcul inverse, les paramètres du matériau seront extraits par la résolution de l'équation appropriée. La fonction coût de ce travail est construite sur la base des composantes de la déformation (ε_{11}, ε_{22} et ε_{12}) et la charge appliquée (f). La charge a été prise en compte pour régulariser et éviter de problème mal-posé connu pour le cas élastique.

$$F(P) = \frac{1}{2}\left(\frac{\sum_{i=0}^{m}\left[\varepsilon_{1,i}^{Exp} - \varepsilon_{1,i}^{Num}\right]^2}{\sum_{i=0}^{m}\left[\varepsilon_{1,i}^{Exp}\right]^2} + \frac{\sum_{i=0}^{m}\left[\varepsilon_{2,i}^{Exp} - \varepsilon_{2,i}^{Num}\right]^2}{\sum_{i=0}^{m}\left[\varepsilon_{2,i}^{Exp}\right]^2} + \frac{\sum_{i=0}^{m}\left[\gamma_{12,i}^{Exp} - \gamma_{12,i}^{Num}\right]^2}{\sum_{i=0}^{m}\left[\gamma_{12,i}^{Exp}\right]^2}\right) + \frac{1}{2}\frac{\left[f^{Exp} - f^{Num}\right]^2}{\left[f^{Exp}\right]^2} \qquad (12)$$

La différence entre la base de données expérimentale et numérique est minimisée par la mise à jour des quatre modules d'élasticité indépendants : E_{11}, E_{22}, G_{12} et ν_{12}.

Optimisation des algorithmes

Afin de mettre à jour les paramètres, un incrément (ΔP) est calculé à chaque itération :

$$p_{k+1} = p_k + \Delta p_k \qquad (13)$$

De cette façon, différentes méthodes peuvent être utilisées comme le gradient conjugué, une méthode de type Gauss-Newton ou les algorithmes de type Marquardt. L'algorithme d'optimisation utilisée dans ce travail est de Levenberg-Marquardt sur la base de la méthode de Gauss-Newton.

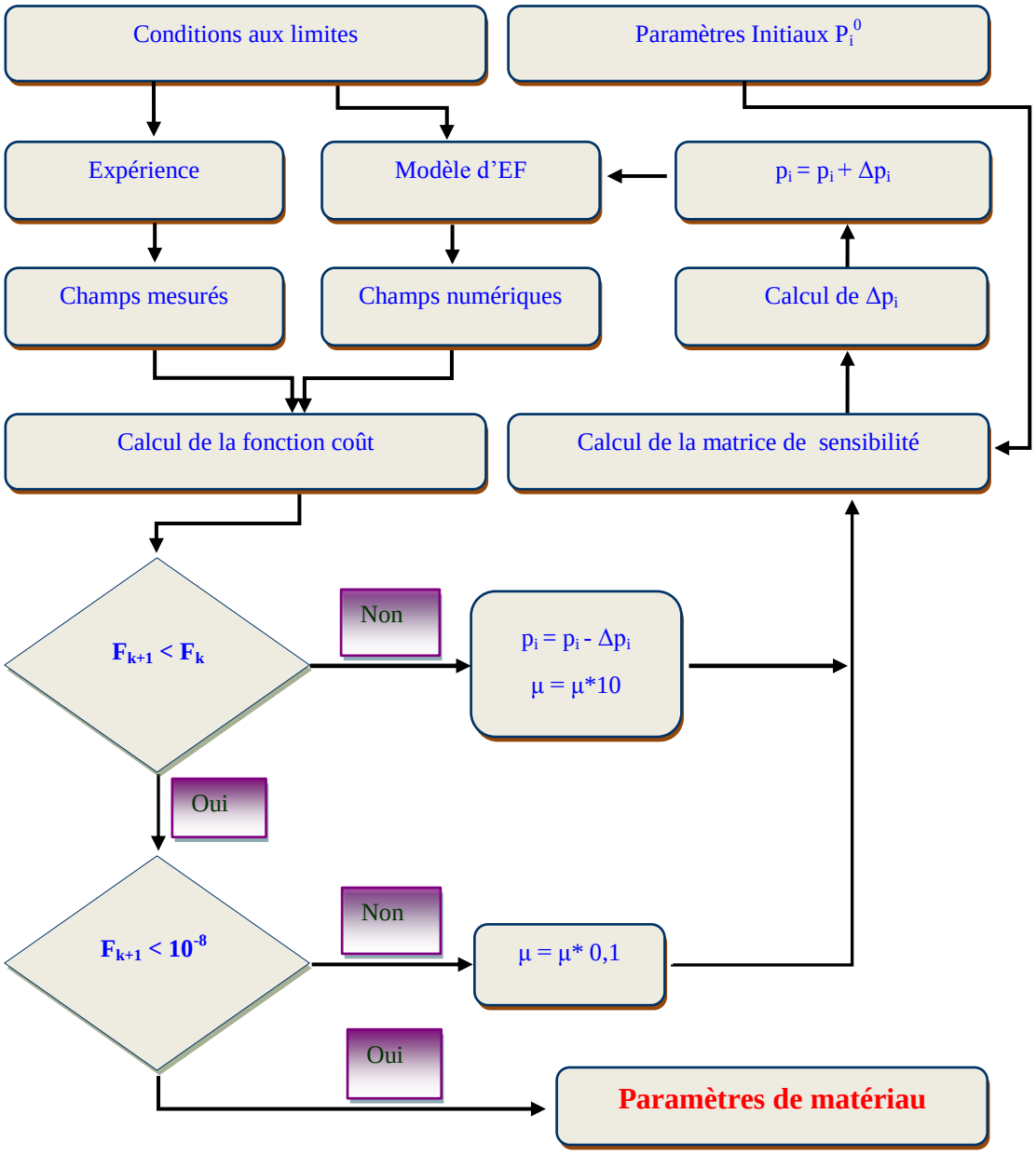

Fig.12. Algorithme d'identification

Calcul de la matrice de sensibilité

La matrice de sensibilité a été calculée par la méthode de différenciation directe pour chaque itération en perturbant les quatre paramètres. En d'autres termes, les paramètres ont été perturbés, un par un et la réponse du système ont été enregistrée pour calculer la sensibilité. Une fois que la matrice de sensibilité a été obtenue ΔP peut être calculé.

5. 1. Convergence et analyse de la stabilité

Avant d'utiliser les champs de déformation mesurés expérimentalement (base de données expérimentale réelle), la méthode d'identification a été vérifiée en utilisant des champs de

déformation calculés (base de données expérimentale artificielle). De cette façon, deux vérifications ont été effectués afin d'examiner la performance de la méthode (test de convergence) et sa stabilité (analyse de stabilité). Le test de convergence est satisfait ainsi que l'analyse de stabilité et donc la méthode peut être appliquée pour la véritable base de données expérimentale.

Afin de simuler le test hétérogène, un maillage structuré rectangulaire majoritairement quadratique avec 714 nœuds, 656 éléments et une ZOI avec 336 éléments a été sélectionné (Fig. 13-a).

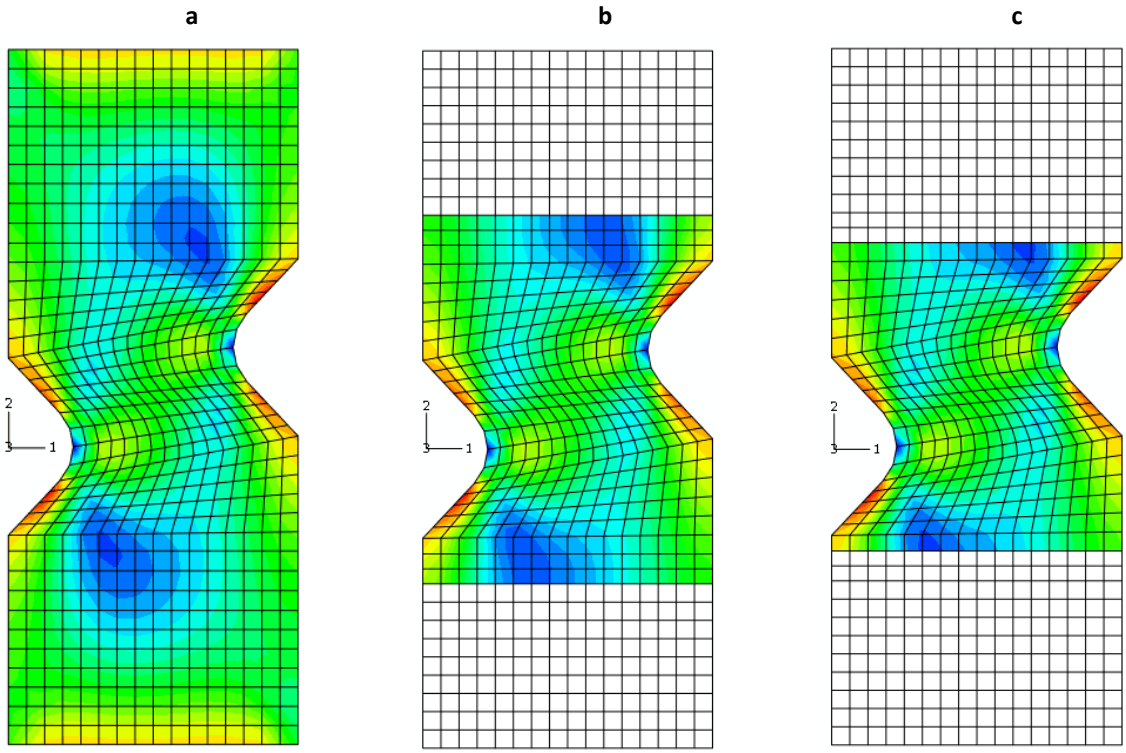

Fig. 13. Les zones d'intérêts (ZOI) avec a) 656, b) 400, c) 336 éléments

Les champs de déformation expérimentale réels sont obtenus à partir de l'essai hétérogène des échantillons composites avec différentes fractions du volume de fil à la température ambiante. Pour déterminer les champs de contraintes expérimentaux, comme mentionné précédemment, deux logiciels ont été utilisés et les résultats ont été comparés.

5.2. Résultats d'identification

5.2.1. Résultats d'identification en utilisant Correli-Q4

Le tableau 12 présente les résultats d'identification qui ont été obtenus en utilisant le logiciel Correli-Q4. Pour chaque échantillon, les calculs ont été effectués à partir de différentes

estimations initiales. Ce tableau montre que lorsque la fraction volumique de fibres augmente les paramètres E_{11}, E_{22} et G_{12} augmentent, mais le coefficient de Poisson diminue.

Tableau 12 Résultats d'identification, la base de données expérimentale créée en utilisant Correli-Q4

V_f	E_{11} (MPa)	E_{22} (MPa)	ν_{12}	G_{12} (MPa)	FC
0	3360±100	3575±20	0,35±0,01	1455±20	0,1100
0,03	3495±60	4575±10	0,33±0,005	1770±10	0,1090
0,03	3535±100	4505±20	0,33±0,005	1785±20	0,0845
0,10	3880±100	6555±90	0,25±0,01	2055±70	0,35

Les déformations (ε_{11}, ε_{22} et ε_{12}) dans chaque élément mesurées expérimentalement, sont comparées aux valeurs numériques obtenues en utilisant les paramètres identifiés. Une bonne corrélation est observée.

5.2.2. Résultats d'identification en utilisant VIC2D

Les paramètres identifiés à l'aide de la base de données expérimentale extraite par VIC2D sont détaillés dans le tableau 13. Une bonne corrélation est trouvée en comparant ces résultats aux résultats détaillés dans le tableau 12.

Tableau 13- Résultats d'identification, la base de données expérimentale créée en utilisant VIC2D

V_f	E_{11} (MPa)	E_{22} (MPa)	ν_{12}	G_{12} (MPa)
0	3430±70	3550±20	0,345±0,005	1480±10
0,03	3470±80	4120±20	0,33±0,01	1650±20
0,05	3670±80	4760±20	0,305±0,005	1705±20
0,10	3980±50	6440±10	0,255±0,005	2230±10

Les champs de déplacement et de déformation déterminés expérimentalement en utilisant VIC2D sont comparés aux champs obtenus par calcul à partir des paramètres identifiés. De bonnes corrélations entre les champs expérimentaux et numériques sont observées.

A partir des résultats expérimentaux, il est possible de valider le module de Young dans la direction de la charge (E_{22}) pour tous les échantillons. Il est également possible de vérifier l'E_{11} dans les échantillons sans fibre qui pourrait être identique à l'E_{22} dans le même échantillon. De résultats des essais de traction, l'E_{22} est d'environ 3300, 4200 et 5300 MPa pour les échantillons avec 0, 6 et 12% fraction volumique de fil. Les résultats de l'identification (E_{22}) ont été comparés aux résultats obtenus par essai de traction et une conformité satisfaisant a été observée.

Afin de vérifier les valeurs identifiées, ces paramètres ont été calculés pour différentes fractions volumiques de fil en utilisant le logiciel Sim-CEEC. développé par F. Meraghni sur la base du modèle de Mori-Tanaka. Les résultats sont détaillés dans le tableau 14. La comparaison des paramètres calculés avec les résultats identifiés est satisfaisante.

Tableau 14. Paramètres du matériau obtenu en utilisant le modèle Mori-Tanaka (E_f=30000 MPa, ν_f=0.3)

V_f	E_{11} (MPa)	E_{22} (MPa)	ν_{12}	G_{12} (MPa)
0	3500	3500	0,36	1287
0,03	3716	4284	0,31	1350
0,05	3854	4807	0,29	1394
0,10	4194	6116	0,24	1511

6. Conclusion

Ce travail est consacré à l'élaboration et l'analyse de comportement thermomécanique d'un composite constitué d'une matrice en résine époxyde renforcée par des fils en alliage à mémoire de forme (AMF). Le fil, en NiTi écroui a été soumis à trois traitements thermiques afin d'obtenir des caractéristiques de transformation différentes. Trois types d'échantillons, nommés pull-out, traction simple et éprouvettes à géométrie complexe ont été réalisés. Les composites ont été fabriqués par moulage suivi d'une cuisson et d'une post-cuisson. Les tests ont été effectués à trois températures (20, 80 et 90 °C) à vitesse constante.

L'effet de la transformation martensitique sur l'initiation et la propagation de la décohésion a été étudié à partir de l'essai d'arrachement. D'après les observations in situ, la décohésion commence à partir du point d'entré des fils et continue vers la fin de la longueur noyée. Il est observé que lorsqu'il n'y a pas de transformation martensitique la décohésion se propage rapidement alors qu'elle est plus lente quand il y a transformation ou réorientation de la martensite. Il a été constaté expérimentalement que, lorsqu'il n'y a pas de transformation de phase l'IFSS est d'environ 9 MPa alors qu'elle est d'environ 14 MPa lorsque la transformation martensitique / réorientation se produit dans le fil.

Le comportement mécanique de la matrice de résine, l'effet de la température d'essai et de la fraction volumique de fil ont été déterminés en utilisant le test de traction simple. Il est constaté que la transformation martensitique du fil influe de manière significative le comportement mécanique des échantillons composites.

Il est proposé qu'en présence de la matrice la transformation se produit simultanément en plusieurs points qui peut générer la décohésion en plusieurs endroits en même temps. C'est pour ça qu'on a observé une intermittence de zones décollées et non décollées.

Afin d'estimer les propriétés élastiques du matériau composite dans les directions perpendiculaire et parallèle à l'axe du fil, les échantillons à géométrie complexe ont été soumis à un chargement simple. Les champs hétérogènes de déplacement/ de déformation générés grâce à la géométrie complexe ont été mesurés et les paramètres du matériau ont été identifiés à partir de la méthode inverse développée. Les résultats ont ensuite été comparés aux résultats obtenus par la méthode de Mori-Tanaka. Le champ de déformation obtenu numériquement, à partir des paramètres identifiés a été comparé à ceux obtenus expérimentalement. Une bonne conformité a été trouvée dans les deux cas.

La contrainte résiduelle, le refroidissement sous la contrainte peut affecter les caractéristiques de transformation d'un fil d'AMF enrobé. En plus, la transformation se produisant dans le fil en présence d'une matrice peut être différente de celle du fil seul. La méthode d'identification peut être appliquée pour estimer les paramètres réels de fils NiTi dans ces conditions. A cet effet, il est nécessaire d'utiliser une matrice dont le niveau de déformation est à l'ordre de 7%. Ceci peut être réalisé soit en changeant l'état de cuisson pour préparer des échantillons plus ductile ou en faisant des essais à 80 °C. Ce dernier nécessite d'utiliser un système d'acquisition d'image spécifique à cette température.

Elaboration et caractérisation de composites intelligents NiTi/ époxyde - Effets de la transformation martensitique sur le comportement mécanique et sur la décohésion interfaciale

RESUME :

Ce travail est consacré à l'élaboration et l'analyse de comportement thermomécanique d'un composite constitué d'une matrice en résine époxyde renforcée par des fils en alliage à mémoire de forme (AMF). Le fil, en NiTi écroui a été soumis à trois traitements thermiques afin d'obtenir des caractéristiques de transformation différentes. Trois types d'échantillons, nommés : pull-out, traction simple et éprouvettes à géométrie complexe ont été réalisés. Les composites ont été fabriqués par moulage suivi d'une une cuisson et d'une post-cuisson. Les tests ont été effectués à trois températures (20, 80 et 90 ° C) et à vitesse de chargement constante.

Des échantillons mono-filaments ont été réalisés et soumis à un essai d'arrachement afin d'étudier l'effet de la transformation martensitique sur l'initiation et la propagation de la décohésion. D'après les observations in situ, la décohésion commence à partir du point d'entré des fils et continue vers la fin de la longueur noyée. Il a été constaté expérimentalement que, la transformation martensitique dans le fil diminue la vitesse de propagation de la décohésion interfaciale et augmente la résistance de l'interface au cisellement.

Le comportement mécanique de la matrice, l'effet de la température d'essai et de la fraction volumique de fil ont été déterminés en utilisant le test de traction simple. Les essais ont été conduits à trois températures. Il est constaté que la transformation martensitique se produisant dans le fil influe de manière significative le comportement mécanique des échantillons composites. De cette façon, en utilisant le fil avec une contrainte de transformation plus grande améliore la résistance du composite à la traction. Ceci est réalisé soit en augmentant la température d'essai ou en faisant un traitement thermique à une température plus basse. Il est proposé que en présence de la matrice la transformation se produit simultanément en plusieurs points. On observe alors, une intermittence de zones décollées et non décollées.

Dans ce travail, les échantillons à géométrie complexe ont été conçus et fabriqués afin d'estimer les propriétés élastiques du matériau composite dans deux directions (perpendiculaire et parallèle à l'axe du fil). Les spécimens avec un mouchetis aléatoire ont été soumis à un chargement simple. Les champs hétérogènes de déplacement/ de déformation générés grâce à la géométrie complexe des échantillons composites ont été mesurées. Une méthode inverse a été développée et les paramètres du matériau ont été identifiés. Les résultats ont ensuite été comparés aux résultats obtenus par la méthode de Mori-Tanaka. Le champ de déformation obtenu numériquement, à partir des paramètres identifiés a été comparé à ceux obtenus expérimentalement. Une bonne corrélation a été trouvée dans les deux cas.

Mots clés : Alliage à mémoire de forme (AMF), NiTi, transformation martensitique, composite, décohésion.

ARTS ET MÉTIERS ParisTech

ParisTech INSTITUT DES SCIENCES ET TECHNOLOGIES PARIS INSTITUTE OF TECHNOLOGY

Elaboration and characterization of NiTi/epoxy smart composite - Effects of martensitic transformation on mechanical behavior and interface debonding

ABSTRACT

In this work a near equiatomic NiTi shape memory wire epoxy matrix composite is studied. The NiTi wire in as drawn condition was subjected to three heat treatments in order to prepare the wires with different transformation characteristics. Three metallic moulds were designed for different types of samples, namely pull-out, tensile and heterogeneous test specimens. The composite specimens were elaborated by casting followed by curing and post curing process. The tests were conducted at three temperatures (20, 80 and 90 °C) and at a constant cross-head speed.

The single NiTi wire specimens with a long embedded length were subjected to the pull-out test in order to study the effect of martensitic transformation/reorientation on the debonding initiation and also on the debonding propagation. For comparison, several steel wire samples were prepared through the same procedure. From in-situ observations, the debonding begins from wire entry point and proceeds to the embedded end. It was observed that when no phase transformation occurs in the wire, the debonding propagates rapidly whilst it is slow when there is wire phase transformation or martensitic reorientation. It was found that the debonding rate depends on the displacement rate as well as the length change during phase transformation. It has been experimentally found that, the interfacial shear strength increases when the martensitic transformation takes place.

The mechanical behavior of the resin matrix and the effect of test temperature, wire volume fraction have been determined using standard tensile test. The tests have been conduced at three temperatures. It is found that the martensitic transformation occurring in the wire affect the mechanical behavior of the composite specimens. In this way, using the wire with larger transformation stress enhances the composite tensile strength. This is achieved either by increasing the test temperature or by using the wires heat treated at lower temperatures. The tensile strength increases also by increasing the volume fraction of wires. It is proposed that on the constraint of matrix, the transformation occurs simultaneously at several points that result in intermittent debonded and bonded zones.

In this work the samples with complex geometry were designed and fabricated in order to estimate the elastic properties of the composite material in two directions (perpendicular and parallel to the wire axis). The specimens with random speckle were then subjected to the simple loading. The heterogeneous displacement/strain fields generated due to the complex geometry of the composite samples were measured. An inverse method was established in this work and the material parameters were identified. The results were then compared to the results obtained by Mori-Tanaka method. Moreover, the numerical strain fields obtained using the identification parameters was compared to the experimental ones. A good correlation was found in both cases.

Keywords : Shape memory alloy (SMA), martensitic transformation, composite, debonding.

ARTS ET MÉTIERS ParisTech

ParisTech INSTITUT DES SCIENCES ET TECHNOLOGIES PARIS INSTITUTE OF TECHNOLOGY